Enabling Controlled Material Synthesis and Processing via Predictive Modeling and Simulation

by

Guanglong Huang

A dissertation submitted in partial fulfillment
of the requirements for the degree of
Doctor of Philosophy
(Materials Science and Engineering and Scientific Computing)
in the University of Michigan
2023

Doctoral Committee:

Professor Katsuyo Thornton, Chair
Professor Vikram Gavini
Associate Professor Liang Qi
Assistant Professor Wenhao Sun

Guanglong Huang

umjihgl@umich.edu

ORCID iD: 0000-0002-2627-0901

Dedication

In honor of my grandfather and grandmother

Acknowledgements

First and foremost, I am grateful to Prof. Katsuyo Thornton, for being my research advisor during my undergraduate, master and Ph.D. study. Her invaluable feedback and insightful advice on my research projects enable me to deliver high-quality papers and conference presentations. It is difficult to imagine finalizing this dissertation without her help and support. I would also like to express my gratitude to Prof. Liang Qi, Prof. Vikram Gavini, and Prof. Wenhao Sun for serving on my committee and providing valuable inputs over the course of my dissertation research.

Additionally, I would like to give my appreciation to Thornton group members, both past and present, for the help they offered to my research study. Dr. David Montiel provided me with many useful guidance on phase-field crystal modeling, phase-field modeling and heat transfer modeling. Sicen Du gave me a clear explanation on the level-set method. I am thankful to Mojue Zhang, Praveen Soundararajan, Alexander Mensah, Zachary Croft, Eymana Maria, and Archi Agrawal, for collaborating with me on various research projects. I also want to express my gratitude to Vishwas Goel, Yanjun Lyu, Jason Luce, Dr. Saeed Kazemiabnavi, Dr. Hui-Chia Yu, Dr. Beck Andrews, Dr. S M Golam Mortuza, Dr. Erik Hanson, Dr. Alex Chadwick and Dr. Doaa Taha, for their helpful conversations.

I would like to thank all my experimental collaborators, Daniel O'Nolan, Gabrielle E. Kamm, Karena W. Chapman, Rebecca D. McAuliffe, Gabriel M. Veith, Allison Wustrow, James R. Neilson, Jonathan J. Denney, Yusu Wang, Adam A. Corrao, Peter G. Khalifah, Matthew J. Higgins, Jiwoong Kang, Marcel Chlupsa, Ashwin J. Shahani, for their kindness in providing their

measurement results to us, which facilitated our development and validation of models and algorithms.

I would also like to acknowledge the funding agencies and computational resources that made my research possible. My study on phase-field modeling of abnormal grain growth was supported by the National Science Foundation under Award No. DMR-2003719. My work on phase-field modeling of metathesis reactions, on heat-transfer modeling, as well as on algorithm development were supported as part of GENESIS: A Next Generation Synthesis Center, an Energy Frontier Research Center funded by the U.S. Department of Energy (DOE), Office of Science, Basic Energy Sciences under award No. DE-SC0019212. The research on phase-field crystal modeling was primarily supported by the National Science Foundation (Grant DMR-1507033) with additional support by the U.S. Department of Energy, Office of Basic Energy Sciences, Division of Materials Sciences and Engineering, under Award No. DE-SC0008637 as part of the Center for Predictive Integrated Structural Materials Science (PRISMS Center) at the University of Michigan. Computational resources and services were provided by the Extreme Science and Engineering Discovery Environment (XSEDE) Stampede2 at the TACC through allocation No. TG-DMR110007, which is supported by National Science Foundation grant number ACI-1548562, a U.S. Department of Energy Office of Science User Facility located at Lawrence Berkeley National Laboratory, operated under Contract No. DE-AC02-05CH11231, and Advanced Research Computing at the University of Michigan, Ann Arbor.

In addition, I want to thank my friends and colleagues, for their support, advice, and encouragement on my class assignments/projects and graduate life. I want to express my gratitude to Hengyang Lu and Hua Lin, from Ambarella Corporation, for their invaluable advice on my internship project.

Finally, I would like to convey my profound appreciation to my family for their unconditional love and unwavering support. My grandmother is knowledgeable in many disciplines, and she often shared with me her understanding and thoughts on art and science, motivating me to explore the mechanisms behind interesting phenomena, which finally leads to my decision in pursuing a PhD degree. My grandfather was not an expert in cooking but in order for me to have a healthy breakfast before heading to the school, as well as a good dinner after my daily study, he studied cooking and practiced the skills day after day. My father is good at computers, and his enthusiasm in working with computers aroused my interest to explore various computer software and practice programming skills. When I encountered difficulties and had no idea how to proceed, my mother always sat with me, listened to my concerns and complaints, helped me analyze the situation, and provided me with insightful suggestions. Lastly, I want to express my sincere gratitude to my wife, Dr. Xiaoer Hu. The lovely moments we had together greatly helped me persist in pursuing a PhD degree.

Table of Contents

List of Tables

List of Figures

Abstract

Computational models that can predict materials' evolution under synthesis and processing conditions, along with complementary experimental characterizations, are powerful tools that provide insights into the process designs for materials with tailored properties. This dissertation presents a collection of computational models and methods that enable predictions of material structures under different conditions and sample-temperature control during experiments.

The first part of this dissertation describes computational models for simulating phase transformations, microstructure evolution, and mechanical behavior. A phase-field model that captures the evolution of ionic concentrations and phase fractions during solid-state metathesis (SSM) reactions was first presented. This model was employed to investigate the effect of mobilities of ions on the reaction dynamics. We identified the expressions for effective mobility for each type of ions and showed that the type of ions with a larger effective mobility dominates the diffusion and that the rate of the overall process is set by an overall characteristic mobility of the reaction. This phase-field model was then utilized to predict the phase evolutions during the FeS_2 synthesis reaction. The simulation predicted nonplanar phase evolution, which was recently observed in the experiment via transmission electron microscopy. The model was also applied to study the effect of particle packing on the reaction rate, along with a lattice model. Simulations suggested that reactions could occur more rapidly when the sample is densified since each particle within the sample is more likely to have a larger number of reactive neighbors and a particle with more reactive neighbors tends to react faster. Two phase-field models that describe the evolution

of microstructure with dislocations were then discussed. A simple model assuming a uniform intra-granular dislocation density was employed to study the macroscale translation of grains during non-isothermal annealing. Grain translation was observed from the simulations, which was the net effect of a grain with a medium dislocation density consuming an adjacent grain with a higher dislocation density and simultaneously being consumed by another adjacent grain with a lower dislocation density. An extended model that considers intra-granular dislocation densities variation was utilized to study the effect of cyclic heat treatment on the microstructure evolution. We showed that this extended model yielded results that closely resemble the experimental data and that non-self-similar evolution leading to multi-modal grain size distribution was observed in the simulations after dislocations were injected into the microstructure three times. Finally, the relaxation of flat and buckled triangular monolayers of atoms was achieved using a phase-field-crystal model.

The second part of this dissertation presents heat transfer models designed to assist in sample-temperature control and a machine learning algorithm for parameter optimization. First, a heat transfer model that describes the temperature distribution within a sample in an optical floating zone (OFZ) experiment was discussed. The effectiveness of the machine learning algorithm was demonstrated by applying it to determine uncertain parameters in the heat transfer model for the OFZ experiment. The parameterized OFZ model accurately reproduced both steady-state thermal profiles and time-dependent temperatures. Additionally, a coupled thermal and Joule heating model was implemented to predict the thermal profiles of a sample heated by a gradient heater designed to produce a temperature gradient within the sample. The parameterized model was used to study the effect of the heater geometry on the resulting thermal profiles within the sample.

Chapter 1 Introduction

1.1 Overarching goals

Precisely controlling the structure of materials at both atomic and microstructural scale during synthesis and processing is key to produce materials with desired properties. It is therefore necessary to investigate the effect of processing conditions on the resulting material structures. However, characterization of material structures under different conditions via repeated experiments is time consuming and is also limited by the temporal and spatial scale resolved by characterization tools. To facilitate the exploration of the processing parameter space, computational models are often employed. For example, models of phase transformation can take potential processing parameters as input and predict the resulting microstructure as a function of time. The analysis of model outputs sheds light on the material structures and consequently their properties for a given input condition. In this dissertation, we describe a set of computational models and methods to simulate the processes of phase transformations, microstructure evolution, as well as heat transfer during the materials synthesis and processing. We show that these model, after being properly parameterized against available experimental data, can be utilized to predict many key quantities, such as composition, phase fractions, and grain size distributions. These models fill the gaps in the experimental characterization and provide insights into the designs of synthesis and processing conditions, with the ultimate goal to enable enhanced material properties and performance.

In this chapter, we describe the motivations for three critical applications of simulations in materials synthesis and processing, namely, solid-state metathesis (SSM) reactions (see Section

1.2), stored-energy-driven grain growth (see Section 1.3), and precise temperature control within the samples during thermal processing (see Section 1.4). Additionally, we discuss in Section 1.5 the necessity of leveraging machine learning algorithms to automatically determine uncertain parameters for computational models.

1.2 Motivation – Solid-state metathesis reactions*

Material synthesis involves the transformation of precursor phases to target phases. It is necessary to control the synthesis condition, *e.g.,* temperature and pressure, in order for the precursor phases to transform into the desired product phases. This is especially true when the target material is metastable. Solid-state metathesis (SSM) reactions (or double displacement reactions) are a promising route to synthesizing both stable and metastable products at lower temperatures than traditional solid-state routes [1,2]. In SSM reactions, cations or anions in precursor compounds exchange to form products and are often driven by the formation of a thermodynamically stable byproduct, such as an alkali salt.

Kinetic control is utilized in SSM reactions to alter activation barriers and the reaction pathway. The products formed during SSM reactions can be controlled by altering the synthesis conditions and precursor compounds. For example, Martinolich et al. [2] showed that the SSM reaction between $FeCl_2$ and Na_2S_2 precursors that were prepared in ambient air yielded FeS_2 without crystalline intermediates that would otherwise be formed when the precursors were prepared in an air-free condition. Wustrow et al. [3] showed that the required temperature for the SSM reaction to synthesize $YMnO_3$ is approximately 700 °C when either $CaMn_2O_4$ or $MgMn_2O_4$

* Adapted from G. Huang, D. Montiel, R. D. McAuliffe, G. M. Veith, and K. Thornton, "Phase-Field Modeling of Solid-State Metathesis Reactions with the Charge Neutrality Constraint," Computational Materials Science **221**, 112080 (2023).

is used to react with YOCl. However, this temperature is reduced to approximately 550 °C when both precursor oxides react with YOCl.

In order to elucidate the fundamental mechanisms underlying these observations and to identify the factors that affect the thermodynamics and kinetics, it is essential to follow the phase transformation as it progresses and identify which phases form. While experimental characterization tools, such as x-ray diffraction/reflectivity [4], transmission electron microscopy [5], and tomographic approaches [6,7], are becoming increasingly powerful, there is not yet a method that fully resolves the short temporal and small spatial scales involved in phase transformation processes. To fill the gaps in experimental observations and to work in concert with these experimental data in the effort to develop the full understanding of SSM reactions, a computational model that describes the evolution of the ionic concentrations as well as phase fractions is required.

1.3 Motivation – Stored-energy-driven grain growth

The physical property of a material, such as toughness [8,9], hardness [10,11], and strength [9,12] are strongly influenced by its microstructure. Therefore, it is critical to understand the mechanisms for the microstructure evolution in order to achieve desired properties in a material. This is especially true for polycrystalline materials since the mechanical processing or heat treatment of such materials could vastly alter their grain sizes, morphologies, and texture, leading to a change in their properties.

In polycrystalline materials, grain boundaries exist at the interfaces of grains with different crystal orientations. In normal grain growth, which is driven by capillarity (or, equivalently, grain boundary energy), large grains progressively grow and consume their adjacent small grains that have more grain boundaries (and thus energy) per volume [13]. In such a case, after sufficient

evolution, a state of self-similar evolution can be reached in which the scaled distribution of grain sizes remains unchanged [14,15]. In some situations, however, a few grains grow exceptionally faster than others, leading to a non-self-similar grain-size distribution [14,15]. This phenomenon is referred to as abnormal grain growth (AGG). While abnormal grain growth is detrimental to materials properties in some situations [16,17], it has been found to be useful in some applications, such as the fabrication of Fe-Si electrical steels with low core loss [18] and superior magnetic properties [19] and the production of Fe-based shape memory alloys with superior pseudoelastic properties [20].

Consequently, many efforts have been made to explore the methods to induce AGG in a polycrystalline sample. For example, AGG is reported to occur when the sample is deformed by a small amount and is annealed afterwards [21]. Alternatively, the sample is mechanically deformed to induce a plastic deformation at high temperature to generate dynamic AGG [22]. However, these methods require a sample of simple shape and careful operations, to avoid a sample fracture [23], making it difficult to scale up the production. Recently, it is reported by Omori et al. [23] that AGG can be triggered by cyclic heat treatment. They first annealed a Cu-17%Al-11.4 % Mn sample at a high temperature (at which only BCC-β phase could exist in equilibrium) and then repeatedly cooled and heated the sample to below and above FCC-α solvus temperature, during which they observed AGG. Higgins et al. [24] postulated that the stored energy introduced within the grains via the formation of dislocations during non-isothermal annealing provides an additional driving force for grain boundary migration, which promotes the grains with lower stored energy to consume the grains with higher stored energy, resulting in the AGG.

To verify the hypothesis mentioned above and to provide a better understanding of how the combined capillary driving force and the driving force due to the stored energy affects the

microstructure evolution for an alloy sample undergoing non-isothermal annealing, a computational model that considers both driving forces is necessary.

1.4 Motivation – Precise temperature control within the samples during thermal processing

Temperature is arguably the most universally explored environmental variable for non-ambient studies of materials structure during material synthesis and processing. A precise control of the sample temperature is necessary to induce desired phase transformation and microstructure evolution. Although traditional crucible-based furnaces are relatively straightforward to operate, they have two major drawbacks. First, a crucible could introduce impurity to the sample, which may degrade the material property. Second, the temperature-dependent studies using traditional furnaces requires the collection of data as a sample is progressively heated or cooled, either continuously or in discrete steps. In practice, these measurements are limited by how fast the temperature can be changed, the achievable temperature range, and the number of temperatures that can be sampled simultaneously with a single experiment (e.g., by imposing a temperature gradient over the sample). Many research efforts have been made to address these issues. For example, the optical floating zone (OFZ) furnace [25,26] avoids the contact between the sample and the heat source by leveraging the lights from lamps to heat a sample. The gradient heater approach [27] is introduced to generate variable temperatures within a sample such that temperature-dependent quantities can be measured concurrently across the sample, which significantly reduce the time needed to repeat the experiment with different temperatures.

In order to utilize these novel furnace approaches to effectively control the sample temperature, it is necessary to understand how the temperature changes with time during the heating and cooling stages of these furnaces, as well as to elucidate the effect of the furnace geometry on the resulting steady-state thermal profiles. Although these measurements can be

performed solely in experiments, the process is time-consuming and laborious, especially when a time-dependent behavior of the thermal profiles at multiple positions is needed, or when a large number of various furnace geometries needs to be studied. A computational heat transfer model, when parameterized properly, can be utilized to make accurate predictions for time- and position-dependent thermal profiles in these furnaces, providing understanding of the furnace thermal environments and ultimately facilitating the furnace design.

1.5 Motivation – Parameter determination for computational models*

Numerous computational models are continuously being developed in an effort to understand the physics behind the experimental observations. These models include optical [28-30], electrical [31-33], acoustic [34-36], heat transfer [37-39] and mechanical [40-42] models. A computational model generally includes parameters representing material properties and experimental conditions. In order for a physical model to be quantitatively predictive, accurate values of these physical parameters are needed. This is especially true for the parameters on which the model predictions depend strongly. For models in which parameters are either unknown or uncertain, comparison with experimental results can be used to determine or refine the possible range of these parameters. However, to alleviate the need for manual trial-and-error tuning of parameters, which can be inefficient and time-consuming (especially when many parameters are uncertain), an algorithm that can automate the determination of the parameters that provide the best fit between the model predictions and experimental measurements is useful and sometimes necessary.

* Adapted from G. Huang, M. Zhang, D. Montiel, P. Soundararajan, Y. Wang, J. J. Denney, A. A. Corrao, P. G. Khalifah, and K. Thornton, "Automated Extraction of Physical Parameters from Experimentally Obtained Thermal Profiles Using a Machine Learning Approach," Computational Materials Science 194, 110459 (2021).

1.6 Dissertation outline

This dissertation presents computational methods (e.g., phase-field models, heat transfer methods, and machine learning algorithms) developed or implemented for a series of applications involved in material synthesis and processing, such as solid-state metathesis reactions, stored-energy-driven grain growth, and sample-temperature control during experiments. Chapter 1 and Chapter 2 discuss the motivation, background, and general simulation methods for this dissertation. Chapter 3-8 provide detailed simulation methods, results and discussions for each application. The simulation results are often presented along with the experimental results, which are performed by our experimental collaborators. These experimental data are used to provide the context of study, inform computational models, or conduct comparison between the simulations and experiments.

Chapter 2 provides the background information for the applications discussed in this dissertation, such as materials synthesis, microstructure and optical floating zone experiment, and a general description of the computational methods employed in this dissertation, namely, phase-field models, smoothed boundary methods, level set methods, heat transfer equations, and an algorithm for parameter optimization.

Chapter 3 describes a phase-field model developed to simulate binary solid-state metathesis reactions. The free energy functional and governing equations employed in the phase-field model are first presented. Then the nondimensionalization of the phase-field equations are discussed. Finally, the coupling of the phase-field model with the smoothed boundary method are described.

Chapter 4 demonstrates the effectiveness of the phase-field model discussed in Chapter 3 for the SSM reactions and showcases three applications. First, the effect of mobilities of the ions on the dynamics of a binary SSM reaction is investigated. Next, a thin-film reaction for the

synthesis of FeS_2 is simulated using this phase-field model, and the agreements between the simulation and the experiment are discussed. Finally, the reactions occurring between $NaFeO_2$ and LiBr particles, with two configurations of precursor particles, are simulated, which is combined with a lattice model to reveal the effect of packing density of the sample on the reaction rate.

Chapter 5 presents a phase-field model to describe stored-energy-driven grain growth. First, the details of the model, including the free energy functional, governing equations, nondimensionalization, and initial conditions are explained. Next, the microstructure evolution for capillary-driven grain growth and stored-energy-driven grain growth is simulated. Finally, the magnitude of grain center translation and driving forces predicted in microstructure evolution are compared for two cases.

Chapter 6 extends the phase-field model in Chapter 5 by considering a spatially varying dislocation density field. First, the updated model formulation for order parameters and dislocation density fields is presented. Next, a simulation initiated with experimental microstructure and dislocation densities is performed using the extended model, and the resulting microstructure is compared with the experimental measurements. Finally, a set of large-scale simulations of the microstructure evolution is conducted to examine the effect of cyclic heat treatment on the behavior of microstructure evolution.

Chapter 7 describes the applications of parameterized heat transfer models to examine the thermal profiles for the samples heated in an optical floating zone furnace and a gradient heater furnace. First, the process of automated parameter determination for a heat transfer model of an optical floating zone furnace is presented. The agreements in steady-state thermal profiles and time-dependent temperatures between predictions and experimental observations are discussed. Next, the parameterization of a gradient heater model that couples both heat transfer equations and

Joule heating equations is described. The effect of heating-wire configurations and furnace geometry on the thermal profile of the sample is explored using the parameterized model.

Chapter 8 presents a phase-field crystal model for describing two-dimensional materials. The stabilization of a flat and a bending monolayer of atoms in both two and three dimensions are discussed.

Chapter 9 summarizes the dissertation and provides suggestions for future work.

Chapter 2 Background and Methods

2.1 Material synthesis and processing

2.1.1 Common material categories and methods for their synthesis

Materials can be in general divided into four categories: metal, ceramic, polymer, and composites. Metals (or alloys) are commonly produced via mechanical alloying [43], vapor deposition [44], power metallurgy [45], and other metallurgical processes [46]. Ceramics can be synthesized using sol-gel processes [47], hydrothermal methods [48], solid-state reactions [49]. Polymers are produced through atom transfer radical polymerization [50], reversible addition-fragmentation chain transfer [51], ring-opening polymerization [52], and other polymerization reactions [53]. Composites are made by mixing two or more materials discussed above via methods such as hand lay-up [54], spray-up [55], filament winding [56], pultrusion [57], and resin transfer molding [58]. In order to synthesize a material with a desired property, it is necessary to choose an appropriate method and apply proper experimental conditions, such as temperature and pressure. This requires a deep understanding of how different methods and conditions could affect the process involved in a certain synthesis process. In this thesis, we focus on discussing the synthesis of ceramic materials, such as a FeS_2 compound, using a solid-state metathesis reaction, as well as the thermal processing of a Cu-17%Al-11.4%Mn alloy. A general approach for solid-state synthesis is presented in Section 2.1.2. The solid-state metathesis reaction is discussed in Section 2.1.3. The methods for conducting thermal processing, including heat treatment and cyclic heat treatment, are discussed in Section 2.1.4 and 2.1.5, respectively.

2.1.2 Solid-state synthesis

Solid-state reactions are one of the most common methods to produce inorganic materials. Traditional solid-state reactions typically involve grinding precursors into powders and mixing them at an elevated temperature, at which precursor phases turn into product phases via the diffusion of atoms or ions. The reaction rate, however, are often low since the reaction process is limited by the diffusion of the involving species. Consequently, a sufficiently high temperature must be applied to the precursor for the reaction to complete in a timely manner, frequently limiting the outcome of the reactions to those that are thermally stable. *Chimie Douce* (or "soft chemistry"), such as dehydration, dihydroxylation, and redox reactions, often require a lower temperature for the reactions to occur [59], and thus provides the possibility to synthesize metastable compounds [60]. Moreover, application of alkali chalcogenide fluxes [61-63] has also been reported to facilitate the synthesis of kinetically stable materials.

2.1.3 Solid-state metathesis reactions[*]

Solid-state metathesis (SSM) reactions were first investigated by Treece et al. [64], Gillan et al. [65], and Parkin et al. [66,67] in the 1990s. They are a promising route to synthesizing both stable and metastable products at lower temperatures than traditional solid-state routes [1,2]. In SSM reactions, cations or anions in precursor compounds exchange to form products and are often driven by the formation of a thermodynamically stable byproduct, such as an alkali salt. A binary SSM reaction is represented by

$$\mathrm{AX} + \mathrm{BY} \rightarrow \mathrm{AY} + \mathrm{BX}. \tag{2.1}$$

[*] Adapted from G. Huang, D. Montiel, R. D. McAuliffe, G. M. Veith, and K. Thornton, "Phase-Field Modeling of Solid-State Metathesis Reactions with the Charge Neutrality Constraint," Computational Materials Science **221**, 112080 (2023).

Here, two cations are denoted by A and B, and two anions are denoted by X and Y. The precursor phases are denoted by AX and BY, and the product phases are denoted by AY and BX. In an SSM reaction, the bonds between AX and BY break and new bonds between AY and BX form. In Ref. [66], two possible mechanisms have been proposed to describe the reaction pathway in a typical binary SSM reaction. One mechanism is that ionic species diffuse after the original bonds between AX and BY break until new bonds are formed. The other mechanism is that, after the bonds break, the ions are reduced or oxidized to their elemental form and then recombined into products later due to high reaction temperature. It is worth noting that both mechanisms represent extreme cases [66] and the actual reaction pathway is more complex in general.

2.1.4 Heat treatment[*]

Heat treatment is a thermal process that applies to a sample that alters its microstructure and consequently its mechanical properties [68]. A cycle of heat treatment typically involves heating the sample to a predetermined heat treatment temperature with a certain rate, maintaining at this temperature for a controlled amount of time, and cooling with a predetermined rate. The heating and cooling rates, heat treatment temperature, and holding period constitute a heat treatment schedule, which needs to be carefully designed based on the shape, size, and other properties of the sample, as well as its desired properties after heating treatment. For example, a low heating rate is often required for large samples to prevent the development of internal stress that leads to material failure, due to the gradient of temperature. A more homogeneous structure can be formed within the sample by slow heating, which reduces the subsequent holding time. A

[*] Adapted from
(1) T.V. Rajan, C. P. Sharma, and A. K. Sharma, *Heat Treatment: Principles and Techniques*, second edition, PHI Learning (2012).
(2) F. J. Humphreys and M. Hatherly, *Recrystallization and Related Annealing Phenomena*, second edition, Elsevier (2004).

high heating rate, however, is beneficial to those materials that are prone to oxidation. The heat treatment temperature is selected based on the targeted phases to transform into, which could be identified from a phase diagram. The holding duration at high temperature depends on the heat treatment temperature, in addition to the heating rate discussed above. It is reported [68] that a longer heating duration is often required for a lower heat treatment temperature because of the slower kinetics. Finally, the rate of cooling could affect the resulting microstructure. For example, slow cooling of austenitized iron-carbon alloys yields pearlite, an equilibrium microstructure consisting of alternating layers of ferrite and cementite, while rapid cooling yields martensite, a metastable microstructure [69].

Here, we discuss two common heat treatment methods: annealing and quenching. Annealing frequently refers to a process in which the sample is heated to a temperature above its recrystallization point and is usually slowly cooled after a sufficient holding time to allow for recrystallization and grain growth to take place. Quenching refers to a process that involves rapidly cooling the sample from the heat treatment temperature to a low temperature (e.g., room temperature) by exposing the sample to air or water and thus avoids the undesired phase transformation that would otherwise occur. The sample after quenching often possesses high hardness but tends to be more brittle since the process of grain growth has not completed due to the rapid cooling.

Heat treatment is extensively utilized in the processing of metallic and ceramic materials. For example, it is commonly applied along with the mechanical processes, such as forging, rolling, and extrusion, to produce metallic materials. These combined steps are referred to as *thermomechanical processing*. Careful control of thermal and deformation conditions is required during simultaneous heat treatment and mechanical processing to obtain a sample with desired

shape and mechanical properties[70]. Heat treatment can also be leveraged for solid-state synthesis of ceramic materials. Elevating the temperature provides the precursor phases with sufficient energy to overcome the reaction energy barrier to transform into the desired product phases, as well as facilitates the reactions by increasing the mobility of ionic species.

2.1.5 Cyclic heat treatment[*]

Some methods require multiple heat treatment cycles to achieve desired material properties. For example, precipitation hardening aims to increase the yield strength of an alloy by generating fine particles within the alloy to hinder the movement of dislocations. Such heat treatment typically involves two cycles. The first cycle is called solutionizing, during which the alloy is heated to a high temperature and is rapidly quenched after a certain duration of holding. The alloy, after quenching, is a supersaturated solid solution. The alloy is then heated to a moderate temperature and is hold at this temperature before being slowly cooled. This process is termed aging, during which fine and dispersed particles are formed [71]. In Section 2.2.2, we provide another example for cyclic heat treatment, which is used to induce an abnormal grain growth.

2.2 Microstructure evolution

2.2.1 Grain growth[†]

In polycrystalline materials, microstructure is composed of a large number of grains that are separated by grain boundaries. Since these boundaries possess excess energy, their reduction drives larger grains to grow and smaller grains to contract and eventually disappear during

[*] Adapted from T.V. Rajan, C. P. Sharma, and A. K. Sharma, *Heat Treatment: Principles and Techniques*, second edition, PHI Learning (2012).
[†] Adapted from F. J. Humphreys and M. Hatherly, *Recrystallization and Related Annealing Phenomena*, second edition, Elsevier (2004).

annealing. This phenomenon is referred to as grain growth, or capillary-driven grain growth. The kinetics of grain growth was first studied by Burke et al. [72]. The driving force for a grain boundary to migrate, P, arising from the curvature of boundary, is given by

$$P = \gamma\left(\frac{1}{R_1} + \frac{1}{R_2}\right), \tag{2.2}$$

where γ is the grain boundary energy, and R_1 and R_2 are the principal radii of curvature for the boundary. For a grain boundary that is part of a grain of spherical shape with radius R, Equation (2.2) can be simplified as

$$P = \frac{2\gamma}{R}. \tag{2.3}$$

Assuming that all the grain boundaries have an identical grain boundary energy and that R is proportional to the average radius, $\bar{R}$, of the grains, Equation (2.3) can be written as

$$P = \frac{k_1\gamma}{\bar{R}}, \tag{2.4}$$

where k_1 is a constant. The derivative of average radius with respect to time is proportional to the driving force [72]:

$$\frac{d\bar{R}}{dt} = k_2 P, \tag{2.5}$$

where $\bar{R}$ is the average grains radius at time t, and k_2 is a constant. Substituting Equation (2.4) into (2.5) yields

$$\frac{d\bar{R}}{dt} = \frac{k_1 k_2 \gamma}{\bar{R}}. \tag{2.6}$$

Solving for $\bar{R}$ in Equation (2.6) yields

$$\bar{R}^2 = 2k_1 k_2 \gamma t + 2k_3, \tag{2.7}$$

where k_3 is a constant, which can be determined by substituting the value $\bar{R} = \bar{R}_0$ at the initial time $t = 0$ into Equation (2.7). Substituting the resulting value $k_3 = \bar{R}_0^2/2$ into Equation (2.7) yields

$$\bar{R}^2 - \bar{R}_0^2 = 2k_1k_2\gamma t. \tag{2.8}$$

Applying a square root to both sides of the equation yields

$$\sqrt{\bar{R}^2 - \bar{R}_0^2} = \sqrt{2k_1k_2\gamma}t^{1/2}. \tag{2.9}$$

When the grains grow for a sufficient time such that $\bar{R} \gg \bar{R}_0$, Equation (2.9) becomes [72]

$$\bar{R} = k_4 t^{1/2}, \tag{2.10}$$

where $k_4 = \sqrt{2k_1k_2\gamma}$. Therefore, the average grain radius is proportional to $t^{1/2}$ and is expected to increase over time. Substituting Equation (2.10) into Equation (2.4) yields

$$P = k_5 t^{-1/2}, \tag{2.11}$$

where $k_5 = k_1\gamma/k_3$. Equation (2.11) implies that the driving force P is proportional to $t^{-1/2}$ and thus decreases with time.

Hillert [15] proposed a relationship to describe the change in the radius of an individual grain with respect to time:

$$\frac{dR}{dt} = k_6 M\gamma\left(\frac{1}{\bar{R}} - \frac{1}{R}\right), \tag{2.12}$$

where $k_6 = 0.5$ in 2D and 1 in 3D, and M is the mobility of the grain boundaries. By solving this equation, Hillert showed that the distribution of a scaled grain radius, $\hat{R} = R/\bar{R}$, at the steady state is given by [15]

$$f(\hat{R}) = (2e)^{\beta}\frac{\beta\hat{R}}{\left(2 - \hat{R}\right)^{2+\beta}}\exp\left(\frac{-2\beta}{2 - \hat{R}}\right), \tag{2.13}$$

where $\beta = 2$ in 2D and 3 in 3D. Since the predicted distribution of a scaled grain radius is independent of time at steady state, a self-similar evolution is expected after the grain growth proceeds for a sufficient period of time.

2.2.2 Abnormal grain growth[*]

In some situations, a few grains grow exceptionally faster than others, leading to a bimodal distribution of the grain size [14,15]. Such evolution is referred to as abnormal grain growth (AGG). Many studies have been conducted to identify its origin. For example, AGG was reported to occur within the materials with a strong texture component [73-76]. Due to the presence of the strong texture, most of the grain boundaries have a low misorientation and thus possess a low grain boundary energy, leading to a small driving force for the grain boundary migration to occur between these grains. A few grains, however, may contain a different texture, which results in high-energy grain boundaries. These boundaries tend to migrate much faster than the other ones, leading to AGG. Additionally, in two-phase systems, the second-phase particles are proposed to exert a pinning pressure on the grains in the matrix phase [77]. As a result, when the average grain size reaches a certain limit, which depends on the number and size of the second-phase particles, only those grains that are significantly larger than the average grain size can grow [15], resulting in the phenomena of AGG.

Recently, Omori et al. [23] reported a cyclic heat treatment (CHT) method to obtain AGG. Specifically, they first annealed a Cu-Al-Mn sample at 900 °C, at which only BCC-β phase could exist in equilibrium. The sample is then cooled to below the FCC-α solvus temperature (726 °C), during which α-phase progressively precipitates within the β matrix. The sample is then heated to

[*] Adapted from G. Huang, Z. Croft, M. Chlupsa, A. Mensah, D. Montiel, A. J. Shahani, and K. Thornton, "Phase-Field Modeling of Stored-Energy-Driven Grain Growth," In preparation.

above α solvus temperature, during which α phases dissolves. The combination of cooling and heating constitutes a cycle of heat treatment. They repeatedly observed AGG when multiple cycles of heat treatment were conducted for the Cu-Al-Mn sample. Kusama *et al.* [78] carefully designed the annealing schedule for CHT and showed that large single crystals can be produced with induced AGG. Omori et al. [23] proposed that the subgrain structures formed within the preexisting grains in the process of cyclic heat treatment play an important role in driving the abnormal grain growth. Specifically, they postulated that the recurrent precipitation and dissolution of α phases within the β matrix during the non-isothermal annealing resulted in the loss of coherency of α-β interfaces, leading to the generation of dislocations within the sample and, as a result, the subgrain structures, which remain after precipitates dissolve. Omori *et al.* [79] and Kusama *et al.* [78] utilized the energy of subgrain boundaries as an estimate to quantify the additional driving force for AGG to occur during CHT.

Higgins et al. [24] interpreted this additional energy as the stored energy, a common term used to describe the excess energy that drives recrystallization, due to the presence of dislocations [80]. They postulated that the stored energy introduced within the grains via the formation of dislocations during the process of non-isothermal annealing would give rise to a driving force for the grains with lower stored energy to consume the grains with higher stored energy, leading to the reduction of the total energy. They justified their hypothesis by performing real-time X-ray imaging experiments during CHT and showing that the grains in a Cu-Al-Mn sample with high dislocation density were consumed by those with low dislocation density. After ruling out the effects from the texture, particle dragging, and particle pinning, they proposed the stored energy due to the presence of dislocation as the primary mechanism for AGG during the CHT of the Cu-Al-Mn system.

2.3 Optical floating zone experiment*

In an optical floating zone (OFZ) crystal growth experiment [25,26], a light source from one or more high power lamps or lasers is focused at the intersections between a vertical upper feed rod and a lower seed rod, allowing a narrow molten zone to be stabilized between these rods. During the growth, both rods are translated downward through the apparatus, causing continuous crystallization on the seed rod and the continuous replenishment of the liquid zone by melting of the feed rod. Although the heat is initially deposited only at the focal point of the light source (*e.g.*, in the molten zone), this energy is continuously transported across the sample rods and dissipated via radiation, convection, and conduction. A schematic for the setup of a typical OFZ experiment is shown in Figure 2.1.

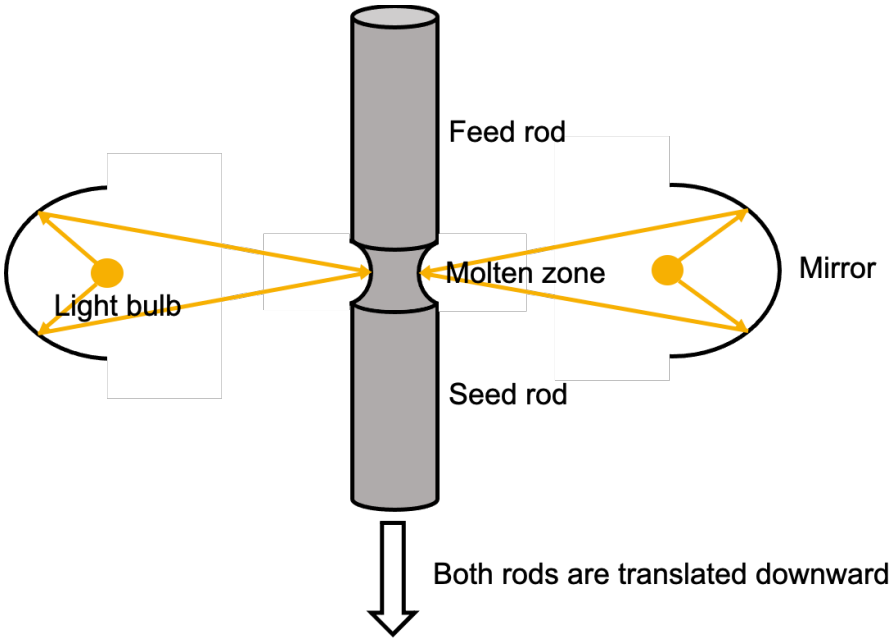

Figure 2.1. Schematic showing a typical optical floating zone experiment.

* Adapted from G. Huang, M. Zhang, D. Montiel, P. Soundararajan, Y. Wang, J. J. Denney, A. A. Corrao, P. G. Khalifah, and K. Thornton, "Automated Extraction of Physical Parameters from Experimentally Obtained Thermal Profiles Using a Machine Learning Approach," Computational Materials Science 194, 110459 (2021).

The temperature variation across the sample rod can have a major effect on the outcome of the OFZ crystal growth process but is in general very difficult to measure experimentally. For many years, there were only a few publications reporting experimentally measured sample rod temperatures, one of which was accomplished using a thermocouple placed inside a hole drilled into a sample rod [81] and the rest of which used less reliable measurement technique of having the thermocouple external to the sample (where it is more likely to experience fluctuations due to convection and where its own direct light absorption can lead to incorrectly reported temperatures). As a consequence, a few models have been developed that consider the coupled optical and heat transfer physics involved. In Ref. [82], Lan et al. calculated the incident heat flux onto the sample using two different models: a finite-source model, where light bulbs are assumed to be of a finite volume, and a point-source model, where the light bulbs are assumed to be point sources. A heat transfer model that considers thermal conduction within the sample, energy balances at the interfaces between the melt and solid, convection and radiation from the sample to the ambient environment, and free surfaces between gas and the melt was utilized to obtain the temperature profiles across the sample. They compared their predictions to measured temperatures at a few positions along the sample and obtained a good agreement. In Ref. [83], Yan et. al. further examined the effect of the geometry of the lamp filament and the effect of a small variance of lamp power (68% – 72% of four 1500 W halogen lamps) on the temperature field of the sample. Other modeling studies of the optical and thermal transport phenomena in an OFZ can be found in Refs. [84,85]. However, none of the aforementioned studies provide a comprehensive comparison (temperatures at a number of positions) between model predictions and experimentally measured temperature profiles under different lamp power settings (0% – 100% of the maximum power), likely due to the difficulties in measuring the time-dependent, spatially varying temperature of the

sample. As a result, an extensive comparison of the simulated and experimental temperatures had not been performed.

2.4 Modeling heat transfer within solids*

To computationally model the heat transfer within solids, three heat-transfer mechanisms must be considered, namely, conduction, convection, and radiation. The thermal conduction is the process of heat transport due to temperature gradient within the bulk of objects. It is described by [86]

$$\rho C_p \frac{\partial T}{\partial t} - \nabla \cdot (k \nabla T) = Q, \tag{2.14}$$

where ρ is the density, C_p is the heat capacity, T is the temperature, t is time, k is the thermal conductivity, and Q is the power density from a source within the bulk. The first term on the left-hand side is necessary when transient states need to be studied, while the steady state is described by setting the first term that is proportional to $\frac{\partial T}{\partial t}$ to zero.

When the object of interest is a solid, unless the effect of gas flow surrounding the object significantly affects the temperature profiles within the object, the effect of convection in the surrounding gas is commonly included as a boundary condition for the modeled object, given by Newton's law of cooling [86]

$$-\boldsymbol{n} \cdot \boldsymbol{q}_{air} = h(T_{amb} - T), \tag{2.15}$$

where $\boldsymbol{q}_{air}$ the heat flux over the surface of the object, T_{amb} is the ambient temperature, and h is the heat transfer coefficient. The expression for h depends on the geometry of the object, as well

* Adapted from D. O'Nolan, G. Huang, G. E. Kamm, A. Grenier, C. H. Liu, P. K. Todd, A. Wustrow, G. T. Tran, D. Montiel, J. R. Neilson, S. J. L. Billinge, P. J. Chupas, K. S. Thornton, and K. W. Chapman, "A Thermal-Gradient Approach to Variable-Temperature Measurements Resolved in Space," Journal of Applied Crystallography 53, 662 (2020).

as the flow conditions (e.g., natural air convection, forced convection, orientation of the surface, etc.) [86].

There are two types of thermal radiation: surface-to-surface radiation [87,88] and surface-to-ambient radiation. The former describes the heat transfer due to thermal radiation between the surface of an object and those of other objects, while the latter describes the radiation of the heat from the surface of an object to the surrounding gas. For the surface-to-surface radiation, we consider a point, *P*, on one of the surfaces, which we denote as the surface of interest, *S*. The net outgoing radiative heat flux, J, at this point is given by

$$J(\boldsymbol{r}_P) = (1-\alpha)G(\boldsymbol{r}_P) + \epsilon e_b\big(T(\boldsymbol{r}_P)\big), \tag{2.16}$$

where $\boldsymbol{r}_P$ indicates the position of point *P*, α is the absorptivity of surface *S*, G is the incident radiative flux onto the surface at point *P*, and ϵ accounts for the difference in material's emissivity with respect to that of a black body. The first term in Equation (2.16) accounts for reflection at point *P* on *S.* The second term accounts for emission, where $e_b(T)$ is the black body radiation power per unit area, given by the Stefan–Boltzmann law,

$$e_b(T) = \sigma T^4, \tag{2.17}$$

where σ is the Stefan-Boltzmann constant. The spatial dependence of variables indicated in Equation (2.16) is omitted below for brevity. The flux, *G*, at point *P* on *S* is given by

$$G = \int_{S'} \frac{(-\boldsymbol{n}'\cdot\boldsymbol{r})(\boldsymbol{n}\cdot\boldsymbol{r})}{\pi|\boldsymbol{r}|^4} J' dS' + \left(1 - \int_{S'} \frac{(-\boldsymbol{n}'\cdot\boldsymbol{r})(\boldsymbol{n}\cdot\boldsymbol{r})}{\pi|\boldsymbol{r}|^4} dS'\right) e_b(T_{amb}). \tag{2.18}$$

The first term in Equation (2.18) accounts for radiation from all unobstructed surrounding surfaces, *S'*, that are facing the surface of interest, *S*. The second term accounts for incident ambient radiation. The vector, $\boldsymbol{r}$, points from point *P* on *S* to a point *P'* on *S'*, $\boldsymbol{n}$ and $\boldsymbol{n}'$ are the outward normal vectors at *P* and *P'*, respectively, T_{amb} is the ambient temperature far from the apparatus,

and J' is the net outgoing heat flux from *P'* on *S'*. The ambient view factor, $1 - \int_{S'} \frac{(-\boldsymbol{n}'\cdot\boldsymbol{r})(\boldsymbol{n}\cdot\boldsymbol{r})}{\pi|\boldsymbol{r}|^4} dS'$, accounts for the fraction of ambient radiation on *P* that is not blocked by *S'*. The heat flux onto the surface *S* due to surface-to-surface thermal radiation, $-\boldsymbol{n}\cdot\boldsymbol{q_{ss}}$, is given by

$$-\boldsymbol{n}\cdot\boldsymbol{q_{ss}} = G - J = \epsilon[G - e_b(T)]. \tag{2.19}$$

The surface-to-ambient thermal radiation is given by:

$$-\boldsymbol{n}\cdot\boldsymbol{q_{sa}} = \epsilon\sigma(T_{amb}^4 - T^4). \tag{2.20}$$

For the work in this thesis, we solve the above equation with object geometries corresponding to the experiment using COMSOL Multiphysics® software [89], which is a software that pre-implemented the heat transfer equations discussed above. A heat transfer model might involve additional equations, such as heat absorption equations. The model could be coupled with other models, such as Joule heating, to describe more complex phenomena. Some examples are discussed in Chapter 7.

2.5 Approaches for model parameter determination

2.5.1 Two categories of methods for automated parameter determination[*]

As discussed in Chapter 1 Section 1.5, a computational model requires an accurate set of parameters for it to be predictive. Although some of the parameters are either reported in literature or can be easily measured from experiments, other parameters are unknown or uncertain. There are two major approaches to finding the parameters through automation: interpolation methods and iterative methods. Interpolation methods usually employ a functional form to describe the relationship between a set of independent variables (in the present case, input parameters) and

[*] Adapted from G. Huang, M. Zhang, D. Montiel, P. Soundararajan, Y. Wang, J. J. Denney, A. A. Corrao, P. G. Khalifah, and K. Thornton, "Automated Extraction of Physical Parameters from Experimentally Obtained Thermal Profiles Using a Machine Learning Approach," Computational Materials Science 194, 110459 (2021).

dependent variables (e.g., the difference between simulated results and experimental measurements). In polynomial regression [90,91], a polynomial functional form is proposed and the coefficients for each term are determined by fitting the functional form to known independent and dependent variables. In ordinary kriging [92,93], each dependent variable of interest can be represented as a weighted average of known dependent variables, with the weights being assigned based on the distance between them in the parameter space. The optimal parameters are determined by solving for local minima of the functional form. The accuracy of these interpolation methods is highly dependent on the number of known pairs of independent and dependent variables. To achieve high accuracy, an exhaustive sampling of the parameter space is usually required, which is computationally intensive, especially when the parameter space is large and high dimensional. An alternative approach is the use of iterative methods, where a local or global minimum of an objective/cost function that is designed to represent errors between experimental measurements and sampling simulations is iteratively estimated. These methods usually start with assigning an initial range for each parameter and randomly sampling a number of vectors in the parameter space defined by the possible range of each parameter. The ranges of these parameters are then successively refined following rules specified by an algorithm in order to reduce the cost/objective function value. For example, in a genetic algorithm [94], the sampled vectors (named population in this method) with lower cost would be more likely to be selected as the parents in the current iteration and would be utilized to generate vectors for next iteration (or children), via crossover and mutation operation. In a particle swarm optimization [94-97], the position of each sampled vector (or particle) is updated, so as to reduce its distance from its own previous optimal position (defined as the one with lowest cost) and the previous global optimal position. In a general pattern search algorithms [97,98], such as a coordinate search algorithm [99] and a Hooke-Jeeves

algorithm [97,100], the parameter space is shifted based on the sampled vectors that yield the lowest cost in each iteration and is refined using a mesh size factor defined by the algorithm.

2.5.2 A novel machine learning method to determine uncertain parameters[*]

Here, we introduce a method that is similar to a general pattern search algorithm but shifts and refines the range of each parameter based on statistical information obtained from a number of sampled vectors, rather than a single vector with the lowest cost function value. Due to the fact that cost function could have a few local minima, the lowest cost at one point does not necessarily guarantee that the cost evaluated at its surrounding is lower than those evaluated at the points in the regions further away. In our approach, we instead evaluate the mean and standard deviation for sampling simulations in each iteration that yield low errors and shift and refine the parameter space based on them. The algorithm therefore utilizes the collective information from all the sampling simulations, and the parameter space is updated in a manner that the mean cost, averaged from all the sampled vectors, decreases rapidly, which allows for a robust optimization against different shapes of cost functions. In our algorithm, the parameters of interest are either unknown or uncertain. An uncertain parameter is a parameter for which a range of values was previously reported in literature; this range is selected as the initial range for the parameter. For unknown parameters, the initial range is estimated based on known physical constraints and prior knowledge of the behavior of related materials. The possible range for the uncertain and unknown parameters is then iteratively refined using the average value and standard deviation of the sampling simulations that yield a low error (we are selecting the parameter vectors that are at the 10^{th}

[*] Adapted from G. Huang, M. Zhang, D. Montiel, P. Soundararajan, Y. Wang, J. J. Denney, A. A. Corrao, P. G. Khalifah, and K. Thornton, "Automated Extraction of Physical Parameters from Experimentally Obtained Thermal Profiles Using a Machine Learning Approach," Computational Materials Science 194, 110459 (2021).

percentile or lower in error among the samples in each iteration) until a convergence criterion is satisfied. The final set of the sample data is then used to determine the optimized set of parameter values via an interpolation method. A flowchart illustrating the algorithm steps is shown in Figure 2.2.

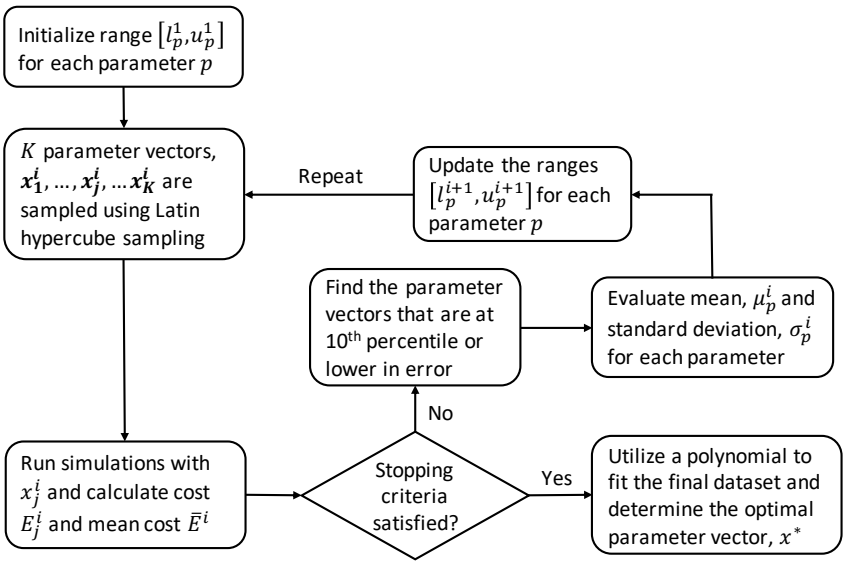

Figure 2.2. Flow chart showing the algorithm for extraction of physical parameters. Reproduced with permission [101]. Copyright 2021, Elsevier.

A parameter vector is a vector composed of n parameters that is sampled from a parameter space, $\boldsymbol{X^i}$, a subspace of an n-dimensional real space, $\mathbb{R}^n$, which can be mathematically written as:

$$\boldsymbol{X^i} = \left\{\boldsymbol{x} \in \mathbb{R}^n \mid l_p^i \leq x_p \leq u_p^i, p \in \{1, \ldots, n\}\right\}. \tag{2.21}$$

The lower $\left(l_p^i\right)$ and upper $\left(u_p^i\right)$ bounds on each dimension, p, in iteration, i, are iteratively updated. Hereafter, the superscript i indicates the iteration number. In each iteration, K vectors are sampled. A jth-sampled parameter vector, $\boldsymbol{x_j^i}$, is a point in $\boldsymbol{X^i}$. The objective/cost function of each sampled vector, $\boldsymbol{x_j^i}$, is defined as an averaged error, E_j^i, between the set of values, $y_{sim,k}$, obtained

from the simulation with the parameter vector, $\boldsymbol{x_j^i}$, and experimentally measured values, $y_{exp,k}$, using a root mean square error (RMSE):

$$E_j^i(\boldsymbol{x_j^i}) = RMSE(\boldsymbol{x_j^i}) = \sqrt{\frac{1}{M}\sum_{k=1}^{M}\left[y_{sim,k}(\boldsymbol{x_j^i}) - y_{exp,k}\right]^2}, \tag{2.22}$$

where $y_{exp,k}$ is the k^{th} experimental observation, $y_{sim,k}$ is the k^{th} simulated observation obtained using a parameter vector, respectively, and M is the total number of observations (e.g., the number of discrete points at which the temperature is compared) for each simulation. The average cost, $\bar{E}^i$, in each iteration is evaluated using the following formula:

$$\bar{E}^i = \frac{1}{K}\sum_{j=1}^{K} E_j^i, \tag{2.23}$$

where K stands for the number of simulations resulting from the sampled parameters in each iteration. The objective of this algorithm is to iteratively reduce the average cost $\bar{E}^i$ until the change of $\bar{E}^i$ is less than a threshold from iteration $i-1$ to iteration i.

The initial bounds l_p^1 and u_p^1 for each parameter are assigned based on either literature-reported values or physical constraints. Then, K parameter vectors are generated within the assigned ranges using Latin hypercube sampling (LHS) [102]. We utilized a built-in function in MATLAB® to implement the sampling of parameters in the parameter space.

The model with each parameter vector, $\boldsymbol{x_j^i}$, in iteration i is simulated, and the RMSE between simulated and experimental observations at M points is computed using Equation (2.22). The parameter vectors that are at the r^{th} percentile or lower in error are selected, where r defines the cutoff, from which the average value μ_p^i and the standard deviation σ_p^i of each parameter is calculated. If r is too large, it will result in slow convergence, while if too small it will not yield

statistically meaningful information and it will increase the number of the sampling calculations required. We found setting $r = 10$ in general works well, although the optimal choice of r could depend on the number of available training examples. The mean and standard deviation are then utilized to update the lower and upper bounds of each parameter for next iteration $(i + 1)$ using

$$u_p^{i+1} = \mu_p^i + \gamma\sigma_p^i, \tag{2.24}$$

$$l_p^{i+1} = \mu_p^i - \gamma\sigma_p^i, \tag{2.25}$$

where γ is an adjustable constant parameter that determines the width of parameter ranges for the next iteration. If the value of γ is too large, the parameters range may never converge; if the value is too small, the parameter space could be trapped in a local minimum and the determined parameter vector can be suboptimal.

An average cost $\bar{E}^i$ is calculated at each iteration, i. The stopping criterion is considered met when the change of this error, $\Delta E^i = \left|\left(\bar{E}^i - \bar{E}^{i-1}\right)/\bar{E}^{i-1}\right|$, is less than 10^{-3} in two consecutive iterations. When the stopping criterion is met, we employ a second-order polynomial with n variables to fit the final dataset and consider the position of the local minimum of that polynomial to be the optimal value, x_p^*, for each parameter p. Specifically, the sampled vectors from the final dataset that consists of the 10th percentile of the final sampling calculations are chosen to be independent variables and their corresponding cost are selected as dependent variables. This percentile threshold may also depend on the specifics of the model and training data. We normalize the independent variables by subtracting their mean values from them and dividing them by their standard deviations. Specifically, a mean, μ_p, and standard deviation, σ_p, are calculated from all the p^{th} elements. Each element, x_p, of an independent variable, $\boldsymbol{x_j} = (x_{1,j}, \dots x_{p,j}, \dots, x_{n,j})$, is normalized to $\tilde{x}_{p,j}$ as follows:

$$\tilde{x}_{p,j} = \left(x_{p,j} - \mu_p\right)/\sigma_p, \tag{2.26}$$

resulting in normalized vector $\tilde{\boldsymbol{x}}_{\boldsymbol{j}}$. The cost function of each normalized vector, is then approximated as a second-order polynomial with the following form:

$$\hat{E}\left(\tilde{\boldsymbol{x}}_{\boldsymbol{j}}\right) = \sum_{p=1}^{n}\left(a_p\tilde{x}_{p,j}^2 + b_p\tilde{x}_{p,j} + \sum_{q=p+1}^{n}\left(c_{pq}\tilde{x}_{p,j}\tilde{x}_{q,j}\right)\right) + d, \tag{2.27}$$

where $\hat{E}\left(\tilde{\boldsymbol{x}}_{\boldsymbol{j}}\right)$ is the predicted cost for each vector, $\tilde{\boldsymbol{x}}_{\boldsymbol{j}}$. The constants a_p, b_p, c_{pq}, and d are determined via the nonlinear least-squares solver in MATLAB®. The constant a_p is constrained to be greater than zero, which constrains $\hat{E}\left(\tilde{\boldsymbol{x}}_{\boldsymbol{j}}\right)$ to be convex. Taking partial derivative of $\hat{E}\left(\tilde{\boldsymbol{x}}_{\boldsymbol{j}}\right)$ with respect to each parameter and setting them to zero result in the following equation:

$$2a_p\tilde{x}_p^* + b_p + \sum_{k=1}^{p-1}\left(c_{kp}\tilde{x}_k^*\right) + \sum_{q=p+1}^{n}\left(c_{pq}\tilde{x}_q^*\right) = 0, \tag{2.28}$$

where the superscript "*" indicates an optimal value. There are in total n independent equations with n unknown variables. Rearranging them yield the following linear system: $\boldsymbol{A}\tilde{\boldsymbol{x}}^* = -\boldsymbol{b}$

$$\begin{pmatrix} 2a_1 & c_{12} & \cdots & \cdots & \cdots & c_{1n} \\ c_{12} & 2a_2 & & & & c_{2n} \\ \vdots & & \ddots & & & \vdots \\ c_{1p} & & & 2a_p & & c_{pn} \\ \vdots & & & & \ddots & \vdots \\ c_{1n} & c_{2n} & \cdots & \cdots & \cdots & 2a_n \end{pmatrix}\begin{pmatrix} \tilde{x}_1^* \\ \tilde{x}_2^* \\ \vdots \\ \tilde{x}_p^* \\ \vdots \\ \tilde{x}_n^* \end{pmatrix} = \begin{pmatrix} -b_1 \\ -b_2 \\ \vdots \\ -b_p \\ \vdots \\ -b_n \end{pmatrix}. \tag{2.29}$$

The optimal normalized parameter vector can then be solved using $\tilde{\boldsymbol{x}}^* = -\boldsymbol{A}^{-1}\boldsymbol{b}$. Each element $\tilde{x}_p^*$ of the vector is then multiplied by the previous calculated standard deviation, σ_p, and added to the mean, μ_p, to be transformed back to the original parameter space,

$$x_p^* = \tilde{x}_p^*\sigma_p + \mu_p, \tag{2.30}$$

resulting in the optimal parameter vector, $\boldsymbol{x}^*$.

This method is employed in Chapter 7 Section 7.2 to determine uncertain parameters for a heat transfer model of an optical floating zone experiment.

2.6 Phase-field models*

2.6.1 Overview

Phase-field models have been commonly applied to model temporal and spatial evolution of mesoscale microstructure [103-105] during processes such as solidification [106-109], grain growth [24,110-113], spinodal decomposition [114,115], sintering [116,117], and electrochemical reactions [118-121]. Continuous field variables are utilized in phase-field models to describe the quantities of interest for each application. As compared to sharp interface methods [122-124] in which the position of interfaces between different phases are explicitly tracked during the evolution, the phase-field model employs a diffuse interface approach [125-127], for which an interface is described by a smooth change of a field variable from its value in one phase to is value in the other phase. Phase-field models employ a free energy functional to capture the thermodynamics of the material system to be modeled. The microstructure evolution is obtained by the reduction of this free energy under the constraints that apply in each case.

2.6.2 Field variables

Phase-field models typically contain one or more field variables to describe the quantities involved in each application. There are two types of field variables: conserved or non-conserved field variables. A conserved field variable is employed to describe the physical quantity that satisfies local conservation conditions, such as concentration. On the other hand, a non-conserved

* Adapted from G. Huang, D. Montiel, R. D. McAuliffe, G. M. Veith, and K. Thornton, "Phase-Field Modeling of Solid-State Metathesis Reactions with the Charge Neutrality Constraint," Computational Materials Science **221**, 112080 (2023).

field variable, or order parameter, is utilized to describe the quantities that do not satisfy local conservation conditions, such as the orientation for grains.

2.6.3 Free energy functional

The free energy functional, $\mathcal{F}$, of a phase-field model is commonly constructed as an integral of the sum of a few free energy density terms, over the system volume, V:

$$\mathcal{F} = \int_V \left(f_{\text{bulk}} + f_{\text{gradient}} + f_{\text{additional}}\right) dV. \tag{2.31}$$

Here, f_{bulk} is the bulk energy density term, which encodes the thermodynamics of the material system. Although a realistic bulk free energy landscape measured in the experiment or calculated using density functional theory can be used to construct f_{bulk}, one can also choose to mathematically construct such an energy form. For example, the following form can be used to describe a material system with two equilibrium phases:

$$f_{\text{bulk}} = W(\phi - \phi_1)^2(\phi - \phi_2)^2. \tag{2.32}$$

Here, ϕ is the field variable, and W is the coefficient for the bulk energy density. The function has two local minima at $\phi = \phi_1$ and $\phi = \phi_2$. When ϕ stands for a conserved field variable, ϕ_1 and ϕ_2 are chosen to reflect the stable composition. When ϕ is used to describe a non-conserved order parameter, ϕ_1 and ϕ_2 are the values associated with each state. Additional field variables are necessary to model a more complex material system. For those cases, Equation (2.32) needs to be modified to take these additional field variables into account. In this thesis, we will present two examples of bulk free energy density term, one for solid-state metathesis reactions in which charge neutrality condition must be considered (see Chapter 3), and the other for polycrystalline microstructure evolution with dislocations in which stored energy must be included in the driving force (see Chapter 5 and Chapter 6).

The second term in the integral of Equation (2.31), f_{gradient}, is the gradient energy density term, which is used to penalize a large gradient in field variables. A common form used for this term is given by [103,126]

$$f_{\text{gradient}} = \frac{\kappa}{2}\sum_{i=1}^{N}|\nabla\phi_i|^2, \tag{2.33}$$

where κ is the gradient energy coefficient, and N is the total number of field variables employed in a phase-field model. The values of W and κ can be determined based on the value of interfacial energy, a material parameter, and the interfacial width, a model parameter. Since the interfaces in phase-field models are diffuse, the interfacial width is a model parameter. In this thesis, we define the width of an interface, l_{int}, to be

$$l_{int} = 2\sqrt{\frac{2\kappa}{W}}. \tag{2.34}$$

When ϕ_1 and ϕ_2 are taken to be 0 and 1, respectively, the equilibrium profile of ϕ with respect to the position x is given by

$$\phi = \frac{1}{2}\left[1 + \tanh\left(\frac{2(x - x_0)}{l_{int}}\right)\right], \tag{2.35}$$

where x_0 is the center of the interface where $\phi = 0.5$. The profile is shown in Figure 2.3.

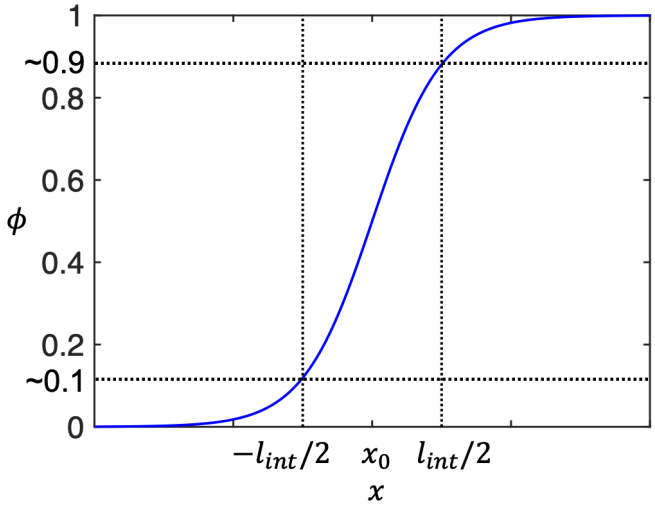

Figure 2.3. The equilibrium profile of ϕ, when $\phi_1 = 0$ and $\phi_2 = 1$.

With this definition, each field variable varies from approximately 10% to 90% of their maximum value between $x_0 - l_{int}/2$ and $x_0 + l_{int}/2$. For instance, in the example for which ϕ_1 and ϕ_2 are 0 and 1, respectively, ϕ is ~0.1 at $x = x_0 - l_{int}/2$, and ~0.9 at $x = x_0 + l_{int}/2$.

Although the first two energy density terms in Equation (2.31) might suffice for some phase-field models, the third term, $f_{\text{additional}}$, could be utilized to describe additional constraints or physics for a materials system. In Chapter 3 of this thesis, for example, we employ a set of Lagrange multipliers as this additional energy density term to impose constraints on mass conservation and electroneutrality during solid-state metathesis reactions. In Chapter 5 and Chapter 6, we utilize a stored energy term as this additional energy density term to consider the effect of the stored energy on microstructure evolution.

2.6.4 Governing equations

Two types of governing equations are commonly used to describe the evolution of field variables. For a conserved field variable, such as a concentration field, $c(\boldsymbol{r}, t)$**,** the following mass conservation equation [103,128] is utilized to describe its evolution:

$$\frac{\partial c(\boldsymbol{r},t)}{\partial t} = -\nabla \cdot J. \tag{2.36}$$

Here, the flux J is given by

$$J = -M\nabla\mu = -M\nabla\frac{\delta\mathcal{F}}{\delta c}, \tag{2.37}$$

where $\mu = \frac{\delta\mathcal{F}}{\delta c}$ is the chemical potential, and M is the mobility for the quantity the field variable describes.

For a non-conserved order parameter, such as a grain orientation, η, the Allen-Cahn dynamics [129] is employed to describe its evolution:

$$\frac{\partial\eta}{\partial t} = -L\left(\frac{\delta F}{\delta\eta}\right), \tag{2.38}$$

where L is the mobility parameter for the quantity the field variable describes.

2.6.5 Linear stability analysis[*]

When evolving a governing phase-field equation, the initial fluctuation in the order parameter may grow or decay. Linear stability analysis is commonly employed to predict whether a certain wavelength will grow or not, given the evolution dynamics. To demonstrate this concept, we show its application to the Cahn-Hilliard dynamics. Substituting a free energy functional that includes the bulk free energy density term and the gradient energy density term into Equation (2.36) yields

$$\frac{\partial c(\boldsymbol{r},t)}{\partial t} = \nabla \cdot \left[M\nabla\left(\frac{\partial f_{bulk}}{\partial c} - \kappa\nabla^2 c\right)\right]. \tag{2.39}$$

In this section, the following double-well form of f_{bulk} is considered,

$$f_{bulk} = W[c(\boldsymbol{r},t) - c_1]^2[c(\boldsymbol{r},t) - c_2]^2, \tag{2.40}$$

[*] Adapted from R. W. Balluffi, S. M. Allen, and W. C. Carter, *Kinetics of Materials*, John Wiley & Sons (2005).

where W is the coefficient for the bulk energy density, $c(\boldsymbol{r}, t)$ is the field variable for the concentration, and c_1 and c_2 are the two equilibrium concentrations. This equation can be linearized by setting the mobility to its characteristic value, M_0, near the concentration around which the equation is linearized, and applying the chain rule, which leads to [130]

$$\frac{\partial c(\boldsymbol{r}, t)}{\partial t} = M_0 \left[\frac{\partial^2 f_{bulk}}{\partial c^2} \nabla^2 c - \kappa \nabla^4 c \right]. \tag{2.41}$$

Taking the second derivative of f_{bulk} with respect to c yields

$$\frac{\partial^2 f_{bulk}}{\partial c^2} = 2W[(c - c_1)^2 + 4(c - c_1)(c - c_2) + (c - c_2)^2]. \tag{2.42}$$

When $c(\boldsymbol{r}, t)$ is perturbed with a one-dimensional wave, $\epsilon(t)\sin(\beta x)$, from its initial value, c_0, the concentration field can be written as

$$c(\boldsymbol{r}, t) = c_0 + \epsilon(t)\sin(\beta x), \tag{2.43}$$

where $\epsilon(t)$ is the time-dependent amplitude of the wave, $\beta = \frac{2\pi}{\lambda}$ is the wavenumber, and λ is the wavelength. Substituting Equation (2.43) into Equation (2.41) and keeping only the first-order terms in $\epsilon(t)$ yield

$$\frac{\partial \epsilon(t)}{\partial t} \sin(\beta x) = M_0[k_0 \nabla^2(\epsilon(t)\sin(\beta x)) - \kappa \nabla^4(\epsilon(t)\sin(\beta x))]. \tag{2.44}$$

Note that when evaluating $\frac{\partial^2 f_{bulk}}{\partial c^2}$ at $c(\boldsymbol{r}, t) = c_0 + \epsilon(t)\sin(\beta x)$, we omit the terms that involve $\epsilon(t)$ because these terms multiplied with $\nabla^2(\epsilon(t)\sin(\beta x))$ result in higher order terms in $\epsilon(t)$. Consequently, the expression of $\frac{\partial^2 f_{bulk}}{\partial c^2}$ is equal to a constant k_0, given by

$$k_0 = 2W[(c_0 - c_1)^2 + 4(c_0 - c_1)(c_0 - c_2) + (c_0 - c_2)^2], \tag{2.45}$$

which is less than 0 within the spinodal regime. The two terms in Equation (2.44) that involve the gradient operator are given by

$$\nabla^2(\epsilon(t)\sin(\beta x)) = -\beta^2\epsilon(t)\sin(\beta x) \tag{2.46}$$

and

$$\nabla^4(\epsilon(t)\sin(\beta x)) = \beta^4\epsilon(t)\sin(\beta x). \tag{2.47}$$

Substituting Equation (2.46) and (2.47) into Equation (2.44) yields

$$\frac{\partial\epsilon(t)}{\partial t} = -M_0[k_0\beta^2 + \kappa\beta^4]\epsilon(t). \tag{2.48}$$

Solving Equation (2.48), which is now an ordinary differential equation, yields

$$\epsilon(t) = \epsilon(0)e^{-M_0[k_0\beta^2+\kappa\beta^4]t} = \epsilon(0)e^{R(\beta)t}, \tag{2.49}$$

where $R(\beta) = -M_0[k_0\beta^2 + \kappa\beta^4]$ is the amplification factor. The fluctuation will grow when $R(\beta) > 0$, or when

$$\beta < \beta_{\text{crit}} = \sqrt{-\frac{k_0}{\kappa}}, \tag{2.50}$$

where β_{crit} is the critical wavenumber below which the fluctuation grows. The maximum amplification factor is obtained when $\frac{\partial R(\beta)}{\partial\beta} = 0$, or when

$$\beta_{\max} = \sqrt{-\frac{k_0}{2\kappa}}. \tag{2.51}$$

A typical curve for $R(\beta)$, which sets $c_1 = 0.1$, $c_2 = 0.9$, and $c_0 = \frac{c_1+c_2}{2} = 0.5$, is shown in Figure 2.4. The amplification factor is greater than 0 when $\beta < \beta_{\text{crit}}$ and maximized at $\beta = \beta_{\max}$.

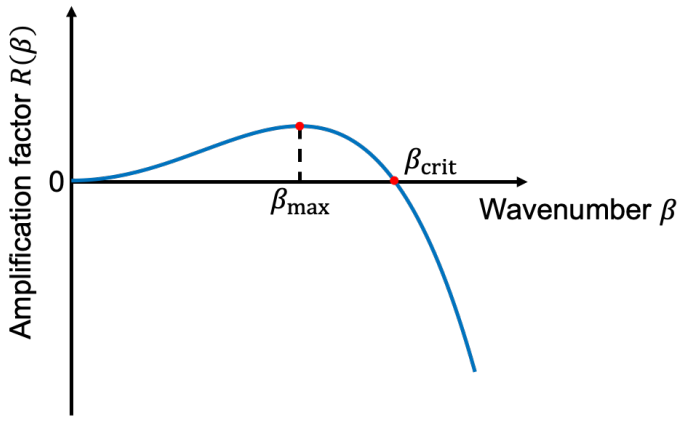

Figure 2.4. Amplification factor, $R(\beta)$, vs. wavenumber, β. The amplification factor is greater than 0 when $\beta < \beta_{crit}$ and maximized at $\beta = \beta_{max}$.

2.7 The smoothed boundary method

In order to accurately describe the microstructure evolution, it is necessary to impose a precise boundary condition. When the modeled geometry is of irregular shape, however, it is challenging to apply boundary conditions on the geometry. One approach to overcome this issue is to employ a smoothed boundary method (SBM), which leverages a domain parameter to allow for imposing boundary conditions on irregular boundaries. The SBM was initially introduced by Refs. [131-133] to solve diffusion equations with no-flux boundary condition and was later extended by Yu et al. [134] to solve partial differential equations with general boundary conditions. This method introduces a domain parameter, ψ, which is 1 inside the domain, 0 outside the domain, and smoothly varies from 1 to 0 at the boundary of the domain.

Although the smoothed boundary method can be applied to various partial differential equations [135-137], we demonstrate the derivation using the diffusion equation, which possess a relatively simple form, as an example to show how Neumann and Dirichlet boundary conditions can be imposed using the method.

The governing equation for diffusion according to Fick's second law is given by

$$\frac{\partial c}{\partial t} = -\nabla \cdot J + S = -\nabla \cdot (D\nabla c) + S, \tag{2.52}$$

where c is the concentration, J is the flux, S is the source term, D is the diffusion coefficient. Multiplying Equation (2.52) with ψ yields

$$\psi \frac{\partial c}{\partial t} = \psi \nabla \cdot (D\nabla c) + \psi S. \tag{2.53}$$

The first term on the right-hand side of Equation (2.53) can be mathematically manipulated using the generalized form of the product rule of differentiation ($\nabla \cdot (f\boldsymbol{g}) = \nabla f \cdot \boldsymbol{g} + f\nabla(\boldsymbol{g})$) as

$$\psi \nabla \cdot (D\nabla c) = \nabla \cdot (\psi D\nabla c) - \nabla\psi \cdot (D\nabla c). \tag{2.54}$$

Substituting Equation (2.54) into Equation (2.53) yields [134]

$$\psi \frac{\partial c}{\partial t} = \nabla \cdot (\psi D\nabla c) - \nabla\psi \cdot (D\nabla c) + \psi S. \tag{2.55}$$

2.7.1 Neumann boundary condition

The inward flux, J_B, at the boundary is given by

$$n \cdot J = -\frac{\nabla\psi}{|\nabla\psi|}(D\nabla c) = J_B, \tag{2.56}$$

where $n = \frac{\nabla\psi}{|\nabla\psi|}$ is the unit normal inward vector. Rearranging Equation (2.56) yields

$$-\nabla\psi(D\nabla c) = |\nabla\psi| J_B. \tag{2.57}$$

Substituting Equation (2.57) into the second term on the right-hand side of Equation (2.55) and rearranging the resulting equation yield [134]

$$\frac{\partial c}{\partial t} = \frac{1}{\psi}[\nabla \cdot (\psi D\nabla c) - |\nabla\psi| J_B + \psi S]. \tag{2.58}$$

When a no-flux boundary condition is imposed ($J_B = 0$) and no additional term needs to be considered, Equation (2.58) reduces to the form that was presented in Refs. [131-133]

$$\frac{\partial c}{\partial t} = \frac{1}{\psi}\nabla \cdot (\psi D \nabla c). \tag{2.59}$$

2.7.2 Dirichlet boundary condition

Multiplying Equation (2.55) with ψ yields

$$\psi^2 \frac{\partial c}{\partial t} = \psi \nabla \cdot (\psi D \nabla c) - \psi \nabla \psi \cdot (D \nabla c) + \psi^2 S. \tag{2.60}$$

Again, using the generalized product rule, the second term on the right-hand side of Equation (2.60) can also be written as

$$-\psi \nabla \psi \cdot (D \nabla c) = -D[\nabla \psi \cdot \nabla(\psi c) - c|\nabla \psi|^2]. \tag{2.61}$$

Substituting Equation (2.61) into Equation (2.60) and rearranging the resulting equation yield

$$\frac{\partial c}{\partial t} = \frac{1}{\psi}\nabla \cdot (\psi D \nabla c) - \frac{D}{\psi^2}[\nabla \psi \cdot \nabla(\psi c) - C_0|\nabla \psi|^2] + S. \tag{2.62}$$

Here, the field c before $|\nabla \psi|^2$ is replaced by C_0, the boundary value to be imposed.

2.8 A distance function and level-set method

Although phase-field methods eliminate the needs to explicitly track the interfaces during the microstructure evolution, it is still sometimes necessary to locate the interfaces, as well as to determine a distance function, $d(\boldsymbol{r})$, the distance from a point to its nearest interface, when initializing the microstructure for a phase-field model. For instance, importing a complex experimental microstructure, in which different phases are separated by sharp interfaces as the initial condition for a phase-field model, may require generating $d(\boldsymbol{r})$ based on the experimental microstructure, which can then be fed into a hyperbolic tangent function to generate field variable profiles with a diffuse interface.

Here, we describe the level-set method [124,138-140], which takes a field with sharp interface between each phase and produce a distance function $d(\boldsymbol{r})$, which is 0 at the interfaces,

positive on one side of the interfaces, and negative on the other side. Given an initial field, $\phi(\boldsymbol{r})$, the distance function $d(\boldsymbol{r})$ is obtained by iteratively evolving the following equation until convergence:

$$\frac{\partial \phi}{\partial t} = \text{sign}(\phi)(1 - |\nabla \phi|). \tag{2.63}$$

Here, $\text{sign}(\phi)$ is a smoothed sign function of ϕ, which is given by

$$\text{sign}(\phi) = \frac{\phi}{\sqrt{\phi^2 + \epsilon^2}}, \tag{2.64}$$

where ϵ is a small number employed here to avoid numerical instability for small ϕ. In this thesis, the gradient of ϕ, $\nabla\phi$, is numerically evaluated using a first-order upwind scheme [138,141]. For simplicity, we describe this scheme here in one dimension and denote $\phi'(x)$ as the first derivative of ϕ at position x. We note that the same discretization scheme could be applied to all the dimensions when multiple dimensions are considered. First, $\phi'(x)$ is evaluated using both the forward and backward schemes, resulting in ${\phi_f}'(x)$ and ${\phi_b}'(x)$, respectively

$$\phi_f'(x) = \frac{\phi(x + \Delta x) - \phi(x)}{\Delta x} \tag{2.65}$$

and

$$\phi_b'(x) = \frac{\phi(x) - \phi(x - \Delta x)}{\Delta x}, \tag{2.66}$$

where Δx is the grid spacing. When $\text{sign}(\phi) > 0$, we take

$$\phi'(x) = \max\{\max[0, \phi_b'(x)], \max[0, -\phi_f'(x)]\}. \tag{2.67}$$

When $\text{sign}(\phi) < 0$, we have

$$\phi'(x) = \max\{\max[0, -\phi_b'(x)], \max[0, \phi_f'(x)]\}. \tag{2.68}$$

We define the convergence to be reached when the spatial average of the absolute value of the change in ϕ between two iterations, $\frac{1}{V}\int_V |\phi(t+\Delta t) - \phi(t)|\, dV$, is less than 10^{-6}.

Chapter 3 Phase-Field Modeling of Solid-State Metathesis Reactions with the Charge Neutrality Constraint

3.1 Introduction

As discussed in Chapter 1 Section 1.2, a computational model is required to facilitate the understanding of solid-state metathesis (SSM) reactions. In this chapter,[*] we present a phase-field approach to simulate the evolution of ionic concentrations and phase fractions in solid-state metathesis reactions. In Section 3.2, we present a phase-field model for simulating a simple SSM reaction in which all the ions are assumed to have an identical absolute value of charge numbers. In Section 3.3, we generalize the model to consider ions with different absolute value of charge numbers. In Section 3.4, we discuss the nondimensionalization of phase-field equations. In Section 3.5, we describe the relationship between the diffusion coefficient and mobility of each ion in the proposed phase-field model. In Section 3.6, we explain how the energy scale for the proposed phase-field model is determined. In Section 3.7, we couple the phase-field model with the smoothed boundary method to extend the model to simulate the SSM reactions between particles.

3.2 A phase-field model for a simple SSM reaction

We begin by presenting a phase-field model that describes a special SSM reaction in which all the ions are assumed to have an identical absolute value of charge numbers and the

[*] Sections 3.2 – 3.6 are adapted from G. Huang, D. Montiel, R. D. McAuliffe, G. M. Veith, and K. Thornton, "Phase-Field Modeling of Solid-State Metathesis Reactions with the Charge Neutrality Constraint," Computational Materials Science **221**, 112080 (2023). Section 3.7 is adapted from G. E. Kamm, G. Huang, S. M. Vornholt, R. D. McAuliffe, G. M. Veith, K. S. Thornton, and K. W. Chapman, "Relative Kinetics of Solid-State Reactions: The Role of Architecture in Controlling Reactivity," Journal of the American Chemical Society **144**, 11975 (2022).

stoichiometric coefficients (*i.e.,* the coefficients in front of the compounds to balance the reaction) are unity for all the phases. Such a reaction can be written as

$$AX + BY \rightarrow AY + BX, \tag{3.1}$$

where two cations are denoted by A and B, and two anions are denoted by X and Y. The precursor phases are denoted by AX and BY, and the product phases are denoted by AY and BX.

As discussed in Chapter 2 Section 2.1.3, two pathways were proposed for a binary SSM reaction – one assuming that ions diffuse to form products without undergoing redox reactions and the other assuming that the ions are first reduced or oxidized to their elemental form before being recombined into products. Although the actual reaction pathway is more complex in general and these pathways represent extreme cases, we propose the present phase-field model based on the first mechanism. This model assumes a direct SSM reaction and does not consider intermediate compounds. Additionally, for simplicity we assume that each of the reactant phases is unstable in the presence of the other reactant at a sufficiently high temperature. Although a density functional theory calculation may be required to rigorously examine the stability of the reactants, the assumption is consistent with the fact of the rapid formation of salts observed in SSM reactions. For example, it is reported in Ref. [2] that grinding MCl_2 (M = Fe, Co, Ni) and Na_2S_2 precursor particles at room temperature in air yield immediate formation of NaCl. Therefore, we employ a free energy landscape with two local minima at compositions corresponding to the two product phases. While this assumption is not necessary, it allows for a simple model that recovers expected behavior observed in SSM reactions. We note that intermediate species can be incorporated if we employ a more complex free energy functional, which will be left for future work. In addition, we assume that the rate of phase transformations is limited by the diffusion of ions. In other words, the nucleation of product phases is considered instantaneous. Furthermore, we assume that the

molar volume of phases is proportional to the number of their constituent ions. Thus, the molar volume of all the phases in Equation (3.1) is considered identical under this assumption. The phase-field model, under the assumptions stated above, is presented below.

3.2.1 Free energy functional

A total free energy functional, $\mathcal{F}$, is constructed as the integral over the system volume of a bulk energy density, f_{bulk}, a gradient energy density, f_{gradient}, and a term to impose constraints, $f_{\text{constraint}}$:

$$\mathcal{F}(\boldsymbol{c}) = \int_V \left(f_{\text{bulk}} + f_{\text{gradient}} + f_{\text{constraint}}\right) dV, \tag{3.2}$$

where $\boldsymbol{c} = [c_A, c_B, c_X, c_Y]$ is a vector in which each element $c_i = c_i(\boldsymbol{r}, t)$ denotes the mole fraction of ion i ($i \in \{\text{A}, \text{B}, \text{X}, \text{Y}\}$), which depends on position, $\boldsymbol{r}$, and time, t. The bulk energy density provides a thermodynamic energy landscape with two local minima (equal to zero) at compositions corresponding to the products. We assume that the phase transformation occurs under constant temperature. Therefore, the dependence of free energy on temperature is omitted in our model. The bulk energy density is given by

$$f_{\text{bulk}}(\boldsymbol{c}) = W \prod_{\alpha \in \{\text{AY,BX}\}} \left[\sum_{i \in \{\text{A,B,X,Y}\}} (c_i - c_i^{\alpha})^2 \right], \tag{3.3}$$

where W is the coefficient for the bulk energy density, c_i^{α} is the equilibrium mole fraction of ion i in product phase α, given by

$$c_i^{\alpha} = \begin{cases} 0.5, & i \text{ in phase } \alpha, \\ 0, & \text{otherwise.} \end{cases} \tag{3.4}$$

The gradient energy density term [103,126] sets a finite width for interfaces between phases and is given by

$$f_{\text{gradient}}(\nabla \boldsymbol{c}) = \frac{\kappa}{2} \sum_{i \in \{\text{A,B,X,Y}\}} |\nabla c_i|^2, \tag{3.5}$$

where κ is the gradient energy coefficient. The values of W and κ are uniquely determined once the interfacial energy and the interfacial width, a model parameter, are set. In this work, we define the interfacial width, l_{int}, to be

$$l_{int} = 2\delta = 2\sqrt{\frac{2\kappa}{W}}. \tag{3.6}$$

Mole fractions vary from approximately 10% to 90% of their maximum values across an interface with this definition of interfacial width. We assume that every site is occupied by an ion in the case of crystalline solid, and thus the sum of mole fractions of ions at each position must be equal to unity. Furthermore, we assume that no charge localization occurs during the reaction, *i.e.,* the system is charge neutral throughout and the current density at each position is divergence free at all times. This assumption, along with the aforementioned assumption of redox-free reactions, give rise to the constraint of electroneutrality. Unlike the electrochemical model in Ref. [120] that utilizes the Poisson's equation to obtain the electrostatic potential based on the local charge density, the models that assume electroneutrality [118,142-144] have been commonly employed to circumvent the requirement to resolve the thin double layer (with a typical thickness of a few nanometers [121]), allowing simulations of morphological evolution over a much larger length scale. Employing this constraint is therefore beneficial to the modeling of solid-state metathesis reactions, in which the precursor size varies from tens of nanometers [145] to tens of microns [3,146].

We employ two Lagrange multipliers in our model to impose the two sets of constraints. In addition, we include a negative-mole-fraction penalty term in the free energy functional to

prevent mole fractions from becoming negative, which may occur due to the shape of $f_{\text{bulk}}(\boldsymbol{c})$. These constraints are encoded into a constraint term, which is given by

$$f_{\text{constraint}}(\boldsymbol{c}) = -\Lambda_1(\boldsymbol{c})\left[\left(\sum_{i\in\{\text{A,B,X,Y}\}} c_i\right) - 1\right] - \Lambda_2(\boldsymbol{c})\left(\sum_{i\in\{\text{A,B,X,Y}\}} z_i c_i\right) + \left[\sum_{i\in\{\text{A,B,X,Y}\}} g_i(c_i)\right], \tag{3.7}$$

where z_i is the charge number of ion i. The function $g_i(c_i)$ in Equation (3.7) is given by

$$g_i(c_i) = \begin{cases} 0, & c_i \geq 0 \\ \zeta c_i^2, & c_i < 0 \end{cases}, \tag{3.8}$$

where ζ is a tunable coefficient for the negative-mole-fraction penalty term.

3.2.2 Governing equations

The evolution of $c_i(\boldsymbol{r}, t)$ is described by a mass conservation equation [103,128]:

$$\frac{\partial c_i(\boldsymbol{r}, t)}{\partial t} = -\nabla \cdot J_i, \tag{3.9}$$

where the flux is given by chemical potential gradient [128]:

$$J_i = -M_i \nabla \mu_i = -M_i \nabla \frac{\delta \mathcal{F}}{\delta c_i}. \tag{3.10}$$

Here, μ_i and M_i are the chemical potential and mobility of the ion i, respectively. The mobility M_i of the ion i is approximately related to its diffusion coefficient, D_i, by

$$M_i \approx D_i \Phi_{\text{i}}^{-1}, \tag{3.11}$$

where Φ_i is an approximate conversion factor for the ion i. A derivation of Φ_i is presented in Section 3.5. Equation (3.11) is commonly employed in the literature [147-149] to link the mobility and the diffusion coefficient, which is exact when a model only involves one independent field variable. The applicability to this model is presented in Section 3.5. We assume that each M_i is a constant, rather than being a function of the concentration, in order to maintain computational efficiency and to provide insight into how the reaction process depend on the magnitude of the

mobilities. We note that it has been found that different form of mobility does not affect the morphological evolution [150,151]. Although it may affect the kinetics [151], quantitatively predicting the kinetics is not the focus of this work. Substituting Equations (3.2) - (3.8) into Equation (3.10) yields

$$J_i = -M_i \left[\nabla \left(\frac{\partial f_{\text{bulk}}}{\partial c_i} - \kappa \nabla^2 c_i + \frac{\partial g_i}{\partial c_i} \right) - \nabla \Lambda_1(\boldsymbol{c}) - z_i \nabla \Lambda_2(\boldsymbol{c}) \right]. \tag{3.12}$$

Note that the terms involving $\frac{\partial \Lambda_1(\boldsymbol{c})}{\partial c_i}$ and $\frac{\partial \Lambda_2(\boldsymbol{c})}{\partial c_i}$ vanish when deriving Equation (3.12) due to the constraints on the sum of mole fractions and of electroneutrality. The derivative, $\frac{\partial f_{\text{bulk}}}{\partial c_i}$, in Equation (3.12) is given by

$$\frac{\partial f_{\text{bulk}}}{\partial c_i} = W \left\{ \sum_{\alpha \in \{\text{AY,BX}\}} \left[2(c_i - c_i^{\alpha}) \sum_{\substack{j \in \{\text{A,B,X,Y}\} \\ \beta \in \{\text{AY,BX}\}, \beta \neq \alpha}} \left(c_j - c_j^{\beta} \right)^2 \right] \right\}. \tag{3.13}$$

The derivative, $\frac{\partial g_i}{\partial c_i}$, in Equation (3.12) is given by

$$\frac{\partial g_i}{\partial c_i} = \begin{cases} 0, & c_i \geq 0 \\ 2\zeta c_i, & c_i < 0 \end{cases}. \tag{3.14}$$

The gradient of two Lagrange multipliers, $\nabla \Lambda_1$ and $\nabla \Lambda_2$ can be calculated, considering zero net mass flux and net charge flux:

$$\sum_{i \in \{\text{A,B,X,Y}\}} J_i = \sum_{i \in \{\text{A,B,X,Y}\}} z_i J_i = 0. \tag{3.15}$$

Substituting Equation (3.12) into Equation (3.15) yields

$$K_1 \nabla \Lambda_1(\boldsymbol{c}) + K_2 \nabla \Lambda_2(\boldsymbol{c}) - G_1(\boldsymbol{c}) = 0 \tag{3.16}$$

and

$$K_2 \nabla \Lambda_1(\boldsymbol{c}) + K_3 \nabla \Lambda_2(\boldsymbol{c}) - G_2(\boldsymbol{c}) = 0, \tag{3.17}$$

where

$$K_1 = \sum_{i\in\{\mathrm{A,B,X,Y}\}} M_i, \tag{3.18}$$

$$K_2 = \sum_{i\in\{\mathrm{A,B,X,Y}\}} z_i M_i, \tag{3.19}$$

$$K_3 = \sum_{i\in\{\mathrm{A,B,X,Y}\}} z_i^2 M_i, \tag{3.20}$$

$$G_1(\boldsymbol{c}) = \sum_{i\in\{\mathrm{A,B,X,Y}\}} M_i \nabla\left(\frac{\partial f_{\mathrm{bulk}}}{\partial c_i} - \kappa\nabla^2 c_i + \frac{\partial g_i}{\partial c_i}\right), \tag{3.21}$$

$$G_2(\boldsymbol{c}) = \sum_{i\in\{\mathrm{A,B,X,Y}\}} z_i M_i \nabla\left(\frac{\partial f_{\mathrm{bulk}}}{\partial c_i} - \kappa\nabla^2 c_i + \frac{\partial g_i}{\partial c_i}\right). \tag{3.22}$$

Solving for $\nabla\Lambda_1$ and $\nabla\Lambda_2$ from Equations (3.16) and (3.17) and expressed these gradients in terms of $K_1, K_2, K_3, G_1(\boldsymbol{c})$ and $G_2(\boldsymbol{c})$, we obtain

$$\nabla\Lambda_1(\boldsymbol{c}) = \frac{1}{K_1K_3 - K_2^2}\left[K_3G_1(\boldsymbol{c}) - K_2G_2(\boldsymbol{c})\right], \tag{3.23}$$

$$\nabla\Lambda_2(\boldsymbol{c}) = \frac{1}{K_1K_3 - K_2^2}\left[K_1G_2(\boldsymbol{c}) - K_2G_1(\boldsymbol{c})\right]. \tag{3.24}$$

Substituting the flux equation (Equation (3.12)) with the Lagrange multipliers given by Equations (3.23) and (3.24) into the mass conservation equation (Equation (3.9)) yields a set of four governing equations

$$\frac{\partial c_i}{\partial t} = \nabla\cdot\left\{M_i\left[\nabla\left(\frac{\partial f_{\mathrm{bulk}}}{\partial c_i} - \kappa\nabla^2 c_i + \frac{\partial g_i}{\partial c_i}\right) - \nabla\Lambda_1(\boldsymbol{c}) - z_i\nabla\Lambda_2(\boldsymbol{c})\right]\right\}, \text{ for } i = \mathrm{A,B,X,Y}. \tag{3.25}$$

One may employ these governing equations, which have the advantages of compact formulation and parameters and flexibility for extension. However, this set of equations requires solving for six field variables, which is computationally intensive. These equations can be further reduced to a set of two independent time-evolution equations by considering the constraints of

charge neutrality and on the sum of the mole fractions. Substituting Equations (3.23) and (3.24) into Equation (3.12) yields

$$J_A = -\frac{1}{\Omega_0}(\Omega_{AA}\nabla h_A + \Omega_{AB}\nabla h_B + \Omega_{AX}\nabla h_X + \Omega_{AY}\nabla h_Y), \tag{3.26}$$

$$J_B = -\frac{1}{\Omega_0}(\Omega_{BA}\nabla h_A + \Omega_{BB}\nabla h_B + \Omega_{BX}\nabla h_X + \Omega_{BY}\nabla h_Y) = -\frac{z_X - z_A}{z_X - z_B}J_A - \frac{z_X - z_Y}{z_X - z_B}J_Y, \tag{3.27}$$

$$J_X = -\frac{1}{\Omega_0}(\Omega_{XA}\nabla h_A + \Omega_{XB}\nabla h_B + \Omega_{XX}\nabla h_X + \Omega_{XY}\nabla h_Y) = -\frac{z_B - z_A}{z_B - z_X}J_A - \frac{z_B - z_Y}{z_B - z_X}J_Y, \tag{3.28}$$

$$J_Y = -\frac{1}{\Omega_0}(\Omega_{YA}\nabla h_A + \Omega_{YB}\nabla h_B + \Omega_{YX}\nabla h_X + \Omega_{YY}\nabla h_Y), \tag{3.29}$$

where

$$h_i = \frac{\partial f_{\text{bulk}}}{\partial c_i} - \kappa\nabla^2 c_i + \frac{\partial g_i}{\partial c_i} \qquad \text{for i} = \text{A, B, X, Y,} \tag{3.30}$$

$$\Omega_0 = \frac{(z_A - z_B)^2}{M_X M_Y} + \frac{(z_A - z_X)^2}{M_B M_Y} + \frac{(z_B - z_X)^2}{M_A M_Y} + \frac{(z_A - z_Y)^2}{M_B M_X} + \frac{(z_B - z_Y)^2}{M_A M_X} + \frac{(z_X - z_Y)^2}{M_A M_B}, \tag{3.31}$$

$$\Omega_{AA} = \frac{(z_B - z_X)^2}{M_Y} + \frac{(z_B - z_Y)^2}{M_X} + \frac{(z_X - z_Y)^2}{M_B}, \tag{3.32}$$

$$\Omega_{BB} = \frac{(z_A - z_X)^2}{M_Y} + \frac{(z_A - z_Y)^2}{M_X} + \frac{(z_X - z_Y)^2}{M_A}, \tag{3.33}$$

$$\Omega_{XX} = \frac{(z_A - z_B)^2}{M_Y} + \frac{(z_A - z_Y)^2}{M_B} + \frac{(z_B - z_Y)^2}{M_A}, \tag{3.34}$$

$$\Omega_{YY} = \frac{(z_A - z_B)^2}{M_X} + \frac{(z_A - z_X)^2}{M_B} + \frac{(z_B - z_X)^2}{M_A}, \tag{3.35}$$

$$\Omega_{AB} = \Omega_{BA} = \frac{(z_A - z_X)(-z_B + z_X)}{M_Y} + \frac{(z_A - z_Y)(-z_B + z_Y)}{M_X}, \tag{3.36}$$

$$\Omega_{AX} = \Omega_{XA} = \frac{(z_A - z_B)(z_B - z_X)}{M_Y} + \frac{(z_A - z_Y)(-z_X + z_Y)}{M_B}, \tag{3.37}$$

$$\Omega_{AY} = \Omega_{YA} = \frac{(z_A - z_B)(z_B - z_Y)}{M_X} + \frac{(z_A - z_X)(z_X - z_Y)}{M_B}, \tag{3.38}$$

$$\Omega_{BX} = \Omega_{XB} = -\frac{(z_A - z_B)(z_A - z_X)}{M_Y} - \frac{(z_B - z_Y)(z_X - z_Y)}{M_A}, \tag{3.39}$$

$$\Omega_{BY} = \Omega_{YB} = -\frac{(z_A - z_B)(z_A - z_Y)}{M_X} + \frac{(z_B - z_X)(z_X - z_Y)}{M_A}, \tag{3.40}$$

$$\Omega_{XY} = \Omega_{YX} = -\frac{(z_A - z_X)(z_A - z_Y)}{M_B} - \frac{(z_B - z_X)(z_B - z_Y)}{M_A}. \tag{3.41}$$

Considering the constraints of electroneutrality (i.e., $\sum_{k\in\{\mathrm{A,B,X,Y}\}} z_k c_k = 0$) and on the sum of mole fractions (i.e., $\sum_{k\in\{\mathrm{A,B,X,Y}\}} c_k = 1$), the mole fractions of the ion B and X, c_B and c_X, can be expressed in terms of c_A and c_Y:

$$c_B = -\frac{z_X - z_A}{z_X - z_B} c_A - \frac{z_X - z_Y}{z_X - z_B} c_Y + \frac{z_X}{z_X - z_B}, \tag{3.42}$$

$$c_X = -\frac{z_B - z_A}{z_B - z_X} c_A - \frac{z_B - z_Y}{z_B - z_X} c_Y + \frac{z_B}{z_B - z_X}. \tag{3.43}$$

Substituting Equation (3.42) and (3.43) into Equation (3.30) for $i =$ B and X yields

$$h_B = -\frac{z_X - z_A}{z_X - z_B}\left(\frac{\partial f_{\mathrm{bulk}}}{\partial c_A} - \kappa\nabla^2 c_A\right) - \frac{z_X - z_Y}{z_X - z_B}\left(\frac{\partial f_{\mathrm{bulk}}}{\partial c_Y} - \kappa\nabla^2 c_Y\right) + \frac{\partial g_B}{\partial c_B}, \tag{3.44}$$

$$h_X = -\frac{z_B - z_A}{z_B - z_X}\left(\frac{\partial f_{\mathrm{bulk}}}{\partial c_A} - \kappa\nabla^2 c_A\right) - \frac{z_B - z_Y}{z_B - z_X}\left(\frac{\partial f_{\mathrm{bulk}}}{\partial c_Y} - \kappa\nabla^2 c_Y\right) + \frac{\partial g_X}{\partial c_X}. \tag{3.45}$$

Substituting Equations (3.44) and (3.45) into Equations (3.26) and (3.29) yields

$$J_A = -\frac{1}{\Omega_0}\left[\lambda_{AA}\nabla\left(\frac{\partial f_{\mathrm{bulk}}}{\partial c_A} - \kappa\nabla^2 c_A\right) + \lambda_{AY}\nabla\left(\frac{\partial f_{\mathrm{bulk}}}{\partial c_Y} - \kappa\nabla^2 c_Y\right) + \sum_{i\in\{A,B,X,Y\}} \Omega_{Ai}\frac{\partial g_i}{\partial c_i}\right], \tag{3.46}$$

$$J_Y = -\frac{1}{\Omega_0}\left[\lambda_{YA}\nabla\left(\frac{\partial f_{\mathrm{bulk}}}{\partial c_A} - \kappa\nabla^2 c_A\right) + \lambda_{YY}\nabla\left(\frac{\partial f_{\mathrm{bulk}}}{\partial c_Y} - \kappa\nabla^2 c_Y\right) + \sum_{i\in\{A,B,X,Y\}} \Omega_{Yi}\frac{\partial g_i}{\partial c_i}\right], \tag{3.47}$$

where

$$\lambda_{AA} = \frac{(z_X - z_Y)^2(-z_A + z_B - z_X + z_Y)}{z_B - z_X} + \frac{(z_B - z_Y)^2 + \frac{(z_A - z_X)(z_A - z_Y)(-z_B + z_Y)}{-z_B + z_X}}{M_B} + \frac{z_A^2 + z_B^2 + 2z_X^2 + z_B(-3z_X + z_Y) - z_A(z_X + z_Y)}{M_Y}, \tag{3.48}$$

$$\lambda_{AY} = \frac{(z_A - z_X + \frac{(z_A - z_Y)(z_B - z_Y)}{z_B - z_X})(z_X - z_Y)}{M_B} + \frac{(z_B - z_Y)(z_A - z_B + \frac{(z_X - z_Y)(-z_A + z_Y)}{z_B - z_X})}{M_X} + \frac{(-z_A + z_B)(z_B - z_Y) + (-z_A + z_X)(z_X - z_Y)}{M_Y}, \tag{3.49}$$

$$\lambda_{YA} = -\frac{(z_A + z_B - z_X - z_Y)(z_X - z_Y)}{M_A} + \frac{\frac{(z_A - z_X)(z_X - z_Y)(z_A - z_B + z_X - z_Y)}{-z_B + z_X}}{M_B} + \frac{(z_A - z_B)(z_B + \frac{(-z_A + z_X)(z_A - z_Y)}{-z_B + z_X} - z_Y)}{M_X}, \tag{3.50}$$

$$\lambda_{YY} = \frac{(z_B - z_X)^2 + (z_B - z_Y)^2 + (z_X - z_Y)^2}{M_A} + \frac{(z_A - z_X)(z_A - z_X + \frac{(z_A - z_Y)(z_B - z_Y)}{z_B - z_X})}{M_B} + \frac{(z_A - z_B)(z_A - z_B + \frac{(z_A - z_Y)(z_X - z_Y)}{-z_B + z_X})}{M_X}. \tag{3.51}$$

Substituting Equations (3.46) and (3.47) into Equation (3.9) for $i =$ A and Y yields the governing equations for $c_A(r,t)$ and $c_Y(r,t)$

$$\frac{\partial c_A(\boldsymbol{r},t)}{\partial t} = \frac{1}{\Omega_0}\nabla\cdot\left[\lambda_{AA}\nabla\left(\frac{\partial f_{\text{bulk}}}{\partial c_A} - \kappa\nabla^2 c_A\right) + \lambda_{AY}\nabla\left(\frac{\partial f_{\text{bulk}}}{\partial c_Y} - \kappa\nabla^2 c_Y\right) + \sum_{i\in\{A,B,X,Y\}}\Omega_{Ai}\nabla\frac{\partial g_i}{\partial c_i}\right], \tag{3.52}$$

$$\frac{\partial c_Y(\boldsymbol{r},t)}{\partial t} = \frac{1}{\Omega_0}\nabla\cdot\left[\lambda_{YA}\nabla\left(\frac{\partial f_{\text{bulk}}}{\partial c_A} - \kappa\nabla^2 c_A\right) + \lambda_{YY}\nabla\left(\frac{\partial f_{\text{bulk}}}{\partial c_Y} - \kappa\nabla^2 c_Y\right) + \sum_{i\in\{A,B,X,Y\}}\Omega_{Yi}\nabla\frac{\partial g_i}{\partial c_i}\right]. \tag{3.53}$$

The remaining two mole fractions can be calculated in terms of c_A and c_Y using Equations (3.42) and (3.43). It can be observed from Equations (3.52), (3.53), (3.42) and (3.43) that only the time-evolution equations for the mole fractions of ion A and Y need to be explicitly solved, from which the mole fraction of ion B and X can be subsequently determined. In Equations (3.52) and (3.53),

the negative-mole-fraction penalty terms containing $\left(\frac{\partial g_i}{\partial c_i}\right)$ are localized and negligible in most of the computational domain. They can therefore be disregarded when examining the components of the time-evolution equations. Consequently, the time-evolution equations for the mole fractions of cation A and anion Y can both be considered as a function of the chemical potentials ($\mu_i = \frac{\partial f_{\text{bulk}}}{\partial c_i} - \kappa\nabla^2 c_i$) of ion A and Y. By inspection, one can identify the effective mobility matrix defined by

$$M_{eff} = \frac{1}{\Omega_0}\begin{pmatrix}\lambda_{AA} & \lambda_{AY}\\ \lambda_{YA} & \lambda_{YY}\end{pmatrix}, \tag{3.54}$$

which is in general not symmetric. However, for the simple reaction in which all the ions have the same absolute value of charge numbers, the effective mobility matrix becomes diagonal

$$M_{eff}(z_A = z_B = -z_X = -z_Y) = \begin{pmatrix}M_{\text{cation}} & 0\\ 0 & M_{\text{anion}}\end{pmatrix}, \tag{3.55}$$

where $M_{\text{cation}} = \frac{2}{M_A^{-1}+M_B^{-1}}$ can be interpreted as the effective cation mobility, and $M_{\text{anion}} = \frac{2}{M_X^{-1}+M_Y^{-1}}$ can be interpreted as the effective anion mobility. The same form of the harmonic mean was reported to describe the salt diffusivity (or ambipolar diffusivity) for a binary electrolyte [152] that considers the transport of a cation and an anion.

3.2.3 Determination of phase fractions

Since we assume a diffusion-limited regime, the formation of the product phases is considered instantaneous. The number of moles of the product phases, n_{AY} and n_{BX}, at position $\boldsymbol{r}$ and time $t > 0$, is given by the minimum mole fraction of their constituent ions:

$$n_{\text{AY}}(\boldsymbol{r}, t) = \min(c_A, c_Y), \tag{3.56}$$

$$n_{\text{BX}}(\boldsymbol{r}, t) = \min(c_B, c_X). \tag{3.57}$$

The remaining ions that do not contribute to the product phases determine the number of moles of reactant phases n_{AX} and n_{BY}, which is given by

$$n_{\mathrm{AX}}(\boldsymbol{r}, t) = \max(0, c_A - c_Y), \tag{3.58}$$

$$n_{\mathrm{BY}}(\boldsymbol{r}, t) = \max(0, c_B - c_X). \tag{3.59}$$

The phase fraction, ϕ_α, of the phase $\alpha \in \{\mathrm{AX}, \mathrm{BY}, \mathrm{AY}, \mathrm{BX}\}$, is calculated by dividing the number of moles of phase α by the total amount of phases:

$$\phi_\alpha = \frac{n_\alpha}{\sum_{\beta \in \{\mathrm{AX,BY,AY,BX}\}} n_\beta}. \tag{3.60}$$

3.3 A phase-field model for a general solid-state metathesis reaction

In general, the ions in a binary SSM reaction could have a different absolute value of charge numbers. A general balanced reaction formula that considers the charge number difference is given by

$$p\mathrm{A}_a\mathrm{X}_x + q\mathrm{B}_b\mathrm{Y}_y \rightarrow p'\mathrm{A}_{a'}\mathrm{Y}_{y'} + q'\mathrm{B}_{b'}\mathrm{X}_{x'}. \tag{3.61}$$

Here, the number of A, B, X, Y ions in reactant phases is indicated by lowercase letters a, b, x, y respectively. The number of these ions in the product phases is indicated by a', b', x', y'. The stoichiometric coefficients for $\mathrm{A}_a\mathrm{X}_x$, $\mathrm{B}_b\mathrm{Y}_y$, $\mathrm{A}_{a'}\mathrm{Y}_{y'}$, and $\mathrm{B}_{b'}\mathrm{X}_{x'}$ are denoted by p, q, p', and q', respectively. Their values are listed in Table 3.1.

Table 3.1. Stoichiometric coefficients for a general binary SSM reaction. Reproduced with permission [153]. Copyright 2023, the authors. Published by Elsevier.

p	1
q	$\frac{xb'}{x'b}$
p'	$\frac{a}{a'}$
q'	$\frac{x}{x'}$

All equations discussed in Section 3.2 still hold, except for Equation (3.4) that describes the equilibrium mole fraction of ion i in product phase α, and Equations (3.56) - (3.59) that calculate phase fractions. The molar volume for the phases is no longer considered identical but instead assumed to be proportional to the number of constituent ions in the phases. The equilibrium mole fraction of ion i in product phase α now needs to be expressed in term of a', b', c', and d' and is shown in Table 3.2.

Table 3.2. The equilibrium mole fraction of ion i in product phase α. Reproduced with permission [153]. Copyright 2023, the authors. Published by Elsevier.

i \ α	$\mathrm{A}_{a'}\mathrm{Y}_{y'}$	$\mathrm{B}_{b'}\mathrm{X}_{x'}$
A	$\frac{a'}{a'+y'}$	0
B	0	$\frac{b'}{b'+x'}$
X	0	$\frac{x'}{b'+x'}$
Y	$\frac{y'}{a'+y'}$	0

The numbers of moles of $\mathrm{A}_a\mathrm{X}_x$, $\mathrm{B}_b\mathrm{Y}_y$, $\mathrm{A}_{a'}\mathrm{Y}_{y'}$, and $\mathrm{B}_{b'}\mathrm{X}_{x'}$ phases are calculated following the same assumptions and procedures discussed in Section 3.2.3, although the mole fraction of ions needs to be scaled by a', b', c', and d' to obtain the number of moles of compound phases. They are given by

$$n_{\mathrm{A}_{a'}\mathrm{Y}_{y'}}(\boldsymbol{r},t) = \min\left(\frac{c_A}{a'},\frac{c_Y}{y'}\right), \tag{3.62}$$

$$n_{\mathrm{B}_{b'}\mathrm{X}_{x'}}(\boldsymbol{r},t) = \min\left(\frac{c_B}{b'},\frac{c_X}{x'}\right), \tag{3.63}$$

$$n_{\mathrm{A}_a\mathrm{X}_x}(\boldsymbol{r},t) = \max\left(0, \frac{c_A}{a} - \frac{a'}{ay'}c_Y\right), \tag{3.64}$$

$$n_{\mathrm{B}_b\mathrm{Y}_y}(\boldsymbol{r},t) = \max\left(0, \frac{c_B}{b} - \frac{b'}{bx'}c_X\right). \tag{3.65}$$

The phase fractions of $\mathrm{A}_a\mathrm{X}_x$, $\mathrm{B}_b\mathrm{Y}_y$, $\mathrm{A}_{a'}\mathrm{Y}_{y'}$, and $\mathrm{B}_{b'}\mathrm{X}_{x'}$ can then be calculated using Equation (3.60).

3.4 Nondimensionalization of the phase-field equations

We nondimensionalize the phase-field equations by selecting an energy scale W and a length scale l_0. All energies are scaled by the energy scale, and all lengths (e.g., the domain size) are scaled by the length scale. Unless stated otherwise, the smallest mobility among all the ions, given by $M_{min} = \min(M_A, M_B, M_X, M_Y)$, is used to scale the mobility of each ion. We put an asterisk (*) at the superscript of variables to indicate their dimensionless form. The dimensionless variables are shown in Table 3.3. We employ dimensionless variables for the simulations, but we note that these variables can be converted to dimensional quantities based on the chosen scale of energy, length, and mobility. Once these scaling quantities are chosen, setting the time scale to

$$t_0 = \frac{l_0^2}{WM_{min}}, \tag{3.66}$$

and applying the cancellation law, we obtain the nondimensional form of the governing equations.

Table 3.3. Dimensional and nondimensionalized phase-field variables for solid-state metathesis reactions. Reproduced with permission [153]. Copyright 2023, the authors. Published by Elsevier.

Variable	Nondimensionalized variable
W	$W^* = \frac{W}{W} = 1$
κ	$\kappa^* = \frac{\kappa}{W l_0^2}$
ζ	$\zeta^* = \frac{\zeta}{W}$
M_i	$M_i^* = \frac{M_i}{M_{min}}$
$\boldsymbol{r}$	$\boldsymbol{r}^* = \frac{\boldsymbol{r}}{l_0}$
t	$t^* = \frac{t}{t_0} = \frac{W M_{min}}{l_0^2} t$

3.5 The relationship between the diffusion coefficient and the mobility for an SSM reaction

The mobility of the ionic species can be linked to the corresponding diffusion coefficient. Such a link is needed to identify a proper mobility scale, which is used in converting nondimensional quantities (e.g., dimensionless time) into the corresponding dimensional quantities. In this section, we present a method to convert diffusion coefficients to mobilities (to the order of magnitude) and provide an example for such a conversion in an SSM reaction for the synthesis of FeS_2. For simplicity and without loss of generality, we write the diffusion equation in one dimension as a reduced model:

$$\frac{\partial c_i(x,t)}{\partial t} = \frac{\partial}{\partial x}\left[D_i \frac{\partial c_i}{\partial x}(x,t)\right], \tag{3.67}$$

where D_i is the diffusion coefficient of the ion i, which may depend on the composition. Here, we assume that the values of the off-diagonal terms of a full diffusion tensor are negligible compared to the values of the diagonal terms and, therefore, we omitted off-diagonal terms in Equation

(3.67). In our study, we describe the evolution of $c_i(x,t)$ using the following mass conservation equation with a driving force due to the gradient in chemical potential [103,128]:

$$\frac{\partial c_i(x,t)}{\partial t} = \frac{\partial}{\partial x}\left[M_i \frac{\partial \mu_i(\boldsymbol{c})}{\partial x}\right], \tag{3.68}$$

where $\mu_i(\boldsymbol{c})$ is the chemical potential of the ion i, and M_i is the mobility of the ion i. As discussed in Section 3.2, we assume that each M_i is a constant in our model, but the derivation here does not require such an assumption. Using the chain rule, Equation (3.68) can be written as

$$\frac{\partial c_i(x,t)}{\partial t} = \frac{\partial}{\partial x}\left[M_i \sum_{j\in\{\mathrm{A,B,X,Y}\}} \frac{\partial \mu_i}{\partial c_j}\frac{\partial c_j(x,t)}{\partial x}\right], \tag{3.69}$$

where $\mathrm{A, B, X, Y}$ stand for the four ions. The chemical potential μ_i of the ion i is given by

$$\mu_i = \frac{\partial f_{\mathrm{bulk}}}{\partial c_i} = W\left\{\sum_{\alpha\in\{\mathrm{AY,BX}\}}\left[2(c_i - c_i^{\alpha}) \sum_{\substack{j\in\{\mathrm{A,B,X,Y}\}\\ \beta\in\{\mathrm{AY,BX}\},\beta\neq\alpha}} \left(c_j - c_j^{\beta}\right)^2\right]\right\}, \tag{3.70}$$

where f_{bulk} is the bulk free energy density, which is presented in Equation (3.3). The derivative of the chemical potential μ_i with respect to the mole fraction c_j is given by

$$\frac{\partial \mu_i}{\partial c_j} = \begin{cases} 2W\left[\sum_{\alpha\in\{\mathrm{AY,BX}\}}\sum_{k\in\{\mathrm{A,B,X,Y}\}}(c_k - c_k^{\alpha})^2 + 4\prod_{\alpha\in\{\mathrm{AY,BX}\}}(c_i - c_i^{\alpha})\right], & j = i \\ 4W\left[\left(c_i - c_i^{\mathrm{AY}}\right)\left(c_j - c_j^{\mathrm{BX}}\right) + \left(c_i - c_i^{\mathrm{BX}}\right)\left(c_j - c_j^{\mathrm{AY}}\right)\right], & j \neq i \end{cases} \tag{3.71}$$

where W is the energy scale, and c_i^{α} is the equilibrium mole fraction of ion i in the product phase α. Equating Equation (3.67) with Equation (3.68) yields

$$M_i = \frac{\frac{\partial c_i}{\partial x}}{\sum_{j\in\{\mathrm{A,B,X,Y}\}}\frac{\partial \mu_i}{\partial c_j}\frac{\partial c_j}{\partial x}} D_i = D_i \Phi_i^{-1}, \tag{3.72}$$

where $\frac{\partial \mu_i}{\partial c_j}$ is given by Equation (3.71), and Φ_i is the ratio between D_i and M_i, which varies from ion to ion and from reaction to reaction.

Here, we utilize an SSM reaction for the synthesis of FeS_2 as an example to show a method to estimate the value for Φ_i. The reaction formula is given by

$$Na_2S_2 + FeCl_2 \rightarrow 2NaCl + FeS_2, \tag{3.73}$$

in which Na^+ and Fe^{2+} are the two cations and Cl^- and S_2^{2-} are the two anions. This reaction is detailed in Chapter 4 Section 4.3. Considering the constraints of electroneutrality (*i.e.,* $\sum_{k\in\{Na^+,Fe^{2+},Cl^-,S_2^{2-}\}} z_k c_k = 0$) and on the sum of mole fractions (i.e., $\sum_{k\in\{Na^+,Fe^{2+},Cl^-,S_2^{2-}\}} c_k = 1$), the mole fractions of the ion Fe^{2+} and S_2^{2-}, $c_{Fe^{2+}}$ and $c_{S_2^{2-}}$, can be expressed in terms of c_{Na^+} and c_{Cl^-}:

$$c_{Fe^{2+}} = -\frac{3}{4}c_{Na^+} - \frac{1}{4}c_{Cl^-} + \frac{1}{2}, \tag{3.74}$$

$$c_{S_2^{2-}} = -\frac{1}{4}c_{Na^+} - \frac{3}{4}c_{Cl^-} + \frac{1}{2}. \tag{3.75}$$

Substituting Equations (3.74) and (3.75) into Equation (3.71) for $i = Na^+$, we obtain the partial derivatives of the chemical potential of the Na^+ ion with respect to the compositions:

$$\frac{\partial \mu_{Na^+}}{\partial c_{Na^+}} = 2W\left(\frac{29}{4}c_{Na^+}^2 + \frac{13}{4}c_{Cl^-}^2 + \frac{3}{2}c_{Na^+}c_{Cl^-} - 4c_{Na^+} - 2c_{Cl^-} + 1\right), \tag{3.76}$$

$$\frac{\partial \mu_{Na^+}}{\partial c_{Cl^-}} = 4W\left[2c_{Na^+}c_{Cl^-} - \frac{1}{2}(c_{Na^+} + c_{Cl^-})\right], \tag{3.77}$$

$$\frac{\partial \mu_{Na^+}}{\partial c_{Fe^+}} = 4W\left(-\frac{3}{2}c_{Na^+}^2 - \frac{1}{2}c_{Na^+}c_{Cl^-} + \frac{7}{8}c_{Na^+} + \frac{1}{8}c_{Cl^-}\right), \tag{3.78}$$

$$\frac{\partial \mu_{Na^+}}{\partial c_{S_2^{2-}}} = 4W\left(-\frac{1}{2}c_{Na^+}^2 - \frac{3}{2}c_{Na^+}c_{Cl^-} + \frac{5}{8}c_{Na^+} + \frac{3}{8}c_{Cl^-}\right). \tag{3.79}$$

Taking the partial derivative of Equations (3.74) and (3.75) with respect to x yield

$$\frac{\partial c_{Fe^{2+}}}{\partial x} = -\frac{3}{4}\frac{\partial c_{Na^+}}{\partial x} - \frac{1}{4}\frac{\partial c_{Cl^-}}{\partial x}, \tag{3.80}$$

$$\frac{\partial c_{S_2^{2-}}}{\partial x} = -\frac{1}{4}\frac{\partial c_{Na^+}}{\partial x} - \frac{3}{4}\frac{\partial c_{Cl^-}}{\partial x}. \tag{3.81}$$

Substituting Equations (3.76) - (3.81) into Equation (3.69) for $i = Na^+$, we obtain the governing equation for c_{Na^+}:

$$\frac{\partial c_{Na^+}}{\partial t} = \frac{\partial}{\partial x}\left[M_{Na^+} W \left(U_{Na^+}\frac{\partial c_{Na^+}}{\partial x} + V_{Na^+}\frac{\partial c_{Cl^-}}{\partial x}\right)\right], \tag{3.82}$$

where U_{Na^+} and V_{Na^+} are functions of c_{Na^+} and c_{Cl^-} given by

$$U_{Na^+}(c_{Na^+}, c_{Cl^-}) = \frac{39}{2}c_{Na^+}^2 + \frac{13}{2}c_{Cl^-}^2 + 6c_{Na^+}c_{Cl^-} - \frac{45}{4}c_{Na^+} - \frac{19}{4}c_{Cl^-} + 2, \tag{3.83}$$

$$V_{Na^+}(c_{Na^+}, c_{Cl^-}) = 3c_{Na^+}^2 + 13c_{Na^+}c_{Cl^-} - \frac{19}{4}c_{Na^+} - \frac{13}{4}c_{Cl^-}. \tag{3.84}$$

To examine the dependence of U_{Na^+} and V_{Na^+} on the compositions, we first identify the possible range of the composition space by considering the fact that the mole fractions of the Na^+ and Cl^- ions are between 0 and 2/3 and that the mole fractions of the Fe^{2+} and S_2^{2-} ions are between 0 and 1/2 due to the constraint on charge neutrality. Since $c_{Fe^{2+}}$and $c_{S_2^{2-}}$ can be expressed in terms of c_{Na^+} and c_{Cl^-} using Equations (3.74) and (3.75), we can formulate the constraints on the composition range in terms of c_{Na^+} and c_{Cl^-}:

$$0 \le c_{Na^+} \le 2/3, \tag{3.85}$$

$$0 \le c_{Cl^-} \le 2/3, \tag{3.86}$$

$$3c_{Na^+} + c_{Cl^-} - 2 \le 0, \tag{3.87}$$

$$c_{Na^+} + 3c_{Cl^-} - 2 \le 0. \tag{3.88}$$

The dependence of U_{Na^+} and V_{Na^+} on the composition is shown in Figure 3.1(a) and (b), respectively. We only visualize the regions that satisfy the constraints set by Equations (3.85) − (3.88).

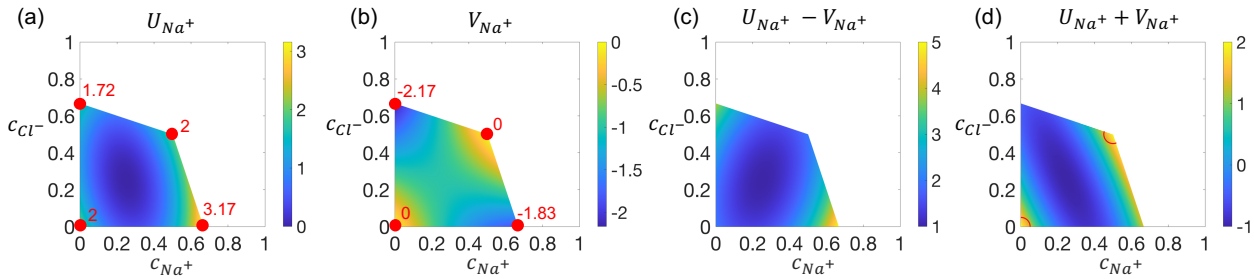

Figure 3.1. The values of (a) U_{Na^+}, (b) V_{Na^+}, (c) $U_{Na^+} - V_{Na^+}$, and (d) $U_{Na^+} + V_{Na^+}$ as a function of c_{Na^+} and c_{Cl^-}. The values of U_{Na^+} and V_{Na^+} at the compositions corresponding to the precursor and product phases are marked in (a) and (b), respectively. Only the regions that satisfy the constraints set by Equations (3.85) − (3.88) are visualized. Reproduced with permission [153]. Copyright 2023, the authors. Published by Elsevier.

It can be observed from Figure 3.1(b) that $V_{Na^+} = 0$ only at the compositions that correspond to the product phases, which indicates that the term in Equation (3.82) that involves $\frac{\partial c_{Cl^-}}{\partial x}$ does not vanish at other compositions. In order to eliminate $\frac{\partial c_{Cl^-}}{\partial x}$ from Equation (3.82), we examine two extremes, one corresponding to the early stage of the conversion process and the other during the intermediate and late stages of the process. For the early stage of the process, we assume that $\frac{\partial c_{c_{Cl^-}}}{\partial x} \approx -\frac{\partial c_{Na^+}}{\partial x}$. This relationship can be observed from simulation results, *e.g.,* in Figure 6(a) of Ref. [145], which shows the simulated mole fractions of the four ions during the early stage of metathesis reaction for the synthesis of FeS_2. We also observed from simulations that $\frac{\partial c_{Cl^-}}{\partial x} \approx \frac{\partial c_{Na^+}}{\partial x}$ after $t^* \approx 20$ (similar to Figure 6(c) of Ref. [145]) and therefore employ this relationship to simplify Equation (3.82) for the intermediate and late stage of the conversion process, during which this condition is approximately met. Equation (3.82) therefore can be written as

$$\frac{\partial c_{Na^+}}{\partial t} = \begin{cases} \frac{\partial}{\partial x}\left(M_{Na^+} W \left[(U_{Na^+} - V_{Na^+})\frac{\partial c_{Na^+}}{\partial x}\right]\right), & \text{the early stage,} \\ \frac{\partial}{\partial x}\left(M_{Na^+} W \left[(U_{Na^+} + V_{Na^+})\frac{\partial c_{Na^+}}{\partial x}\right]\right), & \text{the intermediate/late stages.} \end{cases} \quad (3.89)$$

Comparing the right-hand side of Equation (3.67) for $i = Na^+$ with that of Equation (3.89), we obtain

$$M_{Na^+} = D_{Na^+}\Phi_{Na^+}^{-1}, \quad (3.90)$$

where the conversion factor of the Na^+ ion, Φ_{Na^+}, is given by

$$\Phi_{Na^+} = \begin{cases} W(U_{Na^+} - V_{Na^+}), & \text{the early stage,} \\ W(U_{Na^+} + V_{Na^+}), & \text{the intermediate/late stages.} \end{cases} \quad (3.91)$$

Since Φ_{Na^+} depends on the composition, we examine its range and then conduct an order-of-magnitude estimate for its value. The values of $U_{Na^+} - V_{Na^+}$ and $U_{Na^+} + V_{Na^+}$ are shown in Figure 3.1(c) and (d), respectively. Figure 3.1(c) shows that $U_{Na^+} - V_{Na^+}$ ranges from 1 to 5, and therefore Φ_{Na^+} ranges between W and $5W$ during the early stage of the conversion process. Figure 3.1(d) shows that $U_{Na^+} + V_{Na^+}$ ranges from -1 to 2. However, we note that the evolution during the intermediate and late stages of the simulation mainly occurs via diffusion through the bulk phases (akin to coarsening), with compositions near the product phase values. As defined in Section 3.2, mole fractions vary from approximately 10% to 90% of their maximum values across an interface. We therefore estimate that the bulk phases during the intermediate and late stages of the conversion process have a composition within 10% of the product phase compositions, *i.e.,* within 0.05 of the points (0,0) or (0.5, 0.5) in Figure 3.1(d). The values of $U_{Na^+} + V_{Na^+}$ range from 1.17 to 2 in these compositional ranges, boundaries of which are shown by the two red curves in Figure 3.1(d). Accordingly, the conversion factor Φ_{Na^+} can be estimated to range between $1.17W$ and $2W$ during the intermediate and late stages of the conversion process. Considering early, intermediate, and late stages of the conversion process, Φ_{Na^+} ranges from W to $5W$. Since

we must choose a single value of Φ_{Na^+} in order to convert diffusivity in the literature to a mobility value and also to obtain the characteristic time scale by which the dimensionless simulation time is converted to the approximate physical time, we select

$$\Phi_{Na^+} \approx 2W, \tag{3.92}$$

which is in the range of $W - 5W$ and corresponds to its value at $c_{Na^+} = c_{Cl^-} = 0.5$.

Following the same derivation, the conversion factor Φ_{Cl^-} of the Cl^- ion can be estimated similarly, and due to the symmetry in the equations, the ranges are identical for the sum of the coefficients, $U_{Cl^-} + V_{Cl^-}$ and the difference of the coefficients, $U_{Cl^-} - V_{Cl^-}$. Thus, using the approximate values of Φ_{Na^+} and Φ_{Cl^-}, we obtain

$$M_{Na^+} \approx D_{Na^+}(2W)^{-1}, \tag{3.93}$$

$$M_{Cl^-} \approx D_{Cl^-}(2W)^{-1}. \tag{3.94}$$

3.6 Determination of the energy scale

To relate the energy scale W with the interfacial energy γ and the interfacial width l_{int}, we follow the steps below. First, we calculate γ by integrating the free energy densities, according to Ref. [126]:

$$\gamma = \int_{-\infty}^{\infty} \left[f_{\text{bulk}}(W, c_A, c_B, c_X, c_Y) + \frac{\kappa}{2} \sum_{j\in\{\text{A,B,X,Y}\}} \left(\frac{dc_j}{dx}\right)^2 \right] dx, \tag{3.95}$$

where c_A, c_B, c_X and c_Y are the mole fractions of the ion A, B, X, and Y, respectively, and κ is the gradient energy coefficient. In equilibrium (i.e., when the precursors are fully converted to the products), the mole fractions of three of the ions can be expressed as the remaining ion. Specifically, we denote $c = c_A$ as the mole fraction of the ion A. The mole fractions of the other three ions,

$c_B(c), c_X(c)$, and $c_Y(c)$, can then be expressed as a function of c. Consequently, the second term in the integrand of Equation (3.95) can be written as

$$\frac{\kappa}{2}\sum_{j\in\{\mathrm{A,B,X,Y}\}}\left(\frac{dc_j}{dx}\right)^2=\frac{\kappa}{2}\sum_{j\in\{\mathrm{A,B,X,Y}\}}\left(\frac{dc_j}{dc}\right)^2\left(\frac{dc}{dx}\right)^2=\frac{\kappa}{2}\vartheta\left(\frac{dc}{dx}\right)^2, \tag{3.96}$$

where $\vartheta=1+\sum_{j\in\{\mathrm{B,X,Y}\}}\left(\frac{dc_j}{dc}\right)^2$. Substituting Equation (3.96) into Equation (3.95) yields

$$\gamma=\int_{-\infty}^{\infty}\left[f_{\mathrm{bulk}}(W,c)+\frac{\kappa}{2}\vartheta\left(\frac{dc}{dx}\right)^2\right]dx, \tag{3.97}$$

To obtain a differential equation having solutions corresponding to stationary composition profiles, we substitute the integrand, $I=f_{\mathrm{bulk}}(W,c)+\frac{\kappa}{2}\vartheta\left(\frac{dc}{dx}\right)^2$, into the Euler Equation [154], yielding

$$I-\left(\frac{dc}{dx}\right)\left[\frac{\partial I}{\partial\left(\frac{dc}{dx}\right)}\right]=\mathrm{Constant}, \tag{3.98}$$

or

$$f_{\mathrm{bulk}}(W,c)+\frac{\kappa}{2}\vartheta\left(\frac{dc}{dx}\right)^2-\kappa\vartheta\left(\frac{dc}{dx}\right)^2=f_{\mathrm{bulk}}(W,c)-\frac{\kappa}{2}\vartheta\left(\frac{dc}{dx}\right)^2=\mathrm{Constant}. \tag{3.99}$$

The constant in the equation is zero because both $f_{\mathrm{bulk}}(W,c)$ and $\frac{\kappa}{2}\vartheta\left(\frac{dc}{dx}\right)^2$ tend to be 0 as $x\rightarrow\pm\infty$ (far from the interface). Therefore, Equation (3.99) becomes [126]

$$f_{\mathrm{bulk}}(W,c)=\frac{\kappa}{2}\vartheta\left(\frac{dc}{dx}\right)^2. \tag{3.100}$$

Rearranging Equation (3.100) yields [126]

$$dx=\sqrt{\frac{\vartheta\kappa}{2f_{\mathrm{bulk}}(W,c)}}dc. \tag{3.101}$$

Substituting the gradient energy density with the bulk energy density, Equation (3.97) becomes

$$\gamma = 2 \int_{-\infty}^{\infty} f_{\text{bulk}}(W, c) dx. \tag{3.102}$$

After a change of variable using Equation (3.101), it simplifies to

$$\gamma = \int_{c_\alpha}^{c_\beta} \sqrt{2\vartheta\kappa f_{\text{bulk}}(W, c)} dc. \tag{3.103}$$

where c_α and c_β are the concentrations of the ion A at the two local minima of the double-well potential. The interfacial energy can therefore be expressed as a function of W and κ, $\gamma(W, \kappa)$. According to Equation (3.6), κ can be written in terms of W and the interfacial width l_{int}. Therefore, we can relate W to κ and l_{int}.

Here, we utilize an SSM reaction for the synthesis of FeS_2 as an example to show how the relationship can be obtained. The reaction formula is shown in Equation (3.73). We denote c to be the mole fraction of the Na^+ ion, c_{Na^+}, which is 0 in FeS_2 and 0.5 in NaCl in the products. The equilibrium concentration profile of four ions, $c_{\text{Na}^+}(= c)$, $c_{\text{Fe}^{2+}}$, $c_{\text{S}_2^{2-}}$, and c_{Cl^-}, are given by

$$c = c_{\text{Na}^+}(x) = \frac{1}{4}\left[1 - \tanh\left(\frac{x - x_{int}}{\delta}\right)\right], \tag{3.104}$$

$$c_{\text{Fe}^{2+}}(x) = \frac{1}{4}\left[1 + \tanh\left(\frac{x - x_{int}}{\delta}\right)\right], \tag{3.105}$$

$$c_{\text{S}_2^{2-}}(x) = \frac{1}{4}\left[1 + \tanh\left(\frac{x - x_{int}}{\delta}\right)\right], \tag{3.106}$$

$$c_{\text{Cl}^-}(x) = \frac{1}{4}\left[1 - \tanh\left(\frac{x - x_{int}}{\delta}\right)\right], \tag{3.107}$$

where x_{int} is the position of the interface between the two products NaCl and FeS_2. We can rewrite Equations (3.105) – (3.107) as

$$c_{\text{Fe}^{2+}}(x) = \frac{1}{2} - c, \tag{3.108}$$

$$c_{S_2^{2-}}(x) = \frac{1}{2} - c, \tag{3.109}$$

$$c_{Cl^-}(x) = c. \tag{3.110}$$

Substituting Equation (3.3) and Equation (3.108) – (3.110) into Equation (3.103) yield

$$\gamma = 4\sqrt{2\kappa W}\int_0^{0.5}\left[c^2 + \left(c - \frac{1}{2}\right)^2\right]dc = \frac{\sqrt{2\kappa W}}{3}. \tag{3.111}$$

Rearranging Equation (3.6) yields

$$\kappa = \frac{1}{8} l_{int}^2 W. \tag{3.112}$$

Substituting Equation (3.112) into Equation (3.111) yields

$$\gamma = \frac{1}{6} l_{int} W. \tag{3.113}$$

By solving for W, we obtain

$$W = \frac{6\gamma}{l_{int}}. \tag{3.114}$$

Thus, the energy scale is the interfacial energy divided by the interfacial thickness to a constant factor (which must be identified through the above analysis).

3.7 Phase-field model coupled with the smoothed boundary method

To describe a reaction occurring between round-shaped solid particles that are surrounded by voids, we need to impose boundary conditions at the surfaces of the solid. We couple Equation (3.9) with the smoothed boundary method [134], discussed in Chapter 2 Section 2.7, to set the boundary condition.

A domain parameter, ψ, is employed to describe the domain of interest (in this case, the solid particles). It is equal to 1 in the solid particles, 0 outside the particle, and smoothly varies from 1 to 0 across the boundary. Multiplying Equation (3.9) with ψ yields

$$\psi \frac{\partial c_i}{\partial t} = \psi \nabla \cdot \left(M_i \nabla \frac{\delta \mathcal{F}}{\delta c_i} \right). \tag{3.115}$$

Applying the following identity to the right-hand side of Equation (3.115)

$$\psi \nabla \cdot \left(M_i \nabla \frac{\delta \mathcal{F}}{\delta c_i} \right) = \nabla \cdot \left(\psi M_i \nabla \frac{\delta \mathcal{F}}{\delta c_i} \right) - \nabla \psi \cdot \left(M_i \nabla \frac{\delta \mathcal{F}}{\delta c_i} \right), \tag{3.116}$$

we obtain

$$\psi \frac{\partial c_i}{\partial t} = \nabla \cdot \left(\psi M_i \nabla \frac{\delta \mathcal{F}}{\delta c_i} \right) - \nabla \psi \cdot \left(M_i \nabla \frac{\delta \mathcal{F}}{\delta c_i} \right). \tag{3.117}$$

The inward flux, J_B, at the boundary is given by

$$n \cdot J = -\frac{\nabla \psi}{|\nabla \psi|} \left(M_i \nabla \frac{\delta \mathcal{F}}{\delta c_i} \right) = J_B, \tag{3.118}$$

where $n = \frac{\nabla \psi}{|\nabla \psi|}$ is the unit normal inward vector. Substituting Equation (3.118) into Equation (3.117) yields

$$\frac{\partial c_i}{\partial t} = \frac{1}{\psi} \nabla \cdot \left(\psi M_i \nabla \frac{\delta \mathcal{F}}{\delta c_i} \right) - \frac{|\nabla \psi|}{\psi} J_B. \tag{3.119}$$

When a no-flux boundary condition is imposed at the surface, Equation (3.119) reduces to

$$\frac{\partial c_i}{\partial t} = \frac{1}{\psi} \nabla \cdot \left(\psi M_i \nabla \frac{\delta \mathcal{F}}{\delta c_i} \right). \tag{3.120}$$

3.8 Summary for the phase-field model for solid-state metathesis reaction

In this chapter, we presented a phase-field model that describes the diffusion-limited metathesis reactions in ionic solids. This model tracks the mole fractions of the ionic species, from which the phase fractions are determined. The governing equations were derived using Lagrange multipliers that impose constraints not only on the sum of mole fractions but also of charge neutrality. We described a method to calculate mobilities of ionic species based on their diffusion coefficients. Moreover, we discussed how this phase-field model could be coupled with the

smoothed boundary method to impose boundary conditions for irregularly shaped domain boundaries. The applications of this phase-field model are presented in the next chapter.

Chapter 4 Study of Composition and Phase Evolutions in Solid-State Metathesis Reactions

4.1 Introduction

In this chapter,[*] we demonstrate the capability of the phase-field model presented in Chapter 3 by applying it to perform simulations under various scenarios. In Section 4.2, we utilize the model to examine the effect of mobilities on the dynamics of reactions. In Section 4.3, we predict the process of a thin-film reaction for the synthesis of FeS_2 by tuning the mobilities of ions based on their diffusivities suggested by literature and experiments. In Section 4.4, we leverage the phase-field model and a lattice model to estimate the rate of the reactions with loosely and densely packed reactant particles.

4.2 Examination of mobility effects using a simple SSM model

4.2.1 Simulation setup for examination of mobility effects

In this section, we utilized the SSM model that considers the ions with an identical absolute value of charge numbers presented in Chapter 3 Section 3.2 to study the effect of mobilities of ions on the dynamics of the reaction with the formula $\mathrm{AX} + \mathrm{BY} \rightarrow \mathrm{AY} + \mathrm{BX}$. We initialize the mole fractions of the ions A, B, X, and Y using the following equations:

$$c_{\mathrm{A}}(z; t = 0) = c_{\mathrm{X}}(z; t = 0) = \frac{1}{4}\left[1 - \tanh\left(\frac{z - 0.5L_z}{\delta}\right)\right], \tag{4.1}$$

[*] Sections 3.2 and 3.3 are adapted from G. Huang, D. Montiel, R. D. McAuliffe, G. M. Veith, and K. Thornton, "Phase-Field Modeling of Solid-State Metathesis Reactions with the Charge Neutrality Constraint," Computational Materials Science **221**, 112080 (2023). Section 3.4 is adapted from G. E. Kamm, G. Huang, S. M. Vornholt, R. D. McAuliffe, G. M. Veith, K. S. Thornton, and K. W. Chapman, "Relative Kinetics of Solid-State Reactions: The Role of Architecture in Controlling Reactivity," Journal of the American Chemical Society **144**, 11975 (2022).

$$c_{\mathrm{B}}(z;t=0) = c_{\mathrm{Y}}(z;t=0) = \frac{1}{4}\left[1+\tanh\left(\frac{z-0.5L_z}{\delta}\right)\right], \tag{4.2}$$

where L_z is the size of the simulation domain. The equations initialize the concentrations such that there are identical numbers of AX and BY reactant phases on two sides of the simulation domain, separated by an interface in the midpoint of the domain. For the simulations in this section, we set the interfacial width to be 1/50 of the domain size. The parameters used in this section and their values are summarized in Table 4.1. The initial mole fractions of ions and phase fractions are shown in Figure 4.1.

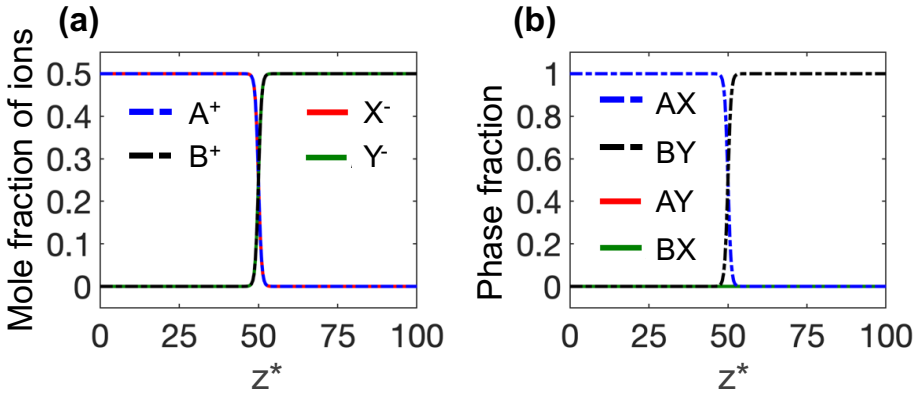

Figure 4.1. Initial condition for the metathesis reaction AX + BY → AY + BX. (a) Initial mole fractions of ions. The legends indicate ionic species. (b) Initial phase fractions. The legends indicate phases. Reproduced with permission [153]. Copyright 2023, the authors. Published by Elsevier.

To examine the effect of mobility of ions on the dynamics of the metathesis reaction, we performed simulations with three sets of mobilities, as summarized in Table 4.2. The time step employed in each simulation is also presented in the last column of the table. The common parameters for all the three simulations are summarized in Table 4.1.

Table 4.1. The common parameters employed in all the three simulations. Reproduced with permission [153]. Copyright 2023, the authors. Published by Elsevier.

Parameters	Variable	Value
Bulk energy coefficient	W^*	1
Gradient energy coefficient	κ^*	0.5
Negative-mole-fraction penalty term coefficient	ζ^*	100
Domain size	L_z^*	100
Grid spacing	Δz^*	0.392

Table 4.2. The mobility of ions and time steps for three simulation cases. Reproduced with permission [153]. Copyright 2023, the authors. Published by Elsevier.

Case number	Mobility of ions				Time step
	M_A^*	M_B^*	M_X^*	M_Y^*	Δt^*
1	1000	1000	1	1	10^{-6}
2	1000	1	100	100	10^{-5}
3	1000	1	10	100	5×10^{-5}

4.2.2 Results and discussion for examination of mobility effects

Figure 4.2(a) – (d) show the evolution of mole fractions for Case 1, in which the mobilities of cations are 1000 times higher than the anion mobilities. The legends for these four plots are shown in Figure 4.2(d). Figure 4.2(e) – (h) show the evolution of phase fractions, with the legends presented in Figure 4.2(h). We observe that the diffusion of cations is dominant throughout the reaction, which is expected since the mobility of the cations is 1000 times higher than that of anions. It is important to note that the reaction process is not limited by the diffusion of the slower species (i.e., two anions in this case), unlike the typical kinetic processes in which the rate limiting step (or the slowest process) determine the rate. This is because the faster diffusers (the two cations)

can exchange while the slower diffusers (the two anions) remain in place and the constraints of electroneutrality and on the sum of mole fraction can both be satisfied by the exchange of two cations. Cation A is rapidly diffusing to the right of the simulation domain, resulting in the formation of AY phases. Similarly, the diffusion of cation B towards the left of the simulation domain yields the rapid formation of BX phases. The anions have a much smaller mobility and therefore remain at their initial positions throughout the reaction.

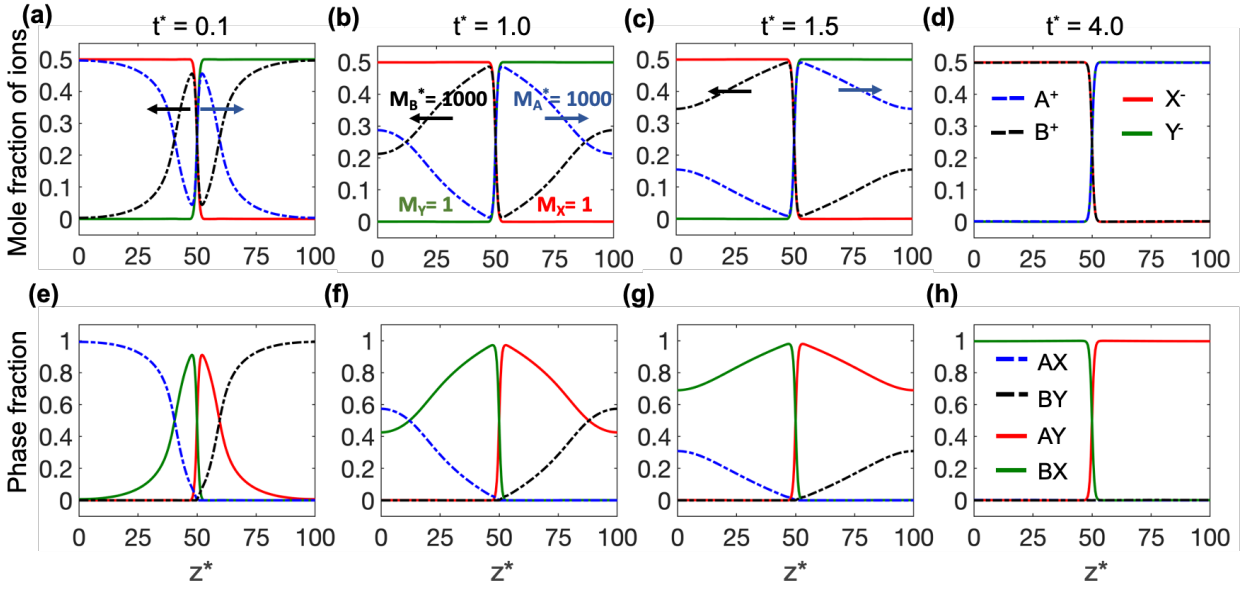

Figure 4.2. The evolution of (a) – (d) mole fractions of ions and (e) – (h) phase fractions in Case 1. The legends for ions are shown in (d) and the legends for phases are shown in (h). Reproduced with permission [153]. Copyright 2023, the authors. Published by Elsevier.

We then examine Case 2, in which cation A has the largest mobility of all four species while cation B has the smallest mobility. The evolution of mole fractions of ions and phase fractions for this case is shown in Figure 4.2. The diffusion of anions is dominant, even though cation A has a higher mobility than the anions. This behavior can be explained by the fact that the cations have a smaller effective mobility (~2) than that (100) of the anions, as defined in Equation (3.55). We can interpret the effective mobility of cations and anions the same way as the equivalent conductance of a pair of two resistors in series, considering the similarity between the concurrent

diffusion of two ions of the same type (*i.e.,* cations or anions) in the SSM reactions and the transport of charges in the electrical circuit with two resistors in series.

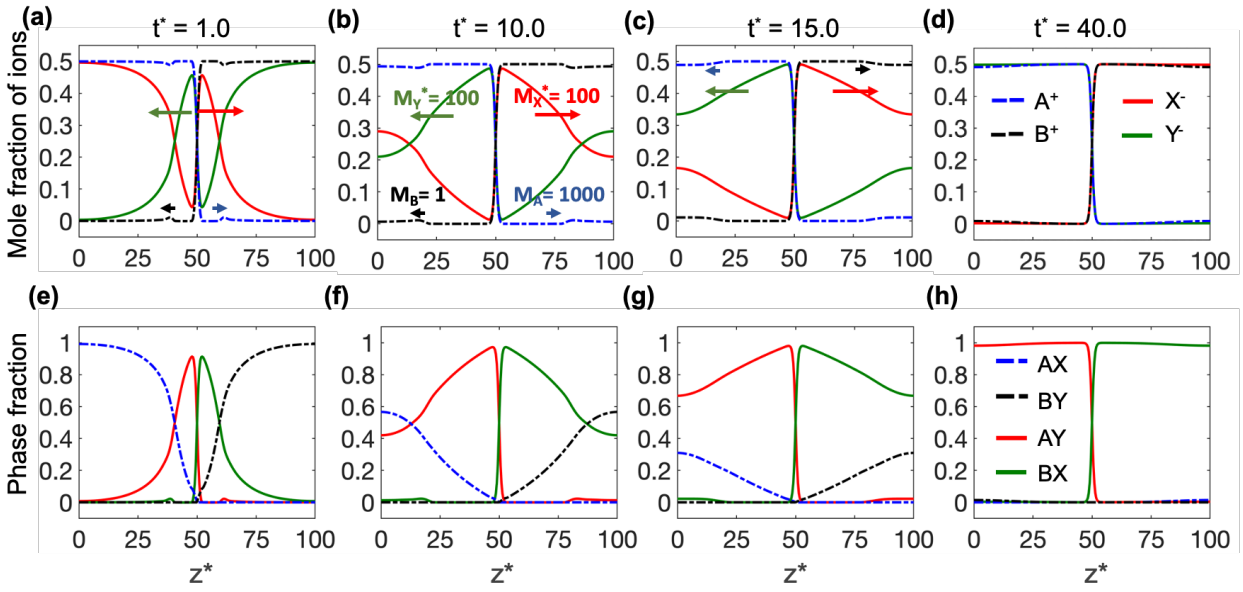

Figure 4.3. The evolution of (a) – (d) mole fractions of ions and (e) – (h) phase fractions in Case 2. The legends for ions are shown in (d) and the legends for phases are shown in (h). Reproduced with permission [153]. Copyright 2023, the authors. Published by Elsevier.

By adding the effective cation mobility and the effective anion mobility (see Equation (3.55) for the definition of the effective mobilities), we obtain a characteristic mobility, M_{overall}, of the overall reaction process (hereafter referred to as *the overall characteristic mobility*):

$$M_{\text{overall}} = M_{\text{cation}} + M_{\text{anion}}. \tag{4.3}$$

The rationale behind this expression is that the reaction has two 'parallel' paths to proceed: either by diffusion of anions, by diffusion of cations, or by their combination. In the extreme case when the anions are immobile (*e.g.,* Case 1), the overall characteristic mobility is equal to the effective mobility of the mobile ions (*e.g.,* cations in Case 1). We can also interpret this overall characteristic mobility the same way as the equivalent conductance of a pair of two resistors in parallel. Since the magnitude of the diffusion flux of ions is proportional to their mobilities, we hypothesize that the overall characteristic mobility sets the rate of evolution. This is indeed the case in our

simulations. For instance, Figure 4.3(a) and (e) and Figure 4.2(a) and (e) represent a similar stage of the reaction based on the concentration and phase profile, but the corresponding dimensionless times are very different, $t^* = 0.1$ for Case 1 and $t^* = 1$ for Case 2. The factor of 10 difference between these times is consistent with the values of overall characteristic mobilities (1001 for Case 1 and ~102 for Case 2), which implies that Case 1 would evolve ~10 times faster than Case 2 (Note that this scaling only applies if the effective cation mobility is sufficiently different from the effective anion mobility).

It is worth noting that the non-dominant ions (cations) still diffuse in Case 2, albeit by a small amount (see the slight change in A^+ and B^+ concentrations in Figure 4.3(a) - (c)), while in Case 1 the non-dominant ions (anions in this case) do not show detectable diffusion. To understand the difference, we further formulate *the characteristic mobility ratio*, which is the ratio of effective mobility of the dominant ions to that of the non-dominant ions. In Case 2 this ratio is ~50:1, while in Case 1 the ratio is 1000:1.

We hypothesize that a characteristic mobility ratio that is closer to unity leads to a more detectable diffusive transport of non-dominant ions since it indicates the effective mobilities for anions and cations are similar. To validate the hypothesis of the characteristic mobility ratio, we examine Case 3, in which the mobility of anion X is reduced by a factor of ten as compared to Case 2 while other mobilities are unchanged. The evolution of mole fractions of ions and the phase transformations are plotted in Figure 4.4. In this case, the ratio is reduced to only ~9.1:1 and, as expected from our hypothesis, diffusion of the non-dominant ions (i.e., cations) is more apparent, although the diffusion is still dominated by the anions. The diffusion of anion X towards the right of simulation domain results in the formation of BX phases on the right and meanwhile allows the same amount of anion Y diffusing to the left and forming AY phases on the left. A small amount

of cation B diffuses to the left and the same amount of cation A diffuses to the right. Phase separation occurs as the reaction progresses. As seen in Figure 4.4(c) and (g), a small amount of BX phases forms within the AY phase and a small amount of AY phases forms within the BX phase. These phases disappear as the reaction continues to progress, and a complete phase transformation is achieved in Figure 4.4(d) and (h).

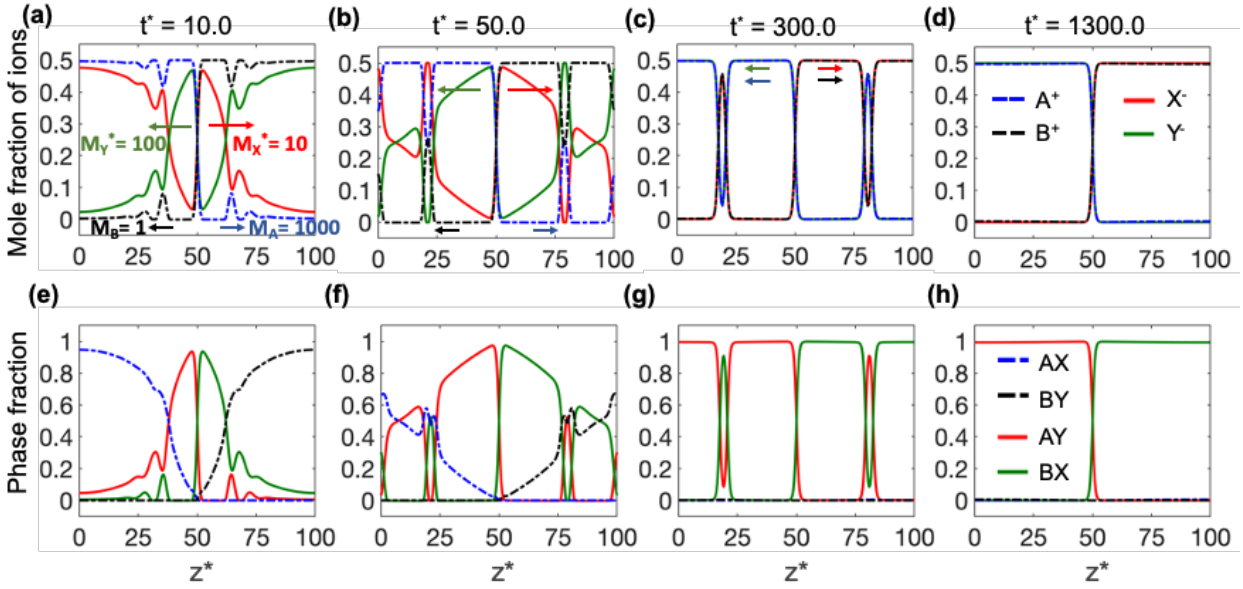

Figure 4.4. The evolution of (a) – (d) mole fractions of ions and (e) – (h) phase fractions in Case 3. The legends for ions are shown in (d), and the legends for phases are shown in (h). Reproduced with permission [153]. Copyright 2023, the authors. Published by Elsevier.

It should be noted that the late-stage evolution is strongly influenced by the mobility of the product phases, which we here assume to be the same as the reactant phases. If the mobility is lower in the product phase, the rate of evolution will be much slower once the product phase is established.

4.2.3 Conclusion for examination of mobility effects

In this section, we demonstrated that different sets of mobility values for ions lead to quantitatively and qualitatively different concentration evolution. We showed that the type of ions

with a larger effective mobility dominates the diffusion. Additionally, we formulated the characteristics mobility of the overall process and, by comparing with the simulation results, showed that the rate of the overall process is set by the overall characteristic mobility, while the ratio of the effective mobilities of cations and anions determines how the process proceeds.

4.3 Prediction of a thin-film experiment for the synthesis of FeS_2

4.3.1 Introduction for the simulation of FeS_2 synthesis

In this section, we utilize the general SSM model discussed in Chapter 3 Section 3.3 to predict the composition and phase evolutions in a thin-film experiment for the synthesis of FeS_2, which has the following reaction formula

$$Na_2S_2 + FeCl_2 \rightarrow 2NaCl + FeS_2. \tag{4.4}$$

In this experiment, the two precursor compounds, Na_2S_2 and $FeCl_2$, were prepared as thin films. The Na_2S_2 is deposited on a Si substrate, and $FeCl_2$ is deposited on the Na_2S_2. A schematic showing the precursor sample is shown in Figure 4.5.

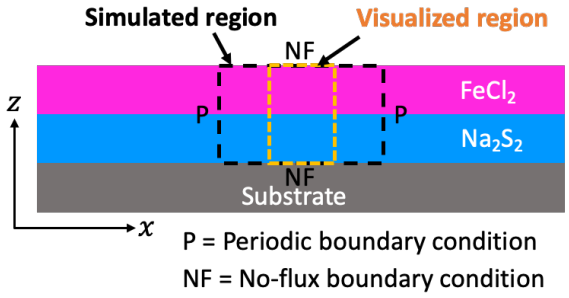

Figure 4.5. A schematic of the thin-film precursor compounds and the substrate. The regions being simulated are bounded by a black dashed box, with periodic boundary conditions and no-flux boundary conditions indicated by P and NF, respectively. Only 40% of the simulated domain is visualized, which is bounded by an orange dashed box. Reproduced with permission [153]. Copyright 2023, the authors. Published by Elsevier.

4.3.2 Simulation method for the simulation of FeS_2 synthesis

We performed the simulation for a portion of the thin-film sample, which is indicated by a black dashed box in Figure 4.5. We assume that the simulated domain is repeated along the horizontal (x) direction and we apply periodic boundary conditions for the left and right boundaries of the simulation domain. We assume no reaction occurs between the $FeCl_2$ and air, as well as between the Na_2S_2 and substrat and employ no-flux boundary conditions for the top and bottom boundaries of the simulation domain.

To capture the interfacial roughness between the precursor compounds, $FeCl_2$ and Na_2S_2, we performed the simulation in two dimensions (rather than one dimension). We initialize the mole fraction of Na^+, Fe^{2+}, Cl^-, and S_2^{2-} ions by

$$c_{\mathrm{Na^+}}(x,z;t=0)=\frac{1}{3}\left[1-\tanh\left(\frac{z-0.5L_z+\eta(x)}{\delta}\right)\right], \tag{4.5}$$

$$c_{\mathrm{Fe^{2+}}}(x,z;t=0)=\frac{1}{6}\left[1+\tanh\left(\frac{z-0.5L_z+\eta(x)}{\delta}\right)\right], \tag{4.6}$$

$$c_{\mathrm{S_2^{2-}}}(x,z;t=0)=\frac{1}{6}\left[1-\tanh\left(\frac{z-0.5L_z+\eta(x)}{\delta}\right)\right], \tag{4.7}$$

$$c_{\mathrm{Cl^-}}(x,z;t=0)=\frac{1}{3}\left[1+\tanh\left(\frac{z-0.5L_z+\eta(x)}{\delta}\right)\right], \tag{4.8}$$

which yield an identical number of moles of Na_2S_2 and $FeCl_2$ precursor phases. The thickness of the sample, L_z, is set to 86 nm to match the sample used in the thin-film experiment discussed above [145]. A perturbation term $\eta(x)$ is used to model the roughness at the interface between the precursor compounds. It is given by

$$\eta(x)=\frac{R}{2}\rho(x), \tag{4.9}$$

where $\rho(x)$ is a uniformly distributed random variable between -1 and 1 with no spatial correlation, and R is the average interfacial roughness.

For this simulation, the thickness of the interface, l_{int}, and the average interfacial roughness are estimated to be 5 nm based on the experimental observations [145]. For the nondimensionalization for this simulation, we select a length scale $l_0 = 1$ nm. The relationship between the energy scale, W, interfacial energy, γ, and l_{int} is obtained using the method discussed in Ref. [126], which is detailed in Chapter 3 Section 3.6. The interfacial energy is reported to be on the order of 0.1 J/m^2 in the literature [155,156]. Accordingly,

$$W = \frac{6\gamma}{l_{int}} = \frac{6 \times 0.1\ \mathrm{J/m^2}}{5\ \mathrm{nm}} = 1.2 \times 10^8 \mathrm{J/m^3}\ . \tag{4.10}$$

To simplify the model, we assume that the mobility of each ion does not depend on the phase in which it is diffusing and thus assign a constant to each mobility. The mobility of the Na^+ and Cl^- ions can be calculated from their respective diffusion coefficients, using Equation (3.11) with the estimated conversion factors $\Phi_{Na^+} = \Phi_{Cl^-} \approx 2W$, as detailed in Chapter 3 Section 3.5. The self-diffusion coefficient of Na^+ at 350 °C (at which the thin-film experiment takes place) is calculated from the temperature-dependent function given in Refs. [157,158] to be 10^{-15} m^2/s and the corresponding mobility, $M_{Na^+} = 4.2 \times 10^{-24}$ m^5/(Js), is determined. Similarly, the self-diffusion coefficient of Cl^- at 350 °C is calculated from the corresponding temperature-dependent function reported in Refs. [157,159] to be 3×10^{-19} m^2/s, and $M_{Cl^-} = 1.2 \times 10^{-27}$ m^5/(Js) = $\frac{3}{10000} M_{Na^+}$ is determined. Although the diffusion coefficients for the Fe^{2+} and S_2^{2-} ions were not previously reported in the literature, we can infer their mobility values based on the observations from the thin-film experiment. The experiment indicates that the diffusion of the anion Cl^- and S_2^{2-} is dominant, followed by the cation Na^+, and that the slowest diffuser is the cation Fe^{2+}. The anion

Cl^- diffuses towards the substrate while the anion S_2^{2-} diffuses towards the surface. These findings suggest that the Fe^{2+} ion has the smallest mobility and the mobility of the S_2^{2-} ion is between that of Na^+ and Fe^{2+} ions. We found that setting the mobility of the S_2^{2-} and Fe^{2+} ions to be $M_{S_2^{2-}} = \frac{1}{6000} M_{Na^+}$ and $M_{Fe^{2+}} = \frac{1}{300000} M_{Na^+}$, respectively, yielded a good qualitative match between the simulation and experiment and therefore employed these values (in their nondimensionalized form) for this simulation. We select the mobility of the Fe^{2+} ion as the mobility scale, M_{min}, and utilize it to nondimensionalize the mobility of each ion. We then substitute M_{min}, W, and l_0 into the definition of t_0 (Equation (3.66)) to calculate the time scale, $t_0 = \frac{t}{t^*} \approx 0.17$ hours, which corresponds to a unit dimensionless time in this simulation. The dimensionless mobility values, along with other parameters employed in this simulation, are summarized in Table 4.3. We note that the selection of mobility values is not unique and there are other values that reproduces the qualitatively consistent results. A more rigorous parameterization via optimization algorithms [97-101] for quantitative agreements will be left for future studies.

4.3.3 *Results and discussion for the simulation of FeS_2 synthesis*

The initialized mole fractions of ions are shown on the top four rows of Figure 4.6(a). The corresponding phase fraction is shown on the last row of Figure 4.6(a). We present the visualization of 40% of the simulated region to allow all the representative stages during the simulation to be shown in one figure. The visualized region is indicated by the orange dashed box in Figure 4.5. The evolution of the mole fractions of the ions and the phase transformations are shown in Figure 4.6(b) – (f). The color bar shown on the right of the figures is used to indicate the value of mole fractions of all the four ions. The color legends indicating distinct phases are shown below the color bar. Each unit dimensionless time corresponds to ~0.17 hours, as discussed above.

Table 4.3. The length, energy, mobility scales, and dimensionless parameters employed in the simulation for the FeS_2 synthesis. Reproduced with permission [153]. Copyright 2023, the authors. Published by Elsevier.

Parameters	Variable	Value
Length scale	l_0	1 nm
Energy scale	W	1.2×10^8 J/m^3
Mobility scale	$M_{\min}$	1.4×10^{-29} m^5/(Js)
Time scale	t_0	≈0.17 hours (calculated)
Bulk energy coefficient	W^*	1
Gradient energy coefficient	κ^*	3.125
Coefficient of negative-mole-fraction penalty term	ζ^*	100
Domain size	L_x^*	430
	L_z^*	86
Grid spacing	$\Delta x^* = \Delta z^*$	0.678
Time step	Δt^*	1×10^{-5}
Mobility of Na^+	M^*_{Na+}	3×10^5
Mobility of Fe^{2+}	M^*_{Fe2+}	1
Mobility of S_2^{2-}	$M^*_{S_2^{2-}}$	50
Mobility of Cl^-	M^*_{Cl-}	90

The anion Cl^- diffuses towards the substrate (below the simulation domain) and the anion S_2^{2-} diffuses towards the surface of the thin-film sample (the top of the simulation domain), as observed in Figure 4.6(a) – (c). A NaCl phase rapidly forms near the substrate and FeS_2 phases form near the surface. Some Na^+ ions diffuse upwards, leading to the formation of two additional NaCl phase domains that are embedded within FeS_2 phases and are parallel to the interface. These embedded NaCl phases can be clearly seen in Figure 4.6(d). The facts that Cl^- and S_2^{2-} rapidly diffuse toward the substrate and surface of the sample, respectively, that a portion of Na^+ ions diffuse across the sample, and that Fe^{2+} primarily stay near the surface of the sample are consistent with those

observed in the thin-film experiments for the synthesis of FeS_2 [145]. As the reaction continues to progress, the Na^+ and Cl^- ions in the additional phase domains diffuse toward the substrate. Due to the roughness of the interface, some embedded NaCl regions disappear faster than the others, leading to the formation of isolated NaCl domains at the top, as seen in Figure 4.6(e). These isolated domains disappear as the reaction continues to progress, as shown in Figure 4.6(f).

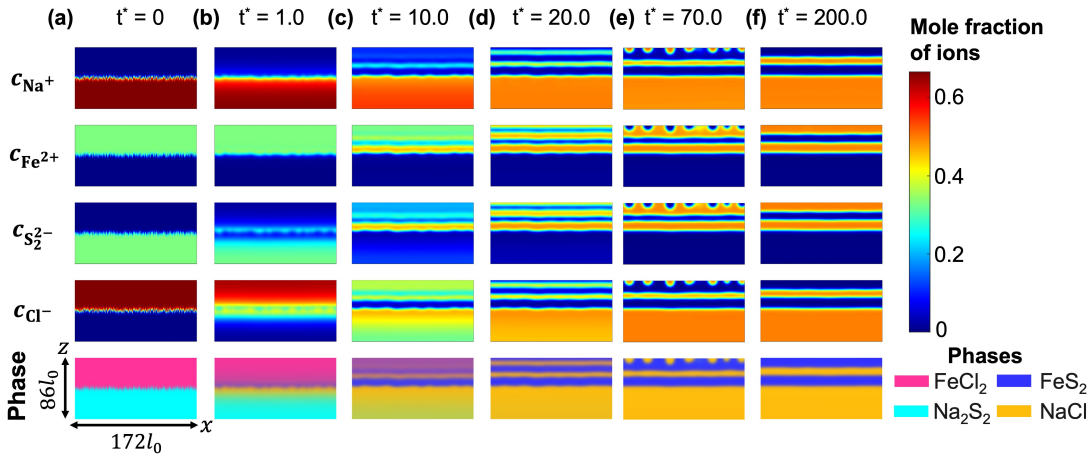

Figure 4.6. The evolution of mole fractions of ions and phase fractions in the simulation for the synthesis of FeS_2. Reproduced with permission [153]. Copyright 2023, the authors. Published by Elsevier.

The simulation shows a complex evolution that involves nonplanar reaction fronts, which was not initially expected. However, a recent study performed by McAuliffe *et al.* [145] utilized TEM to image the cross sections of the thin-film sample and found that the reacted sample contained separate regions of NaCl and FeS_2 phases within the plane, which is consistent with the simulation result. We note that the reactants do not completely convert into products after 17.5 hours ($\sim t^* = 100$) in the experiment, but the simulation suggests that such a conversion is completed after $t^* = 70$ (see Figure 4.6(e)). The faster conversion rate in the simulation most likely stems from an overestimate of the rate-controlling mobility in some phases. More precise parameterization will be left for future work.

While a full investigation that explores how the dynamic behavior changes with thermodynamic and kinetic parameters will be left for a future study, our results do guide the future direction for experiments, which includes employing a thinner sample to stabilize the planarity of interfaces, as well as characterization of the phase morphologies in the plane of the film for thicker samples.

4.3.4 Conclusion for the simulation of FeS_2 synthesis

In this section, we utilized a phase-field model that considers ions with different absolute charge numbers to simulate the synthesis of FeS_2. When the mobilities of the ions were tuned, the diffusion directions of each ion during the reaction matched the observations in the experiment. Specifically, the Cl^- and S_2^{2-} ions were found to rapidly diffuse toward the substrate and surface of the sample, respectively, while only a small portion of Na^+ ions diffused across the sample and the Fe^{2+} ions primarily stayed near the surface of the sample. The simulation yielded a nonplanar evolution when the surface roughness was introduced, which may lead to a formation of nanostructures in the film if the experiment is terminated before the equilibrium state is reached. The simulation could be used to control such nanostructure formation, either to suppress it or control the size scale of the nanostructure.

4.4 Effect of packing density on reaction rate

4.4.1 Introduction for the study of packing-density effect

The effect of packing density of the precursor particles on the reaction rate for solid-state reactions was studied by our experimental collaborator Karena Chapman's group in Stony Brook University. They studied the reaction occurring between $NaFeO_2$ and LiBr

$$NaFeO_2 + LiBr \rightarrow LiFeO_2 + NaBr. \quad (4.11)$$

The reaction completion is measured as a function of time for a densely packed precursor sample and a loosely packed precursor sample. Hereafter, we refer to the densely packed sample and the loosely packed sample as a *densified sample* and a *undensified sample*, respectively. The densified sample contains 85% precursor solid particles (65% of which are LiBr particles and 35% of which are $NaFeO_2$ particles) and 15% pores. The undensified sample contains 25% precursor solid particles (65% of which are LiBr particles and 35% of which are $NaFeO_2$ particles), 11.5% glass diluent, and 63.5% pores. The completion curves for two samples are shown in Figure 4.7.

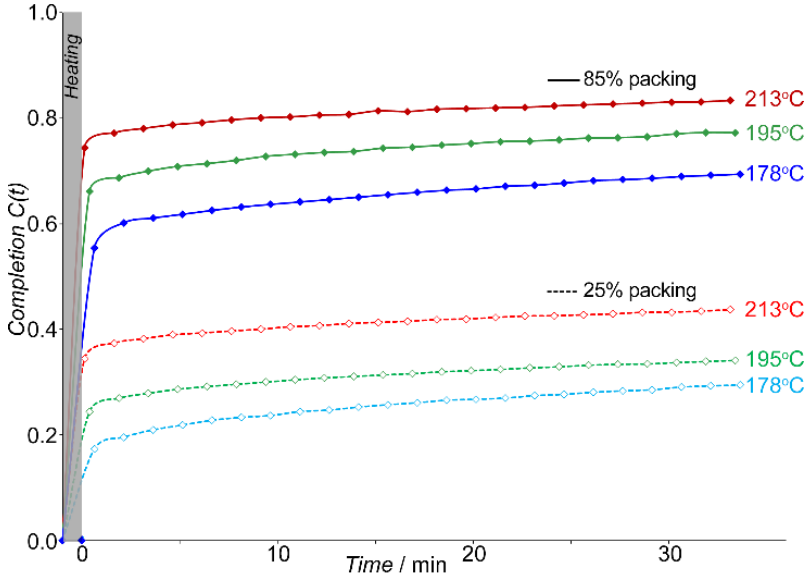

Figure 4.7. The reaction completion, C(t), from isothermal diffraction studies of the ion-exchange reaction between $NaFeO_2$ and LiBr show fast and slow kinetic regimes. Reproduced with permission [146]. Copyright 2022, American Chemical Society.

Regardless of the temperature, a higher reaction rate is observed for the densified sample. To explain its origin, we propose two hypotheses: (1) the precursor particles in the densified sample have more reactive neighbors than those in the undensified sample and (2) the particles surrounded by more reactive neighbors have a higher reaction rate. The two hypotheses, together, could explain the higher reaction rate observed for the densified sample.

To validate the first hypothesis, we developed a lattice model to estimate the distribution of the number of reactive neighbors within densified and undensified samples, as discussed in Section 4.4.2. For the second hypothesis, we conducted a series of phase-field simulations, as discussed in Section 4.4.3, to predict the reaction completion as a function of time for the precursor particles with different number of reactive neighbors. In Section 4.4.4, we combine the findings from Section 4.4.2 and Section 4.4.3 to construct two completion curves, one for the densified sample, and the other for the undensified sample.

4.4.2 Estimating the distribution of the number of reactive neighbors

We propose a lattice model to estimate the distribution of the number of reactive neighbors for densified and undensified samples. We assume a simple cubic lattice, in which each particle has at most 6 nearest neighbors (Nolan *et al.* reported 5.9 in Ref. [160] as the upper bound of the mean coordination number of randomly packed spheres).

We assign one of four values to each point: 0 for pores, 1 for LiBr particles, 2 for $NaFeO_2$ particles, and 3 for SiO_2 glass diluent (undensified sample only). We initialize a uniform mesh of 100^3 grid points, all with value 1. Then we iteratively assign 0 to randomly selected points, until the volume fraction of the solid points (either of precursor phases or SiO_2 glass phase) reduces to a target value, i.e., 25% (precursor particles) + 11.5% (SiO_2 glass) = 36.5% for the undensified sample and 85% for the densified sample. To ensure that no solid point is solely surrounded by pores, the assignment of 0 is performed only when all the solid neighbors of randomly selected points have at least 2 solid neighbors after the assignment. We randomly assign values 1 (LiBr phase), 2 ($NaFeO_2$ phase), and 3 (SiO_2 glass phase) to the solid points, based on their volume ratio measured in the experiments. For the undensified sample, values 1, 2, and 3 are randomly assigned to 44.5%, 24.0%, and 31.5% of the solid points, respectively. For the densified sample, values 1

and 2 are randomly assigned to 65% and 35% solid points, respectively. The resulting model microstructures of undensified and densified samples are shown in Figure 4.8(a) and (b), respectively, with one cross section being highlighted in each case.

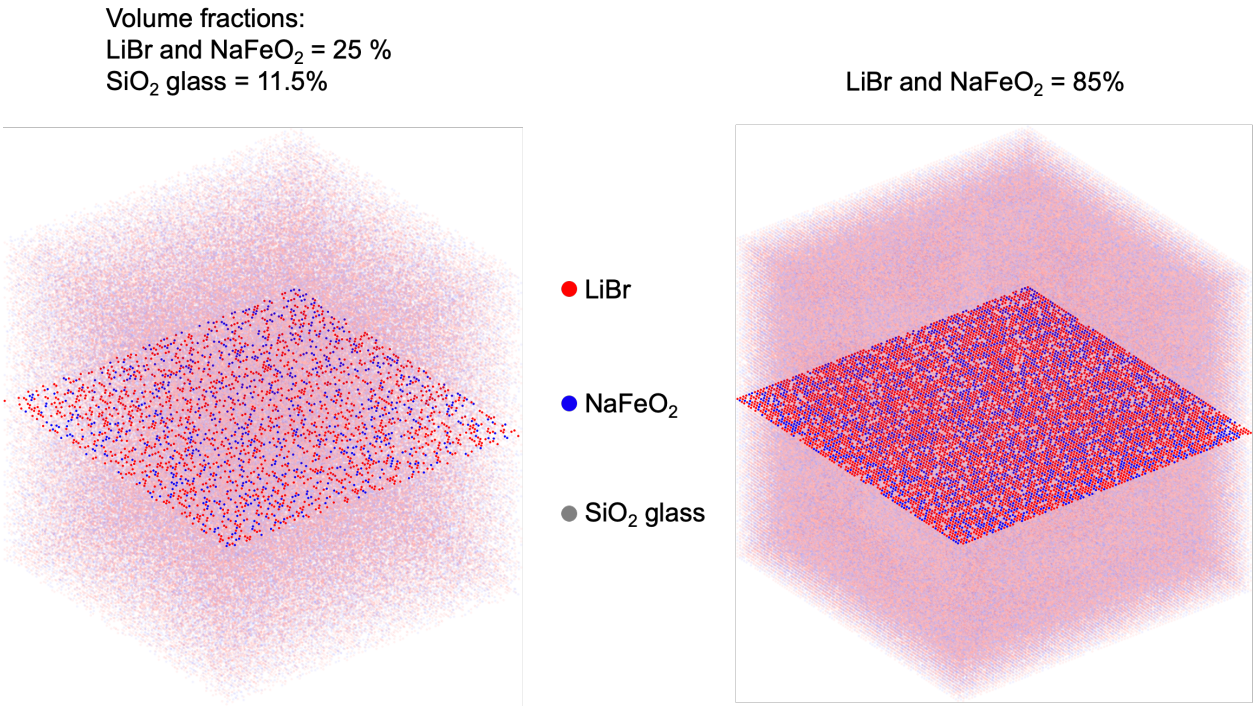

Figure 4.8. Model microstructures for (a) undensified (25% packed) and (b) densified (85% packed) samples. Red, blue, and gray colors are assigned to LiBr particles, $NaFeO_2$ particles, and SiO_2 glass diluent, respectively. One cross section is highlighted in each case. Reproduced with permission [146]. Copyright 2022, American Chemical Society.

The distribution of reactive neighbors was evaluated and is shown in Figure 4.9. As may be expected, the densified model system had a higher average number of reactive direct neighbors compared to the undensified sample (2.31 *cf.* 0.73). In the densified system, a small fraction (8.1%) of particles were not in direct contact with a reactive neighbor (referred to hereafter as *isolated particles*), but 99.6% of these had a reactive next-nearest neighbor. In the undensified system, there was a significant fraction (43.6%) of isolated particles and only 38.2% of these had a reactive next-nearest neighbor. As such, 27% of all particles were 2 or more particles removed from a reactive neighbor; these particles are less likely to participate in the reaction.

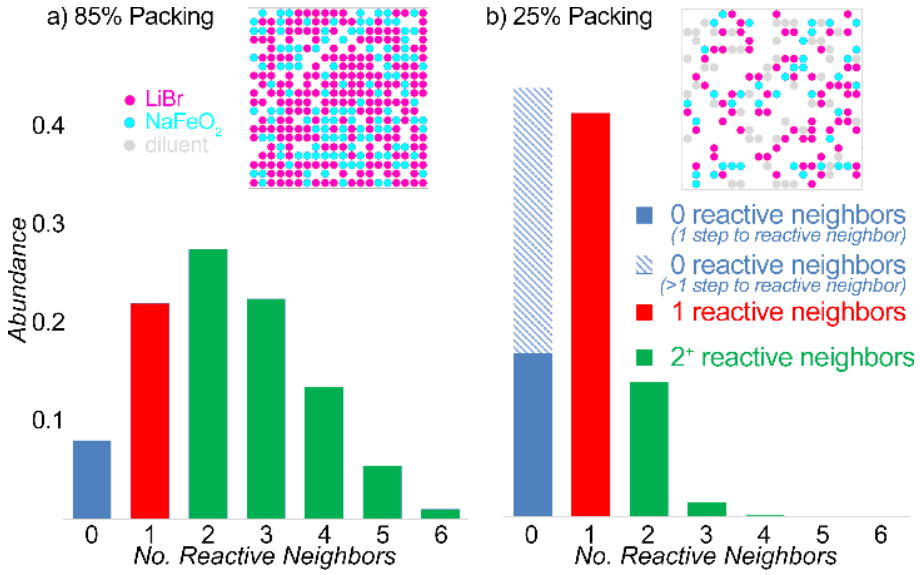

Figure 4.9. The distribution of reactive interparticle contacts in the (a) densified and (b) undensified systems. A portion of cross section of the corresponding model microstructure is shown in the inset in each subfigure. Reproduced with permission [146]. Copyright 2022, American Chemical Society.

4.4.3 Predicting completion for doubly, singly, and indirectly connected particles

To predict the reaction completion as a function of time, we perform phase-field simulations using the model presented in Chapter 3 Section 3.7. We consider two scenarios: (1) the reaction between a periodic array of a LiBr particle and a $NaFeO_2$ particle, and (2) the reaction between a periodic array of a triplet of LiBr particles and a triplet of $NaFeO_2$ particles. The densities of LiBr and $NaFeO_2$ particles are reported to be 3464 kg/m^3 [161] and 4350 kg/m^3 [162], respectively. The molar volumes of LiBr and $NaFeO_2$ are therefore estimated to be 25.1 cm^3/mol and 25.5 cm^3/mol, respectively, by dividing their molar mass by their density. Since we are interested in a qualitative behavior and the phase-field model we employ does not allow volume change during the reaction, we assume an identical molar volume for all the phases and consider an identical amount of $NaFeO_2$ and LiBr particles, which is reasonable given a small difference in their molar volumes (25.1 cm^3/mol vs. 25.5 cm^3/mol).

To set up the initial conditions, we first construct initial phase-indication fields (i.e., 1 within the respective particle, 0 elsewhere), $\eta_{\mathrm{NaFeO_2}}(\boldsymbol{r})$ and $\eta_{\mathrm{LiBr}}(\boldsymbol{r})$, for $\mathrm{NaFeO_2}$ and LiBr particles, respectively, and then generate their signed distance functions, $d_{\mathrm{NaFeO_2}}(\boldsymbol{r})$ and $d_{\mathrm{LiBr}}(\boldsymbol{r})$, followed by initializing the mole fractions, c_i, for all the four ions ($i = \mathrm{Na^+}$, $\mathrm{FeO_2^-}$, $\mathrm{Li^+}$, and $\mathrm{Br^-}$) and a domain parameter field, ψ, as detailed below. A periodic boundary condition is imposed for the simulation domain. For the first scenario, we construct a simulation domain with a near spherical $NaFeO_2$ particle (a sphere with spherical caps removed) placed between two LiBr particles (similarly missing a cap; see Figure 4.10(a) for the cross-section of the geometry). A near hemispherical shape is employed for each LiBr particle due to the periodic boundary condition. The center of the $NaFeO_2$ particle is given by $\left[x_{c,\mathrm{NaFeO_2}}, y_{c,\mathrm{NaFeO_2}}, z_{c,\mathrm{NaFeO_2}}\right]$, and the centers of the LiBr particles on the top and bottom sides are given by $\left[x_{c,\mathrm{LiBr}}, y_{c_1,\mathrm{LiBr}}, z_{c,\mathrm{LiBr}}\right]$ and $\left[x_{c,\mathrm{LiBr}}, y_{c_2,\mathrm{LiBr}}, z_{c,\mathrm{LiBr}}\right]$, respectively. We denote the radii of $NaFeO_2$ and LiBr particles as R_p. To generate the initial phase indication fields, we must have mathematical criteria that indicate the phase at a point (x, y, z). The necessary conditions for selecting the regions within the middle $NaFeO_2$ particle, the top LiBr particle, and the bottom LiBr particle are given by Condition 1, 2, and 3, respectively, as follows:

$$\text{Condition 1: } \left(x - x_{c,\mathrm{NaFeO_2}}\right)^2 + \left(y - y_{c,\mathrm{NaFeO_2}}\right)^2 + \left(z - z_{c,\mathrm{NaFeO_2}}\right)^2 < R_p^2, \tag{4.12}$$

$$\text{Condition 2: } \left(x - x_{c,\mathrm{LiBr}}\right)^2 + \left(y - y_{c_1,\mathrm{LiBr}}\right)^2 + \left(z - z_{c,\mathrm{LiBr}}\right)^2 < R_p^2, \tag{4.13}$$

$$\text{Condition 3: } \left(x - x_{c,\mathrm{LiBr}}\right)^2 + \left(y - y_{c_2,\mathrm{LiBr}}\right)^2 + \left(z - z_{c,\mathrm{LiBr}}\right)^2 < R_p^2. \tag{4.14}$$

In addition, a spherical cap needs to be removed from each particle above its contact plane with the other particle, considering their overlap. To do so, the contact plane between the two adjacent

particles is first identified, and the spherical cap beyond this plane for each particle is excluded. The following condition excludes these spherical caps for the middle $NaFeO_2$ particle:

$$\text{Condition 4: } \left(y > \frac{y_{c,\mathrm{NaFeO_2}} + y_{c_1,\mathrm{LiBr}}}{2} \text{ and } y < \frac{y_{c,\mathrm{NaFeO_2}} + y_{c_2,\mathrm{LiBr}}}{2}\right). \tag{4.15}$$

Similarly, the following conditions exclude the spherical caps for the two LiBr particles on the top and bottom, respectively:

$$\text{Condition 5: } y < \frac{y_{c,\mathrm{NaFeO_2}} + y_{c_1,\mathrm{LiBr}}}{2}, \tag{4.16}$$

$$\text{Condition 6: } y > \frac{y_{c,\mathrm{NaFeO_2}} + y_{c_2,\mathrm{LiBr}}}{2}. \tag{4.17}$$

Now, we have a full set of conditions that are required to indicate the phase at any point in the computational domain. To generate the initial phase-indication fields $\eta_{\mathrm{NaFeO_2}}(\boldsymbol{r})$ and $\eta_{\mathrm{LiBr}}(\boldsymbol{r})$, we employ the following formula:

$$\eta_{\mathrm{NaFeO_2}}(\boldsymbol{r}) = \begin{cases} 1, & \text{if condition 1 and condition 4,} \\ 0, & \text{otherwise,} \end{cases} \tag{4.18}$$

$$\eta_{\mathrm{LiBr}}(\boldsymbol{r}) = \begin{cases} 1, & \text{if (condition 2 and condition 5) or (condition 3 and condition 6),} \\ 0, & \text{otherwise.} \end{cases} \tag{4.19}$$

We employ the level-set method discussed in Chapter 2 Section 2.8 to the $\eta_{\mathrm{NaFeO_2}}(\boldsymbol{r})$ and $\eta_{\mathrm{LiBr}}(\boldsymbol{r})$ fields to generate signed distance functions, $d_{\mathrm{NaFeO_2}}(\boldsymbol{r})$ and $d_{\mathrm{LiBr}}(\boldsymbol{r})$. Specifically, the distance function d_α ($\alpha = \mathrm{NaFeO_2}$ and LiBr) is obtained via the evolution of a dummy field, $\tilde{\eta}_\alpha(\boldsymbol{r})$, initialized with $\eta_\alpha(\boldsymbol{r}) - 0.5$, using Equation (2.63), until the spatial average of the absolute value of the change in $\tilde{\eta}_\alpha$ between two iterations, $\frac{1}{V}\int_V |\tilde{\eta}_\alpha(t + \Delta t) - \tilde{\eta}_\alpha(t)|\, dV$, is less than 10^{-6}. The value of d_α is set by $\tilde{\eta}_\alpha$ after the convergence. The gradient of the field, $\nabla\tilde{\eta}_\alpha$, is calculated using a first-order upwind scheme [138,141]. We apply hyperbolic tangent functions to $d_{\mathrm{NaFeO_2}}(\boldsymbol{r})$ and $d_{\mathrm{LiBr}}(\boldsymbol{r})$ to obtain the initial mole fractions of ions $c_i(\boldsymbol{r}; t = 0)$:

$$c_{\mathrm{Na}^+}(\boldsymbol{r};t=0)=c_{\mathrm{FeO}_2^-}(\boldsymbol{r};t=0)=\frac{1}{4}\left[\tanh\left(\frac{d_{\mathrm{NaFeO}_2}(\boldsymbol{r})}{\delta}\right)+1\right], \tag{4.20}$$

$$c_{\mathrm{Li}^+}(\boldsymbol{r};t=0)=c_{\mathrm{Br}^-}(\boldsymbol{r};t=0)=\frac{1}{4}\left[\tanh\left(\frac{d_{\mathrm{LiBr}}(\boldsymbol{r})}{\delta}\right)+1\right], \tag{4.21}$$

where $\delta=\sqrt{2\kappa/W}$ is half of the interfacial width defined in this phase-field model (where the full thickness is defined as the distance over which the field changes from ~10% to ~90% of the maximum value). The domain parameter, $\psi(\boldsymbol{r})$, is given by

$$\psi(\boldsymbol{r})=\frac{1}{2}\tanh\left(\frac{d_{\mathrm{NaFeO}_2}(\boldsymbol{r})}{\delta}\right)+\frac{1}{2}\tanh\left(\frac{d_{\mathrm{LiBr}}(\boldsymbol{r})}{\delta}\right)+1. \tag{4.22}$$

We employ a similar procedure to construct the initial fields for the second scenario, although in this case, the simulation domain consists of a triplet of near spherical $NaFeO_2$ particles and a combination of a near spherical LiBr particle and a near hemispherical LiBr particle on both ends of the $NaFeO_2$ particles (see Figure 4.10(b) for the cross-section of the geometry). The centers of the $NaFeO_2$ particles are given by $\left[x_{c,\mathrm{NaFeO}_2}, y_{c_1,\mathrm{NaFeO}_2}, z_{c,\mathrm{NaFeO}_2}\right]$, $\left[x_{c,\mathrm{NaFeO}_2}, y_{c_2,\mathrm{NaFeO}_2}, z_{c,\mathrm{NaFeO}_2}\right]$, and $\left[x_{c,\mathrm{NaFeO}_2}, y_{c_1,\mathrm{NaFeO}_2}, z_{c,\mathrm{NaFeO}_2}\right]$. The centers of the LiBr particles are given by $\left[x_{c,\mathrm{LiBr}}, y_{c_1,\mathrm{LiBr}}, z_{c,\mathrm{LiBr}}\right]$, $\left[x_{c,\mathrm{LiBr}}, y_{c_2,\mathrm{LiBr}}, z_{c,\mathrm{LiBr}}\right]$, $\left[x_{c,\mathrm{LiBr}}, y_{c_3,\mathrm{LiBr}}, z_{c,\mathrm{LiBr}}\right]$, and $\left[x_{c,\mathrm{LiBr}}, y_{c_4,\mathrm{LiBr}}, z_{c,\mathrm{LiBr}}\right]$. The values of the center positions, as well as the radius, for the two scenarios, are summarized in Table 4.4. With these initial conditions, the evolutions of the mole fractions are obtained using Equation (3.120). The simulation parameters are summarized in Table 4.5.

Table 4.4. The centers and radii of $NaFeO_2$ and LiBr particles for the two scenarios. The variables with a "*" sign at their superscript indicate that they are dimensionless variables. Reproduced with permission [146]. Copyright 2022, American Chemical Society.

	$NaFeO_2$	LiBr
For both scenarios	$x^*_{c,\mathrm{NaFeO_2}} = x^*_{c,\mathrm{LiBr}} = L^*_x/2$ $z^*_{c,\mathrm{NaFeO_2}} = z^*_{c,\mathrm{LiBr}} = L^*_z/2$ $R^*_p = 10.21$	
Scenario 1	$y^*_{c_1,\mathrm{NaFeO_2}} = L^*_y/2$	$y^*_{c_1,\mathrm{LiBr}} = 0$ $y^*_{c_2,\mathrm{LiBr}} = L^*_y$
Scenario 2	$y^*_{c_1,\mathrm{NaFeO_2}} = L^*_y/3$ $y^*_{c_2,\mathrm{NaFeO_2}} = L^*_y/2$ $y^*_{c_3,\mathrm{NaFeO_2}} = 2L^*_y/3$	$y^*_{c_1,\mathrm{LiBr}} = 0$ $y^*_{c_2,\mathrm{LiBr}} = L^*_y/6$ $y^*_{c_3,\mathrm{LiBr}} = 5L^*_y/6$ $y^*_{c_4,\mathrm{LiBr}} = L^*_y$

Table 4.5. The parameters employed in the simulations. The variables with a "*" sign at their superscript indicate that they are dimensionless variables. Reproduced with permission [146]. Copyright 2022, American Chemical Society.

Parameters	**Variable**	**Value**
Length scale	l_0	1 μm
Bulk energy coefficient	W^*	1
Gradient energy coefficient	κ^*	0.125
Constraint term coefficient	ζ^*	400
Domain size	$L^*_x = L^*_z = L^*$	32.2
	Scenario 1: $L^*_y = L^*$	32.2
	Scenario 2: $L^*_y = 3L^*$	96.6
Grid spacing	$\Delta x^* = \Delta y^* = \Delta z^*$	0.248
Time step	Δt^*	1×10^{-5}
Mobility of Na^+	$M^*_{\mathrm{Na+}}$	2
Mobility of FeO_2^-	$M^*_{\mathrm{FeO_2^-}}$	0.002
Mobility of Li^+	$M^*_{\mathrm{Li+}}$	2
Mobility of Br^-	$M^*_{\mathrm{Br-}}$	0.002

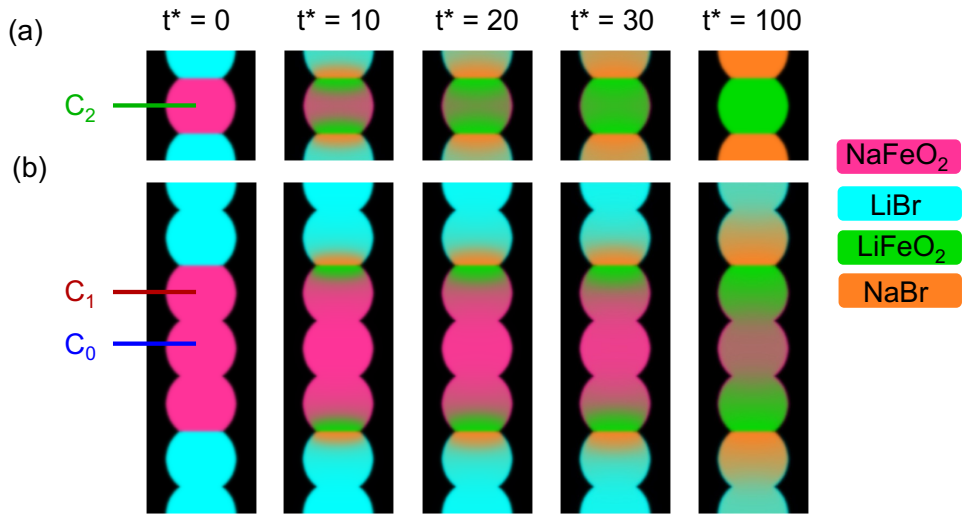

Figure 4.10. Cross-sectional views of the phase evolution during the reactions with (a) a periodic array of a LiBr particle and a $NaFeO_2$ particle, and (b) a periodic array of a triplet of LiBr particles and a triplet of $NaFeO_2$ particles. Reproduced with permission [146]. Copyright 2022, American Chemical Society.

The cross-sectional view of the phase evolution during the reactions for scenario 1 and scenario 2 are shown in Figure 4.10(a) and (b), respectively. As shown in the figures, the precursor particles convert completely into products by t* = 100 for the first scenario, while such completion is not achieved for the second scenario. To quantify the reaction progress, we define a completion percentage, $C(t)$, which is the amounts of products formed divided by the total amounts of compounds, given by:

$$C(t) = \frac{\int_V \left[\phi_{\mathrm{LiFeO_2}}(\boldsymbol{r},t) + \phi_{\mathrm{NaBr}}(\boldsymbol{r},t)\right]\psi(\boldsymbol{r})\,dV}{\int_V \psi(\boldsymbol{r})dV}, \tag{4.23}$$

where $\phi_{\mathrm{LiFeO_2}}(\boldsymbol{r},t)$ and $\phi_{\mathrm{NaBr}}(\boldsymbol{r},t)$ are the phase fractions of $LiFeO_2$ and NaBr, respectively. From the phase-field simulations, we can identify three types of precursor particles: a particle with two reactive neighbors, a particle with one reactive neighbor, and a particle with no reactive neighbors. These particles are marked in Figure 4.10(a) and (b). Their completion percentages are denoted as C_2, C_1, and C_0. As shown in Figure 4.11, the simulated reaction progress depends on

the interparticle contacts. The reaction proceeds most rapidly for the doubly connected particles, followed by the singly connected and indirectly connected particles.

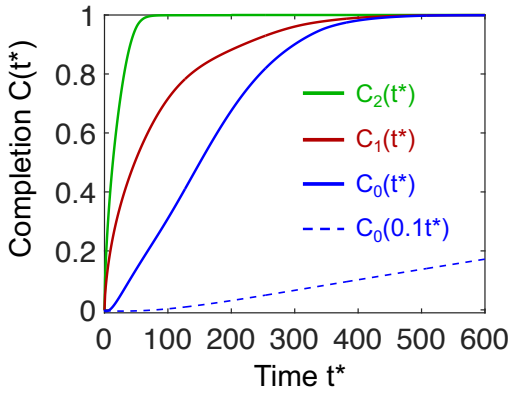

Figure 4.11. The simulated reaction progress in doubly, singly, and indirectly connected particles. Reproduced with permission [146]. Copyright 2022, American Chemical Society.

4.4.4 Predicting completion for the densified and undensified samples

By combining the simulated completion in particles with different connectivity, we can generate an expected composite reaction evolution for both densified sample and undensified sample. The composite reaction completion profiles are constructed based on the distribution of indirectly, singly, and at least doubly connected reactive particle contacts estimated from the lattice model in Section 4.4.2, and the completion percentages simulated in Section 4.4.3, using the following formula:

$$C_{\text{composite}}(t) = \gamma\, p_0 C_0(0.1t) + p_1 C_1(t) + p_2 C_2(t), \tag{4.24}$$

where γ is the fraction of isolated particles that are separated from the next reactive particle by only one particle. We assume that particles that are more than one particle removed from a reactive neighbor have such low reactivity that they can be considered as inactive. Reaction in particles with no direct reactive neighbor is slowed by a factor of 10 to account for the reduction in kinetics (e.g., due to lower mobility in product phases forming between reactive particles), which was not

accounted for in the phase-field model. The constructed completion curves for the densified and undensified samples are shown in Figure 4.12. The two curves qualitatively resemble the experimental completion curves in Figure 4.7. The quantitative matching of the experimental and simulation results will be left for future study.

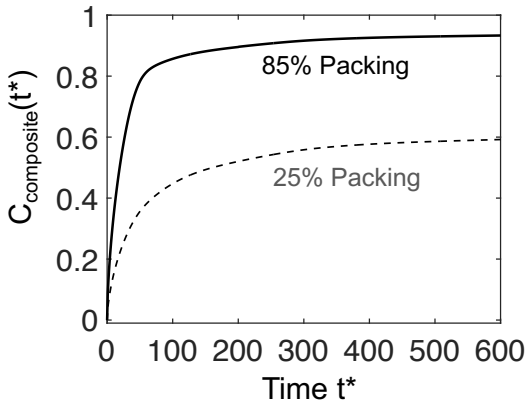

Figure 4.12. Composite reaction profiles obtained by combining the simulated reaction progress and distribution of reactive interparticle contacts, incorporating a delay for reaction of indirectly connected particles. Reproduced with permission [146]. Copyright 2022, American Chemical Society.

4.4.5 Conclusion for the study of packing-density effect

In this section, we leveraged the combined findings from a lattice model and a phase-field model to study the effect of packing density of the sample on the reaction rate. The lattice model suggested that the densified model system had a higher average number of reactive neighbors as compared to the undensified sample. The phase-field model was applied to simulate the phase evolution for two scenarios: one with a periodic array of LiBr particle and a $NaFeO_2$ particle, and the other with a periodic array of a triplet of LiBr particles and a triplet of $NaFeO_2$ particles. The time-dependent completion percentages for doubly, singly, and indirectly connected particles were calculated from the phase-field simulations. Finally, these reaction percentages were combined based on the estimated distribution of reactive neighbors for densified and undensified samples

obtained from the lattice model to construct composite completion curves for the two samples, which qualitatively match the completion curves measured in the experiments. The resulting completion curves indicate that the reactions take place more rapidly in a densified sample because of the larger number of reactive neighboring particles in a denser sample.

Chapter 5 Phase-Field Modeling of Stored-Energy-Driven Macroscale Translation of Grains During Non-Isothermal Annealing

5.1 Introduction

As discussed in Chapter 1 Section 1.3, the microstructure evolution within a sample undergoing non-isothermal annealing may be driven by the stored energy arising from the difference in the dislocation density between grains, in addition to the capillary driving force due to the grain boundary energy. In this chapter,[*] we present a phase-field model to simulate microstructure evolution that accounts for these two mechanisms. In Section 5.2, we discuss the key findings obtained from a cyclic heat treatment experiment performed by our experimental collaborator and propose a phase-field approach to simulate the microstructure evolution. In Section 5.3, we examine the effect of the stored energy on the behavior of microstructure evolution, specifically, the translation of grain centers.

5.2 Experiments and simulation method

5.2.1 Cyclic heat treatment experiment

As discussed in Chapter 2 Section 2.2, abnormal grain growth has recently been identified during cycle heat treatment of polycrystalline alloys. Our experimental collaborators, Ashwin J. Shahani's group, characterized dynamic annealing of a Cu-Al-Mn alloy sample [24] to examine

[*] Adapted from M. J. Higgins, J. Kang, G. Huang, D. Montiel, N. Lu, H. Liu, Y. F. Shen, P. Staublin, J. S. Park, J. D. Almer, P. Kenesei, P. G. Sanders, R. M. Suter, K. Thornton, and A. J. Shahani, "Anomalous Strain-Energy-Driven Macroscale Translation of Grains During Nonisothermal Annealing," Physical Review Materials **5**, L070401 (2021).

the effect of cyclic heat treatment of the sample on the microstructure evolution. They conducted two cycles of heat treatment following the dynamic annealing schedule shown in Figure 5.1.

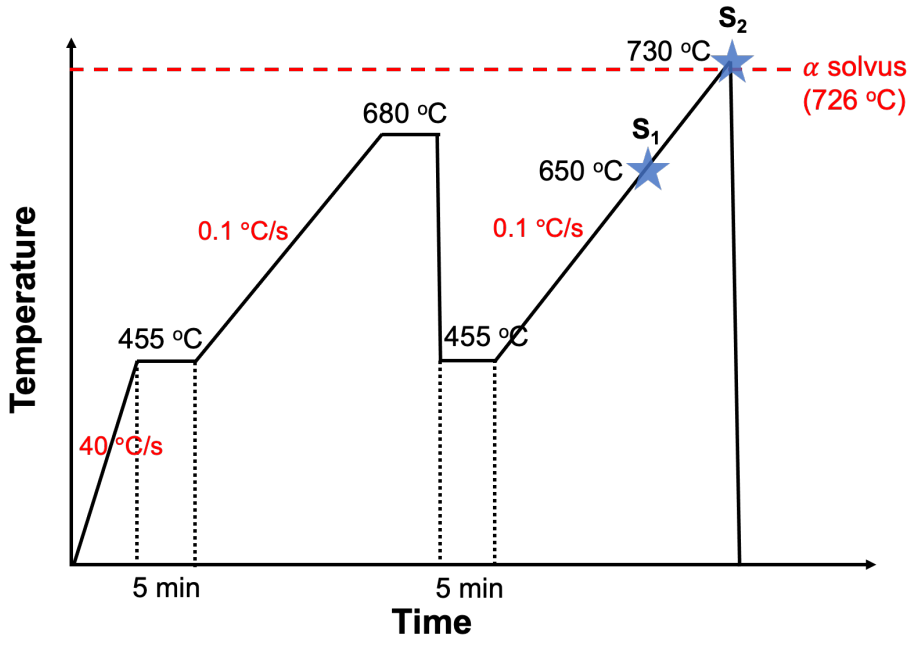

Figure 5.1. Schematic showing the dynamic annealing schedule. Two cycles of heat treatment are conducted for the Cu-Al-Mn sample. The microstructure is examined at state S_1 and S_2 during the second heat cycle. Reproduced with permission [24]. Copyright 2021, American Physical Society.

They examined the microstructure within the sample at state S_1 and S_2 during the second heat cycle. They found that a large grain is consumed by its neighboring small grains in the course of annealing from S_1 to S_2, by tracking and comparing the size of this grain and its surrounding grains. This phenomenon cannot be explained by the traditional understanding of a capillary-driven grain growth, in which the large grains are expected to consume small grains [13,163,164]. Additionally, they observed the center of this shrinking grain translating by 70 μm, which is more than half of the average grain radius in state S_1. This notable grain translation is not expected as well due to considerable back pressure exerted from the adjacent grains [165-167], considering the self-similar nature of a capillary-driven grain growth. To explain these phenomena, we propose that the

formation of dislocations during non-isothermal annealing results in different dislocation densities for each grain, which leads to a difference in the stored energy between grains. This stored energy difference provides an additional driving force for the grains with low-dislocation-density grains to consume high-dislocation-density grains.

To test our hypothesis and provide insights into the microstructure evolution from state S_1 to state S_2, we developed a phase-field model that extends the recrystallization models employed by Moelans et al. [168,169] and Gentry et al. [170], which was built upon them, that account for the contribution of stored energy as the driving force for grain boundary migration. In particular, we derived a set of time-evolution equations for the order parameters that are expressed in terms of the gradient of a dislocation density field, rather than a set of constant dislocation density values, which were employed by Gentry et al. [170]. We note that, however, the time-evolution equation for the dislocation density field still depends on the constant dislocation density values. In this chapter, we assume uniform dislocation density values within each grain for simplicity since the focus of this chapter is to study the effect of the stored energy difference between grains on the microstructure evolution. A spatially varying dislocation density within the grains will be discussed in the next chapter.

5.2.2 Phase-field model for microstructure evolution

Free energy functional and governing equations

A total free energy functional that encodes the thermodynamics of the polycrystalline material system is given by the volume integral of the sum of three energy density terms.

$$\mathcal{F}(\{\eta_i\}) = \int_V \left(f_{\text{bulk}} + f_{\text{gradient}} + f_{\text{stored}}\right) dV, \tag{5.1}$$

where $\{\eta_i(\vec{r},t)\}$ is a set of N space- and time-dependent order parameters, each representing a grain, in a system of volume V. These order parameters indicate grains with different orientations. The value of an order parameter is 1 within the corresponding grain, 0 outside of the grain, and varies smoothly between the two values across the grain boundary. We utilize the functional form proposed by Moelans et al. [171] to calculate the bulk energy density, f_{bulk}:

$$f_{\text{bulk}} = m_0\left[\sum_{i=1}^{N}\left(-\frac{1}{2}\eta_i^2+\frac{1}{4}\eta_i^4\right)+\alpha\sum_{i=1}^{N}\sum_{j>1}^{N}\left(\eta_i^2\eta_j^2\right)+\frac{1}{4}\right], \tag{5.2}$$

where m_0 is the bulk energy density coefficient, and $\alpha = 1.5$ is set to ensure a symmetrical order parameter profile across an interface, as discussed in Ref. [171]. The gradient energy density [103,126], f_{gradient}, is employed to penalize a sharp interface

$$f_{\text{gradient}} = \frac{\kappa}{2}\sum_{i=1}^{N}|\nabla\eta_i|^2, \tag{5.3}$$

where κ is the gradient energy coefficient. An approximate form of the stored energy, which neglects the energy of the dislocation core and assumes isotropic elasticity, is given by [80]

$$f_{stored}(\vec{r},t) = \frac{1}{2}Gb^2\rho(\vec{r},t), \tag{5.4}$$

where G is the shear modulus, b is the magnitude of the Burgers vector, and $\rho(\vec{r},t)$ is the coarse-grained dislocation density at point $\vec{r}$ at time t. The time-evolution of each of the order parameters is driven by the reduction of the free energy as described by Allen-Cahn dynamics [129]:

$$\frac{\partial\eta_i}{\partial t} = -L\left(\frac{\delta F}{\delta\eta_i}\right), \tag{5.5}$$

where L is the mobility of the order parameter. The stored energy contribution to $\delta F/\delta\eta_i$ is given by

$$\left(\frac{\delta F}{\delta \eta_i}\right)_{stored} = \frac{\partial f_{stored}}{\partial \eta_i} = \frac{1}{2} G b^2 \frac{\partial \rho}{\partial \eta_i}. \tag{5.6}$$

We initialize $\rho(\vec{r}, t)$ as a weighted average of the dislocation density of each grain, ρ_i, which is assumed to be uniform in the bulk and constant in time [168-170]:

$$\rho(\{\eta_i(r,t)\}) = \frac{\sum_{i=1}^{N}[\eta_i^2(\vec{r},t)\rho_i]}{\sum_{i=1}^{N}\eta_i^2\,(\vec{r},t)}. \tag{5.7}$$

This expression is used as the basis for deriving a general form of the model that does not require reconstruction of the dislocation density given by Equation (5.7). For a simple interface between two grains described by η_i and η_j, the term $\partial\rho/\partial\eta_i$ is proportional to the difference in dislocation densities, *i.e.*,

$$\frac{\partial \rho}{\partial \eta_i} = \frac{2\eta_i\eta_j^2}{\left(\eta_i^2 + \eta_j^2\right)^2}\left(\rho_i - \rho_j\right). \tag{5.8}$$

This expression is equivalent to that employed by Gentry et. al. [170], and it will be used to derive the approximate form of $\partial\rho/\partial\eta_i$ in terms of the gradient of $\rho(\vec{r}, t)$. Assuming that the profiles of η_i and η_j across the GB along the direction of the GB normal correspond to the equilibrium profiles for a flat interface (without the stored energy contribution), η_i can be expressed as a function of normal coordinate, x, in the analytical form:

$$\eta_i = 1 - \eta_j = \frac{1}{2} - \frac{1}{2}\tanh\left(\frac{x - x_0}{\sqrt{2}W}\right), \tag{5.9}$$

where x_0 represents the midpoint of the interface and $W = \sqrt{\kappa/m_0}$. The term $2\sqrt{2}W$ is a measure of the equilibrium width of the grain boundary. Assuming $\eta_i + \eta_j = 1$, the derivative of $\rho(\vec{r}, t)$ along the x-direction is then given by

$$\frac{\partial \rho}{\partial x} = \frac{\partial \rho}{\partial \eta_i}\frac{\partial \eta_i}{\partial x} + \frac{\partial \rho}{\partial \eta_j}\frac{\partial \eta_j}{\partial x} = \left(\frac{\partial \rho}{\partial \eta_i} - \frac{\partial \rho}{\partial \eta_j}\right)\frac{\partial \eta_i}{\partial x}. \tag{5.10}$$

From Equation (5.8) and the relation $\eta_i + \eta_j = 1$, we obtain

$$\frac{\partial \rho}{\partial \eta_i} - \frac{\partial \rho}{\partial \eta_j} = \frac{2\eta_i \eta_j (\rho_i - \rho_j)}{\left(\eta_i^2 + \eta_j^2\right)^2}. \tag{5.11}$$

Taking derivative of η_i in Equation (5.9) with respect to x yields

$$\frac{\partial \eta_i}{\partial x} = -\frac{\sqrt{2}}{W}\eta_i(1 - \eta_i) = -\frac{\sqrt{2}}{W}\eta_i \eta_j. \tag{5.12}$$

Substituting Equations (5.11) and (5.12) into Equation (5.10) and then solving for $\rho_i - \rho_j$ we obtain

$$\rho_i - \rho_j = -\frac{W}{2\sqrt{2}}\left(\frac{\eta_i^2 + \eta_j^2}{\eta_i \eta_j}\right)^2 \frac{\partial \rho}{\partial x}. \tag{5.13}$$

Substitution of $\rho_i - \rho_j$ from Equation (5.13) into Equation (5.8) yields

$$\frac{\partial \rho}{\partial \eta_i} = -\frac{W}{\sqrt{2}}\frac{1}{\eta_i}\frac{\partial \rho}{\partial x}. \tag{5.14}$$

Although the factor of $1/\eta_i$ would be cancelled for the exact form of $\partial\rho/\partial x$ with an equilibrium interfacial profile in equilibrium (i.e., Equation (5.9)), Equation (5.14) is unstable numerically as η_i approaches zero (away from the grain *i*). For this reason, we need to employ an approximate form of Equation (5.8) as a function of $\partial\rho/\partial x$. We found that the following expression

$$\rho_i - \rho_j = -2\sqrt{2}W\frac{\left(\eta_i^2 + \eta_j^2\right)^3}{\eta_i \eta_j}\frac{\partial \rho}{\partial x}, \tag{5.15}$$

Yields a good approximation for $\partial\rho/\partial\eta_i$ within the interfacial region in equilibrium while avoiding a numerically instability as η_i approaches zero. Effectively, this approximation is equivalent to replacing $\eta_i \eta_j\left(\eta_i^2 + \eta_j^2\right)$ with 1/8, which is the value at the midpoint of the interface (where $\eta_i = \eta_j = 1/2$). By substituting Equation (5.15) into Equation (5.8), we have

$$\frac{\partial \rho}{\partial \eta_i} \approx -4\sqrt{2}W\eta_j\left(\eta_i^2+\eta_j^2\right)\frac{\partial \rho}{\partial x}, \tag{5.16}$$

which avoids numerical instability. Equation (5.16) can be generalized to include all grains in the system, resulting in

$$\frac{\partial \rho}{\partial \eta_i} = -\frac{4\sqrt{2}W\ \nabla\rho\cdot\hat{n}_i}{(\sum_{k=1}^{N}\eta_k^2)^2}\sum_{k\neq i}^{N}[\eta_k(\eta_i^2+\eta_k^2)^3]\,, \tag{5.17}$$

where $\hat{n}_i = -\nabla\eta_i/|\nabla\eta_i|$ is the outward normal vector along the interface of i-th grain. In Equation (5.17), the cubic term within the summation sign cancels out with the square term in the denominator when there are only two grains, which recovers Equation (5.16). In general, there are only two order parameters that are nonzero across a grain boundary away from triple junctions, and therefore this result applies to all grain boundaries away from triple junctions; even though the expression appears to be of high order, in practice, it behaves well numerically due to this cancellation. Equation (5.17) is combined with Equations (5.5) and (5.6) to describe the evolution of each η_i. For the evolution of $\rho(\vec{r},t)$, we take the derivative of Equation (5.7) with respect to time and obtain

$$\frac{\partial \rho}{\partial t} = \frac{\left[\sum_{i=1}^{N}\left(2\eta_i\frac{\partial \eta_i}{\partial t}\rho_i\right)\right](\sum_{i=1}^{N}\eta_i^2) - \left[\sum_{i=1}^{N}\left(2\eta_i\frac{\partial \eta_i}{\partial t}\right)\right][\sum_{i=1}^{N}(\eta_i^2\rho_i)]}{[\sum_{i=1}^{N}\eta_i^2]^2}. \tag{5.18}$$

Equations (5.5) and (5.18) together provide the set of governing equations for the order parameters and the dislocation density field in our model.

Nondimensionalization and numerical solution of the phase-field equations

The following equations [170,171] relate the phase-field model parameters to physical parameters:

$$\kappa = \frac{3}{4}\gamma_{gb}l_{gb}, \tag{5.19}$$

$$L = \frac{4\mu_{gb}}{3l_{gb}}, \tag{5.20}$$

$$W = \frac{6\gamma_{gb}}{l_{gb}}, \tag{5.21}$$

where γ_{gb} is the grain boundary energy, μ_{gb} is the grain boundary mobility, and l_{gb} is the grain boundary width of the diffuse interface. The average grain radius estimated from the experiment was chosen as the unit length for the phase field simulation, l_0, and the grain boundary width was chosen as $l_{gb} = l_0/10$. We nondimensionalize the phase-field variables as follows:

$$\kappa^* = \frac{\kappa}{m_0 l_0^2} = \frac{1}{8}\left(\frac{l_{gb}}{l_0}\right)^2, \tag{5.22}$$

$$L^* = \frac{L}{L} = 1, \tag{5.23}$$

$$m_0^* = \frac{m_0}{m_0} = 1, \tag{5.24}$$

$$\boldsymbol{r}^* = \frac{\boldsymbol{r}}{l_0}, \tag{5.25}$$

$$t^* = tLm_0 = t\left(\frac{8\mu_{gb}\gamma_{gb}}{l_{gb}^2}\right), \tag{5.26}$$

$$\rho^* = \frac{\rho}{\bar{\rho}}, \tag{5.27}$$

$$\bar{f}_{stored}^* = \frac{\bar{f}_{stored}}{m_0} = \bar{f}_{stored}\left(\frac{l_{gb}}{6\gamma_{gb}}\right) = \left(\frac{1}{2}Gb^2\bar{\rho}\right)\left(\frac{l_{gb}}{6\gamma_{gb}}\right), \tag{5.28}$$

$$f_{stored}^* = \frac{f_{stored}}{m_0} = \left(\frac{1}{2}Gb^2\rho\right)\left(\frac{l_{gb}}{6\gamma_{gb}}\right) = \left(\frac{1}{2}Gb^2\bar{\rho}\right)\rho^*\left(\frac{l_{gb}}{6\gamma_{gb}}\right) = \bar{f}_{stored}^* \cdot \rho^*. \tag{5.29}$$

The superscript (*) indicates the nondimensionalized variables. The parameters used in the simulations are summarized in Table 5.1.

Table 5.1. Physical and numerical parameter values used in the simulations. Reproduced with permission [24]. Copyright 2021, American Physical Society.

Parameters	**Values employed in the model**
Grain boundary energy, γ_{gb}	0.595 J/m^2 [78]
Shear modulus, G	28.4 GPa [172]
Magnitude of Burger's vector, b	0.255 nm [78]
Initial average radius of grains, l_0	128 μm
Grain boundary width, l_{gb}	12.8 μm
Energy density coefficient, m_0	2.79×10^5 J/m^3
Average dislocation density, $\bar{\rho}$	1.25×10^{13} m^{-2}
Average stored energy, $\bar{f}^*_{stored}$	0.0414
Grid spacing, $\Delta x^* = \Delta x/l_0$	0.025
Time step, $\Delta t^* = \Delta t(Lm_0)$	0.01 (with stored energy term) 0.1 (without stored energy term)
Number of grid points along x and y directions, $N_x = N_y$	716

The phase-field equations were solved numerically employing the finite difference method with a uniform mesh in space and the forward Euler scheme for time integration. The time step, Δt^*, and grid spacing, Δx^*, used in the simulation are reported along with other parameters in Table 5.1. The value of l_{gb} employed in the model (Table 5.1) is much greater than the physical width of a typical grain boundary. However, mathematical asymptotic analyses [173,174], as well as numerical convergence studies [175-177], have shown that the phase field model can accurately simulate microstructural evolution as long as the interfacial thickness is sufficiently smaller than the characteristic length scale of microstructural features (*e.g.*, the grain size in this case). In this

work, we ensure the accuracy of the prediction by selecting the interfacial thickness to be 1/20 of the initial average diameter.

5.2.3 Initial conditions

To generate the initial conditions for the grain growth simulations, we first placed 80 seeds of size $(7\Delta x)^2$ within which η_i is set to 1 at randomly distributed locations, with all η_i set to zero otherwise. For the simulation with stored energy, the dislocation density values were randomly assigned from a normal distribution with mean of $1.21 \times 10^{13}\,\mathrm{m}^{-2}$ and standard deviation of $3.8 \times 10^{12}\,\mathrm{m}^{-2}$. However, some of these values were assigned to specific grains in order to promote regions featuring observable grain displacement (*e.g.*, sets of three contiguous grains aligned with ascending dislocation density values). This choice was made because such arrangements would naturally occur in a randomly selected case but may be too rare to occur in an 80-grain system with random assignment of dislocation densities. However, we note that the grain exhibiting the greatest displacement in the simulation was in fact not in one of the regions where this adjustment was made. These seeds were then evolved *via* Allen-Cahn dynamics without stored energy for a time $t^* = 200$. The time, t^*, was then reset to zero for the grain growth simulations with stored energy. For this second stage, the dislocation density, $\rho(\vec{r}, t)$, was initialized using Equation (5.7).

5.2.4 Identification of translating grains

To identify the grains with large translation in the phase-field simulations, we examine the degree of overlap between the regions occupied by the grain at the initial and final states. To quantify this, we define the degree of overlap, χ, as

$$\chi = \frac{A_{\mathrm{overlap}}}{\min\left(A_0, A_f\right)}, \tag{5.30}$$

where A_0 and A_f are the areas of the regions occupied by a grain before and after evolution, respectively, and A_{overlap} is the area of the region overlap, calculated by

$$A_{\text{overlap}} = \int \eta_i(t=0)\,\eta_i(t=t_f)\,d\vec{r}. \tag{5.31}$$

5.3 Simulation results and discussion

5.3.1 Microstructure evolution

We employ the phase-field model to simulate two scenarios of grain growth: with and without the effect of stored energy. The system is set up to initially contain 80 grains, as shown in Figure 5.2(a). For the simulation with stored energy, the dislocation density values were chosen randomly from a normal distribution with mean of $1.21 \times 10^{13}\text{m}^{-2}$ and standard deviation of $3.8 \times 10^{12}\text{m}^{-2}$ based on the experimental results from the S_1 state. The intermediate and final states are defined to be the states that contain 77 and 69 grains, respectively. Microstructure evolution that considers the stored energy is shown in Figure 5.2(b) and (c). For comparison, the grain growth simulation result without the contribution of stored energy is presented in Figure 5.2(d) and (e), in which the same set of colors is used to indicate different grains. Even though capillary-driven grain growth occurs in both cases, for the stored-energy-driven case, it can be observed that the grain boundary motion is primarily driven by the differences in the stored strain energy between neighboring grains, leading to grain boundary migration toward regions with lower dislocation density. A grain with a medium value of dislocation density may grow into a neighboring grain with higher value and at the same time be consumed by another neighboring grain with low value on the opposite side; the net result is a large-scale translation of the grain. Two examples are highlighted by the grains marked by A and B in Figure 5.2(a) and (c), whose positions of grain boundaries at $t^* = 0$, 250, and 500 are indicated in blue, green and red, shown

in Figure 5.2(f). The translation of the grains is evidenced by the small degree of overlap between the initial and final regions. Moreover, while the small computational domain size does not permit a quantitative analysis, the simulation demonstrates that stored-energy-driven grain growth results in a grain size distribution having extreme values (Figure 5.3(a), where more small and large grains emerge as compared to the capillary-driven grain growth shown in Figure 5.3(b)). The stored-energy-driven grain growth appears to be leading to a grain microstructure with a bimodal distribution, which is one of the classic signatures of abnormal grain growth [15,178].

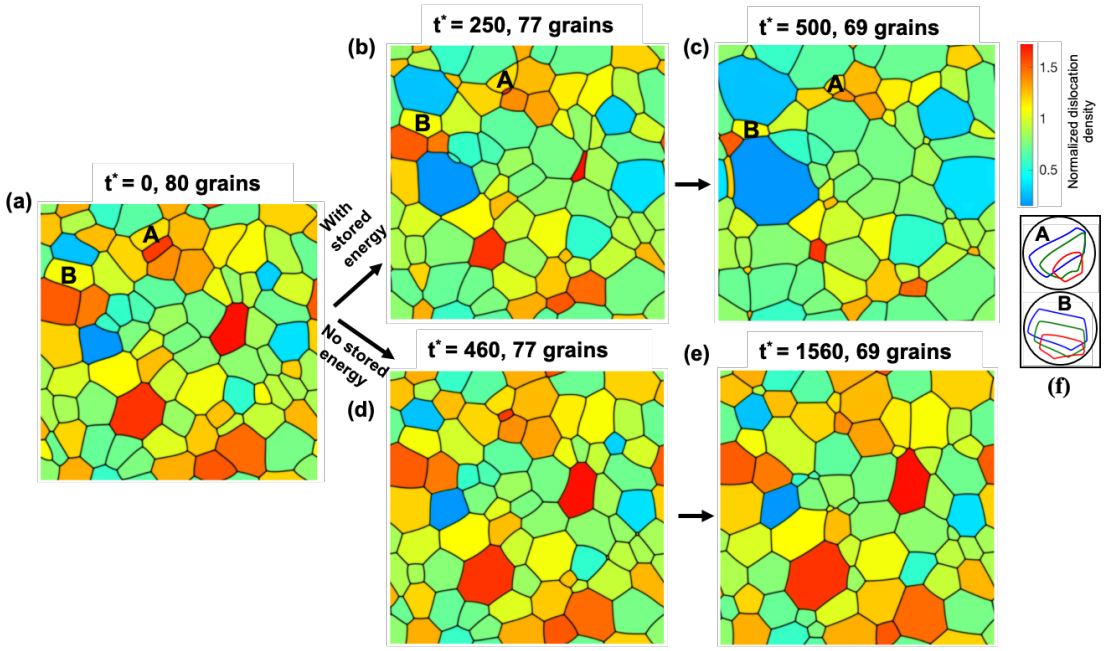

Figure 5.2. Phase-field simulations of grain growth. (a) Initial arrangements of the grains. (b) Intermediate state with 77 grains and (c) final state with 69 grains (with a stored energy term). (d) Intermediate state with 77 grains and (e) final state with 69 grains (without stored energy term). (f) Translations of grains A and B. Blue, green, and red outlines indicate the positions of GBs at time $t^* = 0$, 250, and 500, respectively, of the two grains. Dislocation density shown in the figures is normalized with respect to the mean (1.25×10^{13} m^{-2}) of the dislocation densities of the grains in the initial condition. Color indicates the normalized dislocation density where the stored energy is considered (a – c) and indicates different grains otherwise (d, e). Reproduced with permission [24]. Copyright 2021, American Physical Society.

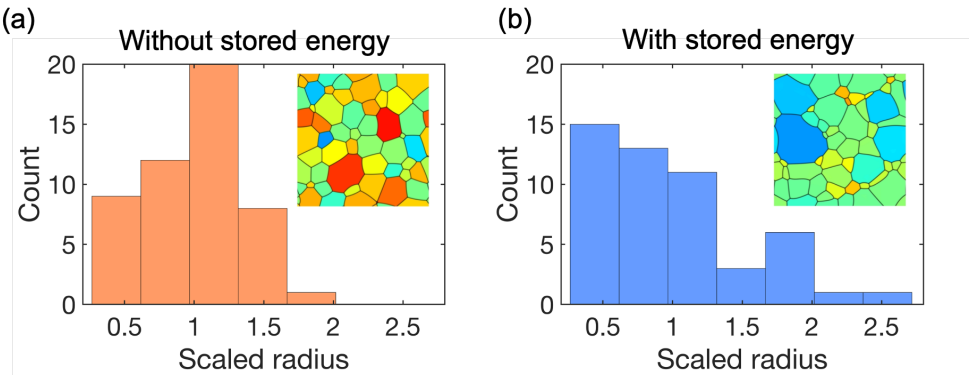

Figure 5.3. Grain size distributions for the microstructure with 50 remaining grains for the simulations (a) with and (b) without the stored energy. The corresponding microstructure used for generating the histogram is shown as an inset. The scaled radius is calculated based on the area of the 2D grain, assuming a circular geometry and divided by the average radius of the specific system. The count was not normalized with the number of grains because of the small statistics and because both cases have the same number of grains. Reproduced with permission [24]. Copyright 2021, American Physical Society.

5.3.2 Translation of grain centers

To quantitatively compare the grain translation in the two cases, we compute the magnitude of the displacement of each grain's center of mass as a function of time. We plot the average displacement of the center-of-mass positions of the grains at different time, as shown in Figure 5.4. The grains that disappear during the evolution are included in this average using their displacement at their final value. The unit length for the displacement is assumed to be 128 μm, the average grain radius estimated from the experiment, and t^* is a nondimensionalized time. The time axis of the capillary-driven case is rescaled so that the initial slopes (the rate of change of the average displacement) of two curves are visually matched. Although the magnitudes of the average displacement of two cases are comparable at the start of the simulation, the average displacement in the strain-energy-driven simulation maintains a higher rate than in the capillary-driven simulation. The latter is driven solely by the reduction of the system's total grain boundary energy (that scales as $t^{-1/2}$, see Chapter 2 Section 2.2.1) [72].

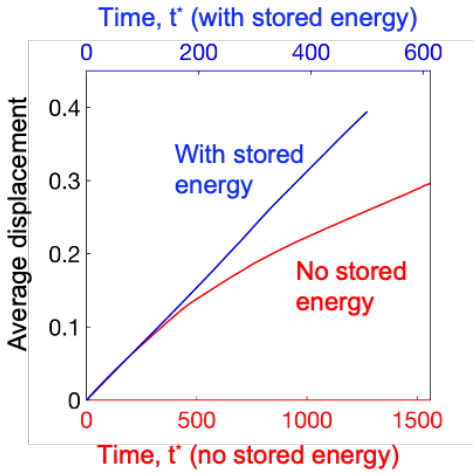

Figure 5.4. Average displacement of the grains' center of mass. The time axis of the capillary-driven case is rescaled so that two curves visually have the same initial slope. Reproduced with permission [24]. Copyright 2021, American Physical Society.

5.3.3 Comparison of driving forces in stored-energy-driven grain growth

To confirm that the driving force due to stored energy difference dominates over the capillary force for the simulation, we calculated and compared them in the stored-energy-driven grain growth simulation. The capillary pressure, $P_{\text{capillary}}$, of a domain is estimated using [179,180]

$$P_{\text{capillary}} = \gamma \Delta H, \tag{5.32}$$

where γ is the grain boundary energy (see Table 5.1), and ΔH is the variation of the curvature of grain boundaries across the system and is defined as

$$\Delta H = 2S_H = 2\sqrt{\frac{1}{A}\int_{\Omega}\left[\left(\sum_{i=1}^{N} H_i \eta_i(\vec{r})\right) - \mu_H\right]^2 dA}, \tag{5.33}$$

where H_i is the curvature of grain i and $\eta_i(\vec{r})$ is the corresponding order parameter, dA is the area element in the simulation domain Ω, $\mu_H = \frac{1}{A}\int_{\Omega}[\sum_{i=1}^{N} H_i \eta_i(\vec{r})]dA$ is the area-weighted average of the curvature and S_H is the area-weighted standard deviation of the curvature. Note that, since we

conduct the simulations here in two-dimensions, the averaging and weighting are performed based on the area; for three-dimensional simulations, they should be done based on the volume. The curvature of grain *i* is estimated using the reciprocal of the equivalent radius, r_i, of the grain:

$$H_i = \frac{1}{r_i} = \sqrt{\frac{\pi}{A_i}}, \tag{5.34}$$

where $A_i = \int_\Omega \eta_i(\vec{r})d\vec{r}$ is the area of grain. The pressure due to stored energy is calculated using

$$P_{stored} = \frac{1}{2} G b^2 \Delta\rho, \tag{5.35}$$

where G and b are the shear modulus and the magnitude of Burger's vector (see Table 5.1), respectively; $\Delta\rho$ indicates the area-weighted variation of the dislocation density and is defined as

$$\Delta\rho = 2S_\rho = 2\sqrt{\frac{1}{A}\int_\Omega \left(\rho(\vec{r}) - \mu_\rho\right)^2 dA}, \tag{5.36}$$

where $\mu_\rho = \frac{1}{A}\int_\Omega \rho(\vec{r})dA$ and S_ρ are the area-weighted mean and standard deviation of the dislocation density over the computational domain, respectively. Again, it is weighted against the area since we perform two-dimensional simulations; for 3D simulations, it should be weighted against the volume. The resulting pressures as a function of time are shown in Figure 5.5. It can be observed from the figure that the driving force due to stored energy is larger than the capillary force for most of the simulation time, indicating that the simulation considering stored energy is primarily driven by the stored energy during most of the evolution simulated. The driving force from the stored energy reduces with time and eventually becomes comparable to the capillary pressure, which explains why cyclic heat treatment is necessary in driving abnormal grain growth. The phase field model developed herein will offer an understanding of how the stored-energy driving force evolves with time and how to optimize such a process to achieve polycrystalline

microstructures with exceptionally large grains, given the rate of dislocation formation during non-isothermal heat treatment.

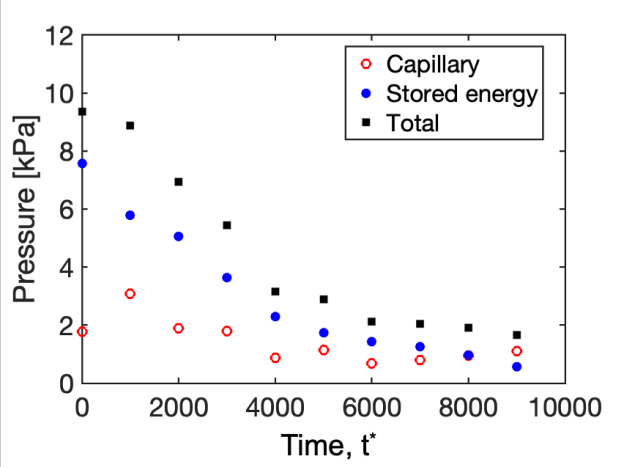

Figure 5.5. Pressures due to stored energy (blue filled circle) and capillarity (red open circle) in stored-energy-driven grain growth. The sum of two pressures is indicated by black squares. Reproduced with permission [24]. Copyright 2021, American Physical Society.

5.4 Conclusion

In this chapter, we discussed the macroscopic translation of grain centers observed in the experiment and proposed that such translation occurs arising from an additional driving force due to the stored energy during the cyclic heat treatment of polycrystalline alloys. To verify this hypothesis, we developed a phase-field model to simulate two scenarios of microstructure evolution, one considering only the capillary driving force, and the other considering an additional driving force due to the stored energy. Notable grain translation was only observed in the latter simulation that takes stored energy into account. The grain translation was found to be the net result of the grains with a medium value of dislocation density consuming their neighboring grains with a large dislocation density and at the same time being consumed by the other neighboring grains with a small dislocation density. Additionally, we quantitatively compared the magnitude of translation of grain centers for two scenarios as a function of time and found that the stored-

energy-driven simulation maintains a higher rate of average displacement. Moreover, we found that the driving force due to stored energy progressively decreased and finally became comparable to the capillary driving force, which implies the necessity for cyclic heat treatment to continuously induce abnormal grain growth.

Chapter 6 Phase-Field Modeling of Stored-Energy-Driven Grain Growth with Intra-Granular Dislocation Densities Variation

6.1 Introduction

As discussed in Chapter 1 Section 1.3, non-isothermal annealing of an alloy could introduce non-uniform dislocations within its microstructure, which provides a driving force for grains with a lower dislocation density to consume grains with a higher dislocation density. In this chapter,[*] we extend the phase-field model discussed in Chapter 5 to allow for spatially varying dislocation density within each grain during microstructure evolution. In Section 6.2, we demonstrate how synchrotron high-energy X-ray diffraction microscopy data of a sample undergoing cyclic heat treatment can inform this model. In Section 6.3, we detail the model formulation that does not require that each grain has a uniform dislocation density. In Section 6.4, we present an approach to distribute multiple grains to an order parameter, which reduces the computational cost. In Section 6.5, we demonstrate that the proposed phase-field model yields results that closely resemble the experimental data, and then we apply the model to examine the effect of cyclic heat treatment on the microstructure evolution.

6.2 Real-time experimental study of microstructure evolution in Cu-Al-Mn

Ashwin J. Shahani's group performed a cycle of heat treatment on a cylindrical $Cu_{71.6}Al_{17}Mn_{11.4}$ alloy, which is processed following Refs. [23,78]. High-energy X-ray diffraction

[*] Adapted from G. Huang, Z. Croft, M. Chlupsa, A. Mensah, D. Montiel, A. J. Shahani, and K. Thornton, "Phase-Field Modeling of Stored-Energy-Driven Grain Growth," In preparation.

microscopy (HEDM) experiments were conducted on this material at the 1-ID beamline of the Advanced Photon Source at Argonne National Laboratory, using a new infrared furnace described in Ref. [24]. The cylindrical samples were vertically mounted on the rotation stage and rotated about an axis parallel to gravity, which is orthogonal to the plane defined by the line focused beam. In a near-field geometry [181], the detector captured 720 diffraction images (0.25° intervals spanning 180°) for each quasi-2D "slice" of the sample, where slices were separated by 7 μm in the first two states and 14 μm in the third, along the axis of rotation. Data were collected at sample-to-detector distances of 10 mm and 12 mm. The schedule for dynamic annealing is shown in Figure 6.1.

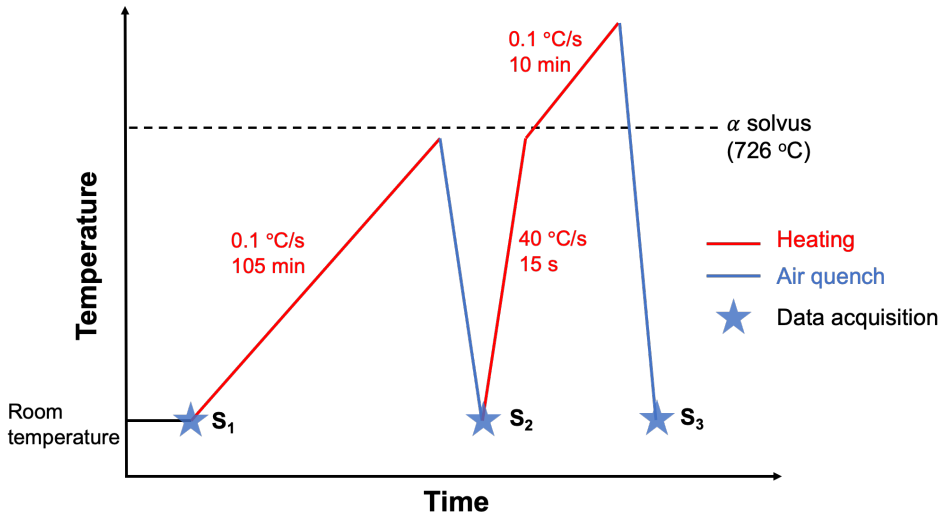

Figure 6.1. Schematic showing dynamic annealing schedule for the interrupted *in-situ* HEDM experiment.

The first acquisition (S_1) was performed at room temperature before any annealing was conducted. The diffraction patterns from *in-situ* far-field HEDM were used to monitor in real time the microstructure evolution upon annealing, and the sample was air quenched when the FCC-α (second-phase particles) spot intensities stopped increasing. The second acquisition (S_2) was performed on this particle-rich state. The annealing process was then resumed with a fast ramp up

to the previous temperature followed by a slower ramp towards and exceeding the FCC-α solvus temperature. After the FCC-α rings disappeared in the far-field HEDM images, the sample was air quenched. The third acquisition (S_3) was performed on the particle-depleted state. The set of three acquisitions ($S_1 \rightarrow S_2 \rightarrow S_3$) represents one cycle of dynamic annealing. After the experiment, the diffraction images were reconstructed in 2D via the forward model [182,183] based HEXOMAP [24] and analyzed via PolyProc [184].

To demonstrate the integrated experimental-computational workflow, we utilize the microstructure and dislocation density obtained in the experiments to inform our phase-field model. While the simulation should ideally be done in three dimensions, in this work, we chose to conduct two-dimensional simulations, which are computationally efficient and sufficient for demonstrating the synergy. Even though it is not our primary focus, we find that simulation predictions match qualitatively with the experimentally observed evolution, as we discuss later.

We employ the grain and dislocation density maps measured at a two-dimensional slice of the sample at states S_1 and S_2, as shown in Figure 6.2. This particular slice is selected since it includes an apparently confined region (i.e., the outer boundaries of this region is nearly static throughout the experiment) that consists of several grains in the S_1 state, indicated by a black contour in Figure 6.2(a) (S_1) and (b) (S_2), reducing the cost of the simulations while allowing for a comparison between experiments and simulations. Additionally, it appears that only few new grains emerge from state S_1 to S_2 (by comparing Figure 6.2(a) and (b)), indicating that the microstructure evolution along the dimension perpendicular to the slice plane does not greatly affect the microstructure evolution within this slice. By comparing Figure 6.2(c) and (d), it is clear that the grain G_1 is consuming the surrounding grains and is the only grain that remains at state S_2. The dislocation density of the confined region at S_1 (see Figure 6.2(e)) is relatively uniform, which

is expected since the sample has not been dynamically annealed at S_1. As the sample is progressively heated from S_1 to S_2, the dislocations are formed within each grain with a different density, which could be attributed to the difference in the density of second-phase particles precipitated during the annealing. The difference in the dislocation density provides a driving force for the grains with a low dislocation density to consume those grains with a high dislocation density. Figure 6.2(f) shows the dislocation density of the confined region at state S_2. It can be observed that the dislocation density is higher within G_1's initial region, as compared to the surrounding, which indicates that the dislocation density at the region traversed by the grain boundary is reduced.

To examine the effect of cyclic heat treatment on the microstructure evolution, it is necessary to track the change of a grain size distribution over time, which requires a sufficiently large number of grains for meaningful statistics throughout the simulation. Since state S_1 contains a large number of grains and corresponds to the starting point of the heat treatment cycle in the experiment, we use the grain size distribution (see Figure 6.3(a)) in state S_1 to initialize a microstructure for the large-scale simulations. The grain size distributions for states S_2 and S_3 are shown in Figure 6.3(b) and (c), respectively. Given the fact that the average grain radius for the entire 3D volume increases by ~40% from state S_1 to S_3 in the experiment, we set this percentage of increase in the average grain radius as the stopping criteria for one simulation cycle of microstructure evolution.

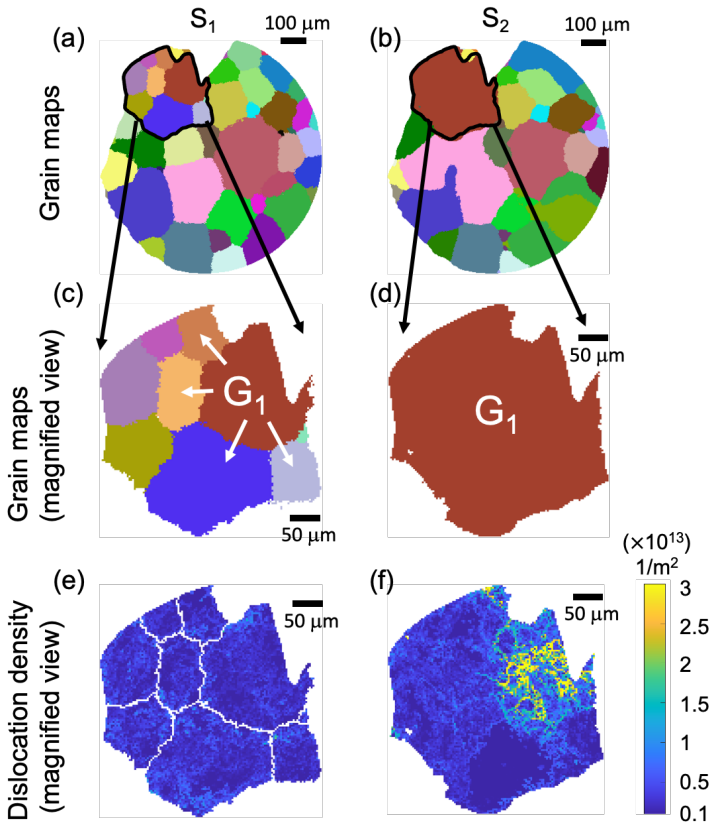

Figure 6.2. Grain and dislocation density maps for a selected slice of the sample, measured at state S_1 (left column) and S_2 (right column). (a) & (b): Grain maps at state S_1 and S_2, respectively. An apparently confined region is indicated by a black contour. Each grain is indicated by a unique, random color. The same color is assigned to the same grain appearing in both states. (c) & (d): Magnified view of the grain map for the confined region at state S_1 and S_2, respectively. Grain G_1 consumes the surrounding grains from state S_1 to S_2, respectively. (e) & (f): Dislocation density within the confined region at state S_1 and S_2, respectively.

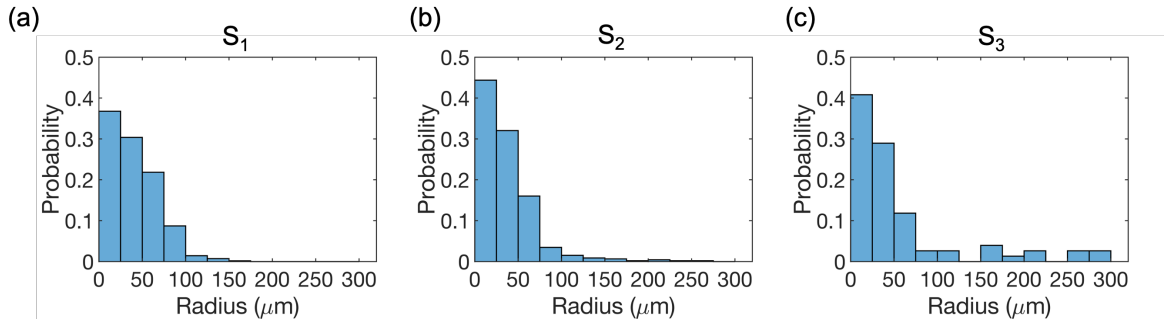

Figure 6.3. Grain size distribution for the entire volume of (a) state S_1, (b) state S_2, and (c) state S_3.

6.3 Phase-field model with intra-granular dislocation densities variation

6.3.1 Overview

We extend the phase-field model for stored-energy-driven grain growth discussed in Chapter 5 in the following aspects. First, the previous model assumes that each grain possesses a uniform dislocation density. However, experimental data show that dislocation density is inhomogeneous even within an individual grain (see Figure 6.2(f)). To account for the spatial variation of dislocation density into the dynamics of grain growth, we introduce an *individual dislocation density field*, ρ_i, for each grain i, which stores not only the initial dislocation density value for that grain but also what the dislocation density value would be if the grain boundary of the grain reaches that position.

Second, in the previous model, the region traversed by a grain boundary is assumed to inherit the dislocation density value of the grain that grows into this region. However, the experiments described above showed that the region traversed by a grain boundary appears to have a reduced dislocation density, as discussed in Section 6.2. While the exact mechanism by which this reduction occurs is yet to be investigated, there are multiple mechanisms that would lead to an elimination of dislocations as a grain boundary migrates, including annihilation of dislocation pairs and absorption of dislocations onto grain boundaries [185,186]. The enhancement of the rate by which these processes occur (vs. recovery in the bulk, which appears to be slow on the time scale of the experiment) is expected from the fact that grain boundary migration requires atomic rearrangements and consequently changes the strain fields. Below, we derive a model for dislocation density evolution that accounts for such a process, which is used to define ρ_i.

6.3.2 Model formulation

Mathematically, it is reasonable to assume that the dislocation is reduced at the rate, $\frac{d\rho}{dx}$, proportional to how many dislocations exist at the grain boundary as the grain boundary migrates:

$$\frac{d\rho}{dx} = -\frac{\rho}{l_e}. \tag{6.1}$$

This differential equation can be solved analytically, yielding

$$\rho = \rho_{gb} \exp\left(-\frac{x}{l_e}\right), \tag{6.2}$$

where ρ_{gb} is the dislocation density just behind the initial grain boundary, x is the distance traversed by the grain boundary, and the constant l_e provides the length scale at which the dislocation density decays by a factor of e in the wake of grain boundary migration. We assume that grain boundaries migrate in their normal direction, which is a simplifying assumption, and therefore the value of x can be determined from a signed distance function using the level-set method discussed in Chapter 2 Section 2.8.

We now detail how this model is implemented. In this section, we denote the grain with index i as G_i. For each grain G_i, we employ a time- and position-dependent order parameter field $\eta_i(\boldsymbol{r}, t)$ to track its evolution. The value of $\eta_i(\boldsymbol{r}, t)$ is 1 within the grain, 0 outside the grain, and varies smoothly from 1 to 0 across its interface. In this work, we omit the effect of recovery, and therefore the dislocation density at a certain position, $\boldsymbol{r}$, retains its initial value until the grain boundary from another grain reaches this point, at which time a reduced dislocation density is assigned according to Equation (6.2). Since we do not allow dislocation density to evolve otherwise, this model introduces a discontinuity in the gradient of dislocation density; if we consider other mechanisms such as recovery, such a discontinuity would be smoothed. We precompute the reduced dislocation density for each grain at the positions outside their initial grain

boundary and store these values into their individual dislocation density field $\rho_i(\boldsymbol{r})$, along with their initial dislocation density values internal to the grain. Specifically, $\rho_i(\boldsymbol{r})$ is defined as

$$\rho_i(\boldsymbol{r}) = \begin{cases} \rho_{0,i}(\boldsymbol{r}), & \text{within Grain } G_i, \\ \max\left(\rho_{\text{base}}, \rho_{gb,i} \exp\left(-\dfrac{|d_i(\boldsymbol{r})|}{l_e}\right)\right), & \text{otherwise.} \end{cases} \tag{6.3}$$

Here, $\rho_{0,i}(\boldsymbol{r})$ is the initial dislocation density within Grain G_i, $\rho_{gb,i}$ is the dislocation density just behind G_i's initial boundary, and $d_i(\boldsymbol{r})$ is the signed distance between the point $\boldsymbol{r}$ and the nearest point to the G_i's initial boundary; note that the sign is taken to be positive within the grain and negative outside, and therefore $d_i(\boldsymbol{r}) < 0$ in Equation (6.3). The term ρ_{base} in Equation (6.3) is the *baseline dislocation density*, i.e., the lower bound for the dislocation density measured in the experiment, that remains even after a long period of annealing. In general, $\rho_{gb,i}$ is a spatially varying quantity, but we here assume it to be a constant for each grain, as discussed in Section 6.3.3. We found that simulations with l_e = 20 μm yield results that closely resemble the experimental observations, and thus we employ this value throughout this work. We estimate the baseline dislocation density ρ_{base} by taking the average of the dislocation density at state S_2 for the regions outside Grain G_1's initial position (indicated in Figure 6.2(c)). While this may slightly overestimate the base value because it may include some enhanced dislocation density near the initial grain boundaries, we deemed this assumption to be reasonable given the statistical variation and uncertainties in the measurements. The value of ρ_{base} is determined to be 3×10^{12} m^{-2}, which is on the same order of magnitude as dislocation densities in well-annealed metals [187]. Further details are provided in Section 6.3.3.

It is necessary to note that the values of $\rho_i(\boldsymbol{r})$ outside the boundaries of the initial grains should not be considered as physical values, other than the fact that it sets the value of the dislocation density if the grain boundary of G_i sweeps the point. Rather, at any point in time, the

actual dislocation density is given by constructing it from $\{\rho_i(\boldsymbol{r})\}$, along with the set of order parameters $\{\eta_i(\boldsymbol{r},t)\}$, using the following interpolation function:

$$\rho(\boldsymbol{r},t) = \frac{\sum_i^N \eta_i^2(\boldsymbol{r},t)\rho_i(\boldsymbol{r})}{\sum_{i=1}^N \eta_i^2(\boldsymbol{r},t)}. \tag{6.4}$$

This formula is identical to those used in Refs. [168-170] and in Chapter 5, except for in these previous works, ρ_i was a constant associated with the i^{th} grain, and therefore these models could not treat intra-granular inhomogeneity nor a decay in the dislocation density as the grain boundaries migrate.

To facilitate the understanding of dislocation density evolution based on the above formulation, we provide schematics in Figure 6.4 showing the change in the dislocation density field as a grain G_i consumes its surrounding grains. The grains that are adjacent to G_i are omitted in Figure 6.4(a) for clarity. Grain G_i, indicated in blue, initially possesses dislocation density $\rho_{gb,i}$ at its grain boundary. As it progressively consumes its surrounding grains and reaches the point A at time t_1, the dislocation density at point A reduces to a value given by $\rho_{gb,i}\exp\left(-\frac{|d_i(A)|}{l_e}\right)$. As it continues to grow, it reduces to the baseline dislocation density ρ_{base}, which is the lower bound of the dislocation density. Thus, as it reaches point B at time t_2, the dislocation density at point B remains at ρ_{base}.

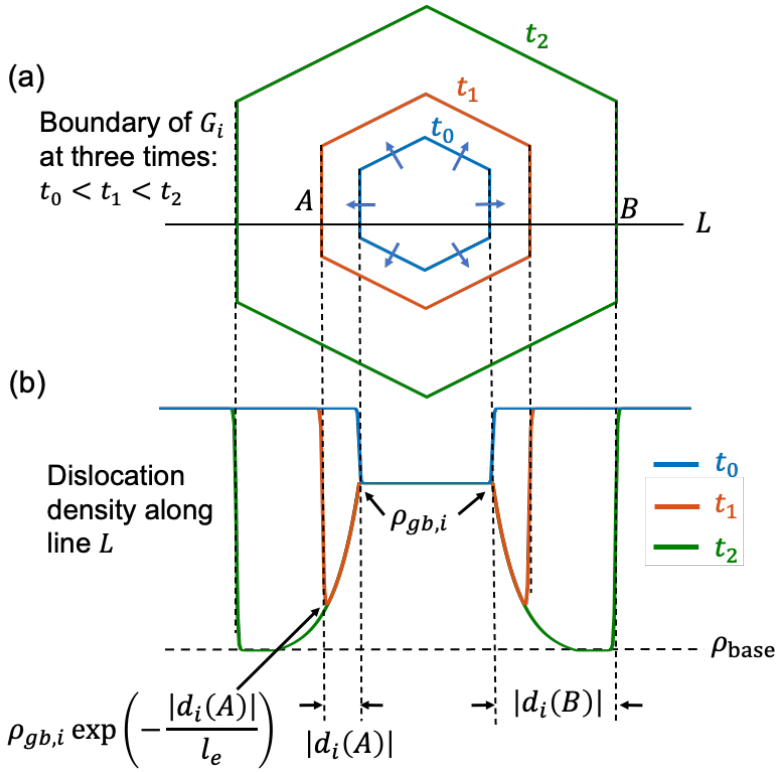

Figure 6.4. Schematics showing the evolution of a dislocation density field at three times, as a grain G_i consumes its surrounding grains, assuming exponential decay of dislocation densities. (a) The boundaries of a growing grain G_i at three times, $t_0 < t_1 < t_2$, which are indicated in blue, red, and green, respectively. The grains that are adjacent to G_i are omitted in this plot for clarity. (b) The dislocation density field along the line L in (a) at the three times. Note that $d_i < 0$.

The free energy functional and governing equation (i.e., Equation (5.1) – (5.4) and Equation (5.5), respectively) discussed in Chapter 5 are employed again for the model in this chapter. Substituting Equation (5.1) – (5.4) into Equation (5.5) yields

$$\frac{\partial \eta_i}{\partial t} = -L\left[m_0\left(-\eta_i + \eta_i^3 + 2\alpha\eta_i \sum_{\substack{j=1 \\ j\neq i}}^{N} \eta_j^2\right) - \kappa\nabla^2\eta_i + Gb^2 \frac{\eta_i}{\sum_{j=1}^{N}\eta_j^2}(\rho_i(\boldsymbol{r}) - \rho)\right]. \tag{6.5}$$

Here, $\rho_i(\boldsymbol{r})$ is no longer a constant and contains the individual dislocation density defined by Equation (6.3). The nondimensionalization scheme discussed in Chapter 5 Section 5.2.2 is

employed to convert dimensional quantities to dimensionless values using the scaling length of 40 μm, which is on the order of the radius of a typical grain in our simulations.

6.3.3 Methods for setting up initial conditions

The initial condition for each simulation is composed of two parts: an initial microstructure described by a set of order parameters $\{\eta_i(\boldsymbol{r}, t = 0)\}$, and a set of corresponding individual dislocation density field, $\{\rho_i(\boldsymbol{r})\}$. In this work, we perform two sets of two-dimensional (2D) simulations. The first set of simulation directly imports a grain map from the experimental cross-sectional data containing a relatively small number of grains, while the second set of simulations leverages the grain size distribution (GSD) from the experimental data to initialize a microstructure that contains a large number of grains.

Initialization of order parameters

First, the microstructure at state S_1 measured in the experiment is processed to produce a set of binary fields $\{n_i(\boldsymbol{r})\}$. For the first set of simulation, the 2D grain map, $\Omega(\boldsymbol{r})$, of the confined region at S_1, which marks the region of each grain with a unique but consecutive integer, is used to initialize a set of $n_i(\boldsymbol{r})$ fields according to

$$n_i(\boldsymbol{r}) = \begin{cases} 1, & \text{if } \Omega(\boldsymbol{r}) = i, \\ 0, & \text{otherwise.} \end{cases} \tag{6.6}$$

For the second set of simulations, the GSD calculated from the entire 3D volume of the sample at the S_1 state is converted to a 2D GSD by implementing an established method in stereology [188,189] in a reversed manner, which is then employed to guide the construction of the initial microstructure. Specifically, the following procedures are implemented:

1. The 3D GSD (N_{3D}, the number of grains as a function of radius for a given bin size) is calculated based on the radii of all the grains in the S_1 state. Specifically, the range that encompasses all the

grain radii is uniformly divided into N_r equally sized intervals. The i^{th} interval is given by $\left[R_{i,\text{lower}}, R_{i,\text{upper}}\right] = [(i-1)\Delta R, i\Delta R]$, where ΔR is the size of the interval in 3D radius. The number of grains that fall within each interval is counted.

2. These numbers are divided by the volume of the sample, V, to obtain the number of grains per unit volume, $N_V(i)$, for each interval i.

3. A sectioning plane is more likely to cut through a larger 3D grain. The total number of sectioning planes obtained from the 3D grains falling within the i^{th} interval, $N_A(i)$, per unit area, is given by [189]:

$$N_A(i) = 2N_V(i)R_{i,\text{upper}}. \tag{6.7}$$

4. The 2D radii of the 3D grains having i^{th} radius range due to cross sectioning varies from 0 to $R_{i,\text{upper}}$. The probability, p_{ij}, that such a radius falls within the j^{th} interval can be calculated based on geometry by [188]

$$p_{ij} = \begin{cases} \frac{1}{R_{i,\text{upper}}}\left(\sqrt{R_{i,\text{upper}}^2 - R_{j,\text{lower}}^2} - \sqrt{R_{i,\text{upper}}^2 - R_{j,\text{upper}}^2}\right), & R_{j,\text{upper}} \le R_{i,\text{upper}}, \\ 0, & \text{otherwise.} \end{cases} \tag{6.8}$$

5. Given the fact that the sections within the j^{th} interval could be obtained from the 3D grains within equal or larger size intervals, the total number of sections per unit area, $N_{2D}(j)$, with radii within interval j, is given by

$$N_{2D}(j) = \sum_{i \ge j}^{N_r} N_A(i)p_{ij}. \tag{6.9}$$

6. The values of $N_{2D}(j)$ is then normalized by its sum to obtain a 2D GSD, $\widetilde{N}_{2D}(j)$.

The 2D GSD is then used to inform the selection of K seeds for the grains. To do so, we first convert $\widetilde{N}_{2D}(j)$ to a cumulative distribution function (CDF). We denote R_i^T to be the radius at

which CDF is equal to $\frac{i}{K}$. The position of the seed, $r_{seed,i}$, for each G_i is initialized with a random value, and the radius of each grain, R_i^P, is calculated based on the area given by the Voronoi tessellation of the seed locations. The resulting CDF (see the blue curve in Figure 6.5) is not typically close to the target CDF (see the red curve in Figure 6.5). To modify the seed locations such that the resulting CDF is closer to the target, $r_{seed,i}$ is iteratively updated by

$$\frac{dr_{seed,i}}{dt} = \sum_{j=1, j\neq i}^{N_c} (R_i^T - R_i^P) R_i^T \left(\frac{1}{d_{ij}^3} - \frac{2R_i^T}{d_{ij}^4} \right) d_{ij}. \tag{6.10}$$

Here, j is the index for grain G_i's N_c nearest grains and d_{ij} is the center-to-center distance between grain i and j. Equation (6.10) progressively adjusts the grain seed positions to reduce the difference between each pair of R_i^T and R_i^P. After the algorithm is applied, a set of seed positions $\{r_{seed,i}\}$ is generated, which gives rise to a set of estimated grain radii $\{R_i^P\}$ that approximately follows the target CDF (see the green curve in Figure 6.5). A set of binary fields $\{n_i(\boldsymbol{r})\}$ is then constructed from $\{r_{seed,i}\}$, using the method discussed in Section 6.4.

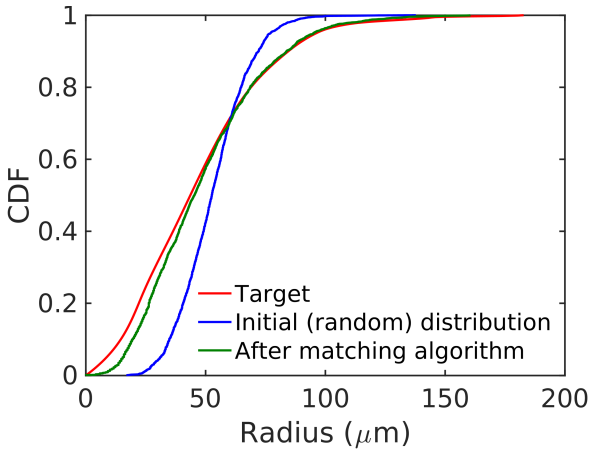

Figure 6.5. Cumulative distribution function (CDF) for the grain radii. The red line indicates the target CDF, the blue line indicates the CDF obtained from radii estimated based on the randomly selected grain seed positions, and the green line indicates the CDF obtained from the radii estimated based on the grain seed positions after the matching algorithm is applied, which is used in the simulation described in Section 6.5.2.

The set of the binary field $\{n_i(\boldsymbol{r})\}$ is evolved via Allen-Cahn dynamics without the stored-energy to obtain their smoothed order parameters, $\{\eta_i(\boldsymbol{r})\}$, which contain complete grain structures with diffuse interfaces. The parameters employed for this smoothing process for the small- and large-scale simulations are summarized in Table 6.1 and Table 6.2, respectively.

Table 6.1. Dimensionless parameters employed for the small-scale simulations to generate order parameters from binary fields.

Parameters	**Variable**	**Value**
Bulk energy coefficient	m_0^*	1
Gradient energy coefficient	κ^*	0.00125
Domain size	l^*	12
Grid spacing	$\Delta x^* = \Delta z^*$	0.025
Time step	Δt^*	0.1

Table 6.2. Dimensionless parameters employed for the large-scale simulations to generate order parameters from binary fields.

Parameters	**Variable**	**Value**
Bulk energy coefficient	m_0^*	1
Gradient energy coefficient	κ^*	9.57×10^{-4}
Domain size	l^*	69.43
Grid spacing	$\Delta x^* = \Delta z^*$	2.19×10^{-2}
Time step	Δt^*	0.1

Construction of individual dislocation density fields

As seen in Equation (6.3), the initial dislocation density $\rho_{0,i}(\boldsymbol{r})$ and the distance function $d_i(\boldsymbol{r})$ for each grain G_i are two required components to construct an individual dislocation density field $\rho_i(\boldsymbol{r})$. Although in reality a cycle of heat treatment involves continuous dislocation generation and microstructure evolution, we simplify this process in this work by injecting all the

generated dislocations, $\Delta\rho_i$, once at the beginning, which is added to the baseline value before the microstructure evolution is simulated. A more sophisticated approach that considers the dynamic generation of dislocations will be left for future work. Given the experimental observations that a majority of the second-phase particles are found on or near the grain boundaries and the fact that a small grain in two dimensions has a larger grain length per area (equivalent to area per unit volume in three dimensions) than a large grain, we propose that the density of the second-phase particles is higher in a small grain. Additionally, it is reported in Ref. [24] that the relationship between the grain-averaged dislocation density and the density of the second-phase particles can be roughly described by a positive linear correlation. We therefore postulate that the value of $\Delta\rho_i$ is inversely proportional to the radius, R_i, of grain G_i, given by the following formula:

$$\Delta\rho_i = \frac{k_\rho}{R_i}. \tag{6.11}$$

The value of k_ρ is estimated by substituting the known values of $\Delta\rho_1$ and R_1 for Grain G_1 within the confined region (see Figure 6.2) into Equation (6.11). The value of $\Delta\rho_1$ is estimated by subtracting the baseline dislocation density from the average dislocation density of G_1 at S_2 within its initial position at S_1. The value of R_1 is estimated based on G_1's area at S_1, assuming a circular shape of the grain. The value of k_ρ is then determined to be 8×10^8 m^{-1}.

When considering multiple cycles, each cycle must be initialized based on either the initial state of the sample or the state from the previous cycle. Hereafter in this section, we add the cycle number on the superscript of the dislocation density to indicate the value at each cycle. The individual dislocation density at positions initially within Grain G_i for the first cycle, $\rho_{0,i}^1(\boldsymbol{r})$, is set by adding $\Delta\rho_i$ to the baseline dislocation density ρ_{base}:

$$\rho_{0,i}^{1}(\boldsymbol{r}) = \Delta\rho_i + \rho_{\text{base}} = \frac{8 \times 10^8\ \text{m}^{-1}}{R_i} + 3 \times 10^{12}\ \text{m}^{-2}. \tag{6.12}$$

To set the individual dislocation density at positions initially outside of Grain G_i, we first apply the level-set method discussed in Chapter 2 Section 2.8 to obtain the distance function, $d_i(\boldsymbol{r})$, based on the order parameter $\eta_i(\boldsymbol{r})$. Since $\rho_{0,i}^{1}(\boldsymbol{r})$ is a constant for the first cycle, as shown in Equation (6.12), the individual dislocation density at the grain boundary, $\rho_{gb,i}^{1}$, is equal to this constant value given by

$$\rho_{gb,i}^{1} = \Delta\rho_i + \rho_{\text{base}} = \frac{8 \times 10^8\ \text{m}^{-1}}{R_i} + 3 \times 10^{12}\ \text{m}^{-2}. \tag{6.13}$$

Equation (6.3) is then employed to generate the individual dislocation density field $\rho_i^1(\boldsymbol{r})$ for the first cycle.

The value of the individual dislocation density at positions initially within G_i for the subsequent cycle C $(C > 1)$, $\rho_{0,i}^{C}(\boldsymbol{r})$, is set by adding $\Delta\rho_i$ to its individual dislocation density at the previous cycle, $\rho_i^{C-1}(\boldsymbol{r})$

$$\rho_{0,i}^{C}(\boldsymbol{r}) = \Delta\rho_i + \rho_i^{C-1}(\boldsymbol{r}) = \frac{8 \times 10^8\ \text{m}^{-1}}{R_i} + \rho_i^{C-1}(\boldsymbol{r}). \tag{6.14}$$

We assume that after each cycle of grain growth, the value of dislocation density at the boundary of each remaining grain is reduced to a value that is sufficiently close to the baseline dislocation density. Thus, for simplicity, the individual dislocation density at the grain boundary at the cycle $C(C > 1)$, $\rho_{gb,i}^{C}$, is set again using Equation (6.13). Then, Equation (6.3) is employed to generate the individual dislocation density field $\rho_i^C(\boldsymbol{r})$ for the subsequent cycle $(C > 1)$.

6.4 Assigning multiple grains to an order parameter

Although the implementation is simple when an order parameter is used to track one grain, the computation becomes expensive when the simulation involves a large number of grains. To enable large-scale simulations of microstructure evolution described in Section 6.3.3 in an efficient manner, a capability to track multiple grains with one order parameter, which reduces the total number of order parameters required for the simulations, is required. However, it is necessary to ensure that the grains tracked by the same order parameter do not overlap during the microstructure evolution to avoid grain coalescence (and, for our model, that the decaying individual dislocation density fields do not overlap, which would introduce numerical artifact). The grain remapping schemes [112,190,191] have been proposed in the literature for phase-field simulations of grain growth, which reassigns a grain to a different order parameter when the grain is too close to another grain tracked by the same order parameter. However, the standard remapping scheme cannot be applied without modifications because of the necessity to track the decay in the dislocation density outside of the grains. Therefore, we take a simpler approach in which grains are placed sufficiently apart initially and are not dynamically remapped.

Conceptually, we assign up to 9 grains to one order parameter to reduce the number of required order parameters (and thus the number of equations to be evolved). To do so, we examine the seed positions and assign each of the seeds to an order parameter index i, with the constraint that they are sufficiently distant from each other. This is accomplished by embedding a buffer zone between the grains assigned to the same order parameter. For each index i, we define the binary field $n_i(\boldsymbol{r})$, containing value 1 in the circular region of radius $3\Delta x$ centered at each of the seed positions assigned to order parameter index i. The detailed procedure is described below.

The entire simulation domain is first uniformly divided into 9 blocks (3 on each row and 3 on each column), as shown in Figure 6.6. Each block is assigned with one of the following block letter A through I. Each block is further separated into nine equally sized cells, which are indicated by the cell number 1 – 9. Each cell within the resulting 9×9 grid can therefore be uniquely indexed by the combination of a block letter and a cell number.

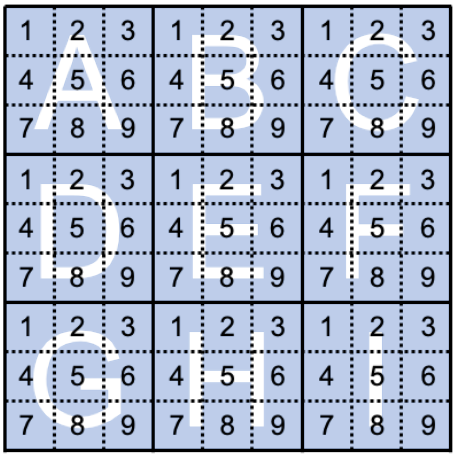

Figure 6.6. Division of the simulation domain for the assignment of order parameters.

The following pseudo code is then employed to initialize the binary fields, $n_i(\boldsymbol{r})$, that contains multiple grains for the large-scale simulations, along with their corresponding mask fields, $\chi_i(\boldsymbol{r})$, which are used for extracting individual grains and will be detailed later, based on the seed positions obtained in Section 6.3.3:

```
Inputs:
(1) a 9×9 grid,
(2) K (x,y) seeds within the grid,
(3) the radius for each seed, seed_radius
Outputs: N pairs of (n_i(r), χ_i(r))
Set the order parameter index, i, to 1
for cell_number in [1, 2, 3, 4, 5, 6, 7, 8, 9]
  while there is any unassigned (x,y) seeds in the cells marked with cell_number
    Initialize a pair of (n_i(r),χ_i(r)) and set them to 0 everywhere
    Set the grain index, j, to 1
    for block_letter in [A, B, C, D, E, F, G, H, I]
      current_cell = grid(block_letter, cell_number)
      if current_cell contains any unassigned (x,y) seed
        Randomly select an unassigned (x,y) seed within current_cell
        Assign 1 to n_i(r) at a circular region centered at (x,y) with seed_radius, assuming
              a periodic boundary condition
```

```
        Assign j to χ_i(r) within the 3×3 cells centered at current_cell, assuming a periodic
              boundary condition
        j = j + 1
      end if
    end for block_letter
    i = i + 1
  end while
end for cell_number
```

Once the set of $\{n_i(\boldsymbol{r},t)\}$ is obtained, the Allen-Cahn equation is used to obtain $\{\eta_i(\boldsymbol{r},t)\}$, as described in Section 6.3.3. As shown in the pseudo code, we additionally construct a mask field, $\chi_i(\boldsymbol{r})$ to enable efficient extraction of individual grains from the entire $\eta_i(\boldsymbol{r},t)$ field during pre- and post-processing. Each mask field $\chi_i(\boldsymbol{r})$ stores the index for the grains that occupy a region consisting of 3 by 3 cells centered at the cell containing the seed position of the grain. In this manner, we allocate a sufficiently large region where the j^{th} grain tracked by the i^{th} order parameter, G_i^j, may reside, but no other grains with the same order parameter could, throughout the simulation. The order parameter for Grain G_i^j, $\eta_i^j(\boldsymbol{r},t)$, can then be obtained using the following formula:

$$\eta_i^j(\boldsymbol{r},t) = \begin{cases} \eta_i(\boldsymbol{r},t), & \text{if } \chi_i(\boldsymbol{r}) = j, \\ 0, & \text{otherwise.} \end{cases} \tag{6.15}$$

It is worth noting that the level-set method is directly applied to the order parameter fields that contain multiple grains to generate the corresponding signed distance functions. In this case, the value of the distance function at each position indicates the distance between this position to the nearest grain boundary. These distance functions are then utilized to construct a set of individual dislocation density fields $\rho_i(\boldsymbol{r})$, each of which contains up to 9 individual dislocation density profiles. The value of $\rho_i(\boldsymbol{r})$ at each point outside of regions initially occupied by the grains indicates the dislocation density value it would take if the grain boundary initially closest to the point reaches that point.

6.5 Simulation results and discussion

6.5.1 Microstructure evolution within a confined region

In this section, we apply the phase-field model to study the evolution of microstructure and dislocation density within an confined region (see Figure 6.2(c) – (f)) observed in the experiment, as discussed in Section 6.2. We select 4 μm as the interfacial width, which is ~1/10 of the radius of a typical grain in our simulations and is sufficient to resolve the grains in the confined region. The order parameters are initialized using the method discussed in Section 6.3.3. Since the boundary of the confined region is not rectangular, we utilize a dummy order parameter, which is not evolved throughout the microstructure evolution, to describe the area surrounding the confined region. The individual dislocation densities are initialized using Equation (6.3), with $\rho_{0,i}(\boldsymbol{r})$ given by Equation (6.12) and $\rho_{gb,i}$ given by Equation (6.13). The dimensionless parameters employed for the simulation are summarized in Table 6.3.

Table 6.3. The dimensionless parameters employed in the simulation for microstructure evolution of the confined region.

Parameters	Variable	Value
Bulk energy coefficient	m_0^*	1
Gradient energy coefficient	κ^*	0.00125
Domain size	l^*	12
Grid spacing	$\Delta x^* = \Delta z^*$	0.025
Time step	Δt^*	0.05

The initial microstructure is shown in Figure 6.7(a). Each grain is assigned with a unique number from 1 – 8. The color indicates the dislocation density within the grains. As shown in Figure 6.7(b), Grain 2 is rapidly consumed by the Grain 3, 4, and 7. It is expected since Grain 2 possesses a higher dislocation density and a smaller size than the surrounding grains, leading to a

large combined driving force due to the capillarity and the stored energy. As microstructure evolution continues to proceed, Grain 3, 4, 5, and 6 are continuously consumed, as shown in Figure 6.7(c) and (d). It is worth noting that the traversed regions that are far away from the initial boundary of the growing grains, such as the left regions of Grain 1 and 8, have a nearly uniform deep blue color, implying the reduction of dislocation density to a baseline value. In addition, some of the grain boundaries, such as the one between Grain 1 and 8 in Figure 6.7(d), become curved during microstructure evolution. Such curved grains, often referred to as island grains or peninsula grains [192,193] have been reported in the samples that have undergone mechanical deformation and subsequent annealing leading to AGG. The simulation results thus indicate that such curved grains could also be induced by heat treatment alone without mechanical processing. Since Grain 8 (with radius ~92 μm) is slightly larger than Grain 1 (with radius ~90 μm), the assigned initial dislocation density for Grain 8 (~1.17×10^{13} m^{-2}) is lower than that for Grain 1 (~1.19×10^{13} m^{-2}). Consequently, Grain 8 eventually consumes Grain 1, as shown in Figure 6.7(e) and (f), which does not agree with the experimental observation that Grain 1 consumes Grain 8, as shown in Figure 6.2(c) and (d).

The disagreement could arise from a few potential reasons. First, the two-dimensional radius was used to determine the initial dislocation density for each grain. Although Grain 1 has a slightly smaller two-dimensional radius than Grain 8, it is possible that Grain 1 has a larger three-dimensional radius than Grain 8. Therefore, it is likely that Grain 1 has a lower dislocation density than Grain 8. Second, simulation is confined to 2D, and the evolution of a cross section within a 3D volume may differ from that of 2D simulations. Moreover, although the density of the second-phase particles is in general expected to be larger within a smaller grain, there may be statistical variations due to the stochastic nature of precipitate nucleation, growth, and subsequent dissolution

that produce dislocations. Finally, it has been known that grain boundary energies are anisotropic, depending on not only the crystalline orientations of the pair of grains but also the relative orientation of the grain boundary [194]. The resulting variation in grain boundary energies would result in different likelihood of precipitating second-phase particles on or near grain boundaries, leading to a spread in the density of dislocations produced by the precipitates.

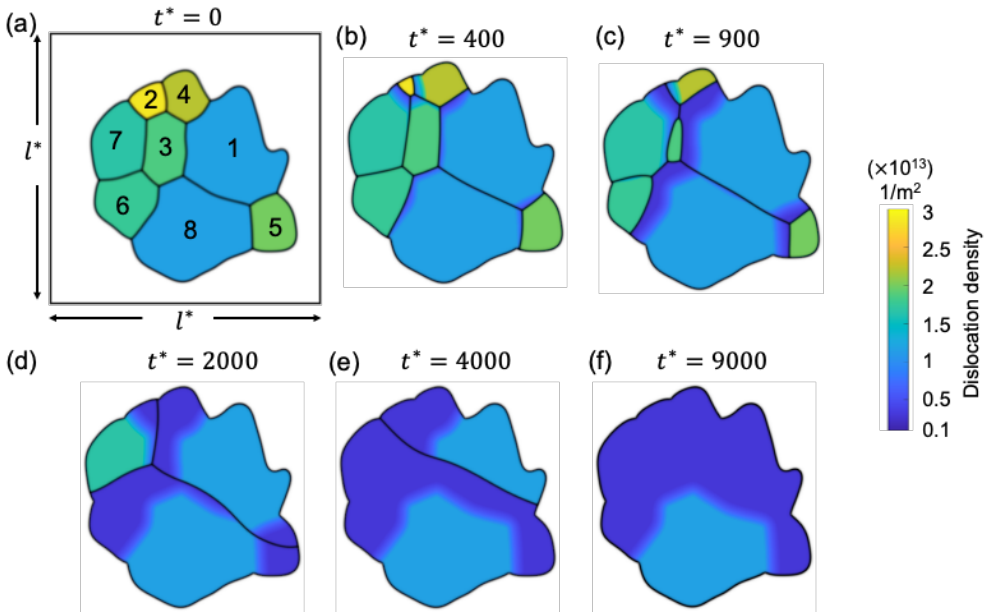

Figure 6.7. The evolution of microstructure and dislocation density within a confined region found in the experiment. A unique number from 1 to 8 is assigned to each grain. Dislocation densities of all the grains are initialized with Equation (6.12). The color indicates the dislocation density. A black box is plotted in (a) to indicate the simulation domain.

Therefore, in reality, the dislocation density within a grain will have a statistical variation around the value determined by Equation (6.12). When the dislocation density of Grain 1 is reduced by ~16%, it was found that the stored energy difference between Grain 1 and 8 provides sufficient driving force and Grain 1 consumes Grain 8 at the end of the simulation. The results of this simulation are shown in Figure 6.8. The early evolution of the two simulations are very similar, as can be seen by comparing Figure 6.7(a) – (c) and Figure 6.8(a) – (c). On the other hand, during the later stage, Grain 1 progressively consumes Grain 8, as shown in Figure 6.8(d) and (e) and is

the only grain that remains at the end of the simulation, as shown in Figure 6.8(f). The high dislocation density at Grain 1's initial position and the low dislocation density at the surrounding region closely resemble the experimental observations shown in Figure 6.2(f). Although a quantitative agreement is not expected because of the 2D nature of the simulations and thus is not a goal of this work, the similarities observed between the experimental observations and simulation results with a reasonable parameters/setup provides support for the proposed model.

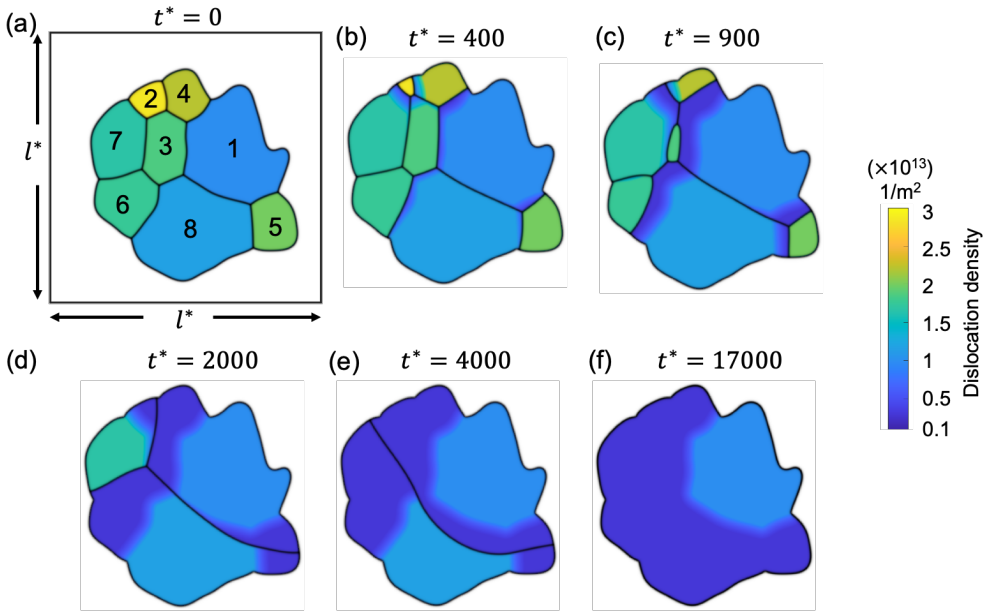

Figure 6.8. The evolution of microstructure and dislocation density within a confined region found in the experiment. A unique number from 1 to 8 is assigned to each grain. Dislocation densities of grain 2 – 8 are initialized with Equation (6.12). Grain 1's dislocation density is reduced by ~16% from the value given by Equation (6.12), which resulted in a better match with the experimental observation. The color indicates the dislocation density. A black box is plotted in (a) to indicate the simulation domain.

6.5.2 Large-scale simulations

In this section, we perform a set of large-scale simulations to examine the effect of cyclic heat treatment on the microstructure evolution. To maintain computational feasibility, the smallest grain to resolve in the simulations is chosen to have a radius of 12 μm. This grain radius requires the interfacial width to be no larger than 3.5 μm such that the bulk region within the smallest grain

occupies at least 50% of the area, assuming circular shape of the grain. We initialize the order parameters using the method discussed in Sections 6.3.3 and 6.4. The individual dislocation densities are initialized using Equation (6.3). For this equation, the values of $\rho_{0,i}(\boldsymbol{r})$ are given by Equation (6.12) when the dislocations are injected for the first time and are given by Equation (6.14) when the dislocations are injected for the second and the third times. The values of $\rho_{gb,i}$ are given by Equation (6.13). The dimensionless parameters employed for the simulations are summarized in Table 6.4. Periodic boundary conditions are utilized throughout the simulations.

Table 6.4. The dimensionless parameters employed in the large-scale simulations.

Parameters	**Variable**	**Value**
Bulk energy coefficient	m_0^*	1
Gradient energy coefficient	κ^*	9.57×10^{-4}
Domain size	l^*	69.43
Grid spacing	$\Delta x^* = \Delta z^*$	2.19×10^{-2}
Time step (with stored energy)	Δt_s^*	0.05
Time step (without stored energy)	Δt_{ns}^*	0.1

The initial microstructure, which contains 1778 grains, is shown in Figure 6.9(a). It can be observed from the figure that a number of small grains are clustered in a chain-like structure. This arrangement is reasonable in 2D given the facts that a large portion of small grains was observed in the experiment at state S_1 (see Figure 6.3(a)) and that these small grains would have to cluster in order to avoid an unphysical (non-equiaxed) grain morphology. The high dislocation density of these small grains yields a high stored energy as compared to their surrounding grains, and consequently, these grains are rapidly consumed, as shown in Figure 6.9(b). The microstructure at the end of the first cycle is shown in Figure 6.9(c). Most grains with high dislocation densities

(i.e., yellow grains) are consumed by their surrounding grains at this stage and the large grains next to these small grains become larger. Statistically, the unscaled GSD broadens, primarily due to the growth in the average grain size, as shown in Figure 6.11(a) and Figure 6.11(b). A second cycle is then simulated, which consists of re-injection of dislocations to the microstructure and subsequent microstructure evolution. The increase of dislocation densities is inversely proportional to the grain radius, and therefore the smaller grains are assigned with a higher increase in dislocation densities, as shown in Figure 6.11(d). An intermediate microstructure and the microstructure at the end of the second cycle are shown in Figure 6.9(e) and (f), respectively. The unscaled GSD continues to broaden, as shown in Figure 6.11(c). A second peak in the GSD appears after the third cycle, as shown in Figure 6.11(d). The comparison of scaled GSDs for each cycle is shown in Figure 6.12(a), in which all the radii are scaled by their average value and the probability is scaled to yield an area of unity under the curve. The scaled GSD continues to evolve throughout the three simulation cycles, exhibiting a slight broadening especially at the later cycles, and a bimodal distribution may start to develop at the end of the third cycle. It has been suggested that a bimodal grain size distribution is one of the signatures of AGG [15,178].

To confirm that dislocation injections are necessary to yield persistent AGG, a simulation that omits the driving force due to the stored energy difference is performed. To allow for a direct comparison, an identical initial microstructure is employed, as shown in Figure 6.10(a). The microstructure at time $t^* = 800$, 1700, and 3300 during the evolution is shown in Figure 6.10(b) – (d), respectively. These three times are selected because they correspond to the final times of the three cycles for the stored-energy-driven grain growth. In this case, the large grains progressively consume the smaller grains surrounding them solely due to capillarity.

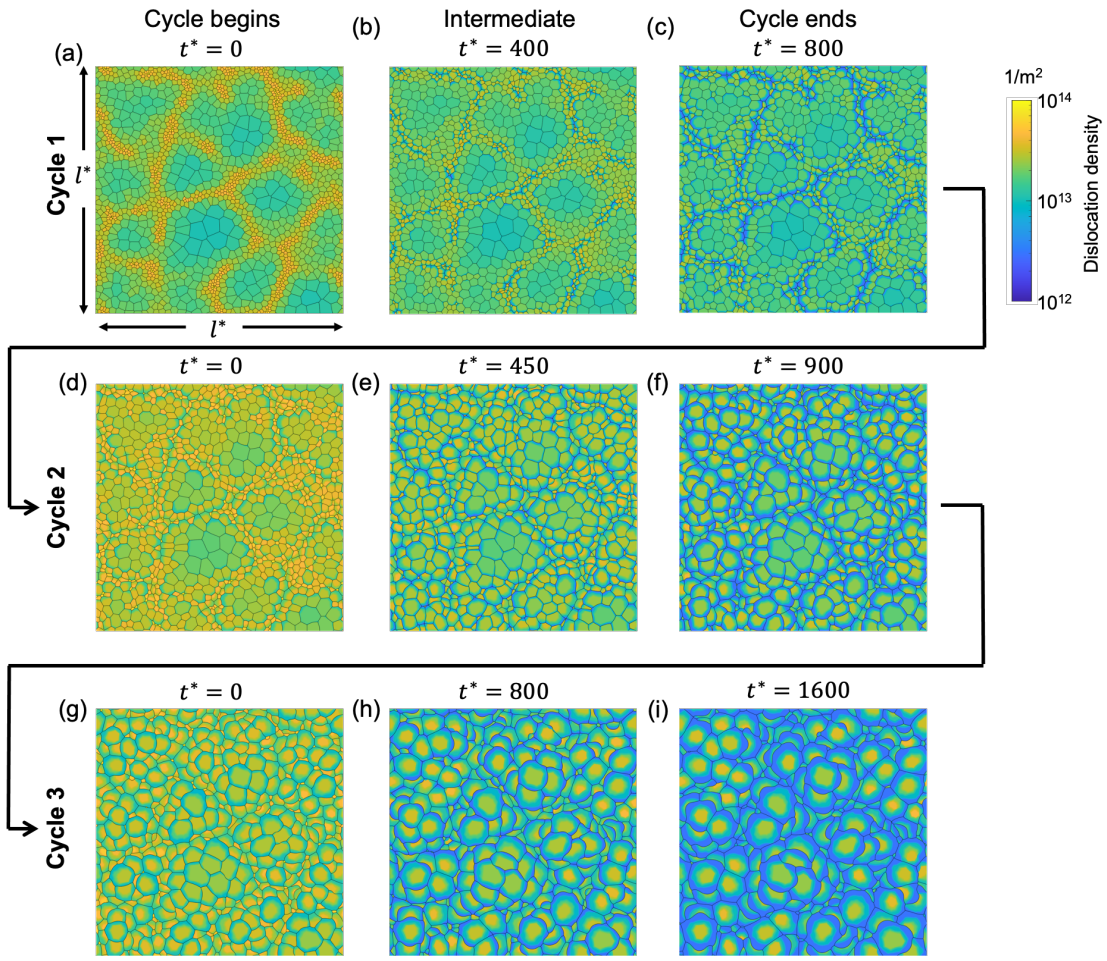

Figure 6.9. Stored-energy-driven microstructure evolution, after the dislocations being injected (a) – (c) once, (d) – (f) twice, and (g) – (i) three times. Each cycle ends when the average grain radius increases by 40%, and the dimensionless time t^* is labeled. The color indicates the dislocation density.

To quantify the rate of the microstructure evolution and to compare such a rate between the simulations with and without the stored energy, we show the average grain radius as a function of time for the two cases in Figure 6.13. The average grain radius during the microstructure evolution with the stored energy for cycles 1, 2, and 3 are indicated by red, blue, and black dots, respectively. The average grain radius during the microstructure evolution without the stored energy is indicated by green dots. A much faster increase in the average radius is observed when the stored energy is considered, which indicates that the microstructure evolution proceeds more

rapidly when dislocations are injected via CHT. Additionally, at the start of each cycle, there is a rapid increase in the average radius, which is due to the large variation in initial dislocation densities. Then, the growth rate decreases as the stored-energy driving force reduces and the system shifts toward normal grain growth. An additional abrupt increase in the average radius in the midcycle in cycle 3, observed from time $t^* = 3000$ to $t^* = 3100$, is caused by a large number of grains (14 grains out of 246 grains) that disappeared between the two times. Unlike the apparent broadening of unscaled GSD observed in the evolution of microstructure with dislocations, the unscaled GSD during capillary-driven grain growth only slightly broadens (see Figure 6.11(e) – (g)). In addition, none of the grains is observed to grow abnormally faster than the others. Consequently, the unscaled GSD remains singly peaked from $t^* = 800$ to 3300. The convergence to self-similarity is observed in scaled GSD, as shown in Figure 6.12(b).

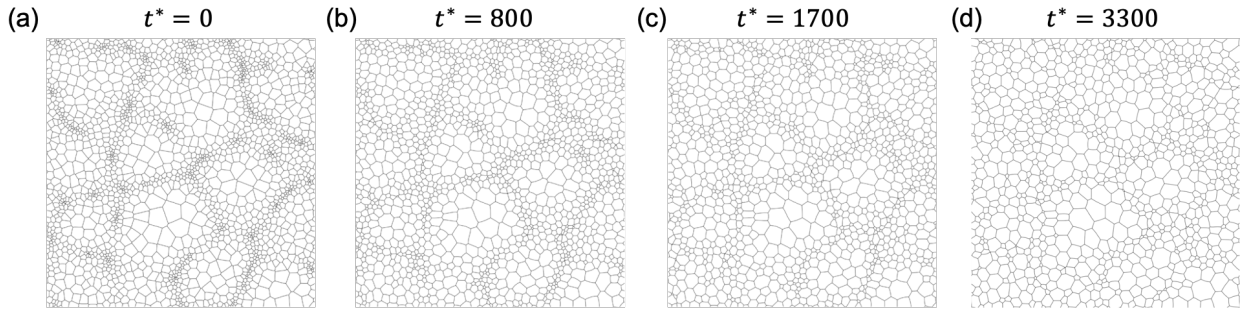

Figure 6.10. Capillary-driven microstructure evolution. Four snapshots are shown at time (a) $t^* = 0$, (b) $t^* = 800$, (c) $t^* = 1700$, (d) $t^* = 3300$.

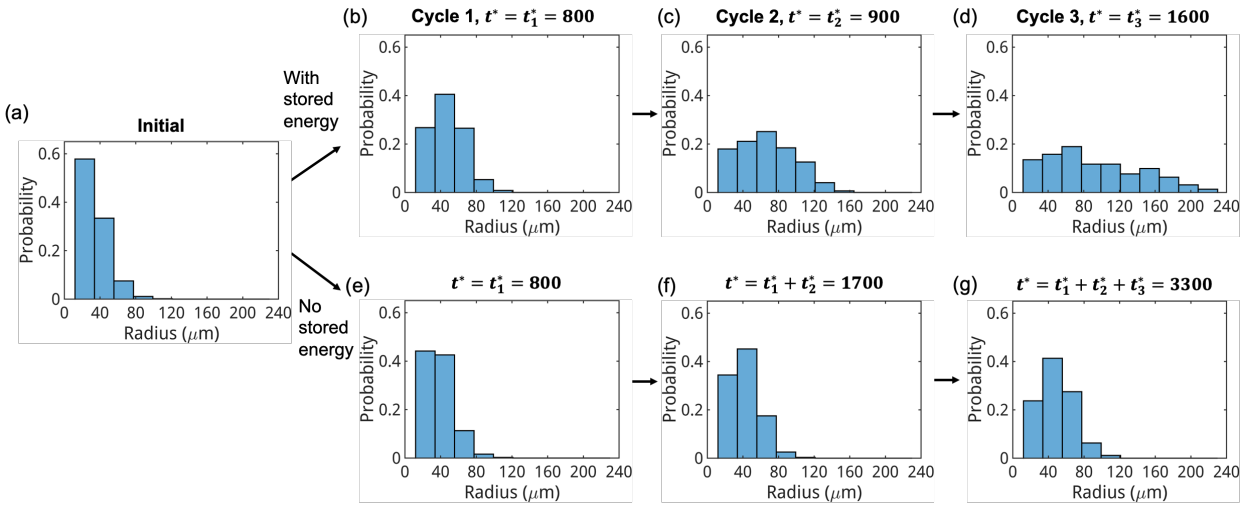

Figure 6.11. Grain size distribution (GSD) during the microstructure evolution. (a) GSD at the initial time, (b) – (d) GSD after first, second, and third cycles with the stored energy, (e) – (g) GSD at $t^* = 800$, $t^* = 1600$, and $t^* = 3300$ for a simulation without the stored energy.

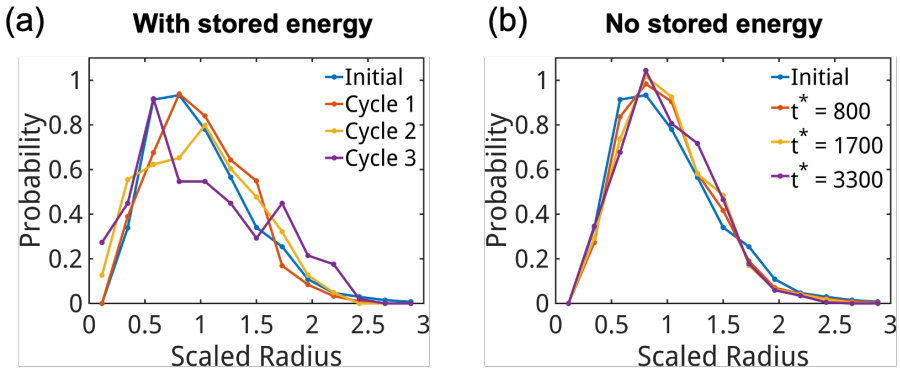

Figure 6.12. Scaled GSD, which plots the probability (scaled to integrate to 1) vs. radius scaled by the average radius (a) from the simulations with the stored energy and (b) from the simulations without the stored energy.

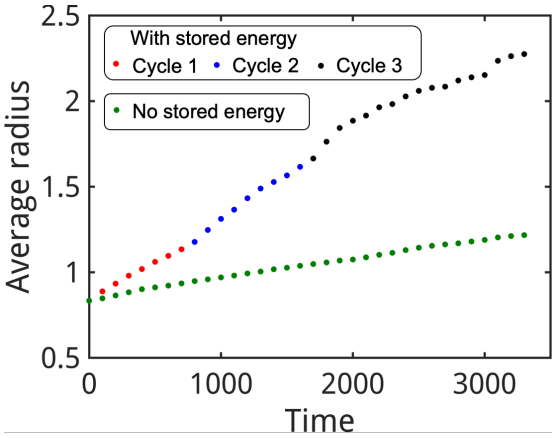

Figure 6.13. Dimensionless average grain radius vs. dimensionless time. The red, blue, and black dots indicate the average grain radius during microstructure evolution with the stored energy for cycle 1, 2, and 3, respectively. The green dots indicate the average grain radius during microstructure evolution without the stored energy.

6.6 Conclusion

We extended the phase-field model in Chapter 5 to simulate the evolution of microstructure and dislocation density within a sample undergoing cyclic heat treatment. As compared to the previous model, this extended model is capable of describing a spatially varying dislocation density and a reduction in dislocation density as grain boundaries migrate, which was observed in the experiments. We conducted simulations based on the assumption that the smaller grains (having higher grain boundary length per unit area (equivalent to area per unit volume in 3D)) have more second-phase particles precipitated per unit volume and thus a larger number of dislocations injected. The simulation predicted a microstructure that closely resembles the experimentally measured microstructure within a region that were confined within a nearly static boundary in the experimental dataset. In addition, the model was utilized to simulate three cycles of stored-energy-driven grain growth within a large microstructure, during which non-self-similar microstructure evolution was observed. In contrast, a simulation without the stored energy yielded a near self-similar evolution. In particular, when the stored energy was included with an assumption that number of dislocations injected scaled as the inverse of the grain radius, it was

found not only that grains grew much faster but also the larger grains preferentially grew. Moreover, although the rate of grain growth with stored energy is much faster at the beginning of each cycle as compared to that without stored energy, the former decreases at the later stage of each cycle as the stored-energy driving force reduces with evolution and the system shifts toward normal grain growth. Therefore, CHT is necessary to continuously provide stored-energy driving force. The simulation results thus suggest that CHT facilitates large grains to grow abnormally due to the stored-energy driving force. Additionally, this chapter provides an integrated experimental-computational workflow, which utilizes the information from experiments to inform grain-growth models and its parameterization. While we here limited our efforts to two-dimensional simulations as a proof of concept, the workflow can be easily adapted to perform more time-consuming, but more accurate three-dimensional simulations, as well as to include additional physical considerations, such as the recovery. Therefore, the work provides a foundation for future development of simulation tools capable of quantitative predictions of microstructure evolution during non-isothermal heat treatment, which will ultimately facilitate the design of optimized processes for solid-state single-crystal growth.

Chapter 7 Controlling Thermal Profiles Using Parameterized Heat Transfer Models

7.1 Introduction

In this chapter, we present two heat transfer models that are used to predict the temperature profiles within two types of furnaces. We first show a heat transfer model that describes the temperature distribution within a sample in an optical floating zone experiment and demonstrate its capability to reproduce steady-state thermal profiles of the sample measured in the experiment, as well as in predicting time-dependent temperatures, after determining uncertain parameters of the model with a machine learning algorithm developed for this purpose. We then describe a coupled thermal and Joule heating model for a gradient heater furnace, in which the sample is heated by two ceramic bars with resistively heated wires around them. We demonstrate that the parameterized model accurately replicates the thermal profiles of a NaCl/Si sample measured in the experiment and is capable of predicting temperature profiles when alternative winding configurations of wires or different geometries of ceramic bars are employed.

7.2 The heat transfer model for optical floating zone (OFZ) experiments*

7.2.1 Introduction for OFZ modeling

As mentioned in Chapter 2 Section 2.3, measuring the sample temperature in OFZ furnace is challenging and is an ongoing research effort. For example, a physical model of a commercial OFZ furnace has been designed to incorporate an optical pyrometer for measuring sample-temperature profiles [195]. However, this approach has two key limitations. First, only surface temperatures can be measured, and second, the heating lamps must be turned off during the

* Adapted from G. Huang, M. Zhang, D. Montiel, P. Soundararajan, Y. Wang, J. J. Denney, A. A. Corrao, P. G. Khalifah, and K. Thornton, "Automated Extraction of Physical Parameters from Experimentally Obtained Thermal Profiles Using a Machine Learning Approach," Computational Materials Science 194, 110459 (2021).

measurements, which can affect the sample temperature. Our experimental collaborator Denney et al. [25] from Peter Khalifah's group in Stony Brook University recently pioneered the first *in situ* synchrotron measurements of temperature profiles that enable temperature profiles in a sample rod heated at a point with lamps to be measured with high precision and high spatial resolution, with ability to resolve horizontal center-to-edge gradient in the sample rod and with the possibility for both steady state and dynamic measurements of temperature profiles. In these measurements, the position-dependent sample temperature is indirectly determined through the refinement of unit cell lattice parameters against synchrotron X-ray diffraction patterns, with the local temperature calculated from the known thermal expansion behavior of the material being studied.

To provide a better understanding of the thermal profiles for the sample within the OFZ experiment as a function of time and space, we propose a heat transfer model, with uncertain parameters being determined to match predicted steady-state thermal profiles of the sample with those measured in the experiment using the machine learning algorithm discussed in Chapter 2 Section 2.5.2. We present the convergence of the algorithm, the refinement of the possible ranges of uncertain parameters, as well as a fitted steady-state temperature profile and time-dependent temperatures obtained with optimized parameters. The resulting model, which does not explicitly consider the process of heat absorption but treats the heat absorbed as a fitting parameter, is computationally efficient and can potentially be used to provide on-demand feedback during *in situ* experiments.

7.2.2 Heat transfer model for OFZ

We build heat transfer models using COMSOL Multiphysics® software [89] to simulate the heat transfer process within a polycrystalline Al_2O_3 sample rod heated by two halogen lamps. The model considers the Al_2O_3 sample to be a cylinder of radius R_s and length L_s. In addition, this

model considers an aluminum metal sample holder of radius, R_h, and length, L_h in contact with the sample because experimental results suggest that the thermal conduction to/from the sample holder cannot be neglected. The geometry considered in the model is shown in Figure 7.1 and values of geometrical quantities are summarized in Table 7.1.

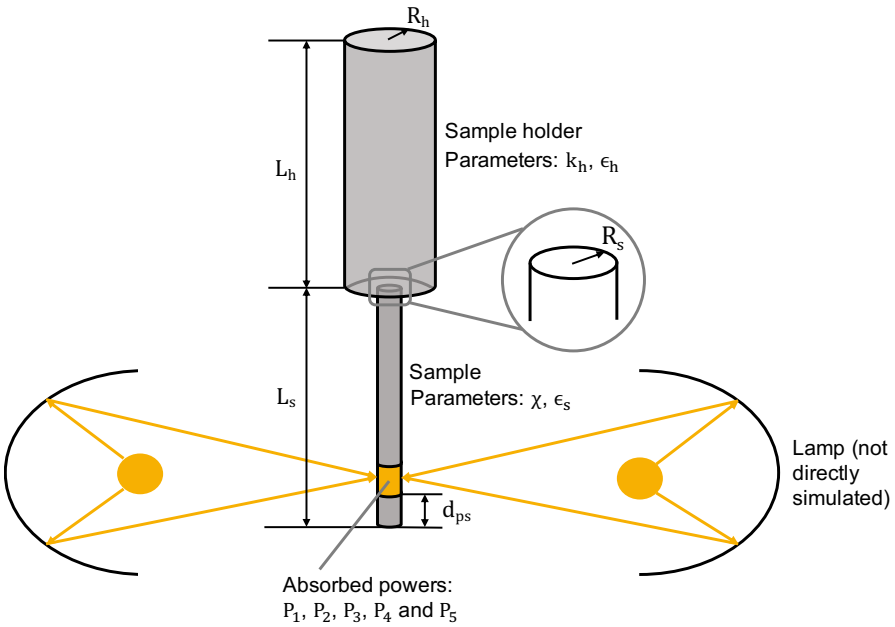

Figure 7.1. Geometry of a heat transfer model for an optical floating zone experiment. The geometrical parameters, as well as the uncertain parameters to be determined are indicated. The process of heat absorption from the lamps was not directly simulated but treated via a set of absorbed powers as fitting parameters. Reproduced with permission [101]. Copyright 2021, Elsevier.

Heat is transported across the sample and sample holder through thermal diffusion, which is described by Equation (2.14). For all simulations, the ambient temperature is assumed to be 298.15 K. The absorbed radiation from two lamps is modeled as a constant power heat source assumed to be uniformly distributed over a cylindrical surface of area S = 47.1 mm^2 located near the bottom end of the sample. The heat absorption equation at this region is

$$-\boldsymbol{n} \cdot \boldsymbol{q}_{src} = q_{src} \quad , \tag{7.1}$$

where $\boldsymbol{n}$ is the unit outward normal vector and $\boldsymbol{q}_{src}$ is the heat flux on the surface area S. Small variations in the alignment of the focused light from the lamps can result in changes in the heat source position. Therefore, the distance between the bottom of the power source and that of the sample, d_{ps}, is treated as an uncertain parameter. The heat loss from the sample and the sample holder is considered to occur through thermal radiation (Equation (2.20)) and natural air convection (Equation (2.15)). For side surfaces of the sample and the sample holder, h is estimated using an empirical relation for thin vertical cylinders [196,197]. For the top surface of the sample holder, h is estimated using empirical relation for upward-facing horizontal plates [86,196]. For the bottom surfaces of the sample and sample holder, h is estimated using empirical relation for downward-facing horizontal plates [86,196].

7.2.3 Training and test data

Two sets of experimentally measured temperature data were utilized for model training and testing. The first set of temperature data, which was used as the training data to obtain the optimized parameter set, was measured via a series of vertical scan experiments. In a vertical scan experiment, the lamps are kept on until the temperature of the sample reaches steady state. The temperatures of the sample along y-direction at $x = 0$ from $z = 0$ to $z = 35$ mm, with a step size of 1 mm, are then determined using X-ray diffraction methods. A schematic indicating the positions at which temperatures are collected is shown in Figure 7.2(a). The experiments were performed five times with the lamp voltage increasing linearly from 20% to 100% of its maximum (resulting in lamp powers of 25.2 W, 73.0 W, 137 W, 216 W, and 300.0 W) and five corresponding temperature profiles were obtained [101].

The second set of temperature data, which was used to test the parameters obtained from the vertical scan data, was taken from a series of time-dependent “jump” scan experiments

[25,101]. In a jump scan experiment, the data are collected at a single point as the sample heats and cools. In each scan, the lamps are switched on for a certain amount of time and then switched off. The temperature at a position (x, z) is measured with respect to time again employing diffraction methods. The procedure is used to obtain time-dependent temperature at positions A, B, C, and D, as shown in Figure 7.2(b). The temperature at position A was collected twice, first with the power of the lamps at 300.0 W and the second time at 104 W. Full power (300.0 W) was used for a single measurement at each other position.

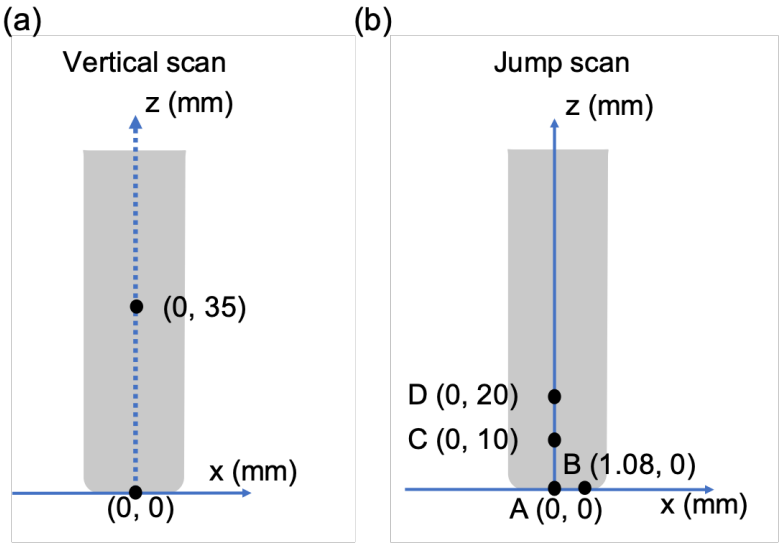

Figure 7.2. Schematics showing a side view of the sample and positions on the sample at which temperatures were determined. The temperature at each point is averaged along *y*-direction, which is perpendicular to *x*-*z* plane. (a) In the vertical scan, the temperature profile was collected from z=0 mm to z=35 mm, with a step size of 1 mm, all at x=0 mm (the center of the projection of the sample rod). (b) In jump scans, the evolving temperature was collected as the lamp was turned on and then off. The temperature changes were followed at points A (with heating at 300.0W and 104W), B (at 300.0W), C (at 300.0W), D (at 300.0W), each over one heating / cooling cycle. Reproduced with permission [101]. Copyright 2021, Elsevier.

For the training stage, the parameters are iteratively optimized such that the simulated steady-state temperature profiles become closer to those obtained experimentally. We employ the algorithm in Chapter 2 Section 2.5.2 to reduce RMSEs by iteratively refining the parameter space. The parameters that required optimization are listed in Table 7.1, where they are labeled with

"optimization" in the respective "source" columns. We set the number of simulations per iteration, K, to 1000. As we will discuss in Section 7.2.4, ten parameters ($n = 10$) need to be determined in total. Therefore, we effectively take only $K^{1/n} \sim 2$ samples along each direction in the parameter space at each iteration step. The model with optimized parameters is then employed to predict time-dependent temperatures and compared to the jump scan test data.

7.2.4 Material properties and simulation parameters

The density of the Al_2O_3 sample, $\rho_s = 2.19 \times 10^3$ kg/m^3, was calculated using the ratio between the measured mass and volume of the sample. A temperature-dependent functional form of specific heat capacity proposed in Ref. [198] is employed to fit to experimentally obtained heat capacity data of Al_2O_3 from 273.15 K to 700 K in Ref. [199]. The resulting form of heat capacity $C_{p,s}(T)$ is

$$C_{p,s}(T[K]) = 984.7 + 3.203 \times 10^{-1} T - \frac{2.707 \times 10^7}{T^2}. \tag{7.2}$$

The thermal conductivity of the alumina sample used in the experiment is assumed to be dependent on the temperature, T, as well as the porosity, ϕ_s, and the grain boundary density of the sample that can affect the effective thermal conductivity. An adjustable constant, χ_s, is used to take the effect of grain boundary density into account. The thermal conductivity of dense alumina ($\phi_s = 0$) throughout a few temperature values can be found in Ref. [200]. A second-order polynomial is utilized to fit to those values from 298 K to 700 K. The resulting functional form of a temperature-dependent thermal conductivity of dense alumina, $k_{0,s}(T)$, is

$$k_{0,s}(T[K]) = 75.60 - 1.586 \times 10^{-1} T + 9.814 \times 10^{-5} T^2. \tag{7.3}$$

The pores in the alumina sample are assumed to be spherical and their thermal conductivity is assumed to be zero. Designating alumina as a matrix phase and the pores as a particle phase, the

thermal conductivity of a porous alumina sample, $k_{1,s}(T, \phi_s)$, can be described by via an effective medium approximation, as discussed in Ref. [201]:

$$k_{1,s}(T[K], \phi_s) = \frac{2(1-\phi_s)}{2+\phi_s} k_{0,s}(T). \tag{7.4}$$

The porosity is calculated using the following equation

$$\phi_s = 1 - \frac{\rho_{exp}}{\rho_{dense}}, \tag{7.5}$$

where $\rho_{exp} = 2.190 \times 10^3$ kg/m^3 and $\rho_{dense} = 3.970 \times 10^3$ kg/m^3 [202] are the density of the alumina sample used in the experiment and that of a dense sample (without pores), respectively. To account for the fact that the grain size of the sample used in the experiment could be different from that in Ref. [200], we further modify the conductivity by a multiplicative adjustable microstructure factor, χ_s. The resulting effective thermal conductivity with $\phi_s = 0.448$ is

$$k_s(T[K], \phi_s = 0.448, \chi_s) = \chi_s(34.07 - 0.715 \times 10^{-1} T + 4.422 \times 10^{-5} T^2). \tag{7.6}$$

The constant χ_s is an unknown parameter to be determined by the optimization algorithm. Considering the fact that the grain boundary density of the sample could be either larger or smaller than the one in Ref. [200] that is used to obtain Equation (7.6), the initial range of χ_s is set as from 0.5 to 1.5. The emissivity ϵ_s is an uncertain parameter, which is presumed to range from 0.28 to 0.48, as discussed in Ref. [203].

The aluminum metal sample holder is assumed to have a density of $\rho_h = 2.70 \times 10^3$ kg/m^3 as reported in Ref. [204]. The same functional form proposed in Ref. [198] is employed to fit to heat capacity data of aluminum from 273.15 K to 700 K in Ref. [205]. The resulting form of heat capacity $C_{p,h}(T)$ is

$$C_{p,h}(T[K]) = 768.7 + 4.530 \times 10^{-1} T - \frac{2.335 \times 10^5}{T^2}. \tag{7.7}$$

A similar expression of effective thermal conductivity for the aluminum sample holder, k_h, can be written as

$$k_h(T[K], \phi_h, \chi_h) = 2\chi_h \frac{(1-\phi_h)}{2+\phi_h} k_{0,h}(T[K]), \tag{7.8}$$

where ϕ_h and χ_h are the porosity and microstructure factor of the aluminum sample holder, respectively. The temperature of the aluminum sample holder remains within 298.15 K and 373.15 K based on the simulations. Due to high thermal conductivity of aluminum, it is reasonable to assume that the heat transport across the sample holder is fast and therefore the temperature within the sample holder is nearly uniform. Moreover, the thermal conductivity within this temperature range is not expected to vary significantly. Therefore, the thermal conductivity of the sample holder can be considered as a constant and found via the optimization. When testing the algorithm, we examined a wide range of thermal conductivities corresponding to temperatures beyond this temperature range due to the uncertainties in impurity and microstructure effects. We chose 240 W/(m·K) (corresponding to well-annealed 99.99+% pure aluminum at T = 373.15 K [206]) as the upper bound of the thermal conductivity. The lower bound of 208 W/(m·K) (corresponding to well-annealed 99.99+% pure aluminum at T = 933.15 K [206]) was selected. While this temperature is out of the expected range of temperatures of the aluminum sample holder in the experiment, it was adopted since there are a number of factors that would reduce the thermal conductivity, including the porosity, grain boundaries, and impurities. For example, this value is that resulting from Equation (7.8) with porosity $\phi_h = 0.01$ and microstructure factor $\chi_h = 0.88$ at T = 373.15 K, which is within a reasonable estimate. The aluminum sample holder is assumed to have a rough surface; for roughened aluminum, the emissivity ϵ_h was reported to range from 0.10 to 0.30 [207].

The power from the lamp is assumed to be uniformly deposited near the bottom tip of the sample rod over a cylindrical surface 3 mm in height (having a surface area of $S = 47.1$ mm^2). The offset distance between the bottom tip of the sample and the bottom edge of the heated region, d_{ps}, is expected to be small and its initial range is therefore assigned to be from 0.01 mm to 2.0 mm. As discussed in Section 7.2.3, five temperature profiles were obtained with five different nominal lamp powers. In our model, we consider the absorbed powers P_1, P_2, P_3, P_4, and P_5, to be five unknown parameters. The parameters discussed above and their initially assigned ranges are summarized in the first and the last column of Table 7.1.

7.2.5 Refinement of the parameter range

The range of each parameter is gradually refined over the iterations. The average cost, $\bar{E}^i$, and the change of the average cost, ΔE^i, are calculated for each iteration and plotted in Figure 7.3(a) and (b), respectively. It can be observed from the figure that ΔE^i first becomes smaller than the defined threshold of 10^{-3} for iteration 16, indicating convergence.

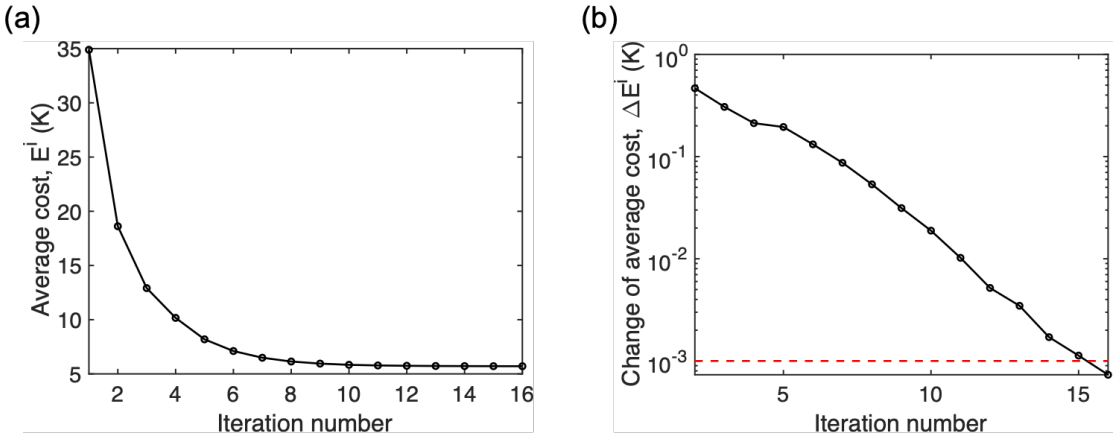

Figure 7.3. (a) The average cost, $\bar{E}^i$ and (b) the change of average cost, ΔE^i in each iteration. The red dashed line indicates the threshold. Reproduced with permission [101]. Copyright 2021, Elsevier.

The process of range refinement of each parameter is shown in Figure 7.4. The mean value and the sampled range calculated from each iteration are indicated by blue circles and solid vertical bars, respectively. It can be observed from the plots that the uncertainty of each parameter is iteratively reduced until the algorithm converges. It is worth noting that that ranges of some parameters (such as absorbed power) decrease more in each iteration as compared to their initial ranges, while those of others (such as k_h and ϵ_h) decrease less. The ratio of the next possible range to the current possible range of each parameter indicates the sensitivity of the cost function on the sampled values within the current parameter range, either because the relative range is wider than those of other parameters or because of the intrinsic sensitivity of the simulation results on that parameter.

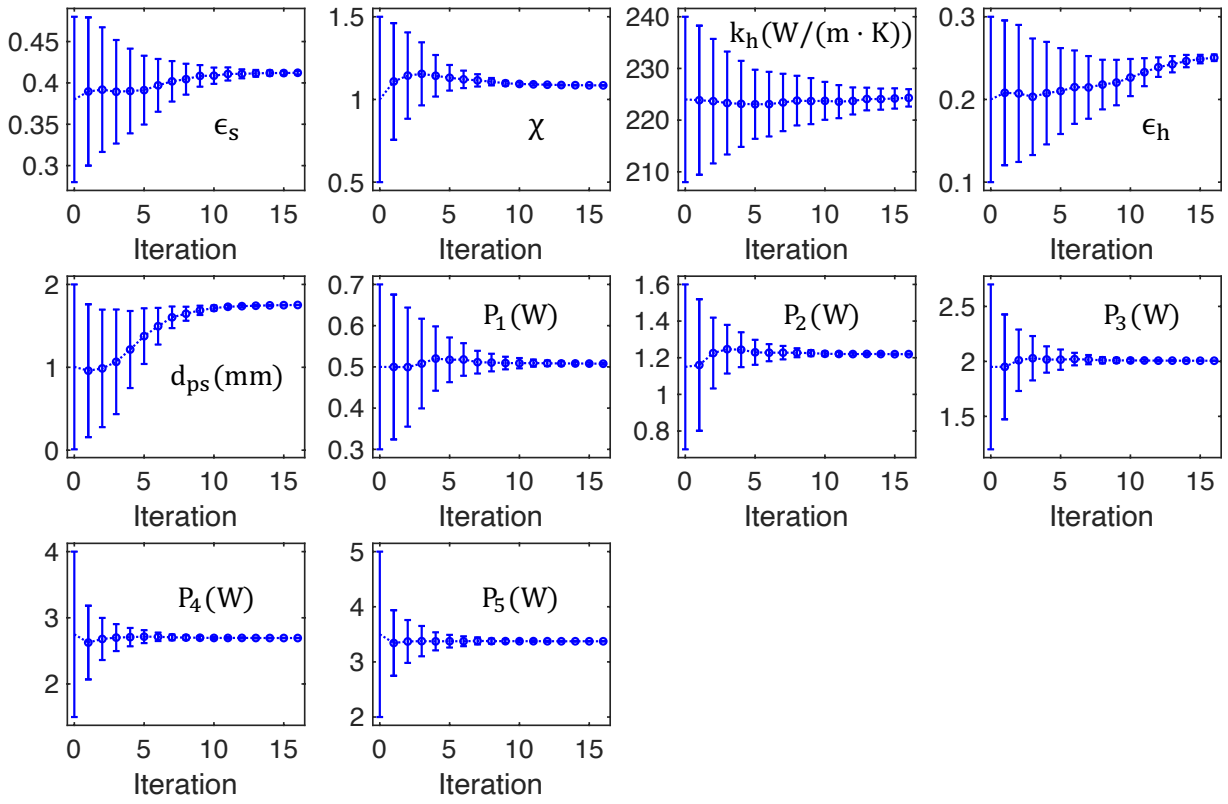

Figure 7.4. Iterative refinement of the parameters. The mean value (indicated by circles) and the sampled range (indicated by vertical bars) of each parameter are updated in each iteration. The range at iteration 0 refers to the initial range of each parameter and therefore no mean value is shown at iteration 0. Reproduced with permission [101]. Copyright 2021, Elsevier.

We utilize the interpolation method discussed in Chapter 2 Section 2.5.2 to obtain the optimal values for each parameter. Specifically, the following second-order polynomial is employed to approximate the errors, $\hat{E}(\tilde{\boldsymbol{x}}_{\boldsymbol{j}})$, as a function of the normalized parameter vectors, $\tilde{\boldsymbol{x}}_{\boldsymbol{j}} = (x_{1,j}, \ldots x_{p,j}, \ldots, x_{n,j})$:

$$\hat{E}(\tilde{\boldsymbol{x}}_{\boldsymbol{j}}) = \sum_{p=1}^{n} \left(a_p \tilde{x}_{p,j}^2 + b_p \tilde{x}_{p,j} + \sum_{q=p+1}^{n} \left(c_{pq} \tilde{x}_{p,j} \tilde{x}_{q,j} \right) \right) + d, \tag{7.9}$$

where the indices for each parameter vector and for each parameter are indicated by j and p, respectively. The resulting fitting constants $a_p, b_p, c_{pq},$ and d are summarized in Table 7.2. The optimized values for each parameter are summarized in the "Values employed in the model" column of Table 7.1.

7.2.6 Simulated temperature profiles with optimized parameters

The steady-state temperature profile simulated from optimized parameters is compared to that obtained from experiments in Figure 7.5(a). The simulated and experimental temperature profiles are in good agreement for all lamp powers. The RMSE between the experimental and simulated data is 5.7 K. The relationship between the nominal power from lamps and the absorbed power, determined via optimization, is plotted in Figure 7.5(b) along with a polynomial fit. The absorbed power, P_6, resulting from the nominal power of 104 W is then estimated to be 1.58 W from this fit, and this value is utilized in the prediction of the time-dependent temperature response since the steady-state measurement had not been carried out at this specific power setting. The resulting times series curves simulated based only on the previously determined parameterization of steady state measurements (without further parameter optimization) are compared in Figure 7.5(c) to the experimentally obtained data. The RMSE is 16.6 K, which is about 4.7 % of the ~350

K overall temperature range across all data sets. The agreement is in general acceptable. The discrepancy could readily arise from the fact that the experimentally measured temperature profiles at different power levels are not necessarily at the steady state, something that can easily occur experimentally because the sample rod temperatures are extracted from the post-experiment fitting of the diffraction data and are thus not known during experiments. Therefore, the parameters obtained from the temperature profiles with a steady-state model can be affected by systematic experimental errors. Moreover, the initial temperature of the sample holder is set to be room temperature in the simulation, but it could be higher in the experiments due to residual heat from previous experiments, which could partially explain a faster increase in temperature in experimental curves as compared to the one in simulated curves.

From these results, we identify a few ways to reduce these experimental uncertainties in the future. First, an insulation can be placed between the sample and the sample holder to avoid significant thermal conduction between them. Second, the temperature could be measured in situ at a certain point or points determined by simulations to ensure either the apparatus has reached the room temperature or to constrain the initial condition. Additionally, simulations with an estimated set of physical parameters can also inform the design of experiments. Given the uncertainties in the experiments, we conclude that the algorithm effectively determines the values of each parameter within an acceptable error, and the steady-state temperature profiles effectively served as training data that allowed the behavior during time-series experiments to be predicted.

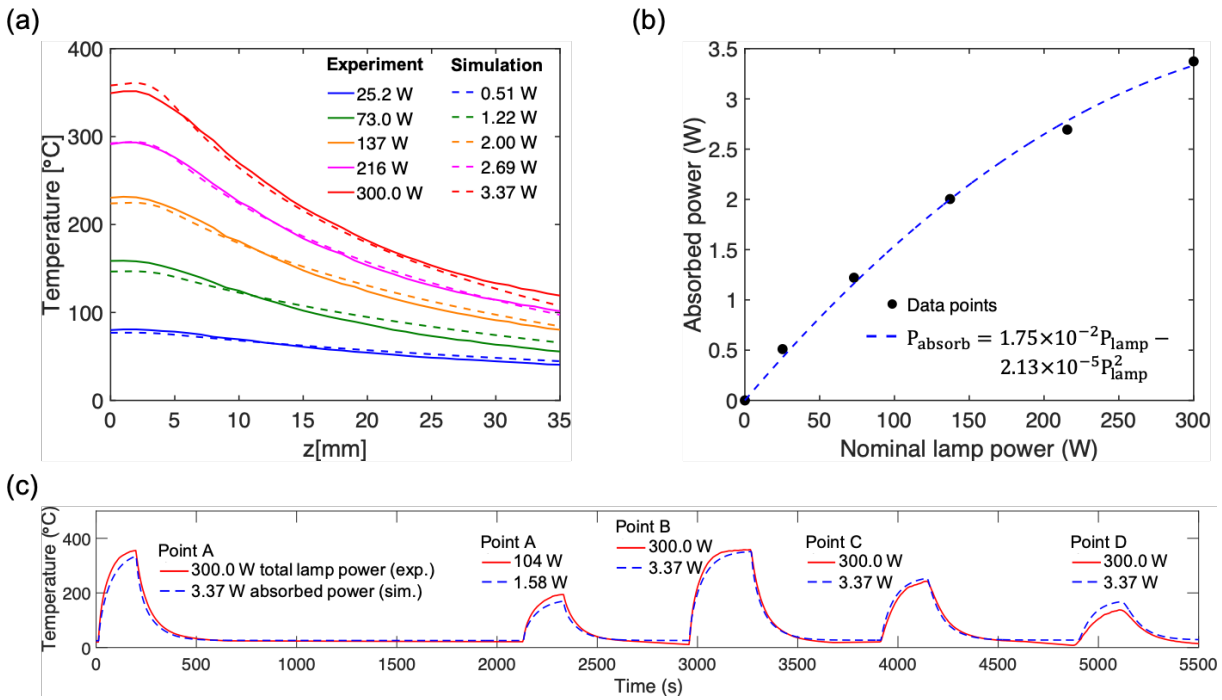

Figure 7.5. Comparison of temperatures profiles from simulations and experiments. (a) Steady-state temperature profiles measured in experiments (solid lines) and simulated with the optimized parameter values (dashed lines). (b) Relationship between absorbed power (calculated from simulations) and the nominal lamp power, with a polynomial fit to their relationship shown as a dashed line. (c) Time-dependent temperatures predicted from the model (dashed blue line) using optimized parameter values from fitting of the steady state data, compared to experimental data (solid red line). Reproduced with permission [101]. Copyright 2021, Elsevier.

Table 7.1. Parameter values used in optimized simulations compared to their initially assigned ranges. Reproduced with permission [101]. Copyright 2021, Elsevier.

Parameters	**Values employed in the model**	**Units**	**Source**	**Initially assigned ranges**
Al_2O_3 sample				
Density ρ_s	2.19×10^3	kg / m^3	Experiment	--
Radius R_s	2.50	mm	Experiment	--
Length L_s	58.9	mm	Experiment	--
Heat capacity $C_{p,s}$	See Equation (7.2)	J / (kg · K)	Literature	--
Thermal conductivity k_s	See Equation (7.6)	W / (m · K)	Literature	--
Correction constant χ_s	1.09	--	Optimization	0.5 – 1.5

Emissivity ϵ_s	0.41	--	Optimization	0.28 – 0.48 [203]
Aluminum sample holder				
ρ_h	2.70×10^3 [204]	kg / m^3	Literature	--
R_h	12.7	mm	Experiment	--
L_h	76.8	mm	Experiment	--
$C_{p,h}$	See Equation (7.7)	J / (kg · K)	Literature	--
k_h	224	W / (m · K)	Optimization	208 – 240 [206]
ϵ_h	0.25	--	Optimization	0.10 – 0.30 [207]
Power setting				
S	47.1	mm^2	Experiment	--
d_{ps}	1.76	mm	Optimization	0.01 – 2.0
P_1	0.51	W	Optimization	0.3 – 0.7
P_2	1.22	W	Optimization	0.7 – 1.6
P_3	2.00	W	Optimization	1.2 – 2.7
P_4	2.69	W	Optimization	1.5 – 4.0
P_5	3.37	W	Optimization	2.0 – 5.0
P_6	1.58	W	Fitting	--
Algorithm parameters (hyper parameters)				
K	1000	--	Designed	--
γ	1.5	--	Designed	--
r	10	--	Designed	--

Table 7.2. Constants determined from the polynomial fitting via Equation (7.9). Reproduced with permission [101]. Copyright 2021, Elsevier.

p	a_p	b_p
1	2.01×10^{-4}	-2.48×10^{-5}
2	1.22×10^{-4}	4.74×10^{-4}
3	2.22×10^{-14}	-3.72×10^{-4}
4	8.17×10^{-14}	-6.37×10^{-4}
5	2.42×10^{-4}	-5.24×10^{-4}
6	8.14×10^{-5}	-9.91×10^{-5}
7	3.07×10^{-4}	1.78×10^{-4}
8	2.49×10^{-4}	2.18×10^{-6}
9	6.73×10^{-5}	6.64×10^{-5}
10	1.39×10^{-4}	1.16×10^{-4}
(p, q)	c_{pq}	
(1,2)	2.82×10^{-4}	

(1,3)	-2.93×10^{-4}
(1,4)	8.92×10^{-5}
(1,5)	-1.52×10^{-4}
(1,6)	-1.61×10^{-4}
(1,7)	-5.82×10^{-5}
(1,8)	-3.23×10^{-4}
(1,9)	1.31×10^{-4}
(1,10)	-3.14×10^{-4}
(2,3)	3.57×10^{-5}
(2,4)	6.38×10^{-6}
(2,5)	-2.88×10^{-4}
(2,6)	-3.84×10^{-5}
(2,7)	-3.42×10^{-5}
(2,8)	-3.86×10^{-5}
(2,9)	-9.89×10^{-5}
(2,10)	-1.76×10^{-4}
(3,4)	-1.90×10^{-4}
(3,5)	-2.19×10^{-4}
(3,6)	1.42×10^{-4}
(3,7)	2.03×10^{-4}
(3,8)	1.50×10^{-4}
(3,9)	3.45×10^{-5}
(3,10)	4.57×10^{-5}
(4,5)	1.71×10^{-4}
(4,6)	8.95×10^{-5}
(4,7)	4.92×10^{-5}
(4,8)	-5.22×10^{-5}
(4,9)	-7.22×10^{-5}
(4,10)	-7.08×10^{-5}
(5,6)	-4.70×10^{-5}
(5,7)	-6.50×10^{-5}
(5,8)	-5.80×10^{-5}
(5,9)	9.76×10^{-5}
(5,10)	4.87×10^{-5}
(6,7)	-3.80×10^{-5}

(6,8)	1.19×10^{-4}
(6,9)	3.97×10^{-5}
(6,10)	1.03×10^{-5}
(7,8)	1.54×10^{-4}
(7,9)	-1.08×10^{-4}
(7,10)	7.29×10^{-5}
(8,9)	-2.44×10^{-4}
(8,10)	1.99×10^{-4}
(9,10)	-1.20×10^{-4}
d	5.70

7.2.7 Conclusion for OFZ modeling

The machine learning algorithm was applied to estimate the optimal parameter values for a heat transfer model that describes the heating of an Al_2O_3 rod in an optical floating zone furnace. Using the algorithm, relevant sample and furnace parameters for describing heat transfer in the system were obtained based on the steady-state temperature profile as the training data without human intervention except for the determination of the initial ranges of parameters. After parameter optimization against this data, experimental steady-state temperature profiles are accurately reproduced with this model. Furthermore, it is demonstrated that the same set of parameters can be used to accurately predict the time-dependent behavior of temperature profiles in the sample rod without any further parameter optimization, a result validated by experimental measurements.

7.3 Coupled heat transfer and Joule heating model for a gradient heater*

7.3.1 Introduction for gradient-heater modeling

As discussed in Chapter 1 Section 1.4, measuring temperature-dependent quantities of a sample using traditional methods is time consuming, as it requires repeated experiments conducted to measure the values of the quantities at various temperatures. Our experimental collaborator, O'Nolan *et al.*[27] from Karena Chapman's group in Stony Brook University recently proposed a gradient heater approach to generate variable temperature profiles within the sample and therefore enable the study of a temperature-dependent quantity in one experiment by measuring the quantity at different position of a sample. This approach is developed based on the flow-cell/furnace design [208]. A sample is placed in between two heating elements. Each heating element is composed of a ceramic bar with heating wires wound around it. The heating wire is resistively heated as the current goes through it. The heat is transported via thermal conduction from the wires to the ceramic bar that, in turn, heats the sample by thermal radiation. A schematic showing top and side views of the gradient heater is provided in Figure 7.6(a) and (b). The spacing between each two adjacent grooves is designed to be non-uniform to induce a temperature gradient in each heating element, which ultimately leads to a variable temperature profile within the sample.

* Adapted from D. O'Nolan, G. Huang, G. E. Kamm, A. Grenier, C. H. Liu, P. K. Todd, A. Wustrow, G. T. Tran, D. Montiel, J. R. Neilson, S. J. L. Billinge, P. J. Chupas, K. S. Thornton, and K. W. Chapman, "A Thermal-Gradient Approach to Variable-Temperature Measurements Resolved in Space," Journal of Applied Crystallography 53, 662 (2020).

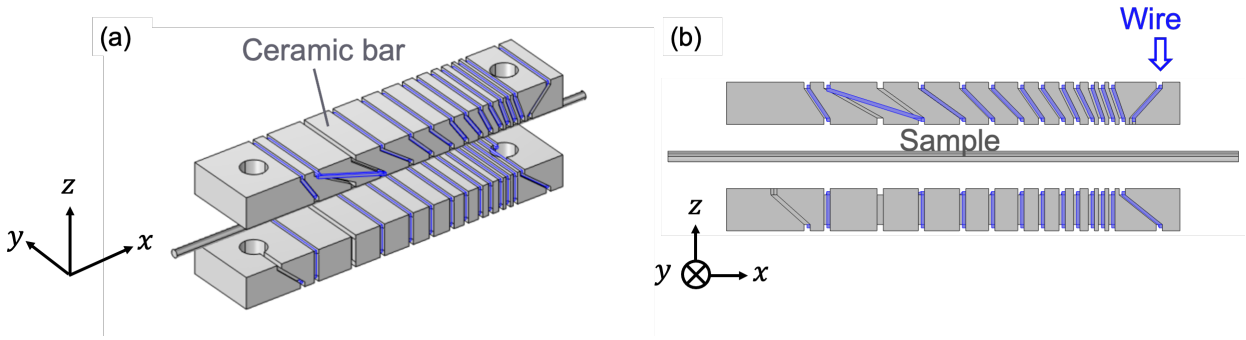

Figure 7.6. (a) Top and (b) side views of the gradient heater. A sample is placed between two heating elements, each of which is composed of a ceramic bar with heating wires wound around it. Reproduced with permission [27]. Copyright 2020, International Union of Crystallography.

In order to generate a target temperature gradient within the sample, it is necessary to select an appropriate geometric configuration of the heat element, including the groove spacing. Although it is possible to experimentally determine these uncertain parameters by trial and error, it is time consuming, especially when multiple temperature gradients are needed. To this end, we proposed a coupled heat transfer and Joule heating model to describe the heating transfer between and within heating elements and sample, as well as the resistive heating of the wires. Model parameterization is conducted by matching the predicted thermal profile of the sample to that of a NaCl/Si sample powder heated by an initial design of the gradient heater, which produces a linear temperature gradient within the sample. Hereafter, we refer to this furnace design as Mark 1 design. We then utilize this parameterized model to study the effect of wiring configuration, ceramic bar width, as well as the position of the sample on the resulting thermal profiles.

7.3.2 Simulation method for gradient-heater modeling

We implement the coupled heat transfer and Joule heating model in COMSOL Multiphysics® [89]. The simulation geometry consisted of NaCl/Si sample powder mixture placed between two heating elements, as shown in Figure 7.6(b). The thermal conduction between the surfaces of wires and heating elements that are in direct contact, as well as within the bulk of each

object, is described by Equation (2.14). For the heating elements and the sample, $Q = 0$. For the wires, Q is the power density from Joule heating, as described by [86,209]

$$Q = \boldsymbol{i} \cdot \boldsymbol{E} = \kappa |\nabla \phi|^2, \tag{7.10}$$

where $\boldsymbol{i}$ is the current density, $\boldsymbol{E}$ is the electric field, κ is the electrical conductivity, and ϕ is the electric potential. Surface-to-surface thermal radiation [87,88] is considered between each pair of surfaces facing each other but not in direct contact. The surfaces of the heating elements and wires that are not facing each other or facing the sample radiate energy to the surrounding environment. Therefore, surface-to-ambient thermal radiation is considered for those surfaces using Equation (2.20). For all the surfaces of the heating elements that are in contact with the air, Newton's law of cooling with constant heat transfer coefficient is applied using Equation (2.15), where h is an uncertain parameter.

The heat transfer mechanisms considered in the model are surface-to-surface radiation, conduction, and Newton's law of cooling. For the simplicity in building the geometry, the wire is approximated as a square rod, rather than a cylinder. We assume that two sides of the wire are in perfect contact with the grooves, and thus heat conduction is applied for these boundaries. The remaining two sides of the wire that are not in contact with the grooves radiate heat to the heating elements and the sample. We assume that the quartz capillary is transparent to radiation and that heat conduction between the sample and the quartz capillary is poor; therefore, the capillary is omitted in the model. We also omit the sample holder from the simulation geometry because it is not in direct contact with the sample but rather it is separated from the sample by the capillary.

7.3.3 Parameterization of the heat-transfer model

The simulated sample temperature values are averaged along the direction of the X-ray beam, which is along the *y*-direction in Figure 7.6(b). We manually tune the uncertain parameters

such that the resulting simulated temperature profile matches that obtained in the experiment with Mark 1 furnace. The parameters are summarized in Table 7.3. The simulated temperature profile with optimized parameters, is shown in Figure 7.7, along with the temperatures measured in the experiment. As can be seen in the figure, the thermal profile predicted by the heat transfer model is in good agreement with the experimentally measured thermal profiles.

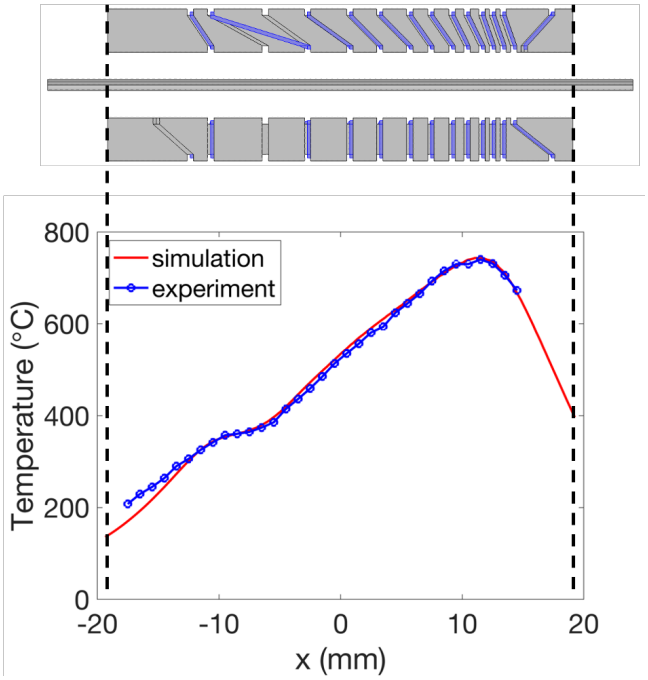

Figure 7.7. The simulated (red) and experimental (blue) temperature profiles. The edges of the heating elements are indicated by the vertical dashed lines. Reproduced with permission [27]. Copyright 2020, International Union of Crystallography.

7.3.4 Controlling the temperature profile

The temperature range spanned by the gradient heater depends on the degree to which the wire spacing varies across the heater. A larger variation in the wire spacing corresponds to a greater temperature range for the same maximum temperature. Three simulations were conducted to examine the temperature profile when the resistive wires are configured in differently, as shown in Figure 7.8. The heating element for Mark 2A has a smaller variation in the wire spacing (with a maximum distance, D of 6.7 mm between the centers of two grooves) than that for Mark 2B (D

= 8.2 mm), followed by Mark 2C (D = 11.4 mm). The minimum distance between the centers of two grooves for the three heating elements are identical. The simulation suggests that a greater temperature span can be achieved with a larger variation in the wire spacing.

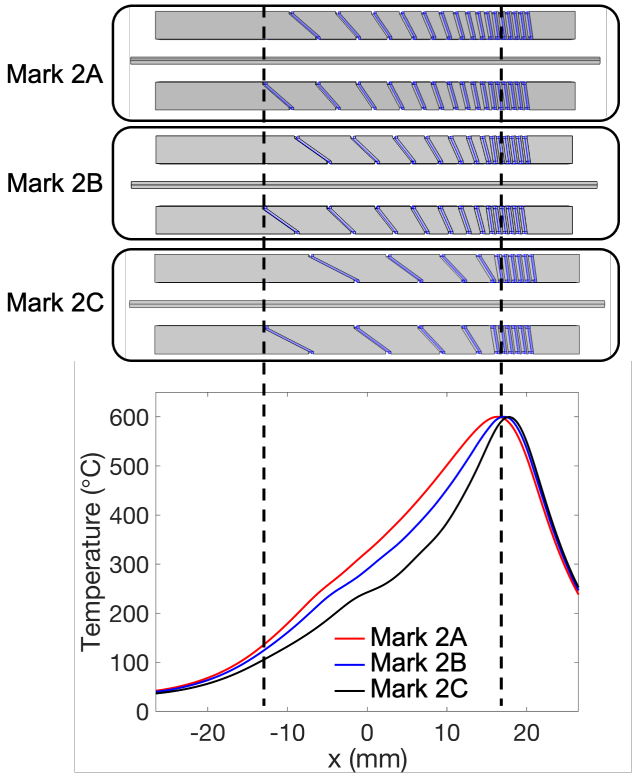

Figure 7.8. The simulated temperature profiles of the sample between two heating elements with various winding configurations. Reproduced with permission [27]. Copyright 2020, International Union of Crystallography.

Simulations were then undertaken to explore the impact of the ceramic bar width on the temperature profile. The simulated temperature profiles, as shown in Figure 7.9, suggests that a wider surface of ceramic bar affords a smoother, more uniform, temperature profile along the sample. This effect is likely due to a smoother temperature profile along the centerline of the surface of the ceramic bar facing the sample afforded by the greater distance from the sides of the ceramic bar where heat loss occurs.

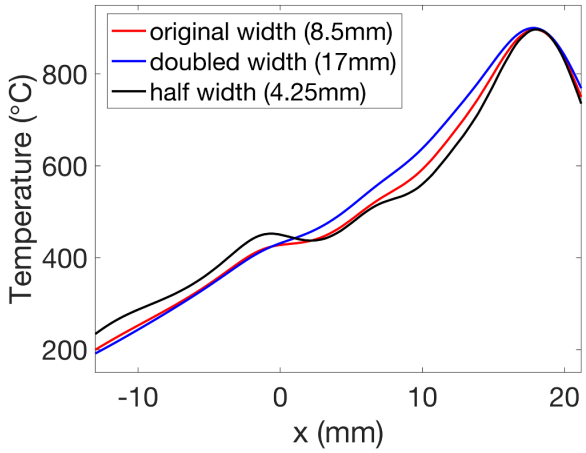

Figure 7.9. The simulated temperature profiles of the sample between two heating elements with different widths of the heating elements (Mark 2C). Reproduced with permission [27]. Copyright 2020, International Union of Crystallography.

We examined the temperature profile of the sample when the sample is offset from the center of the gradient heater (see Figure 7.10). Offsets up to 1 mm results in negligible change in the temperature profile. This offset is much larger than the error in alignment permitted by the cell design, demonstrating that small misalignment would not alter the temperature profile of the sample. By contrast, temperature errors of tens of degrees were observed when the capillary is offset by 3 mm (*i.e.,* within 1 mm of the edge of the ceramic bar). This reflects the benefits of the wide ceramic bar with a rectangular cross section for more robust temperature control.

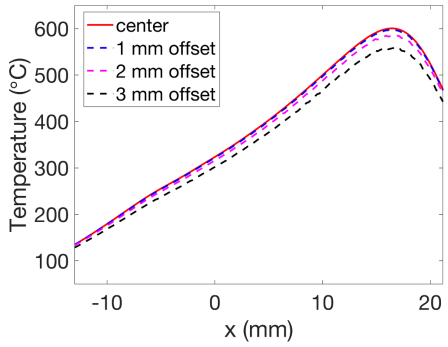

Figure 7.10. The effect of sample being offset in the y-direction (Mark 2A). Reproduced with permission [27]. Copyright 2020, International Union of Crystallography.

Table 7.3. The parameters employed in the simulation, as well as their literature values and sources where available, are presented. The temperatures associated with the literature values ranged from 20°C to 1000°C, which are provided along with parameter values. Reproduced with permission [27]. Copyright 2020, International Union of Crystallography.

Parameters	**Values employed in the model**	**Units**	**Source**	**Range of values**
Ceramic bars				
Heat capacity	7.75×10^2	J / (kg · K)	Literature*	7.75×10^2 (@25 °C, Al_2O_3) – 1.27×10^3 (@976.85 °C, Al_2O_3) [210]
Thermal conductivity	0.55	W / (m · K)	Fitting	0.1 (@ 298.15 °C, Al_2O_3) [211] – 2.0 (@726.85 °C, silica) [212]
Density	1.2×10^3	kg / m^3	Experiment	1.2×10^3
Surface emissivity	0.3	--	Fitting	0.2 (oxidized aluminum) – 0.79 (silica) [213]
Heat transfer coefficient	33	W / (m^2 · K)	Fitting	0.5 – 10^3 [214]
For parameterization				
Length	38.7	mm	Experiment	38.7
Width	3.6	mm	Experiment	3.6
Depth	8.4	mm	Experiment	8.4
For Mark 2A, 2B, and 2C				
Length	53	mm	--	--
Width	3.5	mm	--	--
Depth	8.5	mm	--	--
Heating wires				
Heat capacity	4.6×10^2	J / (kg · K)	Literature*	4.6×10^2 (@20 °C) – 7.2×10^2 (@1000 °C) [215]
Thermal conductivity	20	W / (m · K)	Fitting	11 (@50 °C) – 26 (@1000 °C) [215]
Density	7.1×10^3	kg / m^3	Literature	7.1×10^3 [215]
Surface emissivity	0.7	--	Literature	0.7 [215]

* The lower bound from the literature is selected.

Electrical conductivity	Interpolation*	S / m	Literature	6.63×10^5 (@1000 °C) – 6.90×10^5 (@20 °C) [215]
Cross-sectional area	8×10^{-2}	mm^2	Literature	8×10^{-2} [216]
Heat transfer coefficient	33	$W / (m^2 \cdot K)$	Fitting	0.5 – 10^3 [214]
Applied voltage (for parameterization)	16	V	Experiment†	16 – 19
Applied voltage (for Mark 2A)	14.95	V	--	--
Applied voltage (for Mark 2B)	13	V	--	--
Applied voltage (for Mark 2C in Figure 7.10(a))	10.85	V	--	--
Applied voltage (for Mark 2C, original width in Figure 7.10(b))	16	V	--	--
Applied voltage (for Mark 2C, doubled width in Figure 7.10(b))	24	V	--	--
Applied voltage (for Mark 2C, half width in Figure 7.10(b))	12.6	V	--	--
NaCl/Si mixture sample powder				
Heat capacity	8.6×10^2	$J / (kg \cdot K)$	Literature*	8.6×10^2 (@31.25 °C, NaCl) – 1.0×10^3 (@499.35 °C, NaCl) [217]
Thermal conductivity	0.35	$W / (m \cdot K)$	Fitting	0.13 (@26.85 °C, NaCl) [218] – 1.56×10^2 (@26.85 °C, Si) [219]
Density	2.17×10^3	kg / m^3	Literature*	2.17×10^3 (NaCl) [220] – 2.32×10^3 (Si) [221]
Surface emissivity	0.45	--	Fitting	0.1 (@269.85 °C, Si) – 0.7 (@599.85 °C, Si) [222,223]

* The temperature-dependent electrical conductivity in our model is interpolated using piecewise cubic functions based on the data in the literature.
† The lower bound from the experimental values is selected.

Radius	0.45	mm	Experiment	--
Distance between surfaces of two heating elements that face each other	6.35	mm	Experiment	--
Length (for parameterization)	50	mm	Estimated*	--
Length (for Mark 2A, 2B, and 2C)	60	mm	--	--

7.3.5 Conclusion for gradient-heater modeling

We presented a coupled heat transfer and Joule heating model to predict the temperature profiles within a sample that is heated by a recently proposed gradient heater. The model considers the resistive heating of the wires, the heat transfer due to thermal conduction and surface-to-surface radiation, as well as the heat loss due to natural air convection and surface-to-ambient radiation. We show that the model accurately reproduces the thermal profiles for a NaCl/Si sample heated by a Mark 1 furnace after parameterizing the model. Moreover, we examined the effect of winding configuration, ceramic bar width, and sample position on the resulting temperature profiles, using the parameterized model. Specifically, we found that (1) a larger variation in the wire spacing yields a greater temperature span, that (2) a wider surface of ceramic bar affords a smoother and more uniform temperature profile, and that (3) offsets of the sample from the center of the gradient heater up to 1 mm results in negligible change in the temperature profile. By leveraging the machine learning algorithm, this model can also be used to efficiently and effectively determine the groove spacing required to generate a targeted temperature gradient.

* The length of the sample was measured in comparison with the heating elements; the length value does not influence the resulting thermal profile if it is longer than the heating elements.

Chapter 8 Phase-Field Crystal Modeling of Two-Dimensional Materials

8.1 Introduction

Due to their promising technological applications, interest in research and development of 2D materials has grown in recent years [224-226]. Graphene-based materials are already starting to appear in products such as batteries, headphones, and sports equipment. While research have primarily focused on experimental synthesis and characterization of these materials [227-230], there has also been computational modeling aimed at understanding and controlling the mechanisms that influence the formation of defects during their synthesis [231,232]. Considering the typical length scales and time scales involved in this process, the phase-field crystal (PFC) model [233-235] is a promising alternative to traditional atomistic models for examining defect formation and evolution. This approach has advantages over molecular dynamics simulations, which is limited in both the spatial and temporal scales that can be simulated. It also presents an advantage over traditional phase-field models because it retains atomic features, such as crystalline lattices and defects. Furthermore, the PFC model allows for a systematic coarse-graining approach based on the so-called amplitude expansion method, enabling simulations of larger systems. Existing applications of PFC and amplitude expansion methods include studies of pre-melting of grain boundaries [236,237], dislocation dynamics [237-239], glass formation [240-242], order-disorder phase transitions [243], and structural transformations in binary and ternary alloys [244].

The PFC approach has already been applied to 2D materials. Most studies so far have focused on graphene, the first 2D material that was successfully synthesized and is known to possess high tensile strength and excellent thermal and electrical conductivities [245-248]. In

addition, the PFC model variant required to simulate graphene is relatively simple since it involves only one component. Different approaches have been developed to simulate the honeycomb structure of graphene with the PFC and amplitude expansion models [249-252]. In Ref. [252], Hirvonen et al. performed a comparison of the types of defects and their energies in these models. They compared these results with molecular dynamics (MD) and quantum-mechanical density functional theory (DFT) calculations. In other studies, amplitude expansion [250,253,254] models have been applied to examine the patterns that arise from interactions of 2D films with a substrate. Other applications of the PFC and amplitude models to 2D materials can be found in Refs. [255-260]. However, all of these models are implemented in a 2D computational domain with two coordinates corresponding to those in the plane of the 2D material, and three-dimensional effects are either ignored or accounted for in an indirect manner. For instance, in Ref. [250], interactions between a 2D material and the substrate are modeled via an external effective potential in the PFC free energy. Additionally, experimental and computational observations of out-of-plane buckling near defects [232,261-264] cannot be described by simulations confined in a flat 2D computational domain. Some PFC models [265-269] have been developed to describe particles confined in curved 2D domains. However, these models require simultaneously solving for the PFC order parameter and the phase field that describes the surface. More recently, Elder et al. introduced a PFC model [270] capable of describing out-of-plane deformations in single and multilayer systems using a single-valued field that represents local height with respect to a reference plane. This model has been applied to describe buckling in stacked layers of graphene and hBN [270], out-of-plane fluctuations in free-standing graphene [271,272] and out-of-plane deformations for hBN and graphene/hBN bilayers [273]. This approach, however, does not directly represent atoms in a three-dimensional space, which would be required for studying the mechanical behavior of 2D

materials with more complex structures, such as MoS_2 in which the atoms are not all in the same plane.

Inducing a periodic structure that is confined in the third dimension is challenging within the framework of existing PFC models. Atomic periodicity in traditional PFC models is achieved by including interaction terms in the free energy. These terms can be expressed either as a convolution of a two-point correlation function with the order parameter [274,275] or as an expansion of this convolution in powers of the gradient of the order parameter [235,249]. This type of free energy is traditionally formulated such that it is minimized by either a homogeneous state (a state in which the order parameter is constant throughout the system) or a periodic (crystalline) state that extends in all directions of the system, neither of which is confined within a lower-dimensional layer. Therefore, in this chapter, we introduce a PFC free energy that includes a confining term in the correlation function, allowing for the description of two-dimensional materials in three dimensions.

8.2 Method

8.2.1 Free energy

We start with the general expression for the free energy of the PFC model that includes up to pair-wise interactions, which is given by [235]:

$$F(n) = \int_V \left(\frac{n^2}{2} - \eta \frac{n^3}{6} + \xi \frac{n^4}{12} \right) d\boldsymbol{r} - \frac{1}{2} \int_V n(\boldsymbol{r}) \int_V C_2(\boldsymbol{r} - \boldsymbol{r}') n(\boldsymbol{r}') d\boldsymbol{r}' d\boldsymbol{r}, \tag{8.1}$$

where n is an order parameter defined as $n = (\rho - \rho_0)/\rho_0$, *i.e.*, a density rescaled with respect to a reference density, ρ_0. We take $\eta = \xi = 1$, which arises from the Taylor expansion of the free energy in the classical density functional theory [235]. The first integral in Equation (8.1) represents an ideal contribution, while the second integral represents the contribution from two-

body interactions. The function C_2 is the two-point correlation function, which determines the crystal structure that minimizes the free energy, *i.e.*, the equilibrium structure. Our approach is to design this correlation function to energetically favor confinement in one of the directions and periodicity in the other two directions.

8.2.2 Two-point correlation function

We define a two-point correlation function in reciprocal space that contains two contributions: (1) an isotropic contribution that sets the main interplanar spacing and, (2) an anisotropic contribution that energetically promotes confinement. Hereafter, we designate the z-axis to be parallel to the direction of confinement (i.e., the z-direction). This direction is perpendicular to the plane in which the atomic density is confined. We define the Fourier transform of this two-point correlation function as

$$\hat{C}_2(\mathbf{k}) = \max\{\hat{C}_{2,p}(\mathbf{k}), \hat{C}_{2,c}(\mathbf{k})\}, \tag{8.2}$$

with $\hat{C}_{2,p}$ and $\hat{C}_{2,c}$ given by

$$\hat{C}_{2,p}(\mathbf{k}) = \hat{C}_{2,p}(k) = A_p \exp\left(-\frac{(k-k_0)^2}{2\sigma_p^2}\right) \tag{8.3}$$

and

$$\hat{C}_{2,c}(\mathbf{k}) = A_c \exp\left(-\frac{k^2}{2\sigma_c^2}\right) \exp\left(-\frac{\theta^2}{2\sigma_\theta^2}\right). \tag{8.4}$$

The term $\hat{C}_{2,p}$, a "periodic" contribution, is a simple Gaussian peak around the wavenumber k_0, which energetically favors a crystal structure with main interplanar spacing $\lambda_0 = 2\pi/k_0$. This form of the correlation function is utilized in the single-peaked XPFC model [275], which yields a triangular structure in 2D and a bcc structure in 3D. The proposed term, $\hat{C}_{2,c}$, a "confining" contribution, consists of two factors: 1) an isotropic Gaussian function centered at $k = 0$, and 2) an angular envelope that maximizes $\hat{C}_{2,c}$ along the z-axis. In Equations (8.3) and (8.4), k is the

magnitude of the wave vector, $\boldsymbol{k}$, θ is the smallest angle between $\boldsymbol{k}$ and the z-axis, σ_p and σ_c are the widths of the periodic and confining Gaussian peaks, respectively, and σ_θ is the width of the Gaussian function that defines the angular envelope for the confining contribution. Finally, A_p and A_c are the heights of the periodic and confining Gaussian peaks, respectively. Figure 8.1(a) and (b) show plots of $\hat{C}_2(\mathbf{k})$ for two- and three-dimensional systems, respectively, using the set of parameters defined in Table 8.1.

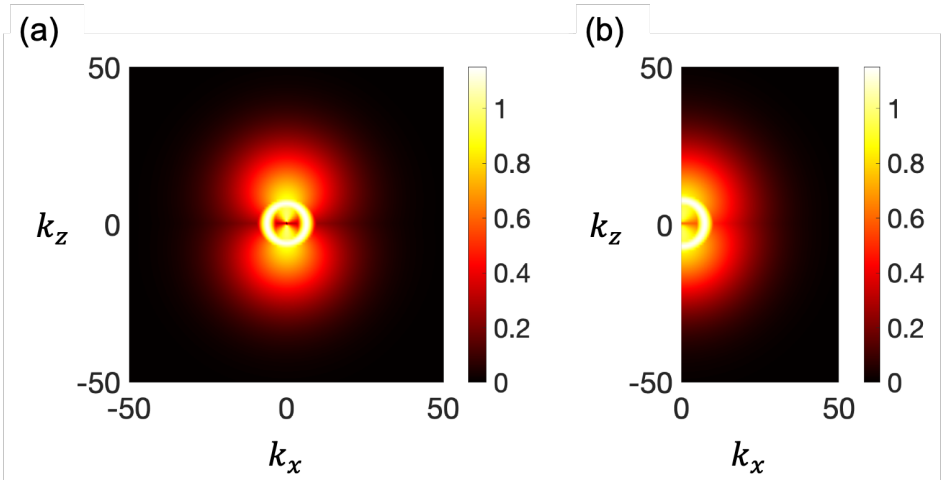

Figure 8.1. Plots for the two-point correlation functions in reciprocal space. (a) The correlation function in 2D. (b) The 2D plot of the 3D correlation function on the $k_x - k_z$ plane. The correlation function features cylindrical symmetry.

Table 8.1. Parameters for the two-point correlation function in 2D and 3D.

Parameter	2D	3D
k_0	2π	$4\pi/\sqrt{3}$
A_p	1.15	1.15
σ_p	$3\pi/5$	$6\pi/(5\sqrt{3})$
A_c	1.0	1.0
σ_c	16.0	16.0
σ_θ	$\pi/3$	$\pi/2$

For all calculations, we select the lattice constant, a_0, defined as the triangle edge length, as the unit length. With the appropriate choice of parameters, the correlation function defined by Eq. (8.2) energetically favors a phase that is periodic along one Cartesian direction in 2D or two Cartesian directions in 3D but is confined in the remaining direction. It is important to note that for the three-dimensional case, $\hat{C}_2(\boldsymbol{k})$ is only anisotropic in the z-direction. Therefore, no particular orientation in the x-y plane is energetically favored. As we show below, $\hat{C}_2(\boldsymbol{k})$ yields a single 1D layer of atom-like bumps in a two-dimensional system and a single 2D layer in three-dimensional system. We also show that a buckled layer can be made more stable than a flat layer with the appropriate choice of the initial conditions and system size in one Cartesian direction perpendicular to the z-direction to induce in-plane compressive stress. This buckling occurs as a mechanism for energy relaxation with respect to the flat state. The isotropic part of the two-point correlation function energetically favors an equilibrium interatomic spacing that cannot be satisfied whenever a flat layer is compressed, creating strain. Therefore, by buckling, the layer can attain interatomic spacing that is closer to the equilibrium value, thereby lowering the strain energy.

8.2.3 Dynamics

In this work, we refer to a state after relaxation as a stationary state because it can either correspond to an equilibrium state or a metastable state. To obtain the stationary state (i.e., an equilibrium state or a metastable state) from a given initial configuration, we evolve the system under globally conserved dynamics. While this dynamics will not necessarily predict the path of the evolution correctly, it is numerically more efficient than locally conserved dynamics and

captures the equilibrium state accurately. The governing equation for globally conserved dynamics is given by

$$\frac{\partial n}{\partial t} = -M\left(\frac{\delta F}{\delta n} - \frac{1}{V}\int_V \frac{\delta F}{\delta n}\, d\mathbf{r}\right), \tag{8.5}$$

where $\delta F / \delta n$ is the variational derivative of the free energy defined in Equation (8.1), given by

$$\frac{\delta F}{\delta n} = n - \frac{\eta}{2}n^2 + \frac{\xi}{3}n^3 - C_2 * n, \tag{8.6}$$

and $C_2 * n$ indicates the convolution between C_2 and n. The globally conserved dynamics of Equation (8.5) ensures that the average order parameter, n_0, remains constant throughout the simulation.

8.2.4 Initial conditions

In this section, we discuss the choice of initial conditions for 2D and 3D simulations. The values of the parameters chosen for the equations describing each initial condition are summarized in Table 8.2.

Table 8.2. Parameters for the initial conditions in 2D and 3D, and reference energy (last row) for all of the cases considered.

Parameters	2D Unstrained	2D Compressed	3D Unstrained	3D Compressed
N_x	17	17	17	17
N_y	N/A	N/A	4	4
Δx	0.0266	0.0256	0.05	0.05
Δy	0.0250	0.0250	0.0495	0.0495
Δz	N/A	N/A	0.05	0.05
B_{init}	1.7	1.7	1.7	1.7
σ	1/4	1/4	1/4	1/4
n_0	−0.35	−0.33	−0.39	−0.36
B_α	0.7	0.1	0.7	0.1
ϵ_x	0	−3.53%	0	−4.71%
F_0	9.47191	8.059327	82.7890	66.4224

We begin by defining $\boldsymbol{r}_{\parallel}$ as any direction parallel to the plane of confinement. We denote L_x, L_y, and L_z as the system size along the *x*-, *y*-, and *z*-directions, respectively, and Δx, Δy, and Δz as the grid spacing along the *x*-, *y*-, and *z*-directions, respectively. The dimensions of the conventional unit cell for a triangular lattice are $a_x = a_0$ and $a_y = \sqrt{3}a_0$. We define N_x as the number of units a_x along the *x*-direction and N_y as the number of units a_y along the *y*-direction. For all systems considered (in 2D and 3D), we employ the following expression to describe the initial (unnormalized) order parameter profile corresponding to a single layer of monoatomic thickness:

$$n_{init}^{u}(\mathbf{r}) = B_{init}E(z)P(\mathbf{r}_{\parallel}), \tag{8.7}$$

where B_{init} is a positive constant. The term $E(z)$ is a Gaussian envelope to confine the order parameter along the z-direction. We define this envelope as

$$E(z) = \exp\left\{-\frac{1}{2\sigma^2}[z - \alpha(x)]^2\right\}, \tag{8.8}$$

where σ is the width of the Gaussian envelope. The function $\alpha(x)$ is the position of the center of atoms. If $\alpha(x)$ is set to a constant value, the initial layer is flat, while a nonuniform $\alpha(x)$ yields a perturbation from the flat state. For all of the perturbed initial conditions, we choose a sinusoid along the *x*-direction. The wavelength of this perturbation is chosen to be L_x, *i.e.*, the system size in the *x*-direction. Thus, $\alpha(x)$ can be written as

$$\alpha(x) = \frac{L_z}{2} + B_{\alpha}\, sin\left(\frac{2\pi}{L_x}x\right), \tag{8.9}$$

where B_{α} is the amplitude of the perturbation, and L_z is the system size along the *z*-direction. Note that the constant $L_z/2$ centers the monolayer in the midpoint of the computational domain along the *z*-direction. In the cases where the system is strained along the *x*-direction, L_x depends on N_x, a_x, and the strain, ϵ_x, in the following manner:

$$\epsilon_x = \frac{L_x - N_x a_x}{N_x a_x} \tag{8.10}$$

or

$$L_x = (\epsilon_x + 1) N_x a_x. \tag{8.11}$$

The term $P(\boldsymbol{r}_\parallel)$ in Equation (8.7) sets the initial atomic periodicity along $\boldsymbol{r}_\parallel$. For a 1D layer in a 2D system, where $\boldsymbol{r}_\parallel = x$, the periodic contribution is defined as

$$P(x) = \cos(k_0 x) = \frac{1}{2} + \frac{1}{2}\cos\left(\frac{2\pi}{\lambda_p} x\right), \tag{8.12}$$

where λ_p is the interplanar distance. For a 2D layer in a 3D system, where $\boldsymbol{r}_\parallel = (x, y)$, the periodic contribution is chosen to represent a triangular lattice. For this lattice structure, the system dimensions along the *x*- and *y*-directions must satisfy Equation (8.11) and $L_y = N_y a_y$. We employ a one-mode approximation to represent the triangular lattice structure:

$$P(\mathbf{r}_\parallel) = \frac{1}{3} + \frac{2}{9}[\cos(\boldsymbol{k_1} \cdot \boldsymbol{r}_\parallel) + \cos(\boldsymbol{k_2} \cdot \boldsymbol{r}_\parallel) + \cos(\boldsymbol{k_3} \cdot \boldsymbol{r}_\parallel)], \tag{8.13}$$

where $\boldsymbol{k_1} = (0,1)\boldsymbol{k_0}$, $\boldsymbol{k_2} = \left(\frac{\sqrt{3}}{2(\epsilon_x+1)}, -\frac{1}{2}\right)\boldsymbol{k_0}$, and $\boldsymbol{k_3} = \left(-\frac{\sqrt{3}}{2(\epsilon_x+1)}, -\frac{1}{2}\right)\boldsymbol{k_0}$. The factor $\frac{\mathbf{1}}{\epsilon_x+1}$ is employed to adjust the lattice spacing to accommodate all atoms in the compressed system. In each instance, the initial order parameter defined in Equation (8.7) must be normalized such that its average is equal to average order parameter value, n_0. The normalized order parameter is thus calculated as

$$n_{init}(\mathbf{r}) = n^u_{init}(\mathbf{r}) - \langle n^u_{init}(\mathbf{r})\rangle + n_0, \tag{8.14}$$

where the angular brackets, $\langle \cdots \rangle$, denote spatial averaging.

8.3 Results and discussions

We summarize the results of the relaxation via Equation (8.5) of an initially perturbed planar layer of monoatomic thickness within a computational domain in two and three dimensions.

For each case, we examine two systems of different sizes. First, we consider a system with size that is selected to yield a stationary (i.e., corresponding to a local energy minimum) unstrained flat layer. Hereafter, we refer to a system of this type as "unstrained." Second, we consider a system that is shorter in one direction (set as the x-direction) than the unstrained system. We refer to a system of this type as "compressed."

For each simulation, regardless of whether the system is unstrained or compressed, we found that a flat periodic state is always obtained after relaxation from unperturbed initial conditions ($B_\alpha = 0$). This is due to the fact that the flat periodic state is in either metastable or unstable equilibrium. Thus, in order to obtain a buckled state, an out-of-plane perturbation with amplitude $B_\alpha > 0$ must be imposed as the initial condition. Whenever a buckled state is found after relaxation, we calculate the relative energy of this state with respect to a reference, $\Delta F_b = F_b - F_0$. We take the reference energy, F_0, to be that of a homogeneous state with a constant order parameter equal to n_0 throughout the system. This energy depends on n_0 and the system size. The values of F_0 for all cases are reported in Table 8.2. We also evaluate the corresponding relative energy of the flat periodic state obtained from unperturbed initial conditions, $\Delta F_f = F_f - F_0$ with respect to the same reference. The two relative energies, ΔF_b and ΔF_f, are then compared to each other to confirm whether the buckled periodic state (obtained from the initially perturbed layer) is truly energetically preferred over the flat periodic state.

We first consider the two-dimensional relaxation of an unstrained system. The initial condition for this case has a relatively large sinusoidal perturbation (see Figure 8.2(a)). As shown in Figure 8.2(b), the state obtained after relaxation is a flat layer of atoms elongated in the z-direction. For the stationary flat periodic state obtained after relaxation of the initial condition depicted in Figure 8.2(a), the calculated relative energy is $\Delta F_f \simeq 3.669 \times 10^{-2}$. Note that the sign

of ΔF indicates the relative stability as compared to the homogeneous state. In this case, since $\Delta F_f > 0$, the relaxed flat periodic state is not the equilibrium state (the state with the absolute minimum energy) of the system; rather, the homogeneous state (in which the order parameter is uniform throughout the system) has a lower energy. Indeed, we have observed that the system does not evolve to the flat periodic state when initial conditions are not sufficiently near the flat periodic state. However, we have observed that the flat periodic state, although strictly not in equilibrium, has a high range of metastability and remains stable against relatively large perturbations.

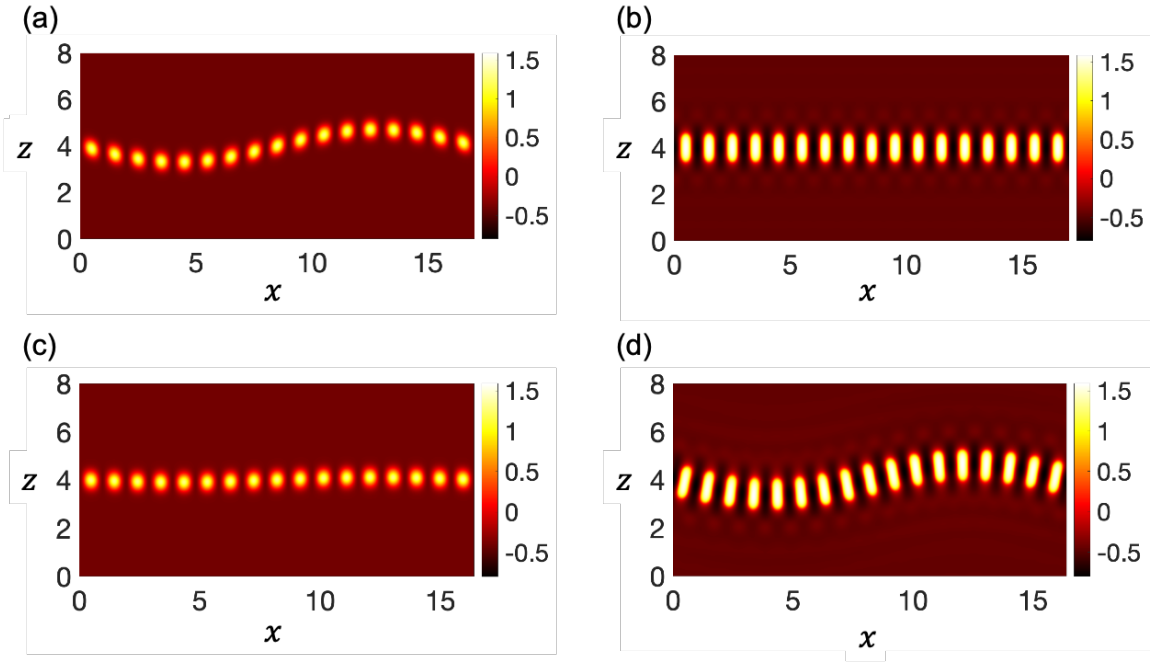

Figure 8.2. Relaxation of 2D systems into flat and buckled 1D monolayers. (a) Initial condition in unstrained system. (b) Stationary flat layer after relaxation. (c) Initial condition in compressed system. (d) Stationary buckled layer after relaxation.

We then consider the relaxation of a compressed system. The initial condition, shown in Figure 8.2(c), was set to a similar sinusoidal perturbation as the one for the unstrained system, but with a smaller amplitude. In this case, the stationary state obtained after relaxation is a buckled layer of atoms, as shown in Figure 8.2(d). The relative energy of the stationary buckled periodic

state with respect to the reference, is $\Delta F_b \simeq -1.692 \times 10^{-3}$. The relative energy of a stationary flat periodic state is $\Delta F_f \simeq 2.873 \times 10^{-3}$. Given that $\Delta F_b < \Delta F_f$, the buckled periodic state is energetically preferred over the flat periodic state.

We apply the same approach to model a 2D monolayer of atoms in a 3D computational domain. The procedure described above is followed to obtain stationary flat and buckled states and evaluate their energies. We first consider the relaxation of an unstrained system in 3D. The initial condition for this case has a relatively large sinusoidal perturbation. The stationary state after relaxation is a flat monolayer of triangular structure with elongated atoms, as shown in Figure 8.3(a). The relative energy for the stationary flat triangular layer is $\Delta F_f \simeq 0.1182$. As with the unstrained 2D case, this energy is positive, which indicates that the flat triangular layer does not correspond to the equilibrium state. However, we also confirmed that this state remains stable against small perturbations.

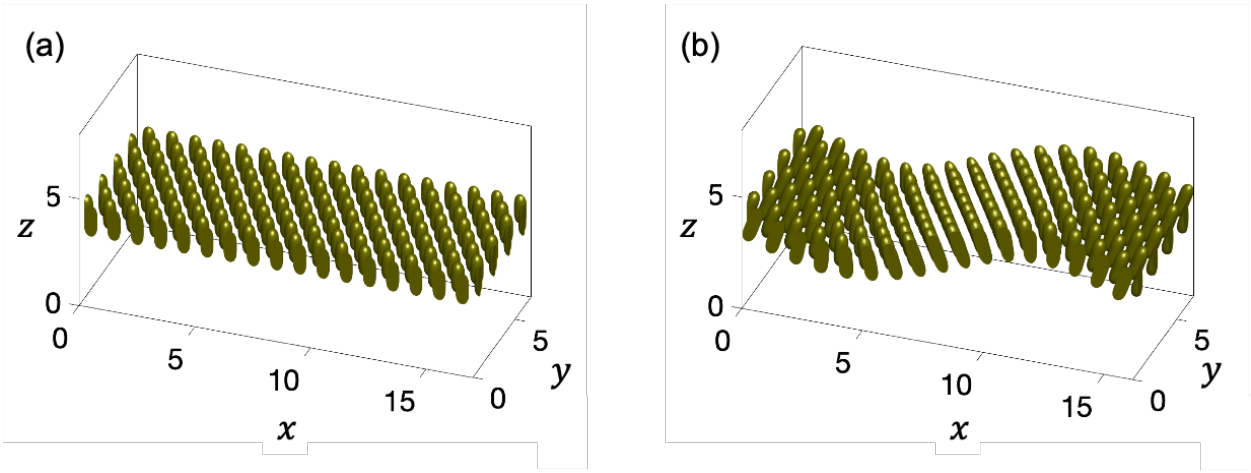

Figure 8.3. Relaxation of 3D systems into flat and buckled 2D monolayers. (a) Stationary flat layer after relaxation of a perturbed unstrained system. (b) Stationary buckled layer after relaxation of a perturbed compressed system.

The last case we consider is the relaxation of a compressed system in 3D. The initial condition for this case has a relatively small sinusoidal perturbation. Figure 8.3(b) shows the

stationary state after relaxation, which corresponds to a buckled layer of triangular structure. The relative energy of the stationary buckled state is $\Delta F_b \simeq -0.8017$. The relative energy of the stationary flat triangular state, obtained via the relaxation of a flat initial condition is $\Delta F_f \simeq -0.6532$, which is higher than that of the buckled state. Therefore, as with the 2D case, the buckled triangular state is energetically preferred over the flat triangular state.

8.4 Preliminary work on model validation

To examine the mechanical behavior of the monolayer (i.e., out-of-plane deformation vs. uniaxial compressive strain), we perform the 3D simulation using the PFC model for a set of strain values within the range [-0.06, 0], with a step size of 0.0025. We identify the amplitude of the resulting sinusoidal out-of-plane displacement as a function of the magnitude of the strain, following the procedures detailed below. First, we utilize the function "imregionalmax" in MATLAB® to determine the positions of the peak values in the order parameter. For each peak, a $5 \times 5 \times 5$ region is extracted to fit the order parameter values using a second-order polynomial of $x, y,$ and z, which is used to determine the more precise value of the peak position. We then average all the peak positions in the x-z plane for the peaks aligned along the y direction. To do so, for the peaks that are within 0.01 from each other in the x and z directions, we average the values of x and z positions, which yields z positions as a function of x. We select four points having the largest z values and fit a second-order polynomial of x to identify the largest displacement of the layer in the positive z direction. Similarly, we fit four points having the smallest value of z to obtain the largest displacement in the negative z direction. Finally, the amplitude of the out-of-plane displacement is estimated to be a half of the difference between the maximum and minimum z values determined above. The amplitude as a function of the magnitude of the strain is shown by the black curve in Figure 8.4. It is worth noting that no apparent out-of-

plane deformation is observed until the magnitude of the strain reaches a transition threshold at approximately 0.01 and that the amplitude of the displacement monotonically increases as the magnitude of the strain continues to increase.

To confirm that the buckling behavior observed in Figure 8.4 is expected, rather than a model artifact, we utilize the plate module in COMSOL Multiphysics® software [89] to calculate the relationship between the amplitude of the out-of-plane displacement and the magnitude of the compressive strain for a thin graphene-like plate as a benchmark. The Young's modulus and Poisson' ratio are reported to be 1 TPa [276] and 0.19 [277], respectively, which are used in the calculation but do not affect the results presented below. To construct the domain similar to that of the PFC monolayer, we set the size of the thin plate in terms of the hexagonal edge length (equivalent to the triangle edge length in the PFC simulations and therefore denoted by a_0), which is reported to be ~1.4 Å [278] for graphene. The length (along x), L, width (along y), W, and the thickness (along z), d, of the plate are set to $17a_0$, $4\sqrt{3}a_0$, and a_0, respectively. The thickness here is taken to be the same as the hexagonal edge length for simplicity, but it should be noted that this value is smaller than the range for the measured thickness of graphene monolayer in literature [279]. The compressive strain, ϵ_x, is imposed by fixing one side of the plate along the length direction and prescribing a displacement of $17\epsilon_x a_0$ on the other side. The stationary structure of the plate is obtained by solving

$$\nabla \cdot (FS)^T + \boldsymbol{F}_V + 6(\boldsymbol{M}_V \times \boldsymbol{n})\frac{z}{d} = 0, \tag{8.15}$$

where F is the deformation gradient, S is the second Piola-Kirchhoff stress tensor, $\boldsymbol{F}_V$ is the body force with respect to the undeformed volume, $\boldsymbol{M}_V$ is the total reaction moment, $\boldsymbol{n}$ is the unit normal vector, and z is the local coordinate along the thickness direction. We note that the value of a_0

does not alter the results as long as the ratio between the plate thickness and the plate length (in the direction of the uniaxial strain) are maintained.

With this plate model, the amplitude of the out-of-plane displacement, scaled by the thickness of the plate, can be calculated as a function of the magnitude of the compressive strain, which is shown by the blue curve in Figure 8.4. A transition from the flat state to the buckled state is observed around 0.01 in the strain magnitude (between 0.01 and 0.0125). The PFC result is in close agreement with the plate model in term of the threshold value (around 0.01). However, the amplitude of the out-of-plane displacement is overestimated by the PFC model beyond the transition to the buckled state. This disagreement may be attributed to the fact that the PFC model exhibit thickening of the monolayer (each peak elongates in the out-of-plane direction), making the effective thickness of the monolayer to be greater than a_0 (triangular edge length). However, in plotting Figure 8.4, we have assumed that the thickness is equal to a_0. If a larger value of d was employed in scaling, the result would be smaller than the values presented in Figure 8.4. Further investigation is required to understand the discrepancy in the amplitude of the out-of-plane displacement.

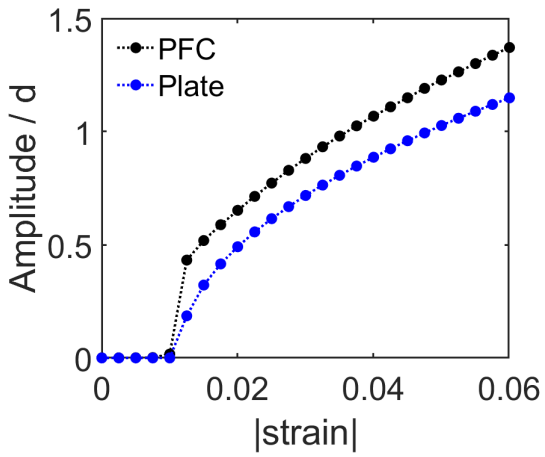

Figure 8.4. The amplitude of the out-of-plane displacement, scaled by the plate thickness, as a function of the magnitude of the compressive strain. The curves in black and blue indicate the data obtained by the PFC model and the plate model, respectively.

8.5 Conclusions

We have introduced a new phase-field crystal model capable of stabilizing single layers in 2D and 3D. We have demonstrated how this approach can simulate layers that buckle as a mechanism for energy relaxation in compressed systems. Through careful parameterization and further refinement, this model could become a powerful tool to study other three-dimensional effects in 2D materials, such as buckling around defects formed at grain boundaries and effects associated with a 2D layer interacting with a substrate. Moreover, by adding an additional order parameter, the model can be readily extended to simulate binary materials, such as hBN. However, more work is required in order to construct a PFC model for 2D materials with quantitative predictability, including material-specific parameterization for various 2D materials,

Chapter 9 Summary and Future Work

9.1 Summary

In this dissertation, a set of computational models were applied to describe solid-state metathesis (SSM) reactions, stored-energy-driven grain growth, and heat transfer in furnaces. These predictive models enable a better understanding of the phase evolution during the SSM reactions, microstructure evolution within a polycrystalline sample undergoing cyclic heat treatment, as well as the thermal profiles of the sample within the furnaces, facilitating precisely controlled materials synthesis and processing.

In Chapter 3, a phase-field model was developed to track the evolution of mole fractions and phase fractions in diffusion-limited solid-state metathesis reactions [153]. The constraints of mass conservation and charge neutrality was imposed by utilizing Lagrange multipliers. A method was presented to link the mobility of the ionic species to their corresponding diffusion coefficients in the SSM reactions. Additionally, the coupling of the phase-field model with the smoothed boundary method was discussed, which allows for the boundary condition to be imposed on an arbitrarily shaped boundary.

The applications of the above-mentioned phase-field model were described in Chapter 4. First, the phase-field model was utilized to study the effect of mobilities of ions on the reaction dynamics. The simulations show that the type of ions (i.e., cations or anions) with a larger effective mobility dominate the diffusion process. An overall characteristic mobility was formulated, which was found to set the rate of the reaction process [153]. Second, the model was employed to simulate a thin-film reaction for the synthesis of FeS_2. The nonplanar evolution reaction front observed in

the simulation is consistent with the experimental observations by McAuliffe *et al.* [145]. Next, the phase-field simulations were leveraged along with a lattice model to estimate the reaction rates for densified and undensified samples. More reactive neighbors were predicted for each particle in a densified sample, which resulted in a faster reaction [146].

In Chapter 5, a phase-field model was presented to describe the microstructure evolution within polycrystalline samples undergoing cyclic heat treatment. This model considers both the capillary driving force and the driving force due to the stored energy arising from the formation of dislocations during non-isothermal annealing [24]. A distinct yet uniform dislocation density was assigned to each grain. Simulations suggest that a few grains with a medium dislocation density consume their adjacent grains with a higher dislocation density and at the same time are consumed by other adjacent grains with a lower dislocation density, leading to the phenomena of grain translation [24]. This observation provides an explanation for the macroscopic translation of grain centers observed in the experiment [24]. In addition, the driving force due to the stored energy was found to decrease over time, which indicates that cyclic heat treatment is necessary to induce continuous abnormal grain growth [24].

In Chapter 6, the above-mentioned phase-field model was extended to allow for describing a spatially varying dislocation density within each grain. The dislocation density of a grain was assumed to decay exponentially when it consumes neighboring grains, until a baseline dislocation density was reached. Two sets of simulations were conducted. In the first simulation, the initial microstructure and dislocation density were inferred from the experimental measurements of a region that was confined within a nearly static boundary in the experimental dataset [280]. The predicted microstructure evolution within this region was found to closely resemble the experimental observations. A set of large-scale simulations were then conducted to explore the

effect of the cyclic heat treatment on the microstructure evolution. A bimodal distribution of grain sizes was observed after the dislocations were injected three times into the microstructure, indicating that multiple cycles of heat treatment provide a few grains with sufficient driving force to grow abnormally [280].

In Chapter 7, two heat transfer models were presented. The first heat transfer model was implemented to the temperature distribution within a sample in an optical floating zone (OFZ) experiment. The model was parameterized using a machine learning algorithm for this purpose [101]. The parameterized OFZ model accurately reproduced the experimentally measured steady-state thermal profiles, as well as time-dependent behavior of temperature profiles. This model could be employed to predict thermal profiles of a sample as a function of time and position and thus facilitates the understanding of the thermal environment in an OFZ experiment and ultimately guides the experimental design. The second heat transfer model was designed for a gradient heater, which produces a temperature gradient within a sample to facilitate the study of temperature-dependent behavior. The parameterized model accurately reproduced the thermal profiles of a NaCl/Si sample measured in the experiment and was used to study the effect of wire configurations, the width of heating elements, and the sample position on the resulting thermal profiles.

Chapter 8 presents a work in developing a phase-field-crystal model for two-dimensional materials. A two-point correlation function that induce periodic arrangements in plane and a confinement in the out-of-plane direction are introduced. The model was utilized to obtain both flat and buckled triangular monolayers of atoms. This model could be further refined to study other three-dimensional effects in two-dimensional materials, such as buckling that occurs around defects formed at grain boundaries.

9.2 Future work

9.2.1 Study of complex metathesis reactions

The phase-field model discussed in Chapter 3 and Chapter 4 makes three major assumptions. First, the diffusivities of the ions were assumed to be a constant, regardless of the phases they belong to. Their diffusivities, however, are typically smaller in product phases than in precursor phases, which could lead to reduction in reaction rates as the reaction proceeds. Therefore, it is necessary to assign each ion with a phase-dependent mobility to enable quantitative predictions for reaction dynamics. Second, the molar volume of each phase was assumed to be proportional to the number of their constituent ions. For a simple reaction in which all the phases have the same number of constituent ions, the molar volumes for all the phases were considered identical with this assumption. Although this assumption allows for a simpler model formulation and still yields qualitatively reasonable reaction dynamics, different phases in general do not possess the same molar volumes. The next step is to incorporate the molar volume difference between phases into the model. Third, the present model considered a free energy landscape with two local minima, which was sufficient to describe a reaction with two stable products. It is, however, unable to simulate a reaction with more products or with intermediate compounds. A more realistic free energy landscape, either inferred from experimental data or calculated from the density functional theory, could be employed to describe these complex reactions.

9.2.2 Dislocation generation and recovery in microstructure evolution

In Chapter 5 and Chapter 6, the density of dislocations expected to be generated during one cycle of heat treatment were assigned to each grain before the microstructure evolution takes place. There are no additional dislocations being injected during the process of the microstructure

evolution. However, these dislocations in reality are formed from time to time throughout the non-isothermal annealing. Thus, a dynamic scheme that continuously injects dislocations to the microstructure should be incorporated into the model as the next step. In addition, the present model does not allow dislocation density to evolve due to recovery and other mechanisms, which may alter the dislocation density distribution and subsequent grain growth. The microstructure is progressively healed when the sample is annealed, regardless of the grain boundary migration. A more sophisticated phase-field model could include an additional term in the governing equation to describe this effect.

9.2.3 Optical floating zone (OFZ) experiment with an enclosed gas environment

The OFZ model presented in Chapter 7 assumes that sample is placed in open air, and therefore the heat loss due to convection is simplified as a boundary condition. Our experimental collaborator Peter G. Khalifah's group recently examined the thermal profiles of the sample that was enclosed in a chamber filled with various types of gas, such as helium and argon. It is therefore necessary to couple computational fluid dynamics with the present model to accurately describe the air flow and convection within the enclosed gas.

9.2.4 Extending the capability of the machine learning algorithm

The machine learning algorithm presented in Chapter 2 Section 2.5.2 was demonstrated to be effective in automatically determining uncertain parameters for the OFZ model in Chapter 7 Section 2.5.2. To increase the robustness of this algorithm in dealing with a cost function with multiple local minima, a clustering method could be first applied to separate the initial parameter space into several small regions such that each region only contains one minimum. Then the machine learning algorithm could be applied to determine the locally optimal parameter set in each

of these regions. Finally, the globally optimal parameter set can be obtained by selecting the parameter set that yields the smallest error.

Additionally, application of this machine learning algorithm to other physical models discussed in this thesis could allow for a rigorous determination of the uncertain parameters in the models. For instance, it can be used to determine mobilities of ions in the phase-field model for solid-state metathesis reactions discussed in Chapter 3 and Chapter 4. In this case, the cost function can be defined as the difference between the predicted composition profiles and measured composition profiles at a few selected times. Moreover, the algorithm can be utilized to determine the exact values of the injected dislocation density for each grain during each cycle of non-isothermal annealing discussed in Chapter 5 and Chapter 6. As shown in Chapter 6 Section 6.5.1, although in general the expression consisting of a constant divided by the grain radius provides a reasonably good estimate of the injected dislocation density during each annealing cycle, the injected value could slightly vary due to statistical variations. Optimized values could be determined using the machine learning algorithm by setting the cost function to calculate the difference between the predicted grain locations (represented by order parameters) and the measured grain locations (i.e., grain maps) at a few selected times.

9.3 Conclusion

To summarize, a set of computational models and methods were developed to simulate phase transformations, microstructure evolution, and relaxation of atomic structures during material synthesis and processing. In addition, heat transfer models were employed to assist in sample-temperature control during experiments, and a machine learning algorithm was developed to facilitate the model-parameter optimization. These models and methods, combined with

experiments, provide insights into the process designs for materials with tailored properties, enabling enhanced material properties and performance.

Bibliography

[1] A. J. Martinolich, R. F. Higgins, M. P. Shores, and J. R. Neilson, Chemistry of Materials **28**, 1854, doi:10.1021/acs.chemmater.6b00027 (2016).

[2] A. J. Martinolich, J. A. Kurzman, and J. R. Neilson, Journal of the American Chemical Society **138**, 11031, doi:10.1021/jacs.6b06367 (2016).

[3] A. Wustrow, G. Huang, M. J. McDermott, D. O'Nolan, C.-H. Liu, G. T. Tran, B. C. McBride, S. S. Dwaraknath, K. W. Chapman, S. J. L. Billinge, K. A. Persson, K. Thornton, and J. R. Neilson, Chemistry of Materials **33**, 3692, doi:10.1021/acs.chemmater.1c00700 (2021).

[4] M. R. Sardela, in *Practical Materials Characterization*, edited by M. Sardela (Springer New York, New York, NY, 2014), pp. 1.

[5] L. Lari, S. Steinhauer, and V. K. Lazarov, J Mater Sci **55**, 12897, doi:10.1007/s10853-020-04917-8 (2020).

[6] M. Gemmi, M. G. I. La Placa, A. S. Galanis, E. F. Rauch, and S. Nicolopoulos, Journal of Applied Crystallography **48**, 718, doi:10.1107/s1600576715004604 (2015).

[7] S. Koneti, L. Roiban, F. Dalmas, C. Langlois, A. S. Gay, A. Cabiac, T. Grenier, H. Banjak, V. Maxim, and T. Epicier, Materials Characterization **151**, 480, doi:10.1016/j.matchar.2019.02.009 (2019).

[8] X. Wen, M. Wan, C. Huang, Y. Tan, M. Lei, Y. Liang, and X. Cai, Materials & Design **180**, 107898, doi:10.1016/j.matdes.2019.107898 (2019).

[9] Y. Tomita and K. Okabayashi, Metallurgical Transactions A **17**, 1203, doi:10.1007/BF02665319 (1986).

[10] S. Weng, Y. H. Huang, F. Z. Xuan, and L. H. Luo, Procedia Engineering **130**, 1761, doi:10.1016/j.proeng.2015.12.325 (2015).

[11] S. Roy, N. Romualdi, K. Yamada, W. Poole, M. Militzer, and L. Collins, JOM **74**, 2395, doi:10.1007/s11837-022-05280-6 (2022).

[12] B. M. Mossaab, M. Zemri, and M. Arab, International Journal of Structural Integrity **10**, 67, doi:10.1108/IJSI-05-2018-0030 (2019).

[13] I. Andersen and Ø. Grong, Acta Metallurgica et Materialia **43**, 2673, doi:10.1016/0956-7151(94)00488-4 (1995).

[14] F. J. Humphreys and M. Hatherly, in *Recrystallization and Related Annealing Phenomena*, edited by F. J. Humphreys, and M. Hatherly (Elsevier, Oxford, 2004), pp. 333.

[15] M. Hillert, Acta Metallurgica **13**, 227, doi:10.1016/0001-6160(65)90200-2 (1965).

[16] T. A. Furnish, D. C. Bufford, F. Ren, A. Mehta, K. Hattar, and B. L. Boyce, Scripta Materialia **143**, 15, doi:10.1016/j.scriptamat.2017.08.047 (2018).

[17] J. Zhang, Y. Shang, Q. Liu, J. Wang, Y. Pei, S. Li, and S. Gong, Crystals **12**, doi:10.3390/cryst12081017 (2022).

[18] H.-K. Park, C.-H. Han, C.-S. Park, J.-T. Park, and H.-D. Joo, Materials Characterization **146**, 204, doi:10.1016/j.matchar.2018.09.047 (2018).

[19] F. Fang, Y. X. Zhang, X. Lu, Y. Wang, M. F. Lan, G. Yuan, R. D. K. Misra, and G. D. Wang, Scripta Materialia **147**, 33, doi:10.1016/j.scriptamat.2017.12.034 (2018).

[20] M. Vollmer, T. Arold, M. J. Kriegel, V. Klemm, S. Degener, J. Freudenberger, and T. Niendorf, Nature Communications **10**, 2337, doi:10.1038/s41467-019-10308-8 (2019).
[21] H. C. H. Carpenter and C. F. Elam, Proceedings of the Royal Society of London. Series A, Containing Papers of a Mathematical and Physical Character **100**, 329, doi:10.1098/rspa.1921.0089 (1921).
[22] J. Ciulik and E. M. Taleff, Scripta Materialia **61**, 895, doi:10.1016/j.scriptamat.2009.07.021 (2009).
[23] T. Omori, T. Kusama, S. Kawata, I. Ohnuma, Y. Sutou, Y. Araki, K. Ishida, and R. Kainuma, Science **341**, 1500, doi:10.1126/science.1238017 (2013).
[24] M. J. Higgins, J. Kang, G. Huang, D. Montiel, N. Lu, H. Liu, Y. F. Shen, P. Staublin, J. S. Park, J. D. Almer, P. Kenesei, P. G. Sanders, R. M. Suter, K. Thornton, and A. J. Shahani, Physical Review Materials **5**, L070401, doi:10.1103/PhysRevMaterials.5.L070401 (2021).
[25] J. J. Denney, Y. Wang, A. A. Corrao, G. Huang, D. Montiel, H. Zhong, E. Dooryhee, K. Thornton, and P. G. Khalifah, Journal of Applied Crystallography **53**, 982, doi:10.1107/s1600576720007062 (2020).
[26] C. Neef, H. Wadepohl, H. P. Meyer, and R. Klingeler, Journal of Crystal Growth **462**, 50, doi:10.1016/j.jcrysgro.2017.01.046 (2017).
[27] D. O'Nolan, G. Huang, G. E. Kamm, A. Grenier, C. H. Liu, P. K. Todd, A. Wustrow, G. T. Tran, D. Montiel, J. R. Neilson, S. J. L. Billinge, P. J. Chupas, K. S. Thornton, and K. W. Chapman, Journal of Applied Crystallography **53**, 662, doi:10.1107/s160057672000415x (2020).
[28] A. Erdmann, T. Fühner, P. Evanschitzky, V. Agudelo, C. Freund, P. Michalak, and D. Xu, Microelectronic Engineering **132**, 21 (2015).
[29] A. Soum-Glaude, I. Bousquet, L. Thomas, and G. Flamant, Solar energy materials and solar cells **117**, 315 (2013).
[30] M. Slootweg, K. Craig, and J. P. Meyer, Solar Energy **187**, 13 (2019).
[31] C. Park, M. M. Khater, A.-H. Abdel-Aty, R. A. Attia, and D. Lu, Alexandria Engineering Journal **59**, 1099 (2020).
[32] M. Verma, S. Basu, R. S. Patil, K. S. Hariharan, S. P. Adiga, S. M. Kolake, D. Oh, T. Song, and Y. Sung, IEEE Transactions on Vehicular Technology **69**, 2563 (2020).
[33] S. Kumar, P. Chand, A. Joshi, and V. Singh, Materials Today: Proceedings **28**, 337 (2020).
[34] R. Abedkarimi, H. Hasani, P. Soltani, and Z. Talebi, The Journal of The Textile Institute **111**, 491 (2020).
[35] A. C. Barros and P. J. Gendron, The Journal of the Acoustical Society of America **146**, EL245 (2019).
[36] A. Rahimi and N. Case, Ultrasonics **103**, 106086 (2020).
[37] M. Sheikholeslami, D. D. Ganji, M. Y. Javed, and R. Ellahi, J. Magn. Magn. Mater. **374**, 36, doi:10.1016/j.jmmm.2014.08.021 (2015).
[38] S. H. Han, L. C. Zheng, C. R. Li, and X. X. Zhang, Applied Mathematics Letters **38**, 87, doi:10.1016/j.aml.2014.07.013 (2014).
[39] Y. Tian and C. Y. Zhao, Energy **36**, 5539, doi:10.1016/j.energy.2011.07.019 (2011).
[40] F. Levrero-Florencio, F. Margara, E. Zacur, A. Bueno-Orovio, Z. Wang, A. Santiago, J. Aguado-Sierra, G. Houzeaux, V. Grau, and D. Kay, Computer methods in applied mechanics and engineering **361**, 112762 (2020).
[41] L. Wang, X. Duan, B. Liu, Q. Li, S. Yin, and J. Xu, Journal of Power Sources **448**, 227468 (2020).

[42] L. Wang, S. Yin, and J. Xu, Journal of Power Sources **413**, 284 (2019).
[43] C. Suryanarayana, Research, doi:10.34133/2019/4219812 (2019).
[44] M. J. Hampden-Smith and T. T. Kodas, Chemical Vapor Deposition **1**, 8, doi:10.1002/cvde.19950010103 (1995).
[45] G. S. Upadhyaya, *Powder metallurgy technology* (Cambridge Int Science Publishing, 1997).
[46] L. Coudurier, D. W. Hopkins, and I. Wilkomirsky, *Fundamentals of Metallurgical Processes: International Series on Materials Science and Technology* (Elsevier, 2013), Vol. 27.
[47] J. D. Mackenzie, Journal of Non-Crystalline Solids **100**, 162, doi:10.1016/0022-3093(88)90013-0 (1988).
[48] S.-H. Yu, Journal of the Ceramic Society of Japan **109**, S65 (2001).
[49] S. Shao, J. Zhang, Z. Zhang, P. Zheng, M. Zhao, J. Li, and C. Wang, Journal of Physics D: Applied Physics **41**, 125408 (2008).
[50] K. Matyjaszewski and J. Xia, Chemical reviews **101**, 2921 (2001).
[51] J. Chiefari, Y. Chong, F. Ercole, J. Krstina, J. Jeffery, T. P. Le, R. T. Mayadunne, G. F. Meijs, C. L. Moad, and G. Moad, Macromolecules **31**, 5559 (1998).
[52] O. Nuyken and S. D. Pask, Polymers **5**, 361 (2013).
[53] R. G. W. Norrish and E. Brookman, Proceedings of the Royal Society of London. Series A. Mathematical and Physical Sciences **171**, 147 (1939).
[54] S. Marouani, L. Curtil, and P. Hamelin, Materials and structures **41**, 831 (2008).
[55] M. H. Zin, K. Abdan, N. Mazlan, E. S. Zainudin, K. E. Liew, and M. N. Norizan, Composites Part B: Engineering **177**, 107306 (2019).
[56] S. T. Peters, *Composite filament winding* (ASM International, 2011).
[57] A. Miller, N. Dodds, J. Hale, and A. Gibson, Composites Part A: Applied Science and Manufacturing **29**, 773 (1998).
[58] S. Laurenzi and M. Marchetti, Composites and their properties, 197 (2012).
[59] A. Wold and K. Dwight, *Solid state chemistry: synthesis, structure, and properties of selected oxides and sulfides* (Springer Science & Business Media, 1993).
[60] D. W. Murphy, C. Cros, F. J. Di Salvo, and J. Waszczak, Inorganic Chemistry **16**, 3027 (1977).
[61] S. A. Sunshine, D. Kang, and J. A. Ibers, Journal of the American Chemical Society **109**, 6202, doi:10.1021/ja00254a060 (1987).
[62] D. P. Shoemaker, D. Y. Chung, J. F. Mitchell, T. H. Bray, L. Soderholm, P. J. Chupas, and M. G. Kanatzidis, Journal of the American Chemical Society **134**, 9456, doi:10.1021/ja303047e (2012).
[63] D. P. Shoemaker, Y. J. Hu, D. Y. Chung, G. J. Halder, P. J. Chupas, L. Soderholm, J. F. Mitchell, and M. G. Kanatzidis, Proceedings of the National Academy of Sciences of the United States of America **111**, 10922, doi:10.1073/pnas.1406211111 (2014).
[64] R. E. Treece, E. G. Gillan, and R. B. Kaner, Comments on Inorganic Chemistry **16**, 313, doi:10.1080/02603599508035775 (1995).
[65] E. G. Gillan and R. B. Kaner, Chemistry of Materials **8**, 333, doi:10.1021/cm950232a (1996).
[66] I. P. Parkin, Chemical Society Reviews **25**, 199, doi:10.1039/cs9962500199 (1996).
[67] I. P. Parkin and A. T. Nartowski, Journal of Materials Science Letters **18**, 267, doi:10.1023/a:1006650332712 (1999).

[68] T. V. Rajan, C. P. Sharma, and A. Sharma, *Heat treatment : principles and techniques* (PHI Learning, New Delhi, 2012), 2nd edn.
[69] W. D. Callister and D. G. Rethwisch, *Materials Science and Engineering: An Introduction* (Wiley, 2009), 8th edn.
[70] S. Yue, in *Metalworking: Bulk Forming*, edited by S. L. Semiatin (ASM International, 2005), p. 0.
[71] M. Pekguleryuz, in *Fundamentals of Magnesium Alloy Metallurgy*, edited by M. O. Pekguleryuz, K. U. Kainer, and A. Arslan Kaya (Woodhead Publishing, 2013), pp. 152.
[72] J. E. Burke and D. Turnbull, Progress in Metal Physics **3**, 220, doi:10.1016/0502-8205(52)90009-9 (1952).
[73] C. G. Dunn and P. K. Koh, JOM **8**, 1017, doi:10.1007/BF03377812 (1956).
[74] P. A. Beck and H. Hu, JOM **4**, 83, doi:10.1007/BF03397656 (1952).
[75] M. L. Kronberg and F. H. Wilson, JOM **1**, 501, doi:10.1007/BF03398387 (1949).
[76] W. G. Burgers and J. L. Snoek, Physica **2**, 1064, doi:10.1016/S0031-8914(35)90194-X (1935).
[77] C. S. Smith, Trans. Metall. Soc. AIME **175**, 15 (1948).
[78] T. Kusama, T. Omori, T. Saito, S. Kise, T. Tanaka, Y. Araki, and R. Kainuma, Nature Communications **8**, 354, doi:10.1038/s41467-017-00383-0 (2017).
[79] T. Omori, H. Iwaizako, and R. Kainuma, Materials & Design **101**, 263, doi:10.1016/j.matdes.2016.04.011 (2016).
[80] F. J. Humphreys and M. Hatherly, in *Recrystallization and Related Annealing Phenomena*, edited by F. J. Humphreys, and M. Hatherly (Elsevier, Oxford, 2004), pp. 215.
[81] S. M. Koohpayeh, D. Fort, A. Bradshaw, and J. S. Abell, Journal of Crystal Growth **311**, 2513, doi:10.1016/j.jcrysgro.2009.02.017 (2009).
[82] C. W. Lan and C. H. Tsai, Journal of Crystal Growth **173**, 561, doi:10.1016/s0022-0248(96)00971-2 (1997).
[83] Y. Z. Yan, M. J. Shi, Q. Wang, and Y. J. Jiang, Journal of Crystal Growth **468**, 923, doi:10.1016/j.jcrysgro.2016.09.026 (2017).
[84] C. W. Lan and B. C. Yeh, Journal of Crystal Growth **262**, 59, doi:10.1016/j.jcrysgro.2003.09.055 (2004).
[85] C. W. Lan, Journal of Crystal Growth **247**, 597, doi:10.1016/s0022-0248(02)02056-0 (2003).
[86] F. P. Incropera, D. P. DeWitt, T. L. Bergman, and A. S. Lavine, *Fundamentals of heat and mass transfer* (John Wiley & Sons, 2007), 6th edn.
[87] M. F. Modest, in *Radiative Heat Transfer*, edited by M. F. Modest (Academic Press, Boston, 2013), pp. 160.
[88] M. F. Modest, in *Radiative Heat Transfer*, edited by M. F. Modest (Academic Press, Boston, 2013), pp. 129.
[89] COMSOL Multiphysics® v. 5.4. www.comsol.com. COMSOL AB, Stockholm, Sweden.
[90] J. A. Stimson, E. G. Carmines, and R. A. Zeller, Sociological Methods & Research **6**, 515 (1978).
[91] E. Ostertagová, Procedia Engineering **48**, 500 (2012).
[92] P. A. Bostan, G. B. M. Heuvelink, and S. Z. Akyurek, International Journal of Applied Earth Observation and Geoinformation **19**, 115, doi:10.1016/j.jag.2012.04.010 (2012).
[93] C. D. Lloyd, Journal of Hydrology **308**, 128, doi:10.1016/j.jhydrol.2004.10.026 (2005).

[94] R. Dwivedi and O. Dikshit, Journal of Applied Geodesy **7**, 135, doi:10.1515/jag-2013-0045 (2013).
[95] R. Eberhart and J. Kennedy, in *MHS'95. Proceedings of the Sixth International Symposium on Micro Machine and Human Science* (IEEE, Nagoya, Japan, 1995), pp. 39.
[96] J. Kennedy and R. Eberhart, in *Proceedings of ICNN'95 - International Conference on Neural Networks* (IEEE, Perth, WA, Australia, 1995), pp. 1942.
[97] M. Wetter and J. Wright, Building and Environment **39**, 989, doi:10.1016/j.buildenv.2004.01.022 (2004).
[98] C. Audet and J. E. Dennis, Siam Journal on Optimization **13**, 889, doi:10.1137/s1052623400378742 (2003).
[99] T. G. Kolda, R. M. Lewis, and V. Torczon, Siam Review **45**, 385, doi:10.1137/s003614450242889 (2003).
[100] R. Hooke and T. A. Jeeves, Journal of the Acm **8**, 212, doi:10.1145/321062.321069 (1961).
[101] G. Huang, M. Zhang, D. Montiel, P. Soundararajan, Y. Wang, J. J. Denney, A. A. Corrao, P. G. Khalifah, and K. Thornton, Computational Materials Science **194**, 110459, doi:10.1016/j.commatsci.2021.110459 (2021).
[102] M. Stein, Technometrics **29**, 143, doi:10.2307/1269769 (1987).
[103] L. Q. Chen, Annual Review of Materials Research **32**, 113, doi:10.1146/annurev.matsci.32.112001.132041 (2002).
[104] T. Koyama, Science and Technology of Advanced Materials **9**, 013006, doi:10.1088/1468-6996/9/1/013006 (2008).
[105] N. Provatas and K. Elder, *Phase-Field Methods in Materials Science and Engineering* (Wiley-VCH, 2010).
[106] W. J. Boettinger, J. A. Warren, C. Beckermann, and A. Karma, Annual Review of Materials Research **32**, 163, doi:10.1146/annurev.matsci.32.101901.155803 (2002).
[107] A. A. Wheeler, W. J. Boettinger, and G. B. McFadden, Physical Review A **45**, 7424, doi:10.1103/PhysRevA.45.7424 (1992).
[108] C. Beckermann, H. J. Diepers, I. Steinbach, A. Karma, and X. Tong, Journal of Computational Physics **154**, 468, doi:10.1006/jcph.1999.6323 (1999).
[109] S. G. Kim, W. T. Kim, and T. Suzuki, Phys Rev E **60**, 7186, doi:10.1103/PhysRevE.60.7186 (1999).
[110] L. Q. Chen and W. Yang, Physical Review B **50**, 15752, doi:10.1103/PhysRevB.50.15752 (1994).
[111] D. Fan and L. Q. Chen, Acta Materialia **45**, 611, doi:10.1016/s1359-6454(96)00200-5 (1997).
[112] C. E. Krill and L. Q. Chen, Acta Materialia **50**, 3057, Pii s1359-6454(02)00084-8 (2002).
[113] Y. Suwa and Y. Saito, Materials Transactions **44**, 2245, doi:10.2320/matertrans.44.2245 (2003).
[114] H. Nishimori and A. Onuki, Physical Review B **42**, 980, doi:10.1103/PhysRevB.42.980 (1990).
[115] D. J. Seol, S. Y. Hu, Y. L. Li, J. Shen, K. H. Oh, and L. Q. Chen, Acta Materialia **51**, 5173, doi:10.1016/s1359-6454(03)00378-1 (2003).
[116] S. Biswas, D. Schwen, J. Singh, and V. Tomar, Extreme Mechanics Letters **7**, 78, doi:10.1016/j.eml.2016.02.017 (2016).

[117] J. Hotzer, M. Seiz, M. Kellner, W. Rheinheimer, and B. Nestler, Acta Materialia **164**, 184, doi:10.1016/j.actamat.2018.10.021 (2019).
[118] W. Pongsaksawad, A. C. Powell, and D. Dussault, Journal of The Electrochemical Society **154**, F122, doi:10.1149/1.2721763 (2007).
[119] A. F. Chadwick, J. A. Stewart, R. Du, and K. Thornton, Journal of the Electrochemical Society **165**, C633, doi:10.1149/2.0701810jes (2018).
[120] J. Guyer, W. Boettinger, J. Warren, and G. McFadden, Phys Rev E **69**, 021603, doi:10.1103/PhysRevE.69.021603 (2004).
[121] S. Bhattacharyya, S. Bandyopadhyay, and A. Choudhury, Journal of the Indian Institute of Science **96**, 257 (2016).
[122] G. Boussinot, C. Hüter, and E. A. Brener, Phys Rev E **83**, 020601, doi:10.1103/PhysRevE.83.020601 (2011).
[123] A. Bhattacharya, A. Kiran, S. Karagadde, and P. Dutta, Journal of Computational Physics **262**, 217, doi:10.1016/j.jcp.2014.01.007 (2014).
[124] L. Tan and N. Zabaras, Journal of Computational Physics **221**, 9, doi:10.1016/j.jcp.2006.06.003 (2007).
[125] D. M. Anderson, G. B. McFadden, and A. A. Wheeler, Annual Review of Fluid Mechanics **30**, 139, doi:10.1146/annurev.fluid.30.1.139 (1998).
[126] J. W. Cahn and J. E. Hilliard, The Journal of Chemical Physics **28**, 258, doi:10.1063/1.1744102 (1958).
[127] M. Tang, W. C. Carter, and R. M. Cannon, Physical Review B **73**, 024102, doi:10.1103/PhysRevB.73.024102 (2006).
[128] R. Folch and M. Plapp, Phys Rev E **72**, 011602, doi:10.1103/PhysRevE.72.011602 (2005).
[129] S. M. Allen and J. W. Cahn, Acta Metallurgica **27**, 1085, doi:10.1016/0001-6160(79)90196-2 (1979).
[130] R. W. Balluffi, S. M. Allen, and W. C. Carter, *Kinetics of materials* (John Wiley & Sons, 2005).
[131] A. Bueno-Orovio and V. M. Perez-Garcia, Numerical Methods for Partial Differential Equations **22**, 435, doi:10.1002/num.20103 (2006).
[132] A. Bueno-Orovio, V. M. Perez-Garcia, and F. H. Fenton, Siam Journal on Scientific Computing **28**, 886, doi:10.1137/040607575 (2006).
[133] A. Bueno-Orovio, Applied Mathematics and Computation **183**, 813, doi:10.1016/j.amc.2006.06.029 (2006).
[134] H. C. Yu, H. Y. Chen, and K. Thornton, Modelling and Simulation in Materials Science and Engineering **20**, 075008, doi:10.1088/0965-0393/20/7/075008 (2012).
[135] R. Termuhlen, K. Fitzmaurice, and H.-C. Yu, Computer Methods in Applied Mechanics and Engineering **399**, 115312, doi:10.1016/j.cma.2022.115312 (2022).
[136] Z. Guo, F. Yu, P. Lin, S. Wise, and J. Lowengrub, Journal of Fluid Mechanics **907**, A38, doi:10.1017/jfm.2020.790 (2021).
[137] P. T. Brewick, Journal of The Electrochemical Society **169**, 011503, doi:10.1149/1945-7111/ac4935 (2022).
[138] M. Sussman, P. Smereka, and S. Osher, Journal of Computational Physics **114**, 146, doi:10.1006/jcph.1994.1155 (1994).
[139] G. Russo and P. Smereka, SIAM Journal on Scientific Computing **21**, 2073, doi:10.1137/S1064827599351921 (2000).

[140] Y. Xiang, L.-T. Cheng, D. J. Srolovitz, and W. E, Acta Materialia **51**, 5499, doi:10.1016/S1359-6454(03)00415-4 (2003).
[141] C. L. Park, P. W. Voorhees, and K. Thornton, Computational Materials Science **85**, 46, doi:10.1016/j.commatsci.2013.12.022 (2014).
[142] Y. Shibuta, Y. Okajima, and T. Suzuki, Science and Technology of Advanced Materials **8**, 511, doi:10.1016/j.stam.2007.08.001 (2007).
[143] Y. Okajima, Y. Shibuta, and T. Suzuki, Computational Materials Science **50**, 118, doi:10.1016/j.commatsci.2010.07.015 (2010).
[144] D. A. Cogswell, Phys Rev E **92**, 011301, doi:10.1103/PhysRevE.92.011301 (2015).
[145] R. D. McAuliffe, G. Huang, D. Montiel, A. Mehta, R. C. Davis, V. Petrova, K. L. Browning, J. R. Neilson, P. Liu, K. Thornton, and G. M. Veith, Chemistry of Materials **34**, 6279, doi:10.1021/acs.chemmater.2c00303 (2022).
[146] G. E. Kamm, G. Huang, S. M. Vornholt, R. D. McAuliffe, G. M. Veith, K. S. Thornton, and K. W. Chapman, Journal of the American Chemical Society **144**, 11975, doi:10.1021/jacs.2c05043 (2022).
[147] B. Zhou and A. C. Powell, Journal of Membrane Science **268**, 150, doi:10.1016/j.memsci.2005.05.030 (2006).
[148] P. K. Chan, MRS Online Proceedings Library (OPL) **710**, DD4.6.1, doi:10.1557/PROC-710-DD4.6.1 (2001).
[149] K. W. D. Lee, P. K. Chan, and X. S. Feng, Chemical Engineering Science **59**, 1491, doi:10.1016/j.ces.2003.12.025 (2004).
[150] P. K. Inguva, P. J. Walker, H. W. Yew, K. Z. Zhu, A. J. Haslam, and O. K. Matar, Soft Matter **17**, 5645, doi:10.1039/d1sm00272d (2021).
[151] H. Manzanarez, J. P. Mericq, P. Guenoun, J. Chikina, and D. Bouyer, Chemical Engineering Science **173**, 411, doi:10.1016/j.ces.2017.08.009 (2017).
[152] J. W. Haverkort, Physical Review Applied **14**, 044047, doi:10.1103/PhysRevApplied.14.044047 (2020).
[153] G. Huang, D. Montiel, R. D. McAuliffe, G. M. Veith, and K. Thornton, Computational Materials Science **221**, 112080, doi:10.1016/j.commatsci.2023.112080 (2023).
[154] K. F. Riley, M. P. Hobson, and S. J. Bence, *Mathematical Methods for Physics and Engineering: A Comprehensive Guide* (Cambridge University Press, Cambridge, 2006), 3rd edn.
[155] E. N. Hodkin and M. G. Nicholas, Journal of Nuclear Materials **43**, 308, doi:10.1016/0022-3115(72)90062-1 (1972).
[156] T. L. Jensen, J. Moxnes, and E. Unneberg, Journal of Computational and Theoretical Nanoscience **10**, 464, doi:10.1166/jctn.2013.2720 (2013).
[157] B. H. Zhang, C. B. Li, and S. M. Shan, Physics and Chemistry of Minerals **43**, 371, doi:10.1007/s00269-016-0801-1 (2016).
[158] D. Mapother, H. N. Crooks, and R. Maurer, J Chem Phys **18**, 1231, doi:10.1063/1.1747916 (1950).
[159] L. G. Harrison, J. A. Morrison, and R. Rudham, Transactions of the Faraday Society **54**, 106, doi:10.1039/tf9585400106 (1958).
[160] G. T. Nolan and P. E. Kavanagh, Powder Technology **72**, 149, doi:10.1016/0032-5910(92)88021-9 (1992).
[161] F. Amin, W. Rehman, M. U. Farooq, R. Hussain, S. ur Rahman, L. Rasheed, S. Khan, and M. H. Abdellatif, ChemistrySelect **8**, e202300152, doi:10.1002/slct.202300152 (2023).

[162] P. Villars, α-NaFeO2 (NaFeO2 rt) Crystal Structure. SpringerMaterials. [online] Available at: https://materials.springer.com/isp/crystallographic/docs/sd_1503056.
[163] N. Lu, J. Kang, N. Senabulya, R. Keinan, N. Gueninchault, and A. J. Shahani, Acta Materialia **195**, 1, doi:10.1016/j.actamat.2020.04.049 (2020).
[164] P. R. Rios and M. E. Glicksman, Acta Materialia **54**, 5313, doi:10.1016/j.actamat.2006.07.010 (2006).
[165] P. R. Rios, G. Gottstein, and L. S. Shvindlerman, Materials Science and Engineering: A **332**, 231, doi:10.1016/S0921-5093(01)01745-2 (2002).
[166] W. W. Mullins, Journal of Applied Physics **59**, 1341, doi:10.1063/1.336528 (1986).
[167] G. Gottstein, A. D. Rollett, and L. S. Shvindlerman, Scripta Materialia **51**, 611, doi:10.1016/j.scriptamat.2004.05.023 (2004).
[168] N. Moelans, A. Godfrey, Y. Zhang, and D. Juul Jensen, Physical Review B **88**, 054103, doi:10.1103/PhysRevB.88.054103 (2013).
[169] N. Moelans, Acta Materialia **59**, 1077, doi:10.1016/j.actamat.2010.10.038 (2011).
[170] S. P. Gentry and K. Thornton, Modelling and Simulation in Materials Science and Engineering **28**, 065002, doi:10.1088/1361-651X/ab9751 (2020).
[171] N. Moelans, B. Blanpain, and P. Wollants, Physical Review B **78**, 024113, doi:10.1103/PhysRevB.78.024113 (2008).
[172] B. Pettersson, The Philosophical Magazine: A Journal of Theoretical Experimental and Applied Physics **20**, 831, doi:10.1080/14786436908228048 (1969).
[173] A. Karma and W.-J. Rappel, Phys Rev E **57**, 4323, doi:10.1103/PhysRevE.57.4323 (1998).
[174] B. Echebarria, R. Folch, A. Karma, and M. Plapp, Phys Rev E **70**, 061604, doi:10.1103/PhysRevE.70.061604 (2004).
[175] D. Fan, L.-Q. Chen, and S. P. Chen, Materials Science and Engineering: A **238**, 78, doi:10.1016/S0921-5093(97)00437-1 (1997).
[176] K. Kassner, C. Misbah, J. Müller, J. Kappey, and P. Kohlert, Phys Rev E **63**, 036117, doi:10.1103/PhysRevE.63.036117 (2001).
[177] A. Karma and W.-J. Rappel, Phys Rev E **53**, R3017, doi:10.1103/PhysRevE.53.R3017 (1996).
[178] J. Dennis, P. S. Bate, and J. F. Humphreys, Materials Science Forum **558-559**, 717, doi:10.4028/www.scientific.net/MSF.558-559.717 (2007).
[179] J. W. Cahn, Transactions of the Metallurgical Society of AIME **239**, 610 (1967).
[180] R. DeHoff, Transactions of the Metallurgical Society of AIME **239**, 617 (1967).
[181] J. V. Bernier, R. M. Suter, A. D. Rollett, and J. D. Almer, Annual Review of Materials Research **50**, 395, doi:10.1146/annurev-matsci-070616-124125 (2020).
[182] R. M. Suter, D. Hennessy, C. Xiao, and U. Lienert, Review of Scientific Instruments **77**, 123905, doi:10.1063/1.2400017 (2006).
[183] S. F. Li and R. M. Suter, Journal of Applied Crystallography **46**, 512, doi:10.1107/S0021889813005268 (2013).
[184] J. Kang, N. Lu, I. Loo, N. Senabulya, and A. J. Shahani, Integrating Mater Manuf Innovation **8**, 388, doi:10.1007/s40192-019-00147-2 (2019).
[185] M. W. Grabski and R. Korski, The Philosophical Magazine: A Journal of Theoretical Experimental and Applied Physics **22**, 707, doi:10.1080/14786437008220941 (1970).
[186] Y. Piao and K. C. Le, Continuum Mechanics and Thermodynamics **34**, 763, doi:10.1007/s00161-022-01088-6 (2022).

[187] G. K. Williamson and R. E. Smallman, The Philosophical Magazine: A Journal of Theoretical Experimental and Applied Physics **1**, 34, doi:10.1080/14786435608238074 (1956).
[188] D. L. Sahagian and A. A. Proussevitch, Journal of Volcanology and Geothermal Research **84**, 173, doi:10.1016/S0377-0273(98)00043-2 (1998).
[189] S. A. Saltikov, in *Stereology*, edited by H. Elias (Springer Berlin Heidelberg, Berlin, Heidelberg, 1967), pp. 163.
[190] I. M. McKenna, M. P. Gururajan, and P. W. Voorhees, J Mater Sci **44**, 2206, doi:10.1007/s10853-008-3196-7 (2009).
[191] C. J. Permann, M. R. Tonks, B. Fromm, and D. R. Gaston, Computational Materials Science **115**, 18, doi:10.1016/j.commatsci.2015.12.042 (2016).
[192] N. Maazi, N. Rouag, A. L. Etter, R. Penelle, and T. Baudin, Scripta Materialia **55**, 641, doi:10.1016/j.scriptamat.2006.06.007 (2006).
[193] J. B. Koo, D. Y. Yoon, and M. F. Henry, Metallurgical and Materials Transactions A **31**, 1489, doi:10.1007/s11661-000-0267-z (2000).
[194] G. S. Rohrer, J Mater Sci **46**, 5881, doi:10.1007/s10853-011-5677-3 (2011).
[195] G. Behr, W. Loser, N. Wizent, P. Ribeiro, M. O. Apostu, and D. Souptel, J Mater Sci **45**, 2223, doi:10.1007/s10853-009-4075-6 (2010).
[196] A. Bejan, *Heat Transfer* (John Wiley & Sons, 1993).
[197] Heat Transfer Module User's Guide. COMSOL Multiphysics® v. 5.4. COMSOL AB, Stockholm, Sweden.
[198] C. H. Shomate, The Journal of Physical Chemistry **58**, 368, doi:10.1021/j150514a018 (1954).
[199] G. T. Furukawa, T. B. Douglas, R. E. McCoskey, and D. C. Ginnings, J Res Nat Bur Stand **57**, 67, doi:10.6028/jres.057.008 (1956).
[200] P. J. Karditsas and M. J. Baptiste, Thermal and structural properties of fusion related materials, 1995.
[201] C. W. Nan, R. Birringer, D. R. Clarke, and H. Gleiter, Journal of Applied Physics **81**, 6692, doi:10.1063/1.365209 (1997).
[202] W. Kim, H. Oh, and I. Shon, International Journal of Refractory Metals & Hard Materials **48**, 376, doi:10.1016/j.ijrmhm.2014.10.011 (2015).
[203] Z. Zivcova, E. Gregorova, W. Pabst, D. Smith, A. Michot, and C. Poulier, J Eur Ceram Soc **29**, 347, doi:10.1016/j.jeurceramsoc.2008.06.018 (2009).
[204] J. F. Shackelford, Y. H. Han, S. Kim, and S. H. Kwon, *CRC Materials Science and Engineering Handbook* (CRC Press-Taylor & Francis Group, 2015), 4th edn.
[205] E. H. Buyco and F. E. Davis, Journal of Chemical and Engineering Data **15**, 518, doi:10.1021/je60047a035 (1970).
[206] J. G. Kaufman, in *Aluminum Science and Technology*, edited by K. Anderson, J. Weritz, and J. G. Kaufman (ASM International, 2018), p. 0.
[207] Optotherm. Emissivity Values. [online] Available at: https://www.optotherm.com/emissivity.
[208] P. J. Chupas, K. W. Chapman, C. Kurtz, J. C. Hanson, P. L. Lee, and C. P. Grey, J. Appl. Crystallogr. **41**, 822, doi:10.1107/s0021889808020165 (2008).
[209] E. M. Purcell and D. J. Morin, *Electricity and magnetism* (Cambridge university press, 2013).
[210] D. A. Ditmars, S. Ishihara, S. S. Chang, G. Bernstein, and E. D. West, J Res Nat Bur Stand **87**, 159, doi:10.6028/jres.087.012 (1982).

[211] T. Shimizu, K. Matsuura, H. Furue, and K. Matsuzak, J Eur Ceram Soc **33**, 3429, doi:10.1016/j.jeurceramsoc.2013.07.001 (2013).
[212] P. Jund and R. Jullien, Physical Review B **59**, 13707, doi:10.1103/PhysRevB.59.13707 (1999).
[213] The Engineering ToolBox (2003). Surface Emissivity Coefficients. [online] Available at: https://www.engineeringtoolbox.com/emissivity-coefficients-d_447.html.
[214] The Engineering ToolBox (2003). Convective Heat Transfer. [online] Available at: https://www.engineeringtoolbox.com/convective-heat-transfer-d_430.html.
[215] Kanthal. Kanthal® A-1 Resistance Heating Wire and Resistance Wire. [online] Available at: https://www.kanthal.com/en/products/material-datasheets/wire/resistance-heating-wire-and-resistance-wire/kanthal-a-1/.
[216] R. Matsuda, R. Kitaura, S. Kitagawa, Y. Kubota, T. C. Kobayashi, S. Horike, and M. Takata, Journal of the American Chemical Society **126**, 14063, doi:10.1021/ja046925m (2004).
[217] A. J. Leadbetter, D. M. T. Newsham, and G. R. Settatree, J Phys Part C Solid **2**, 393, doi:10.1088/0022-3719/2/3/302 (1969).
[218] V. V. Murashov and M. A. White, J Mater Sci **35**, 649, doi:10.1023/A:1004784613181 (2000).
[219] C. J. Glassbrenner and G. A. Slack, Phys Rev **134**, 1058, doi:10.1103/PhysRev.134.A1058 (1964).
[220] W. M. Haynes, *CRC Handbook of Chemistry and Physics.* (CRC Press LLC, Boca Raton: FL, 2013 - 2014), 94th edn.
[221] R. Endo, Y. Fujihara, and M. Susa, High Temperatures-High Pressures **35/36**, 505, doi:10.1068/htjr135 (2003).
[222] N. M. Ravindra, B. Sopori, O. H. Gokce, S. X. Cheng, A. Shenoy, L. Jin, S. Abedrabbo, W. Chen, and Y. Zhang, Int J Thermophys **22**, 1593, doi:10.1023/A:1012869710173 (2001).
[223] T. Satō, Japanese Journal of Applied Physics **6**, 339, doi:10.1143/JJAP.6.339 (1967).
[224] R. Mas-Balleste, C. Gomez-Navarro, J. Gomez-Herrero, and F. Zamora, Nanoscale **3**, 20, doi:10.1039/c0nr00323a (2011).
[225] A. Gupta, T. Sakthivel, and S. Seal, Progress in Materials Science **73**, 44, doi:10.1016/j.pmatsci.2015.02.002 (2015).
[226] B. Luo, G. Liu, and L. Wang, Nanoscale **8**, 6904, doi:10.1039/c6nr00546b (2016).
[227] S. Najmaei, Z. Liu, W. Zhou, X. Zou, G. Shi, S. Lei, B. I. Yakobson, J. C. Idrobo, P. M. Ajayan, and J. Lou, Nat Mater **12**, 754, doi:10.1038/nmat3673 (2013).
[228] K. Kim, Z. Lee, W. Regan, C. Kisielowski, M. F. Crommie, and A. Zettl, ACS Nano **5**, 2142, doi:10.1021/nn1033423 (2011).
[229] Y. M. Shi, W. Zhou, A. Y. Lu, W. J. Fang, Y. H. Lee, A. L. Hsu, S. M. Kim, K. K. Kim, H. Y. Yang, L. J. Li, J. C. Idrobo, and J. Kong, Nano Lett **12**, 2784, doi:10.1021/nl204562J (2012).
[230] P. Y. Huang, C. S. Ruiz-Vargas, A. M. van der Zande, W. S. Whitney, M. P. Levendorf, J. W. Kevek, S. Garg, J. S. Alden, C. J. Hustedt, Y. Zhu, J. Park, P. L. McEuen, and D. A. Muller, Nature **469**, 389, doi:10.1038/nature09718 (2011).
[231] O. V. Yazyev and S. G. Louie, Nat Mater **9**, 806, doi:10.1038/nmat2830 (2010).
[232] O. V. Yazyev and S. G. Louie, Physical Review B **81**, 195420, doi:10.1103/PhysRevB.81.195420 (2010).
[233] K. R. Elder, M. Katakowski, M. Haataja, and M. Grant, Phys. Rev. Lett. **88**, 245701, doi:10.1103/PhysRevLett.88.245701 (2002).

[234] K. R. Elder and M. Grant, Phys. Rev. E Stat. Nonlin. Soft Matter Phys. **70**, 051605, doi:10.1103/PhysRevE.70.051605 (2004).
[235] K. R. Elder, N. Provatas, J. Berry, P. Stefanovic, and M. Grant, Phys. Rev. B Condens. Matter Mater. Phys. **75**, 064107, doi:10.1103/PhysRevB.75.064107 (2007).
[236] A. Adland, A. Karma, R. Spatschek, D. Buta, and M. Asta, Physical Review B **87**, 024110, doi:10.1103/PhysRevB.87.024110 (2013).
[237] Y. J. Gao, Q. Q. Deng, and S. L. Quan, Front. Mater. Sci. **8**, 176, doi:10.1007/s11706-014-0229-9 (2014).
[238] P. Y. Chan, G. Tsekenis, J. Dantzig, K. A. Dahmen, and N. Goldenfeld, Phys. Rev. Lett. **105**, 015502, doi:10.1103/PhysRevLett.105.015502 (2010).
[239] J. Berry, M. Grant, and K. R. Elder, Phys. Rev. E Stat. Nonlin. Soft Matter Phys. **73**, 031609, doi:10.1103/PhysRevE.73.031609 (2006).
[240] G. I. Toth, T. Pusztai, G. Tegze, G. Toth, and L. Granasy, Physical Review Letters **107**, doi:10.1103/PhysRevLett.107.175702 (2011).
[241] J. Berry, K. R. Elder, and M. Grant, Phys Rev E Stat Nonlin Soft Matter Phys **77**, 061506, doi:10.1103/PhysRevE.77.061506 (2008).
[242] J. Berry and M. Grant, Phys. Rev. Lett. **106**, 175702, doi:10.1103/PhysRevLett.106.175702 (2011).
[243] E. Alster, K. R. Elder, J. J. Hoyt, and P. W. Voorhees, Phys Rev E **95**, 022105, doi:10.1103/PhysRevE.95.022105 (2017).
[244] N. Ofori-Opoku, V. Fallah, M. Greenwood, S. Esmaeili, and N. Provatas, Physical Review B **87**, doi:10.1103/PhysRevB.87.134105 (2013).
[245] A. A. Balandin, S. Ghosh, W. Z. Bao, I. Calizo, D. Teweldebrhan, F. Miao, and C. N. Lau, Nano Lett **8**, 902, doi:10.1021/nl0731872 (2008).
[246] A. H. Castro Neto, F. Guinea, N. M. R. Peres, K. S. Novoselov, and A. K. Geim, Rev Mod Phys **81**, 109, doi:10.1103/RevModPhys.81.109 (2009).
[247] C. Lee, X. D. Wei, J. W. Kysar, and J. Hone, Science **321**, 385, doi:10.1126/science.1157996 (2008).
[248] K. S. Novoselov, A. K. Geim, S. V. Morozov, D. Jiang, Y. Zhang, S. V. Dubonos, I. V. Grigorieva, and A. A. Firsov, Science **306**, 666, doi:10.1126/science.1102896 (2004).
[249] S. K. Mkhonta, K. R. Elder, and Z. F. Huang, Phys Rev Lett **111**, 035501, doi:10.1103/PhysRevLett.111.035501 (2013).
[250] K. R. Elder, Z. Chen, K. L. Elder, P. Hirvonen, S. K. Mkhonta, S. C. Ying, E. Granato, Z. F. Huang, and T. Ala-Nissila, J Chem Phys **144**, 174703, doi:10.1063/1.4948370 (2016).
[251] M. Seymour and N. Provatas, Physical Review B **93**, 035447, doi:10.1103/PhysRevB.93.035447 (2016).
[252] P. Hirvonen, M. M. Ervasti, Z. Fan, M. Jalalvand, M. Seymour, S. M. Vaez Allaei, N. Provatas, A. Harju, K. R. Elder, and T. Ala-Nissila, Physical Review B **94**, 035414, doi:10.1103/PhysRevB.94.035414 (2016).
[253] K. R. Elder, G. Rossi, P. Kanerva, F. Sanches, S. C. Ying, E. Granato, C. V. Achim, and T. Ala-Nissila, Phys Rev Lett **108**, 226102, doi:10.1103/PhysRevLett.108.226102 (2012).
[254] K. R. Elder, G. Rossi, P. Kanerva, F. Sanches, S. C. Ying, E. Granato, C. V. Achim, and T. Ala-Nissila, Physical Review B **88**, 075423, doi:10.1103/PhysRevB.88.075423 (2013).
[255] D. Taha, S. K. Mkhonta, K. R. Elder, and Z. F. Huang, Phys Rev Lett **118**, 255501, doi:10.1103/PhysRevLett.118.255501 (2017).

[256] K. Azizi, P. Hirvonen, Z. Y. Fan, A. Harju, K. R. Elder, T. Ala-Nissila, and S. M. V. Allaei, Carbon **125**, 384, doi:10.1016/j.carbon.2017.09.059 (2017).
[257] H. Dong, P. Hirvonen, Z. Fan, and T. Ala-Nissila, Phys Chem Chem Phys **20**, 24602, doi:10.1039/c8cp05159c (2018).
[258] K. L. M. Elder, M. Seymour, M. Lee, M. Hilke, and N. Provatas, Philos Trans A Math Phys Eng Sci **376**, 20170211, doi:10.1098/rsta.2017.0211 (2018).
[259] Z. Y. Fan, P. Hirvonen, L. F. C. Pereira, M. M. Ervasti, K. R. Elder, D. Donadio, A. Harju, and T. Ala-Nissila, Nano Lett **17**, 5919, doi:10.1021/acs.nanolett.7b01742 (2017).
[260] Z. Fan, L. F. C. Pereira, P. Hirvonen, M. M. Ervasti, K. R. Elder, D. Donadio, T. Ala-Nissila, and A. Harju, Physical Review B **95**, 144309, doi:10.1103/PhysRevB.95.144309 (2017).
[261] L. Gao, J. R. Guest, and N. P. Guisinger, Nano Lett **10**, 3512, doi:10.1021/nl1016706 (2010).
[262] T.-H. Liu, G. Gajewski, C.-W. Pao, and C.-C. Chang, Carbon **49**, 2306, doi:10.1016/j.carbon.2011.01.063 (2011).
[263] O. Frank, G. Tsoukleri, J. Parthenios, K. Papagelis, I. Riaz, R. Jalil, K. S. Novoselov, and C. Galiotis, ACS Nano **4**, 3131, doi:10.1021/nn100454w (2010).
[264] Y. Liu, X. Zou, and B. I. Yakobson, ACS Nano **6**, 7053, doi:10.1021/nn302099q (2012).
[265] R. Backofen, A. Voigt, and T. Witkowski, Phys Rev E **81**, doi:10.1103/PhysRevE.81.025701 (2010).
[266] S. Aland, J. Lowengrub, and A. Voigt, Phys Fluids **23**, doi:10.1063/1.3584815 (2011).
[267] C. Kohler, R. Backofen, and A. Voigt, Physical Review Letters **116**, doi:10.1103/PhysRevLett.116.135502 (2016).
[268] S. Aland, A. Ratz, M. Roger, and A. Voigt, Multiscale Model Sim **10**, 82, doi:10.1137/110834718 (2012).
[269] S. Aland, J. Lowengrub, and A. Voigt, Phys Rev E **86**, doi:10.1103/PhysRevE.86.046321 (2012).
[270] K. R. Elder, C. V. Achim, V. Heinonen, E. Granato, S. C. Ying, and T. Ala-Nissila, Physical Review Materials **5**, doi:10.1103/PhysRevMaterials.5.034004 (2021).
[271] E. Granato, M. Greb, K. R. Elder, S. C. Ying, and T. Ala-Nissila, Physical Review B **105**, doi:10.1103/PhysRevB.105.L201409 (2022).
[272] E. Granato, K. R. Elder, S. C. Ying, and T. Ala-Nissila, Physical Review B **107**, doi:10.1103/PhysRevB.107.035428 (2023).
[273] K. R. Elder, Z.-F. Huang, and T. Ala-Nissila, Physical Review Materials **7**, 024003, doi:10.1103/PhysRevMaterials.7.024003 (2023).
[274] M. Greenwood, N. Provatas, and J. Rottler, Phys Rev Lett **105**, 045702, doi:10.1103/PhysRevLett.105.045702 (2010).
[275] M. Greenwood, J. Rottler, and N. Provatas, Phys Rev E Stat Nonlin Soft Matter Phys **83**, 031601, doi:10.1103/PhysRevE.83.031601 (2011).
[276] C. Lee, X. Wei, J. W. Kysar, and J. Hone, Science **321**, 385, doi:10.1126/science.1157996 (2008).
[277] A. Politano and G. Chiarello, Nano Research **8**, 1847, doi:10.1007/s12274-014-0691-9 (2015).
[278] J.-W. Yang, Y. Yuan, and G. Chen, Molecular Physics **118**, 1, doi:10.1080/00268976.2019.1581291 (2019).
[279] C. J. Shearer, A. D. Slattery, A. J. Stapleton, J. G. Shapter, and C. T. Gibson, Nanotechnology **27**, 125704, doi:10.1088/0957-4484/27/12/125704 (2016).

[280] G. Huang, Z. Croft, M. Chlupsa, A. Mensah, D. Montiel, A. J. Shahani, and K. Thornton, In preparation.